REPORT DOCUMENTATION PAGE

Form Approved
OMB No. 0704-0188

Public reporting burden for this collection of information is estimated to average 1 hour per response, including the time for reviewing instructions, searching existing data sources, gathering and maintaining the data needed, and completing and reviewing the collection of information. Send comments regarding this burden estimate or any other aspect of this collection of information, including suggestions for reducing this burden, to Washington Headquarters Services, Directorate for Information Operations and Reports, 1215 Jefferson Davis Highway, Suite 1204, Arlington, VA 22202-4302, and to the Office of Management and Budget, Paperwork Reduction Project (0704-0188), Washington, DC 20503.

1. AGENCY USE ONLY *(Leave blank)*

2. REPORT DATE
6/12/95

3. REPORT TYPE AND DATES COVERED
Final Technical Report: 10/1/91-11/94

4. TITLE AND SUBTITLE
Micromechanics and Constitutive Modeling of Granular Materials in Stress Reversal and Cyclic Loading

5. FUNDING NUMBERS
F49620-92-J-0117

6. AUTHOR(S)
Sia Nemat-Nasser (Professor)

7. PERFORMING ORGANIZATION NAME(S) AND ADDRESS(ES)
University of California, San Diego
Department of Applied Mechanics and Engineering Sciences
Mail Code 0416
9500 Gilman Drive
La Jolla, CA 92083-0416

PERFORMING ORGANIZATION
AFOSR-TR-95
0524

9. SPONSORING/MONITORING AGENCY NAME(S) AND ADDRESS(ES)
Department of the Air Force
Air Force Office of Scientific Research
AFOSR/PKA
110 Duncan Avenue Suite B115
Bolling AFB DC 20332-0001

NA

10. SPONSORING/MONITORING AGENCY REPORT NUMBER
AFOSR F49620-92-J-0117

11. SUPPLEMENTARY NOTES
The view, opinions and/or findings contained in this report are those of the author(s) and should not be construed as an official position, policy, or decision, unless so designated by other documentation.

12a. DISTRIBUTION/AVAILABILITY STATEMENT
Approved for public release; distribution unlimited.

12b. DISTRIBUTION CODE

DTIC
ELECTE
AUG 2 2 1995
S D
F

13. ABSTRACT *(Maximum 200 words)*

The work performed under this grant, focused on fundamental research on cyclic response and response in unloading and stress-reversal regimes of granular materials. The research program included a careful examination of grain-to-grain interaction during load reversal, which results in a dramatic change in the overall response of granular materials, from loading to unloading. This was then followed by a fundamental examination of the cyclic response of granular materials under confinement, with repeated stress reversals. Parallel with the theoretical work, the research program included a series of coordinated experiments using UCSD's special large hollow cylindrical load cell and the biaxial and simple shearing load frames with photoelastic granules. These experiments served several specific purposes: (1) appropriately incorporating lead shot in the large hollow cylindrical sample, a series of X-ray photographs were taken to identify the micromechanical response during load reversal; (2) densification and/or dilatancy measurements in load reversal and cyclic loading provided guidance for the theoretical work; (3) by direct observations, using the biaxial and simple shearing facilities, micromechanical changes in unloading, load reversal, and cyclic loading were examined with the aid of photoelastic granules; and (4) controlled independent experiments were used to validate the resulting models, and to evaluate the key parameters.

14. SUBJECT TERMS
Particulate media, constitutive relation, large hollow cylindrical samples, X-ray radiographs, photo-elastic granules, shear localization, liquefaction

15. NUMBER OF PAGES
136

16. PRICE CODE

17. SECURITY CLASSIFICATION OF REPORT	18. SECURITY CLASSIFICATION OF THIS PAGE	19. SECURITY CLASSIFICATION OF ABSTRACT	20. LIMITATION OF ABSTRACT
UNCLASSIFIED	UNCLASSIFIED	UNCLASSIFIED	UL

Micromechanics and Constitutive Modeling of Granular Materials in Stress Reversal and Cyclic Loading

Accesion For	
NTIS CRA&I	☑
DTIC TAB	☐
Unannounced	☐
Justification	
By	
Distribution /	
Availability Codes	
Dist	Avail and / or Special
A-1	

FINAL TECHNICAL REPORT

October 1, 1991 to November 30, 1994

GRANT NO. AFOSR F49620-92-J-0117

to

University of California, San Diego

by

Air Force Office of Scientific Research

DTIC QUALITY INSPECTED 2

Principal Investigator: **Dr. S. Nemat-Nasser**

19950821 035

FINAL TECHNICAL REPORT

for the period

October 1, 1991 to November 30, 1994

on

Micromechanics and Constitutive Modeling of Granular Materials in Stress Reversal and Cyclic Loading

Grant No. AFOSR-F49620-92-J-0117

Dr. S. Nemat-Nasser, Principal Investigator

University of California, San Diego, La Jolla, California 92093

Table of Contents

Page

1.0 Objectives of Research (Statement of Work) 1

2.0 Status of Research Effort - Research Report 1

3.0 List of Publications 2

4.0 Professional Personnel Associated with the Research Effort 3

- PGR's and Visiting Scholars.
- Graduate Students and Degrees Awarded

5.0 Interactions (Coupling Activities) 4

- Participation at meetings; papers presented; lectures 4
- Consultative and advisory functions to other agencies, laboratories and universities 5

APPENDIX I: Simulation of Cyclic Torsional Tests on Sand

APPENDIX II: Constitutive Model for Three Dimensional Flow

APPENDIX III: Direct Observation of Deformation of Granular Materials Through X-Ray Photography

APPENDIX IV: Residual Shear Strain Effect on Undrained Response of Saturated Cohenless Granules

APPENDIX V: Fabric and Characteristics of Void Shape and Distribution in Granular Masses

1.0 OBJECTIVES OF RESEARCH

The work performed under this grant, focused on fundamental research on cyclic response and response in unloading and stress-reversal regimes of granular materials. The research program included a careful examination of grain-to-grain interaction during load reversal, which results in a dramatic change in the overall response of granular materials, from loading to unloading. This was then followed by a fundamental examination of the cyclic response of granular materials under confinement, with repeated stress reversals. Parallel with the theoretical work, the research program included a series of coordinated experiments using UCSD's special large hollow cylindrical load cell and the biaxial and simple shearing load frames with photoelastic granules. These experiments served several specific purposes: (1) appropriately incorporating lead shot in the large hollow cylindrical sample, a series of X-ray photographs were taken to identify the micromechanical response during load reversal; (2) densification and/or dilatancy measurements in load reversal and cyclic loading provided guidance for the theoretical work; (3) by direct observations, using the biaxial and simple shearing facilities, micromechanical changes in unloading, load reversal, and cyclic loading were examined with the aid of photoelastic granules; and (4) controlled independent experiments were used to validate the resulting models, and to evaluate the key parameters.

2.0 STATUS OF THE RESEARCH EFFORT

Through an integrated experimental and theoretical research effort over the course of this AFOSR grant, we have developed a physically-based constitutive model for the dynamic deformation of particulate media. The constitutive model has been tested for its predictive capabilities, using controlled experiments. In addition, the model has been used to study the stress-wave propagation in granular media.

Two sets of laboratory experiments have been performed, in order to develop a fundamental understanding of the basic physics and to incorporate the observed essential mechanisms into the constitutive models. These experiments are:

(1) Photoelastic model experiments which provide statistical information on the relation between the microstructure (fabric) of a particulate medium and its overall anisotropic response

(2) Coordinated experiments on suitable sands, using UCSD's special hollow cylindrical torsional apparatus, equipped with a unique X-ray system. This provides capability for recording the images of deformed lines and layers of embedded lead-doped granules, while measuring the overall response. This state-of-the-art unique facility, has offered an excellent opportunity to examine the physics of this complex phenomenon.

The formulation of the constitutive model was done by a graduate student, Mr. B. Balendran, as his dissertation for a Ph.D. degree, under the supervision of the PI. Part of this work has been published; see Balendran and Nemat-Nasser (1993a), published in *Journal of the Mechanics and Physics of Solids*. Appendices I and II

summarize parts of this work which have not been published. In particular, Appendix I describes how the model predicts dilatancy and densification in cyclic shearing. Appendix II applies the constitutive model to one-dimensional wave propagation, showing the coupling between pressure and shearing inherent in the response of frictional granular media.

We feel that this physically-based model provides a major constitution in this field. We have developed novel computation algorithms to implement this model into computational codes (see Balendran and Nemat-Nasser, 1993c) which should prove useful in many applications of interest to DOD.

In the experimental part of our research, we have developed unique facilities to study, under controlled conditions, cyclic response of particulate media, under *three-dimensional* stress conditions. Through fully computer-controlled, a hollow cylindrical sample of granular material can be subjected by this device to any load or deformation path. In addition, by embedding lines and layers of load-doped granules, the deformation of lines and surfaces within the specimen has been recorded through X-ray radiography. *This is the only facility of its kind that currently exists in the world.* It has been used to provide clear scientific understanding of the actual deformation mechanisms in cyclic loading of frictional particulate media.

Based on this experimental work, a micromechanical model has been developed, using the energy concept that the PI has proposed over 15years ago;** see Okada and Nemat-Nasser (1994). Appendices I to V detail our yet unpublished contributions in the following areas:

APPENDIX I	Simulation of Cyclic Torsional Tests on Sand
APPENDIX II	Constitutive Model for Three Dimensional Flow
APPENDIX III	Direct Observation of Deformation of Granular Materials Through X-Ray Photography
APPENDIX IV	Residual Shear Strain Effect on Undrained Response of Saturated Cohesionless Granules
APPENDIX V	Fabric and Characteristics of Void Shape and Distribution in Granular Masses

These contributions are being finalized for submission to scientific journals.

3.0 ARTICLES IN PEER-REVIEWED PUBLICATIONS, JOURNALS, BOOK CHAPTERS, AND EDITORSHIPS OF BOOKS. (Fully or partially supported by AFOSR F49620-92-J-0117)

PAPERS PUBLISHED

Nemat-Nasser, S. and B. Balendran, "Plastic Flow of Particulate Media", presented at the Symposium on Plastic Flow and Creep, ASME Applied Mechanics Summer Conference at Arizona State University, April

** Nemat-Nasser, S., and Shokooh, A., "A Unified Approach to Densification and Liquefaction of Cohesionless Sand in Cyclic Shearing. *Geotech. J.*, Vol. 16, (1979) 659-678.

29 - May 1, 1992, *Applied Mechanics D*, Plastic Flow and Creep, H.M. Zbib (ed.) Book No H00737, Vol. 135 (1992), 93-105.

Balendran, B. and S. Nemat-Nasser, "Double Sliding Model for Cyclic Deformation of Granular Materials, Including Dilatancy Effects", *Journal of Mechanics and Physics of Solids,* Vol. 41, No. 3, (1993a) 573-612.

Balendran, B. and S. Nemat-Nasser, "Viscoplastic Flow of Granular Materials", presented at the US-Japan Seminar on Micromechanics of Granular Materials, Potsdam, NY, August 5 - 9, 1991, *Mechanics of Materials, Special Issue of the US-Japan Seminar on Micromechanics of Granular Materials.,* Vol. 16, No. 1-2, (1993b) 1-12.

Balendran, B. and S. Nemat-Nasser, "An Efficient Algorithm for Viscoplastic Flow of Granular Materials", AMD-Vol. 171, *Advances in Numerical Simulation Techniques for Penetration and Perforation of Solids,* ASME (1993c) 111-124.

Okada, N. and S. Nemat-Nasser, "Energy Dissipation in Inelastic Flow of Cohesionless Granular Media", *Géotechnique,* Vol. 44, No. 1, (1994) 1-19.

PAPERS SUBMITTED

Nemat-Nasser, S. and N. Okada, "Direct Observation of Deformation of Granular Materials Through X-Ray Photography," Proceedings of the 10th ASCE Engineering Mechanics Speciality Conference, University of Colorado at Boulder, May 21-24, 1995, submitted.

Nemat-Nasser, S. and N. Okada, "Residual Shear Strain Effect on Undrained Response of Saturated Cohenionless Granules", *Canadian Geotechnical Journal*, submitted 2/95.

PAPERS TO BE SUBMITTED

Nemat-Nasser, S. and Z. Qui "Characteristics of Voids in Granular Mass".

Nemat-Nasser, S., "Universal Bounds for Overall Elastic Moduli of Heterogeneous Materials", to appear in special volume of JEMT, 75th Anniversary of ASME's Materials Division.

4.0 PROFESSIONAL PERSONNEL ASSOCIATED WITH THE RESEARCH EFFORT; DEGREES AWARDED (FULL AND PARTIAL SUPPORT)

Principal Investigator: S. Nemat-Nasser, Professor - Department of AMES

Postdoctoral Research Associates:

- Naoyuki Okada, PGR, 7/1/92 - 11/94 (non -US citizenship)
- Balasingham Balendran, PGR, 3/93 - 7/93 (non -US citizenship, permanant resident)

Visiting Scholars:

- Zong-Lian Qui (Professor, Tsinghua University, Department of Civil Engineering, Beijing, China), non - US citizenship, 8/20/92 - 11/94

Graduate Students: (Advisor: S. Nemat-Nasser) Degree Awarded

N. Okada - Research Assistant, 10/91 - 6/92 Ph.D. Applied Mechanics
Thesis: "Energy Dissipation in Inelastic Flow of Cohesionless Granular Media"

B. Balendran - Research Assistant, 10/91 - 12/92 Ph.D. Applied Mechanics
Thesis: "Physically-Based Constitutive Modeling of Granular Materials"

H. Deng - Research Assistant, 10/91 - 12/92 Ph.D. Applied Mechanics
Thesis: "Dynamic Damage Evolution in, and Failure of Brittle Solids in Compression"

5.0 INTERACTIONS (Coupling Activities)

A. PARTICIPATION AT MEETINGS, PAPERS PRESENTED; LECTURES AT SEMINARS AND WORKSHOPS.

(* Indicates those interactions and presentations which have a more direct relation to this AFOSR award.)

S. Nemat-Nasser, "Target Configurations for Plate-Impact Recovery Experiments," ASME Applied Mechanics, Materials and Aerospace Summer Meeting, Tempe Arizona, April 25-May 2, 1992.

S. Nemat-Nasser, "Metal-Matrix/Ceramic Composites: Estimate of Flow Stress with Lower and Upper Bounds," ASME Applied Mechanics, Materials and Aerospace Summer Meeting, Tempe, Arizona, April 25-May 2, 1992.

*S. Nemat-Nasser, "Physically-Based Modeling for Computational Evaluation of Materials Degradation," *Invited Lecture*, DOE Workshop on Aging of Energy Production and Distribution Systems, Rice University, Houston, Texas, October 11-13, 1992.

*S. Nemat-Nasser, "Dynamic Behavior of Ceramics Under Impact and Penetration: Constitutive Modeling and Experiments at UCSD," DARPA Armor/Anti-Armor Tech Base Program Review, Sandia National Laboratories, January 21, 1993.

*B. Balendran, "Exact Integration of Elastic Perfectly Plastic Constitutive Equations with Non-Coaxality for Large Rotations," Meet'N'93 - Joint Meeting of ASME, SES and ASCE, Charlottesville, VA, June 6-9, 1993.

*H. Deng, "Shear Fault Failure and Its Optimal Direction," Meet'N'93 - Joint Meeting of ASME, SES and ASCE, Charlottesville, VA, June 6-9, 1993.

*S. Nemat-Nasser, "Experimental Statistical Evaluation of Granular Fabric and Microstructurally-Based Measures of Overall Stress," *Invited Lecture*, NSF Workshop on The Statistical Characterization of Material Microstructure and Its Relation to Material Performance, The Catholic University of America, Washington D.C., June 28 - July 1, 1993.

S. Nemat-Nasser, "Experimental Evaluation of Strain, Strain-Rate and Temperature Dependence of Flow Stress at High Strain Rate," Fourth International Symposium on Plasticity and Its Current Applications, Baltimore, MD, July 19-23, 1993.

S. Nemat-Nasser, "Double Inclusion Model and Overall Moduli of Multi-Phase Composites," 1993 WAM - Symposium on Micromechanics of Composites, New Orleans, LA, November 28-December 3, 1993.

S. Nemat-Nasser, "Mechanics of Interface Fracture of Anistropic Bi-Materials," 1993 WAM - Symposium on Ultrasonic Characterization and Mechanics of Interface, New Orleans, LA, November 28-December 3, 1993.

S. Nemat-Nasser, "Large Scale Crack Bridging and Strongly Singular Integral Equations," 1993 WAM - Symposium on Ultrasonic Characterization and Mechanics of Interface, New Orleans, LA, November 28-December 3, 1993.

*S. Nemat-Nasser, "An Efficient Algorithm for Viscoplastic Flow of Granular Materials," 1993 WAM -

Symposium on Advances in Numerical Simulation Techniques for Penetration and Perforation of Solids, New Orleans, LA, November 28-December 3, 1993.

S. Nemat-Nasser, "A New Approach to Computational Crystal Plasticity: FCC Crystals," 1993 WAM - Symposium on Advanced Computational Methods in Material Modeling, New Orleans, LA, November 28-December 3, 1993.

*S. Nemat-Nasser, "Constitutive Modeling of the Behavior of Granular Materials," *Invited Speaker*, Workshop on Theory and Simulation of Compaction and Sintering of Powders, Tulane University, New Orleans, LA, December 3-6, 1993.

S. Nemat-Nasser, "Time-Resolved Measurement of Dynamic Fracture Toughness of Composites Subjected to a Stress Pulse," Symposium on Dynamic Failure Mechanics of Modern Materials, Caltech, Pasadena, February 3, 1994.

S. Nemat-Nasser, "A Duality Principle in Elasticity," 12th US National Congress of Applied Mechanics, Symposium on Multiphase Elasticity and The Dundurs Parameters II Seattle, WA, June 28, 1994.

*S. Nemat-Nasser, "Effects of Particulate Microstructure on Rate-Dependent Fatigue Life of a Class of Advanced Ceramics," Workshop on Mechanics and Statistical Physics of Particulate Materials, IMM/NSF/AFOSR, UCSD, June 8-10, 1994.

*S. Nemat-Nasser, "Characterizing Dynamic Response of Tungsten and Its Alloys," Meeting on Tungsten Alloys for Kinetic Energy Penetrator Application - Research Capabilities and Needs, Army Research Office, Pictanny Arsenal,, NJ, July 28, 1994.

S. Nemat-Nasser, "Bounds for Overall Elastic Properties of Heterogeneous Solids," IUTAM Symposium on Microstructure Property Interactions in Composite Materials, Aalborg, Denmark, August 23-25, 1994.

S. Nemat-Nasser, "Fracturing in Anisotropic Solids," *Principal Lecture*, IUTAM/ISIMM Symposium on Anisotropy, Inhomogeneity and Nonlinearity in Solid Mechanics, University of Nottingham, U.K., September 2, 1994.

S. Nemat-Nasser, "Dynamic Response of Certain CVD Tungsten," Ist Mechanical Engineering Symposium, Prairie View A&M University, October 27-28, 1994.

*S. Nemat-Nasser, "Computational Modeling of Large Deformation and Rotation in Inelastic Flow with Friction," IMECE'94 - Symposium on Computational Material Modeling, Chicago, Ill, November 5-11, 1994.

*S. Nemat-Nasser, "Dynamic and Quasi-Static Compression Fatigue of Silicon Nitride," IMECE '94 - Symposium on Damage Mechanics in Composites, Chicago, November 5-11, 1994.

B. PRINCIPAL INVESTIGATORS CONSULTATIVE AND ADVISORY FUNCTIONS WITH OTHER AGENCIES, LABORATORIES AND UNIVERSITIES.

*AFOSR Contractors Meeting - Mechanics of Materials, Dayton, OH, October 8, 1991.

*AFOSR Contractors Meeting - Particulate Mechanics, Kirtland AFB, January 7, 1992.

NSF Materials Research Science and Engineering Centers Panel Meeting, NSF, Arlington, VA, November 15, 1993.

Workshop on Tantalum and Tantalum Alloys, US Army Armament RDE Center, Picatinny Arsenal, N.J., November 18, 1993.

*Workshop on Theory and Simulation of Compaction and Sintering of Powders, Tulane University, LA, December 3-6, 1993.

*WIPP Fracturing Expert Group, Sub-Group Meeting; Implementation of FxG Recommendations, Albuquerque, NM., December 16, 1993.

*DNA Meeting, Washington D.C., February 24, 1994.

*Think-Tank on Materials Science and Engineering in the 21st Century, IMM - UCSD, May 20, 1994.

*Workshop on Mechanics and Statistical Physics of Particulate Materials, Sponsored by IMM/NSF/AFOSR, University of California, San Diego, La Jolla, CA, June 8-10, 1994.

*DNA Meeting, Washington D.C., June 15, 1994.

*Meeting on Tungsten Alloys for Kinetic Energy Penetrator Application - Research Capabilities and Needs, Army Research Office, Pictanny Arsenal, NJ, July 28, 1994.

APPENDIX I

SIMULATION OF CYCLIC TORSIONAL TESTS ON SAND

Principal Investigator: Sia Namet-Nasser

Postdoctoral Fellow: Bala Balendra

I.1 INTRODUCTION

When a granular mass is subjected to shearing under drained conditions, the individual grains rearrange by sliding and rolling over each other. As a result, there is always a volumetric strain accompanying the shear strain. It has been universally observed in experiments, that a granular mass when subjected to monotonic shearing, initially densifies and subsequently dilates. When a granular mass is subjected to cyclic shearing under constant normal stresses, it always densifies during unloading, resulting in a net densification when the shear strain is completely reversed. When subjected to continuous cyclic loading, the net densification per cycle continues to decrease with the number of cycles until the void ratio reaches asymptotically a minimum value. This subject has been experimentally treated extensively by a number of investigators who have brought into focus essential features of this phenomenon; Silver and Seed (1971), Youd (1970, 1972). Arthur (1971) and Thurairajah (1973) investigated the effect of stress reversal in shear deformation of sand and showed that the anisotropy induced in the sample during shear in one direction alters the deformation characteristics in the other directions of stress application.

The relation between stress and dilatancy for sand under undrained conditions has been investigated by many researchers; see Taylor (1948), Newland and Allely

(1957), Rowe (1962), Roscoe *et al.* (1963), Schofield and Wroth (1968), Matsuoka (1974), and Nemat-Nasser (1980). In particular, Nemat-Nasser (1980) has used an energy equation to explain the phenomena of dilatancy (compaction) in monotonic as well as in cyclic deformation. This has been used by Nemat-Nasser and Takahashi (1984) to simulate the experimental results.

I.2 SIMULATION

In this Appendix we consider the constitutive equations developed by Balendra and Nemat-Nasser (1993a) to simulate the experimental results of cyclic torsional tests on sand under drained conditions, performed in a hollow cylindrical apparatus by Okada (1992). The schematic diagram of the hollow cylindrical sample is given in Fig. I.1a. In the experiment, first, the specimen was isotropically consolidated under an effective pressure of 196 kPa. Upon completion of consolidation, the specimen was subjected to a strain controlled cyclic torsional shearing while the normal stresses are kept constants.

Consider the polar coordinates as shown in Fig. I.1a. The state of the stress in a shell element of the sample in polar coordinate system is given by $\sigma_{rr} = \sigma_{\theta\theta} = \sigma_{zz} = -p$, $\sigma_{r\theta} = \sigma_{rz} = 0$, and $\sigma_{\theta z} = \tau$, where τ is the torsional shear stress measured during the strain controlled test; see Fig. I.1b. During the course of deformation, the inner and outer surfaces of the shell are free to move away or towards the center of the cylinder, causing a hoop strain $\varepsilon_{\theta\theta}$ and a radial strain ε_{rr}. The sample is also free to dilate or contract axially, causing an axial strain ε_{zz}. The volumetric strain, ε_v, is given by the sum of all the normal strains; $\varepsilon_v = \varepsilon_{rr} + \varepsilon_{\theta\theta} + \varepsilon_{zz}$. In the experiment, the shear strain $\varepsilon_{\theta z}$ was controlled and the axial strain and volumetric strain were measured. Since the strain was controlled by

controlling the torsional displacement at the ends of the sample, the sample is also subjected to a spin which is equal to the shear strain $\varepsilon_{\theta z}$, in θz–plane.

In order to simulate the experimental results, we assume that the sample deformed homogeneously along the cylindrical axis. Noting that the thickness (2.5cm) of the sample is small compared to the height (25cm) and to the diameter (22.5cm) of the sample, we neglect the change in thickness, *i.e.* $\varepsilon_{rr} = 0$. As a result of this assumption, this test can be modeled as a simple shearing in the θz–plane under constant pressure. If we denote the θ–direction by x_1 and the z–direction by x_2, this experiment can be modeled by the *Double Sliding Model for Planar Deformation of Granular Materials* developed by Balendra and Nemat-Nasser (1993b).

Shown in Figs. I.2-I.4 are the experimental results of relations between stress ratio ($\mu_f = \tau / p$), volumetric strain (ε_v), axial strain (ε_A), and the shear strain ($\gamma = 2\,\varepsilon_{\theta z}$) in cyclic shearing of *Silica 60* sand with initial void ratio $e_0 = 0.71$ for various amplitudes of shear strain. The stress–strain relations show that the irrecoverable deformation occurs not only in loading but also in unloading and reloading. Even in loading, the elastic range is quite small and can be neglected. In the absence of elastic range, the constitutive equations for the *Double Sliding Model* takes the form,

$$\overset{\circ}{\sigma}_{kk} = 2K\,(D_{kk} - \dot{\gamma} B)\,, \qquad \boldsymbol{\sigma}' = p\,\boldsymbol{\beta}\,,$$

$$\overset{\circ}{\boldsymbol{\sigma}} = 2G\left[\mathbf{D}' - \alpha\,(\mathbf{1} - \boldsymbol{\mu}\otimes\boldsymbol{\mu}):\mathbf{D}' - \dot{\gamma}\frac{\boldsymbol{\mu}}{\sqrt{2}}\right],$$

$$\boldsymbol{\mu} = \zeta\,\frac{\boldsymbol{\beta}}{\sqrt{2}\,\mu_\beta}\,, \qquad \mu_\beta = (\tfrac{1}{2}\boldsymbol{\beta}:\boldsymbol{\beta})^{1/2}\,, \tag{I.2.1a-e}$$

where B is the dilatancy parameter, α is the noncoaxiality coefficient, $\boldsymbol{\beta}$ is the back stress coefficient tensor defining the fabric anisotropy, and where $\zeta = sign\,(G\,\boldsymbol{\sigma}':\mathbf{D}' +$

$K\,\mu_\beta^2 D_{kk}$), denotes whether it is loading or unloading. Evolution of the fabric is denoted by the change in back stress coefficient tensor, $\boldsymbol{\beta}$, as

$$\overset{\circ}{\boldsymbol{\beta}} = \sqrt{2}\,\dot{\mu}_f\,\boldsymbol{\mu} + \rho(\mathbf{1} - \boldsymbol{\mu}\otimes\boldsymbol{\mu}):\mathbf{D}', \quad \mu_f = (\boldsymbol{\beta}:\boldsymbol{\mu})/\sqrt{2}, \tag{I.2.2a,b}$$

where μ_f is the effective frictional resistance in the direction of $\boldsymbol{\mu}$ and where the scalar ρ is related to the shear modulus G and the noncoaxiality coefficient α by

$$\rho = 2G\,(1 - \alpha)\,. \tag{I.2.3}$$

The dilatancy parameter B and the noncoaxiality coefficient α are related to the anisotropic frictional resistance μ_f and the microscopic frictional angle ϕ_μ by

$$B = \tan\delta, \qquad \alpha = -\tan\delta,$$

$$\delta = \phi_f - \phi_\mu, \quad \phi_f = \tan^{-1}\mu_f\,. \tag{I.2.4a-d}$$

The rate of change of the frictional resistance due to plastic shearing is given by the hardening laws.

Substituting the simple shear ($L_{21} = 0$) and constant pressure ($\dot{\sigma}_{11} = \dot{\sigma}_{22} = 0$) conditions into (I.2.1), we have

$$D_{kk} = \dot{\gamma}B\,, \quad D'_{11} = \frac{-W_{12}\sigma_{12}}{G\,(1-\alpha)}, \quad W_{12} = -W_{21} = D_{12} = D_{21}\,,$$

$$\dot{\mu} = G\,(2\zeta D_{12} - \dot{\gamma}), \quad \zeta = sign(D_{12}), \quad \sigma_{12} = \zeta\mu_f\,p\,. \tag{I.2.5a-f}$$

We now approximate the velocity gradient in (I.2.5) by the strain rate for small deformations, *i.e.*, $\mathbf{D} = \dot{\boldsymbol{\varepsilon}}$. We further assume that the elastic strain rate $\dot{\varepsilon}_{12}^e$ is negligible when compared to the plastic strain rate $\dot{\varepsilon}_{12}^p$, *i.e.* $\dot{\gamma} = 2\zeta\dot{\varepsilon}_{12}$. Substituting these assumptions into (I.2.5) for monotonic shearing, we get

$$\frac{d\varepsilon_v}{d\gamma} = B$$

$$\frac{1-\alpha}{\mu_f}\frac{d\varepsilon_{11}'}{d\gamma} = -\frac{p}{2G},$$

$$\sigma_{12} = \zeta \mu_f p, \quad \mu_f = \tan(\phi_f). \tag{I.2.6a-d}$$

We consider a very simple hardening law where the anisotropic frictional resistance, with respect to the rate of shearing is related to its deviation from the maximum saturation value μ_s by,

$$\frac{\delta\mu_f}{d\gamma} = a\,(\mu_s - \mu_f)^2. \tag{I.2.7}$$

Integrating (I.2.7), we get

$$\frac{\gamma - \gamma_0}{\mu_f - \mu_0} = \frac{1}{\mu_s - \mu_0}(\gamma - \gamma_0) + \frac{1}{a\,(\mu_s - \mu_0)^2}, \tag{I.2.8}$$

where μ_0 and γ_0 are the initial values of the effective frictional resistance and the shear strain respectively. The relation between γ/μ_f and γ in the monotonic shearing from the first quarter of the first cycle for which $\mu_0 = \gamma_0 = 0$, is shown in Fig. I.5. The experimental results prove the applicability of the linear relation (I.2.8). The maximum saturation value, μ_s, and the hardening constant, a, are obtained from a regression analysis to be 0.71 and 2.1 respectively. The experimental results of angle of dilatancy are evaluated from,

$$\delta = \tan^{-1}(d\varepsilon_{kk}/d\gamma). \tag{I.2.9}$$

The experimental results of angle of dilatancy and the effective angle of friction are plotted against the shear strain in Fig. I.6. The results prove the applicability of the dilatancy equation (I.2.4c). The microscopic angle of friction ϕ_μ is obtained to be 31°.

The noncoaxial deviatoric strain ε_{11}' is related to the volumetric strain ε_v and the

axial strain ε_{22} by

$$\varepsilon_{11}' = \frac{1}{2}\varepsilon_v - \varepsilon_{22}. \tag{I.2.10}$$

The experimental values of the left hand side of (I.2.6b) is plotted against the shear strain in Fig. I.7. The experimental value is almost constant throughout the loading which is in good agreement with (I.2.6b) for constant pressure test. The value of the shear modulus is obtained to be $2.8p$. So far we have obtained four model parameters from the experimental results of the monotonic shearing alone.

We note that when a granular mass is subjected to shearing under constant pressure, the frictional energy dissipation is proportional to the interparticle frictional coefficient and to the ratio of the number of active contacts to the total number of contacts in the volume. Therefore, the macroscopic angle of friction is a measure of the number of active contacts multipled by the interparticle angle of friction. In cyclic loading, though there is plastic unloading at the time of stress reversal, the number of active contacts for frictional sliding is negligible. At the time of stress reversal, plasticity is only due to the fabric anisotropy where the energy released by shear unloading contributes to the densification. However, during unloading particles rearrange and the number of active contacts in the unloading direction reaches its saturation value rapidly. As the material densifies, the number of active contact increases, resulting in an increase in the microscopic frictional resistance. Therefore, it is reasonable to assume that the microscopic angle of friction is zero at the time of stress reversal and increases hyperbolically to the value ϕ_μ. In this manner, we rewrite the dilatancy equation (I.2.4a)

$$\delta = \phi_f - \phi_\mu \frac{c\gamma}{1 + c\gamma} + c_1(e - e_0),$$

where c is a constant which controls the rate at which the number of active contacts saturates in reverse loading and c_1 corresponds to the change in microscopic frictional resistance with change in void ratio.

We use c=5 and $c_1 = 0$ together with the four parameters obtained from the monotonic shearing to simulate the experimental results for a cycle of shearing with different amplitudes. The results of the theoretical simulation and the experiments are compared in Figs. I.7-I.9. The results show that the simulation duplicate the experimental results to a reasonable degree of accuracy for three different amplitudes.

In simulating the experimental results for one cycle, we neglect the effect of change in density on the microscopic frictional resistance. However, the change in density has a greater effect in continuous cyclic shearing even for small amplitudes because of high densification. In Balendra and Nemat-Nasser (1993a, 1993b), we assumed that the saturation value of the anisotropic frictional resistance to be linearly related to the void ratio. This can be written as

$$\mu_s = \mu_{s0} - b\,(e - e_0),$$

where μ_{s0} is the value obtained from monotonic shearing. Shown in Figs. I.10-I.12 are the comparison of theoretical simulation with experimental results for continuous cyclic shearing. For the theoretical simulation, we use seven parameters; (μ_{s0}, a, ϕ_μ, G, b, c c_1). Four of the seven parameters are obtained from the monotonic shearing experiment; (μ_{s0}, a, ϕ_μ, G). For continuous cyclic shearing, we use $b = 0$, $c = 5$, and $c_1 = 0.05$ for large amplitude (*i.e.* 2.0%), and $b = 0.1$, $c = 5$, and $c_1 = 0.05$ for small amplitudes (*i.e.* 0.5% and 1.0%). The relations between stress, shear strain, and volumetric strain are simulated to a reasonable degree of accuracy. However, the axial strain response is poorly simulated.

REFERENCES

Arthur, J.F.R. (1971). New Techniques to Measure New Parameters, Stress–Strain Behavior of Soils. *Proceedings of Roscoe Memorial Symposium,* pp. 340-346.

Balendran, B., & Nemat-Nasser, S. (1993a). Double sliding model for cyclic deformation of granular materials, including dilatancy effects. *Journal of Mechanics and Physics of Solids,* **41**, No. 3, pp. 573-612.

Balendran, B., & Nemat-Nasser, S. (1993b). Viscoplastic flow of planar granular materials. *Mechanics of Materials*, **16**, pp. 1-12.

Matsuoka, H. (1974). Dilatancy Characteristics of Soil. *Soils and Foundations,* **14**, No. 3, pp. 13-23.

Newland, P.L., and Allely, B.H. (1957). Volume Changes in Drained Triaxial Test on Granular Materials. *Géotechnique,* **7**, No. 1, pp. 17-34.

Okada, N. (1992). Energy dissipation in inelastic flow of cohesionless granular media. Ph.D. thesis, University of California at San Diego.

Roscoe, K.H., Schofield, A.N., and Thurairajah, A. (1963). Yielding of Clays in States Wetter than Critical. *Géotechnique,* **13**, No. 3, pp. 211-240.

Rowe, P. W. (1962). The Stress-Dilatancy Relation for Static Equilibrium of an Assembly of Particles in Contact. *Proc. Roy. Soc.* A. **269**, pp. 500-527

Schofield, A.N., and Wroth, C.P. (1968). Critical State Soil Mechanics. McGraw Hill, New York.

Silver, M.L., and Seed, H.B. (1971). Deformation Characteristics of Sands Under Cyclic Loading. *Journal of the Soil Mechanics and Foundations Division-ASCE,* **97**, No. SM8, pp. 1081-1098.

Taylor, D.W. (1948). Foundamentals of Soil Mechanics. John Wiley, New York.

Thurairajah, A. (1973). Shear Behavior of Sand Under Stress Reversal. 439-445 *Proceedings of the 8th International Conference on Soil Mechanics and Foundation Engineering,* pp.439-445.

Youd, T.L. (1970). Densification and Shear of Sand During Vibration. *Journal of Soil Mechanics and Foundations Division-ASCE,* **96**, No. SM3, pp. 863-880.

Youd, T.L. (1972). Compaction of Sands by Repeated Shear Straining. *Journal of the Soil Mechanics and Foundations Division-ASCE,* **98**, No. SM7, pp. 709-725.

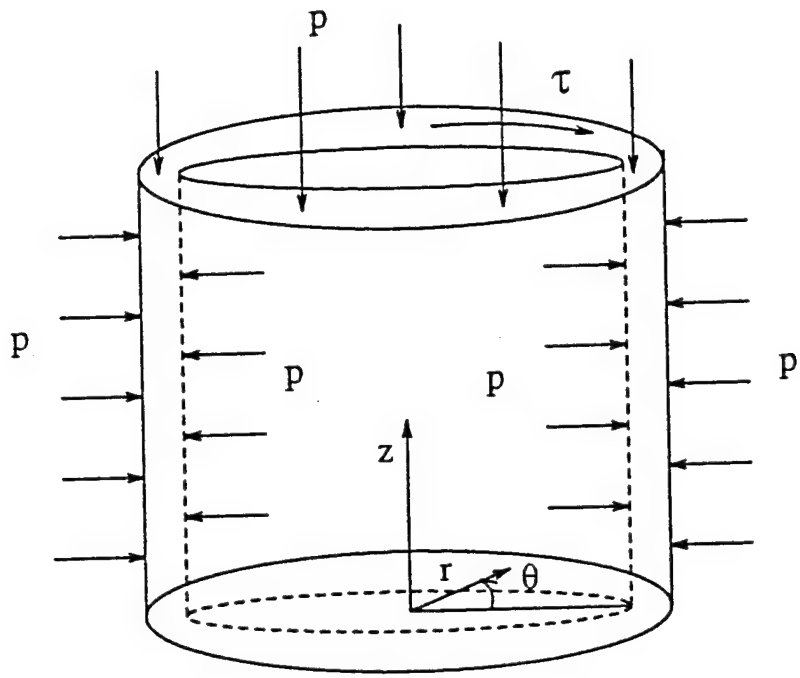

Figure I .1a Schematic diagram of a hollow cylindrical sample subjected to a hydrostatic pressure p and a torsional shear stress τ.

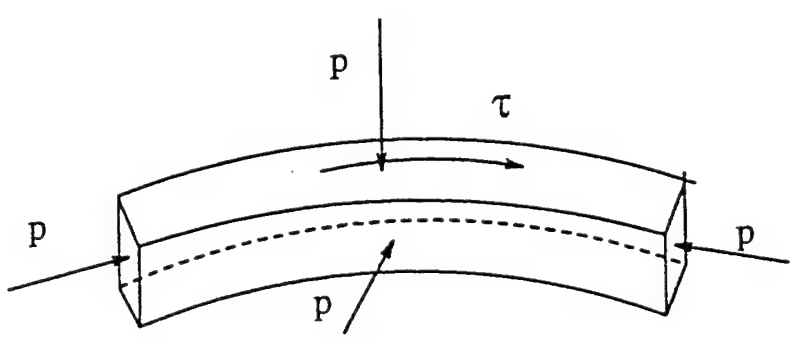

Figure I.1b State of the stress in a ring element of the hollow cylindrical sample.

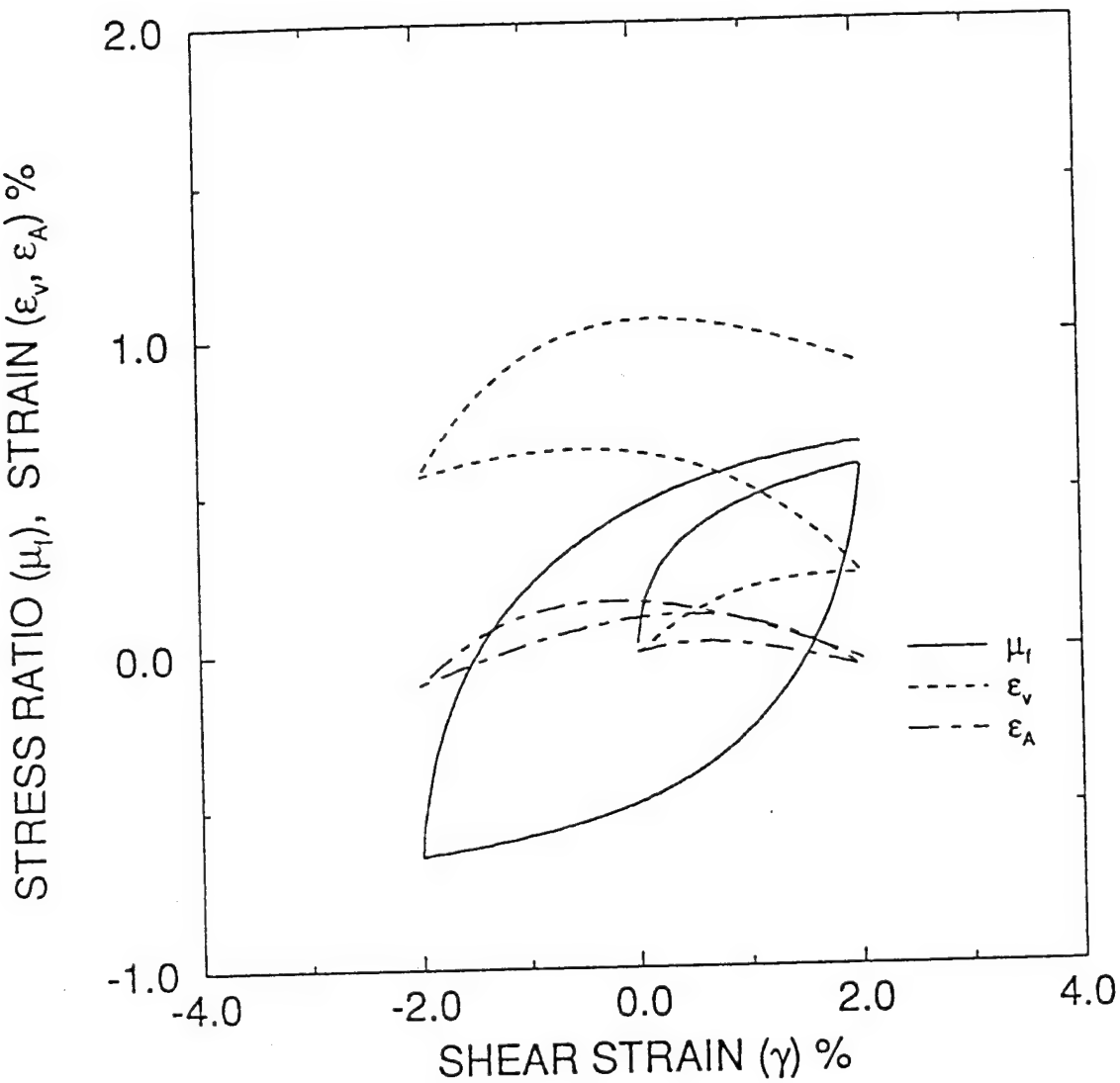

Figure I.2 Experimental relations between stress ratio, volumetric strain, axial strain and the shear strain in cyclic shearing with a shear strain amplitude of 2%.

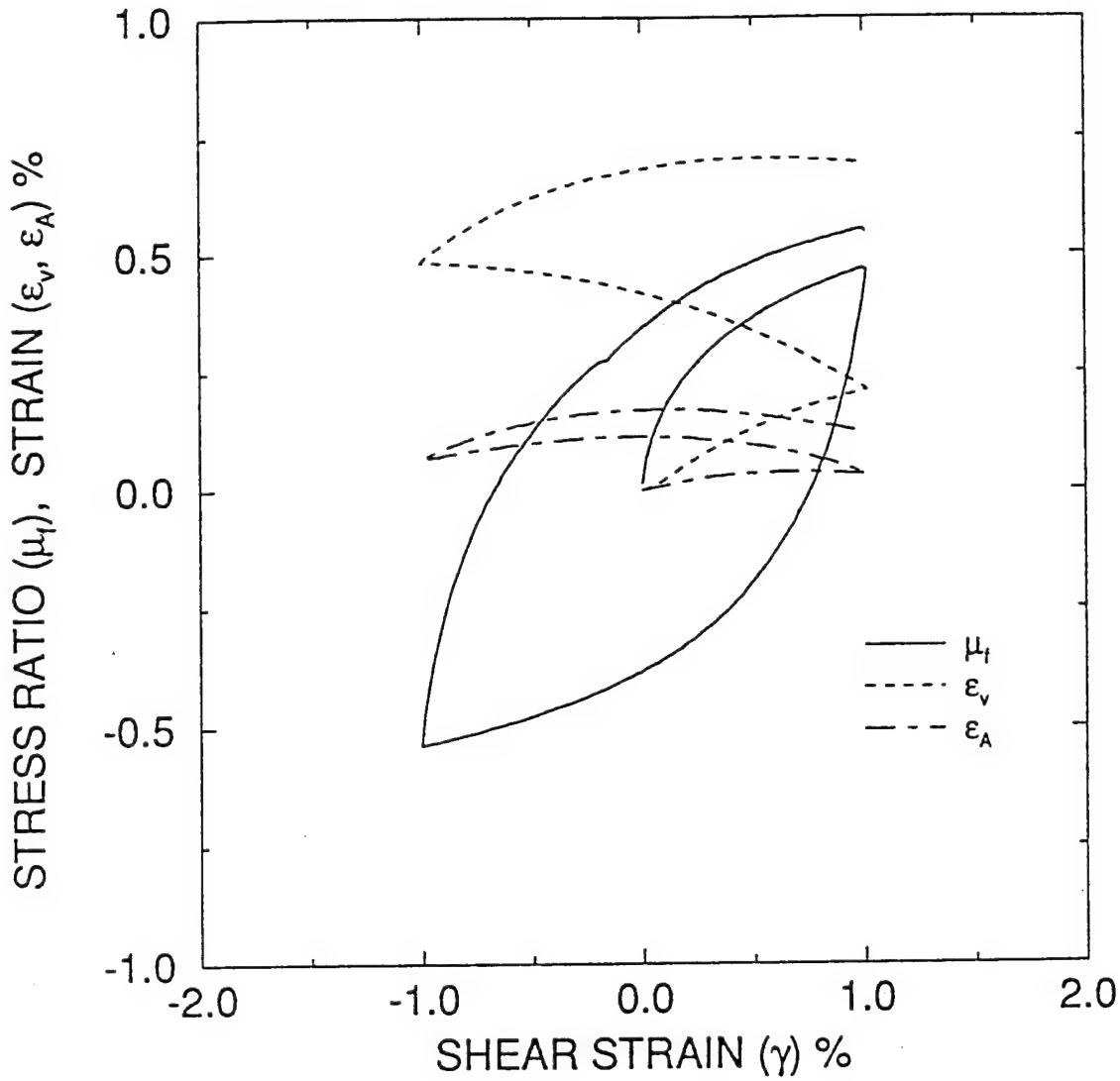

Figure I.3 Experimental relations between stress ratio, volumetric strain, axial strain and the shear strain in cyclic shearing with a shear strain amplitude of 1%.

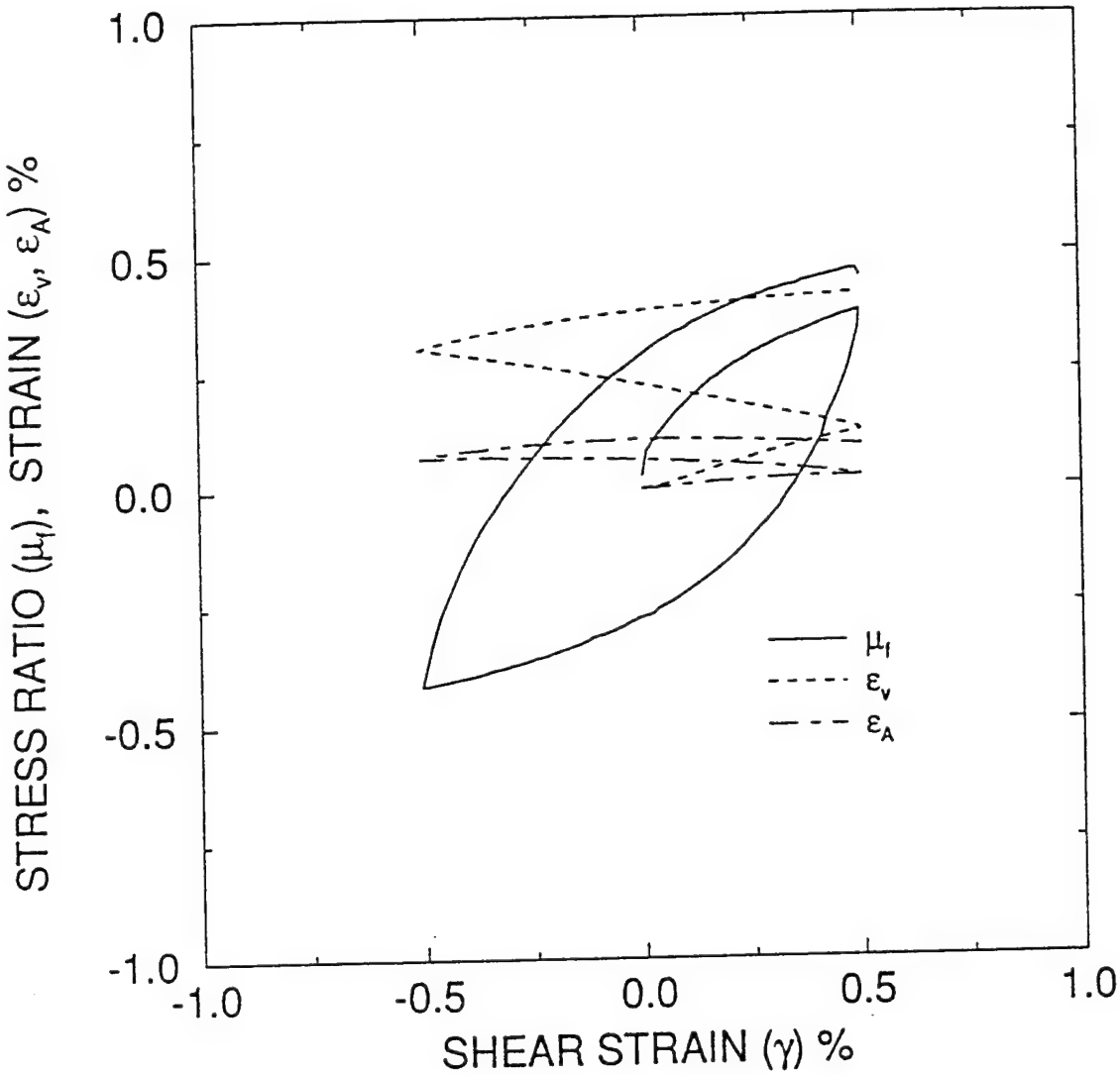

Figure I.4 Experimental relations between stress ratio, volumetric strain, axial strain and the shear strain in cyclic shearing with a shear strain amplitude of 0.5%.

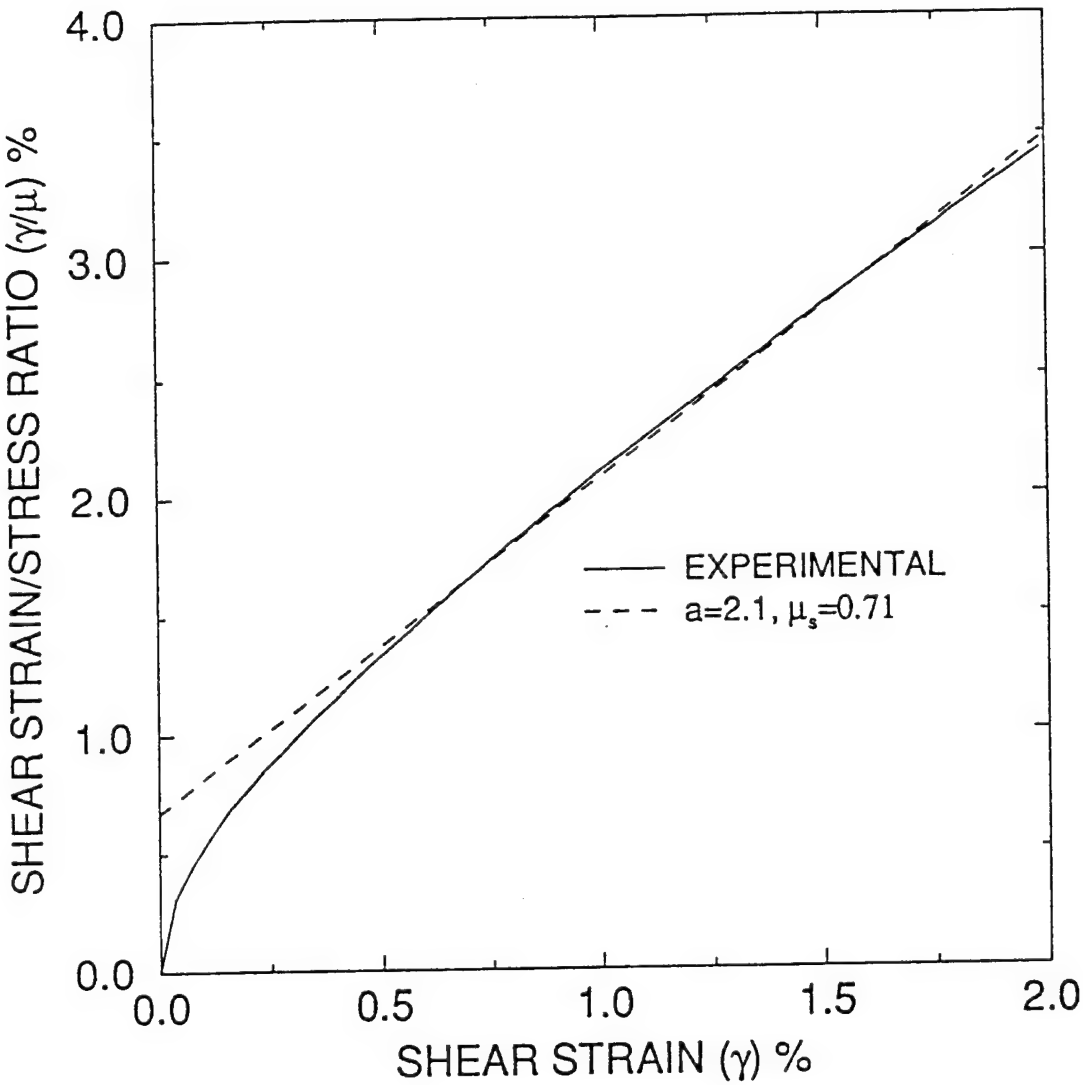

Figure I.5 Evaluation of the hardening rate parameter and the saturation value of anisotropic frictional coefficient from the experimental results for monotonic shearing.

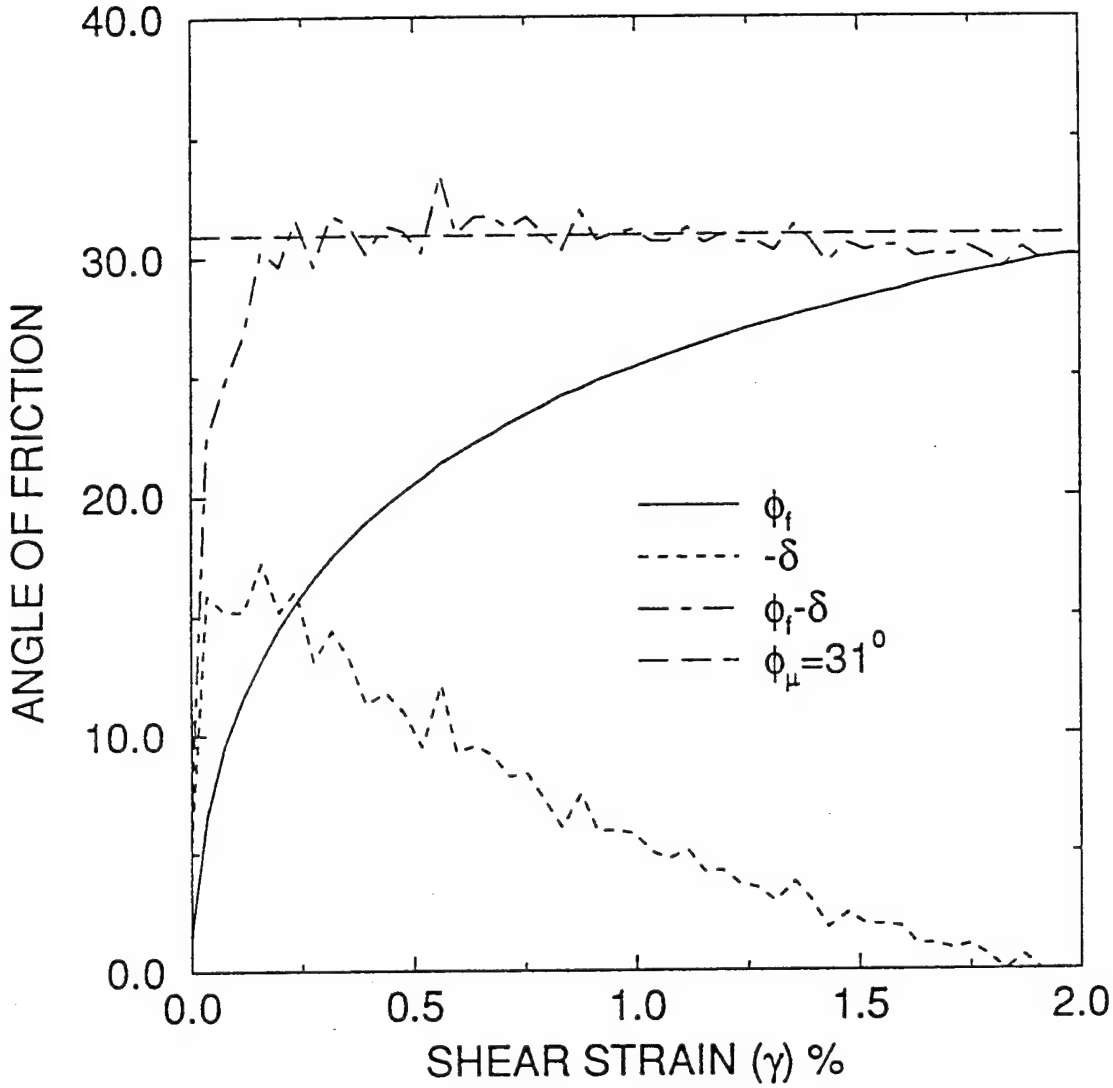

Figure I.6 Evaluation of the microscopic angle of friction coefficient from the experimental results for monotonic shearing.

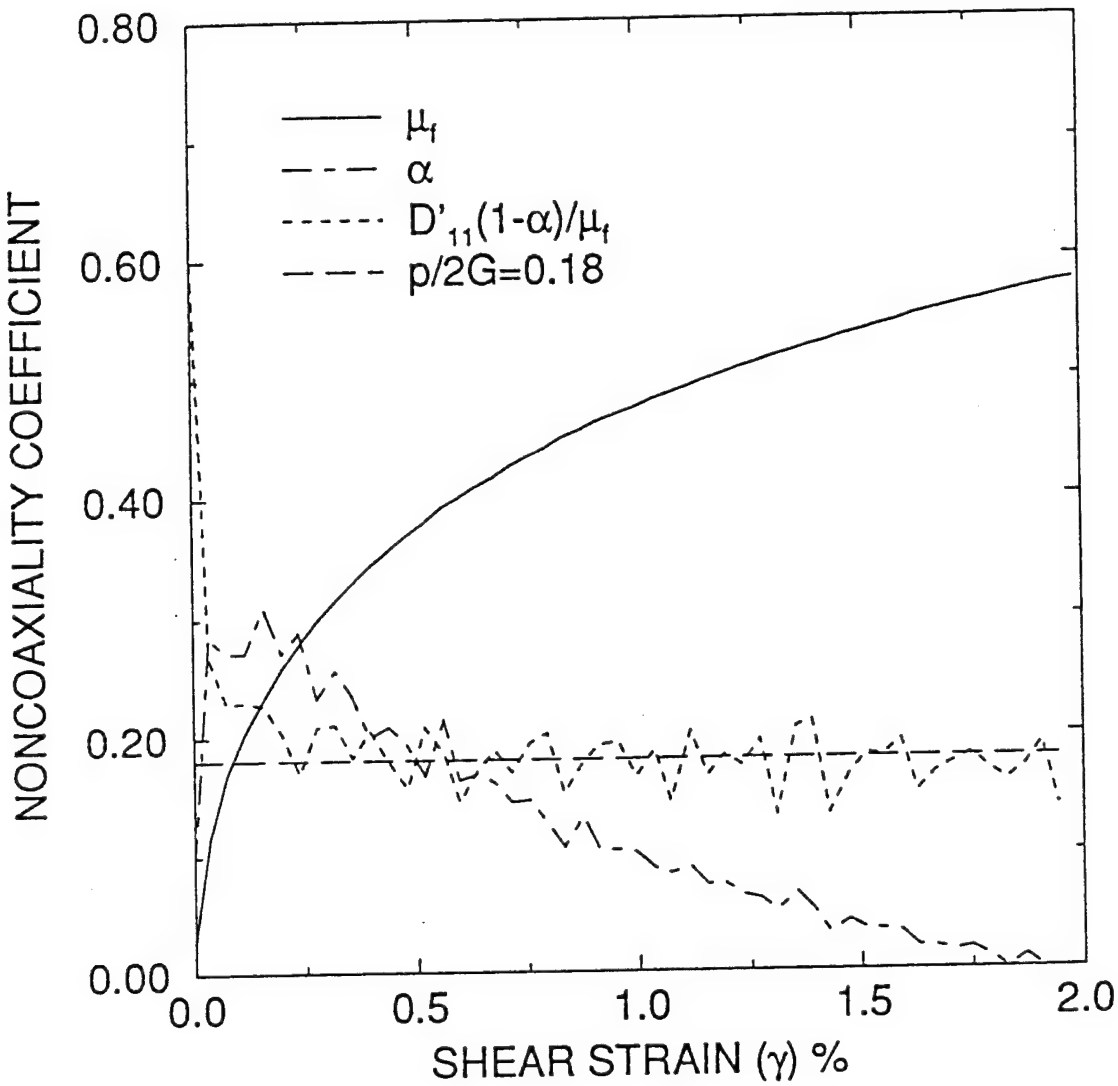

Figure I.7 Evaluation of the shear modulus from the experimental results for non-coaxial deformation in monotonic shearing.

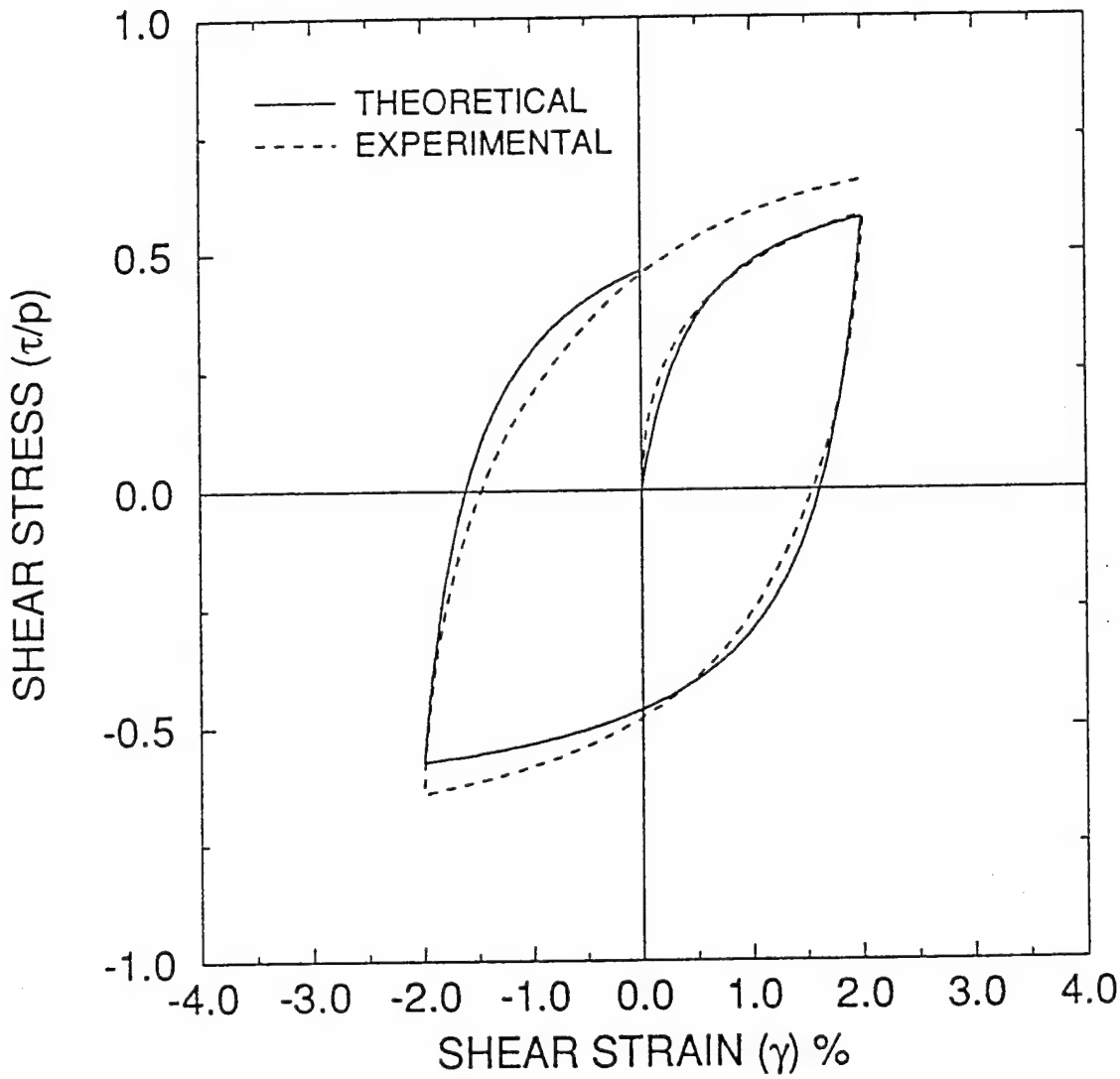

Figure I.8a Comparison of theoretical simulation with experimental results in a cycle of shearing; relation between stress ratio and shear strain (amplitude of the shear strain = 2%).

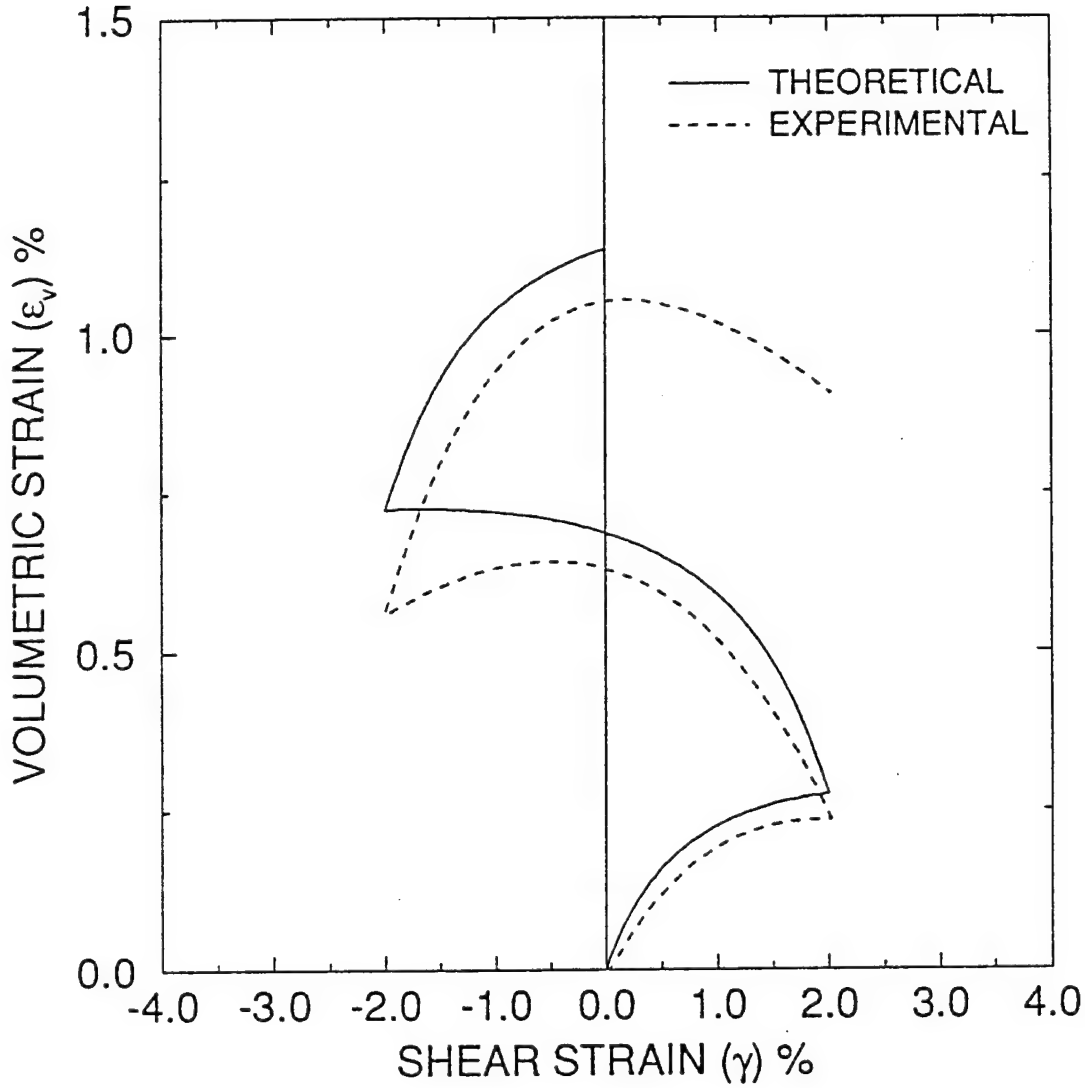

Figure I.8b Comparison of theoretical simulation with experimental results in a cycle of shearing; relation between volumetric strain and shear strain (amplitude of the shear strain = 2%).

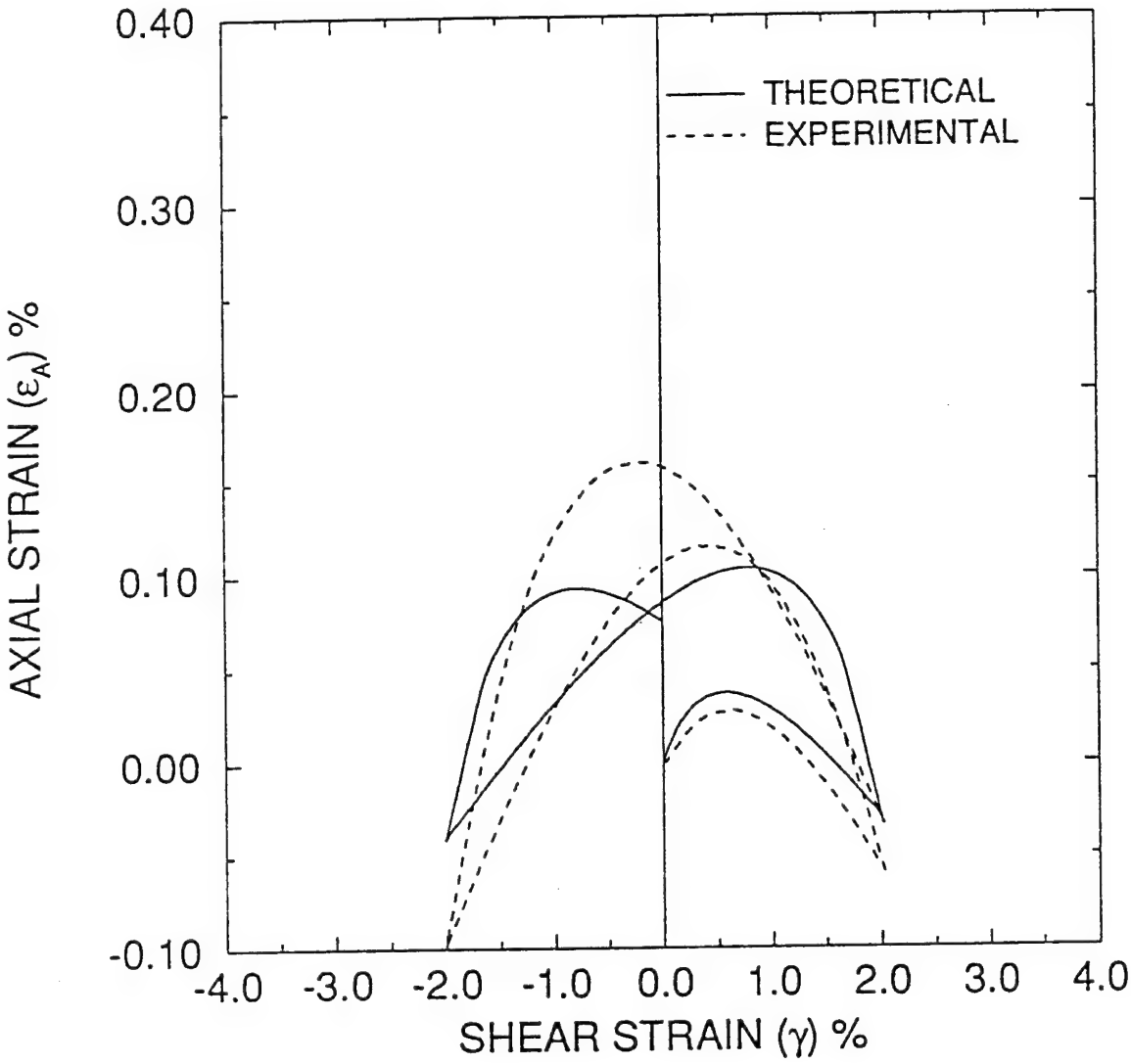

Figure I .8c Comparison of theoretical simulation with experimental results in a cycle of shearing; relation between axial strain and shear strain (amplitude of the shear strain = 2%).

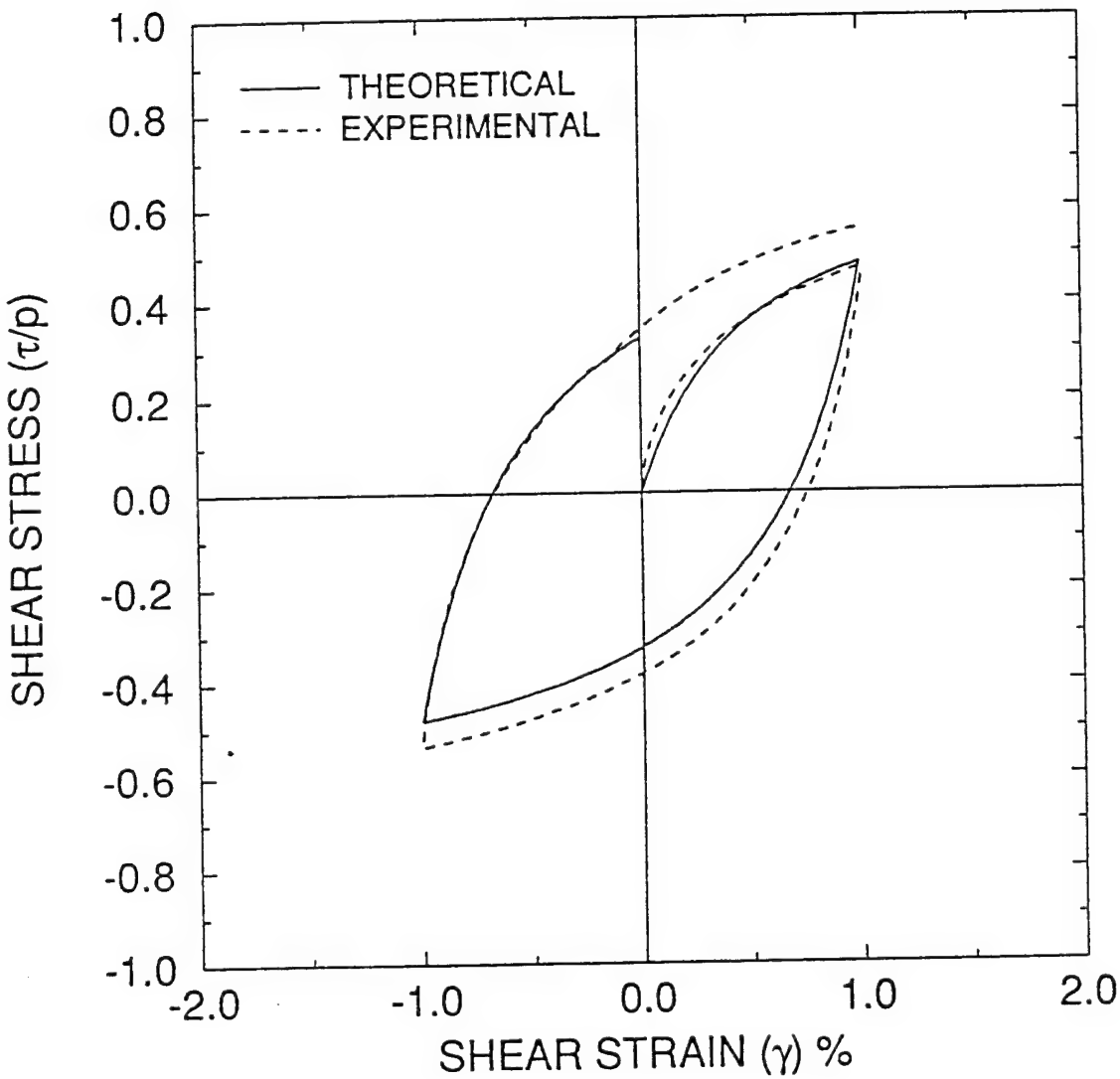

Figure I.9a Comparison of theoretical simulation with experimental results in a cycle of shearing; relation between stress ratio and shear strain (amplitude of the shear strain = 1%).

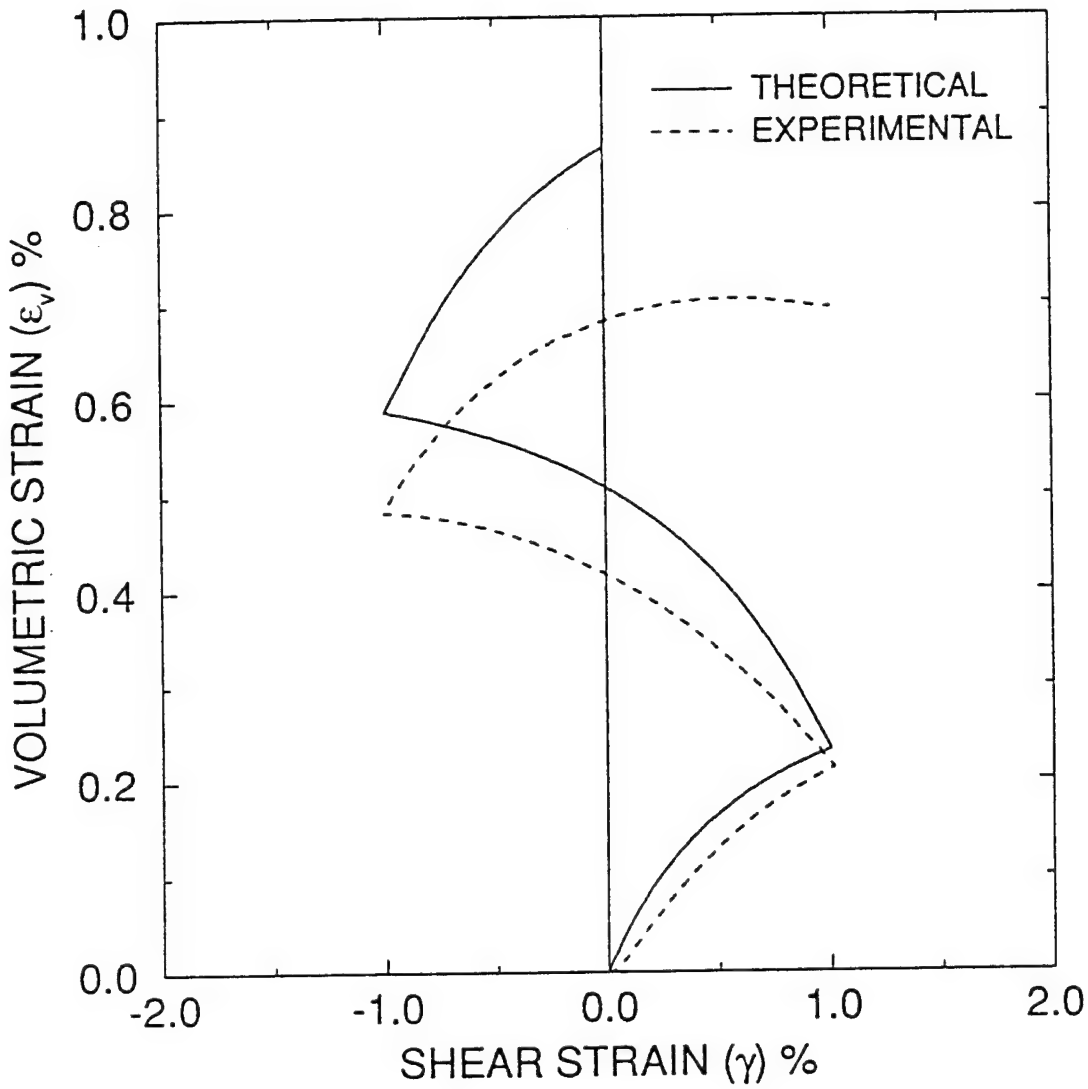

Figure I.9b Comparison of theoretical simulation with experimental results in a cycle of shearing; relation between volumetric strain and shear strain (amplitude of the shear strain = 1%).

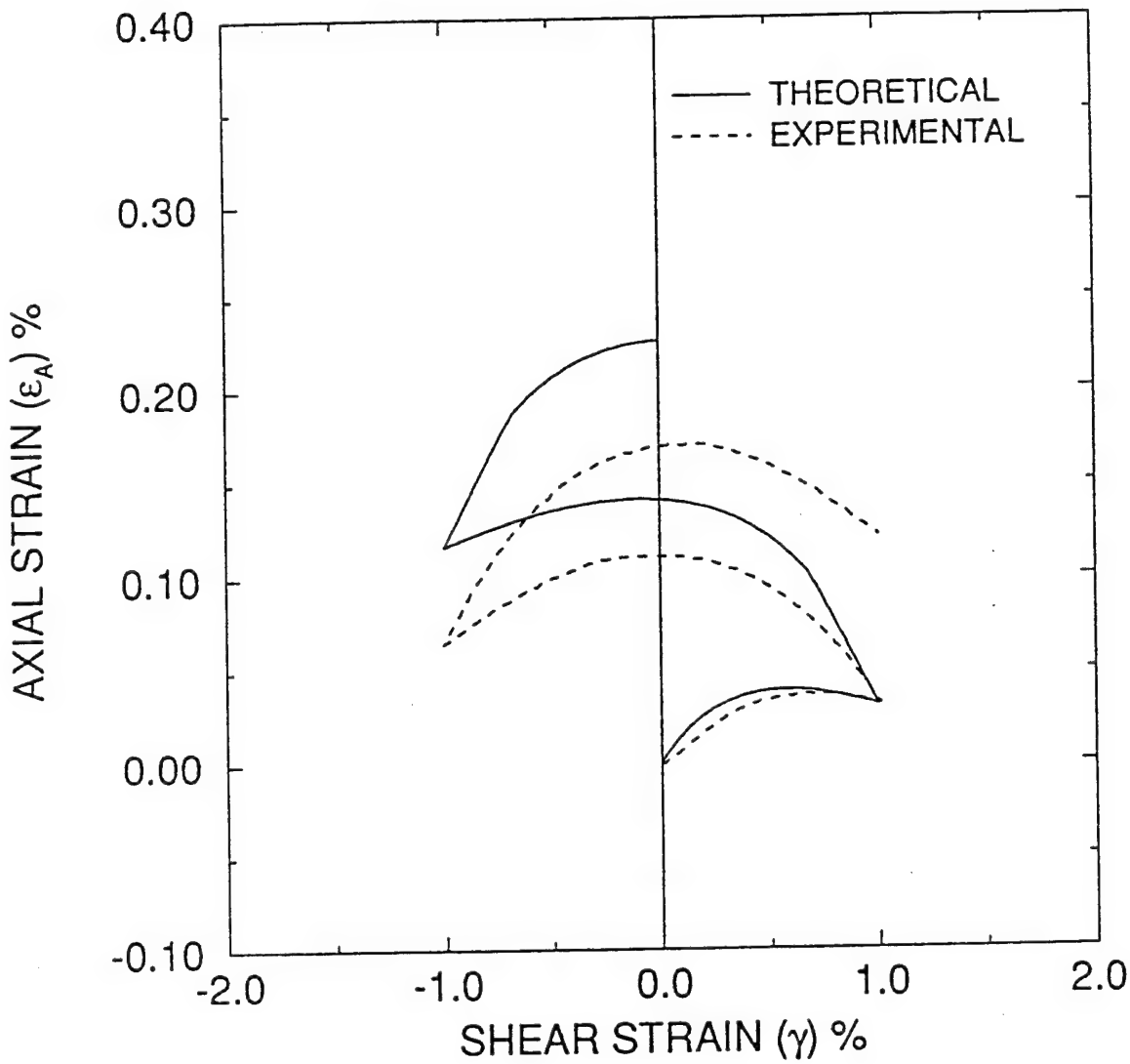

Figure I.9c Comparison of theoretical simulation with experimental results in a cycle of shearing; relation between axial strain and shear strain (amplitude of the shear strain = 1%).

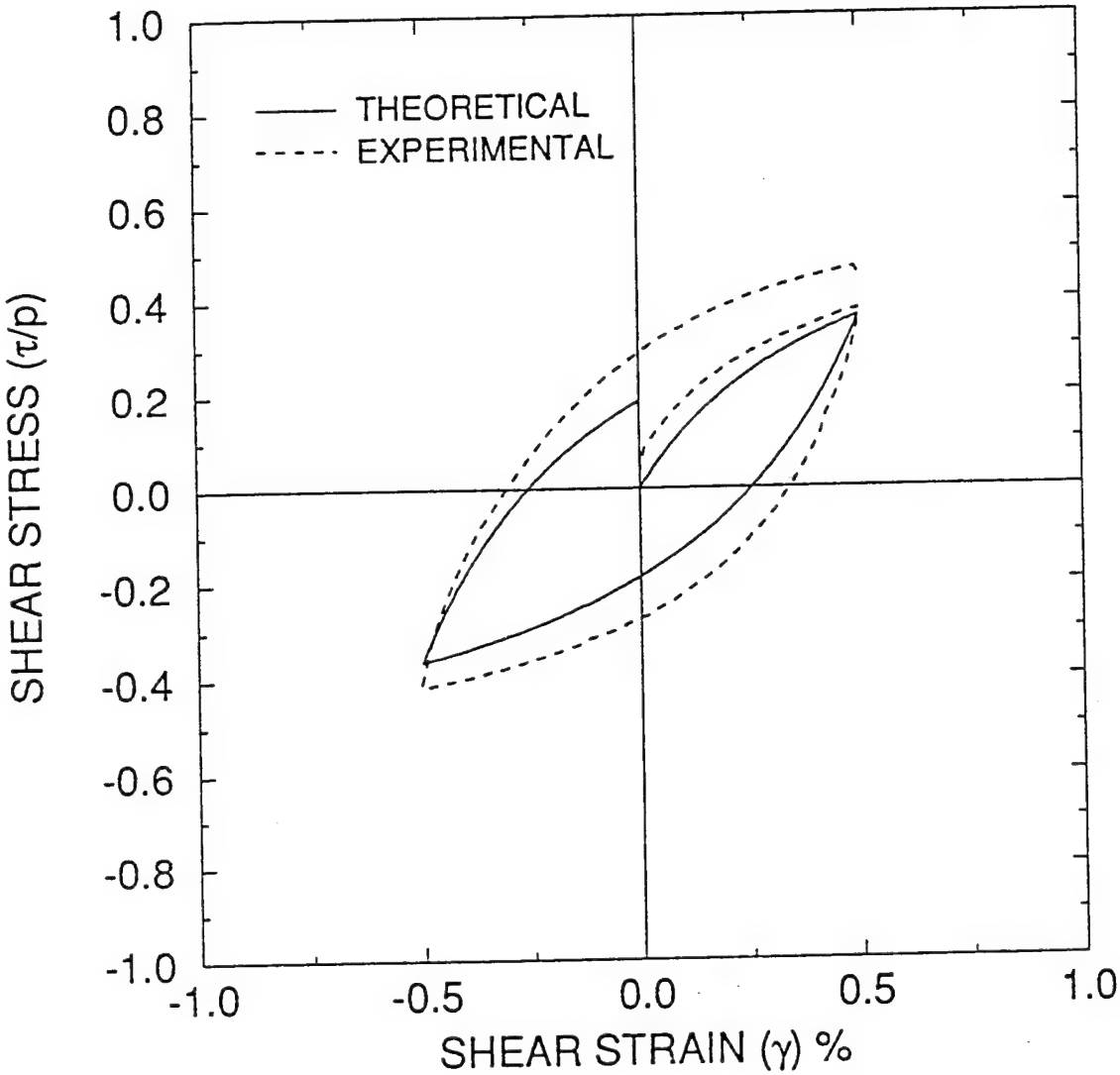

Figure I.10a Comparison of theoretical simulation with experimental results in a cycle of shearing; relation between stress ratio and shear strain (amplitude of the shear strain = 0.5%).

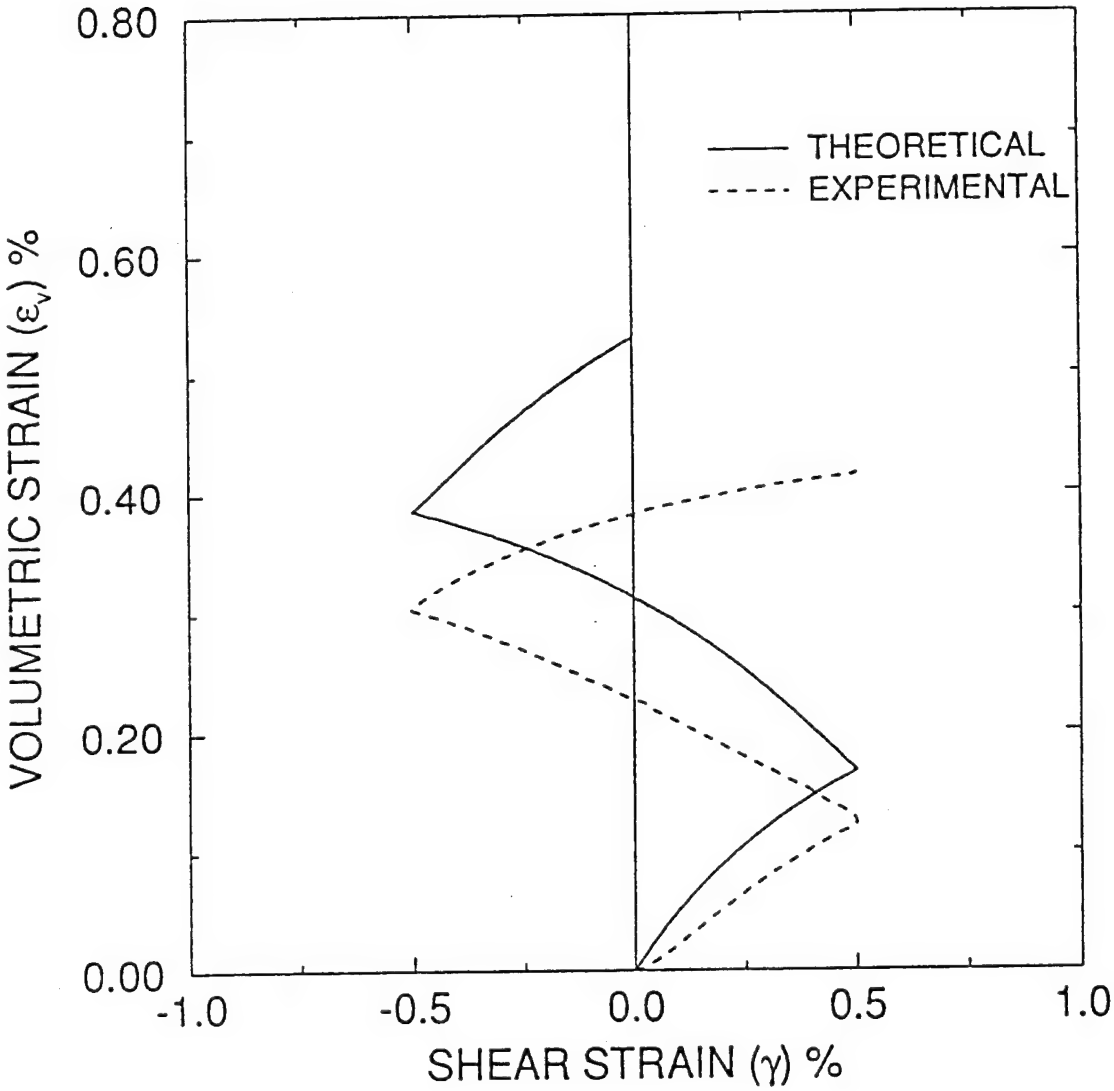

Figure I.10b Comparison of theoretical simulation with experimental results in a cycle of shearing; relation between volumetric strain and shear strain (amplitude of the shear strain = 0.5%).

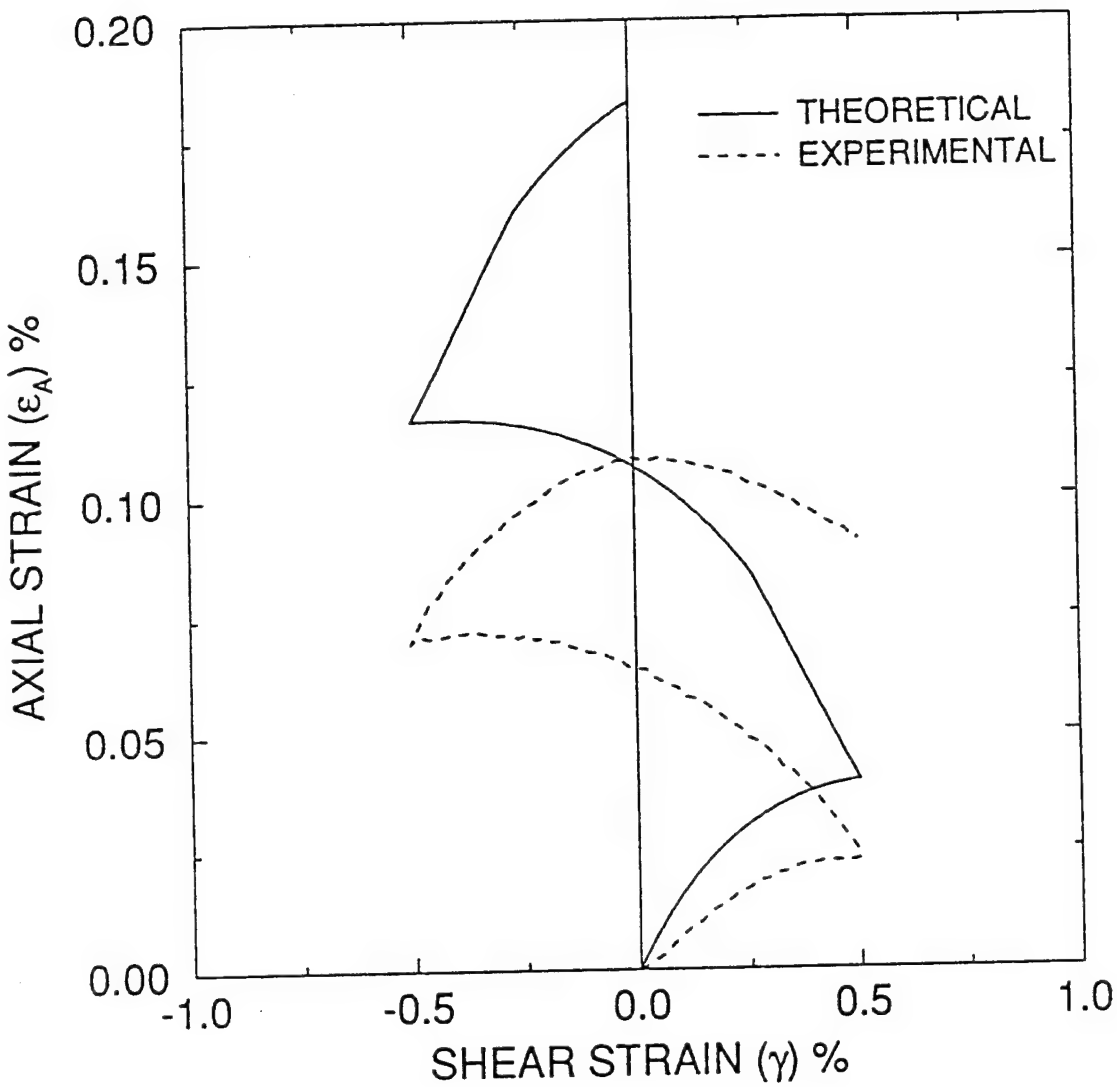

Figure I.10c Comparison of theoretical simulation with experimental results in a cycle of shearing; relation between axial strain and shear strain (amplitude of the shear strain = 0.5%).

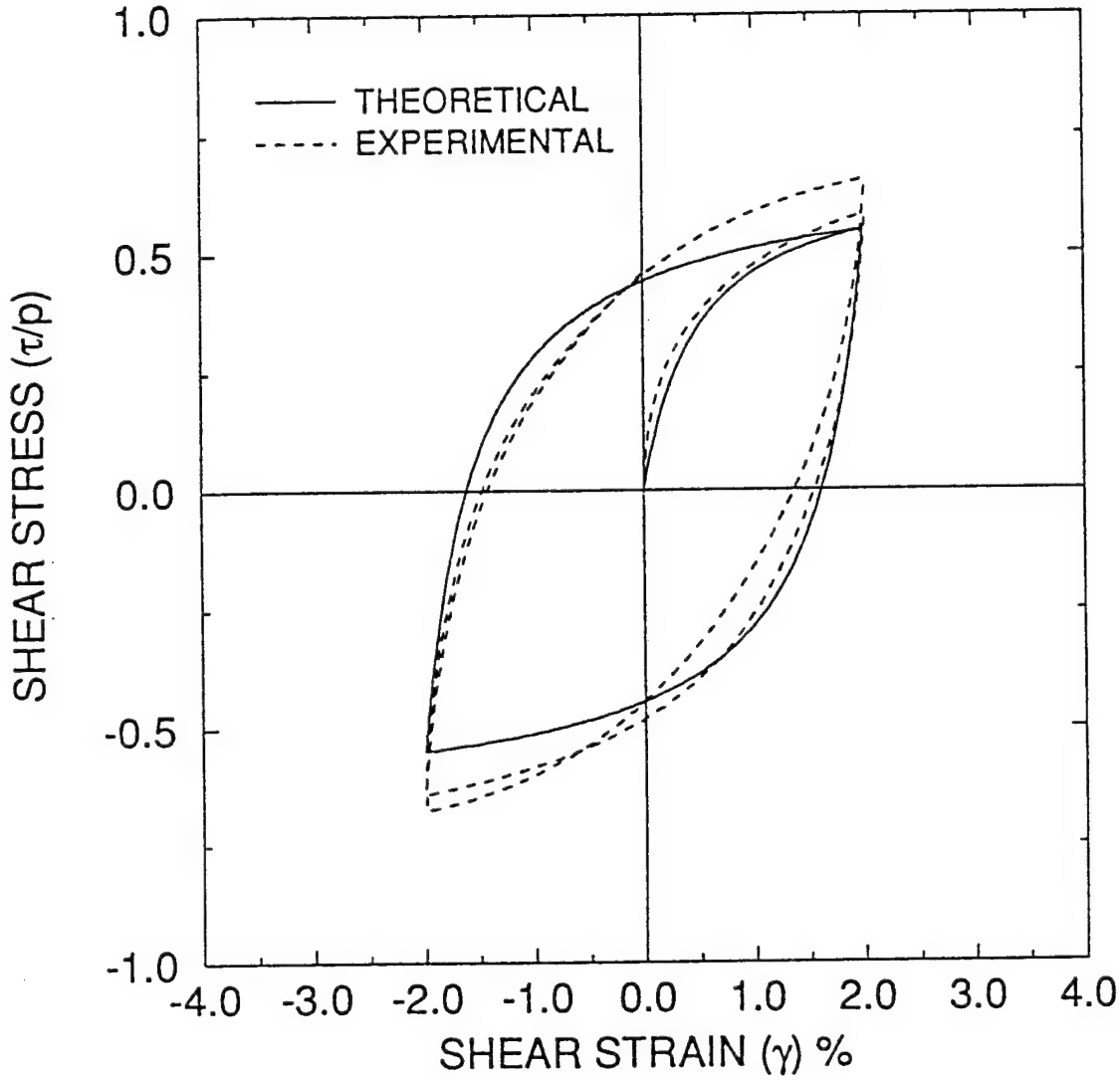

Figure I.11a Comparison of theoretical simulation with experimental results in continuous cyclic shearing; relation between stress ratio and shear strain (amplitude of the shear strain = 2%).

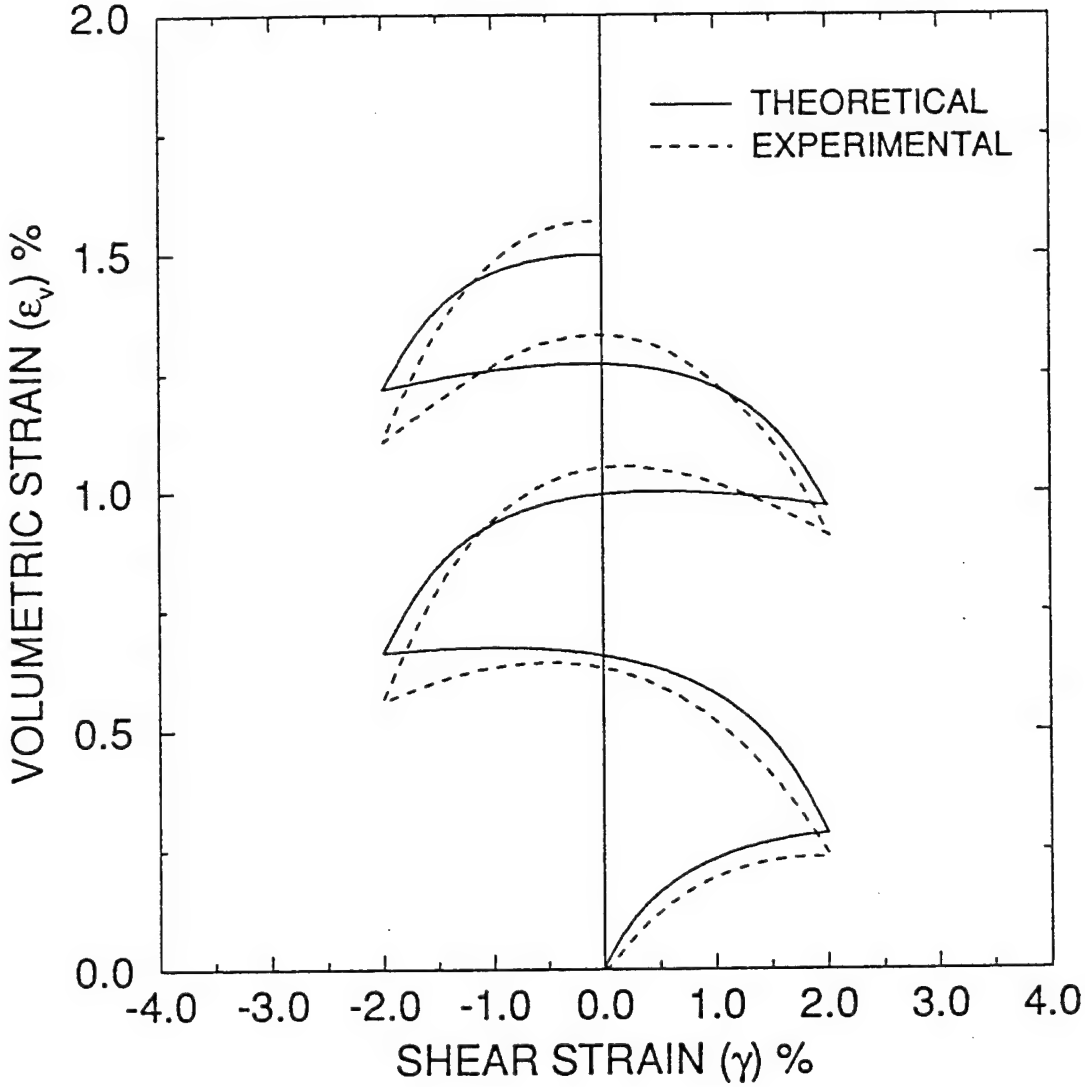

Figure I.11b Comparison of theoretical simulation with experimental results in continuous cyclic shearing; relation between volumetric strain and shear strain (amplitude of the shear strain = 2%).

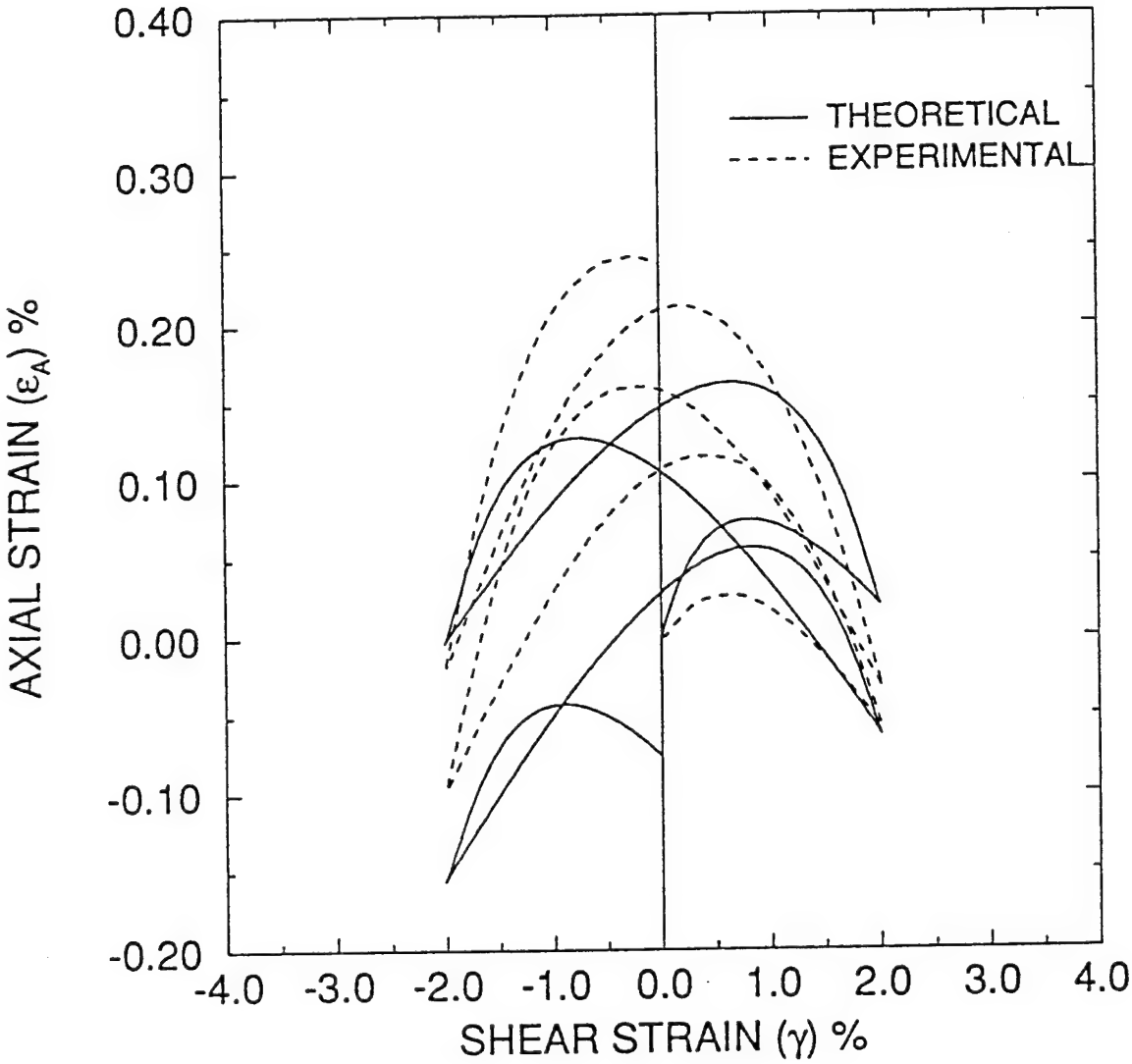

Figure I.11c Comparison of theoretical simulation with experimental results in continuous cyclic shearing; relation between axial strain and shear strain (amplitude of the shear strain = 2%).

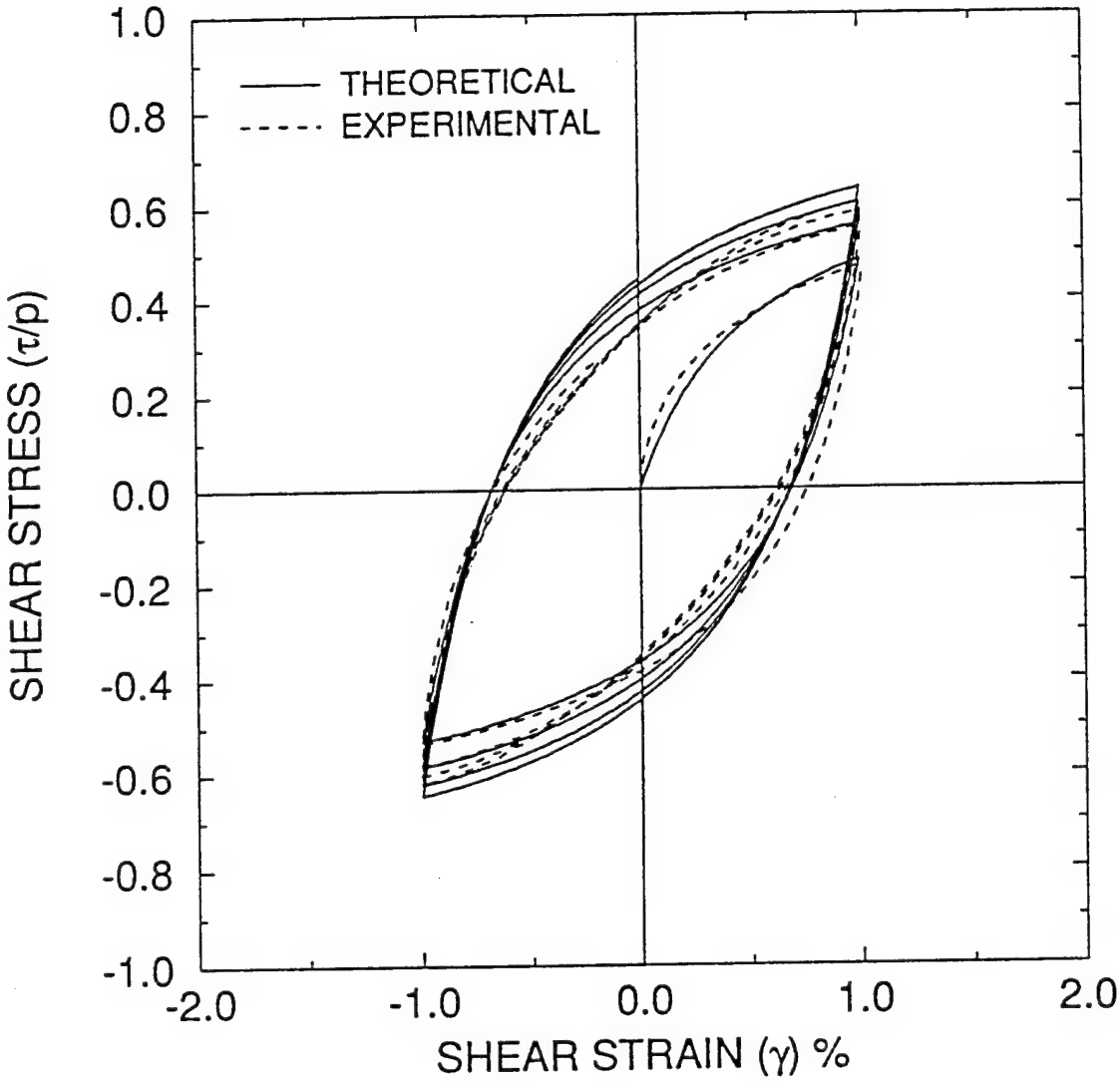

Figure I.12a Comparison of theoretical simulation with experimental results in continuous cyclic shearing; relation between stress ratio and shear strain (amplitude of the shear strain = 1%).

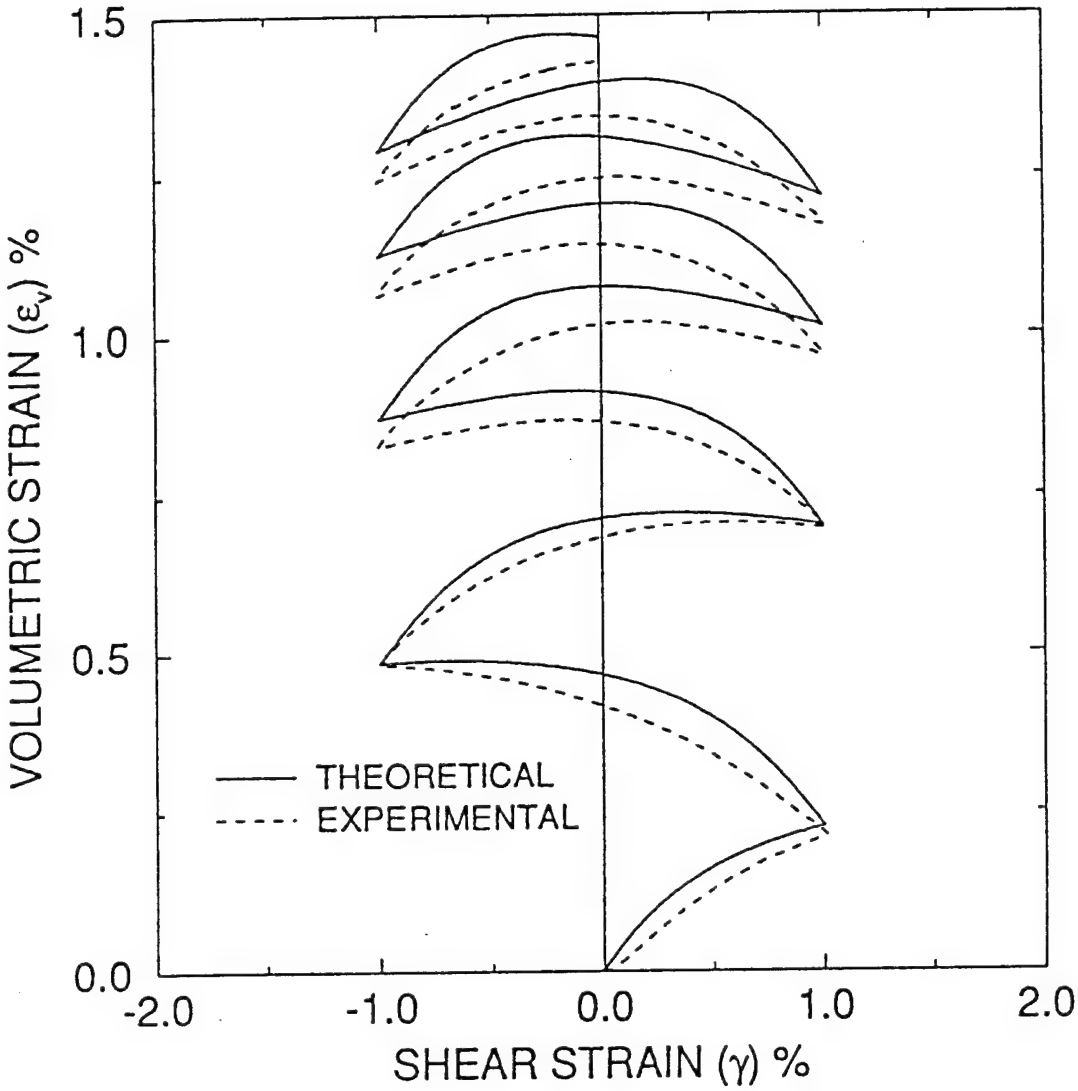

Figure I.12b Comparison of theoretical simulation with experimental results in continuous cyclic shearing; relation between volumetric strain and shear strain (amplitude of the shear strain = 1%).

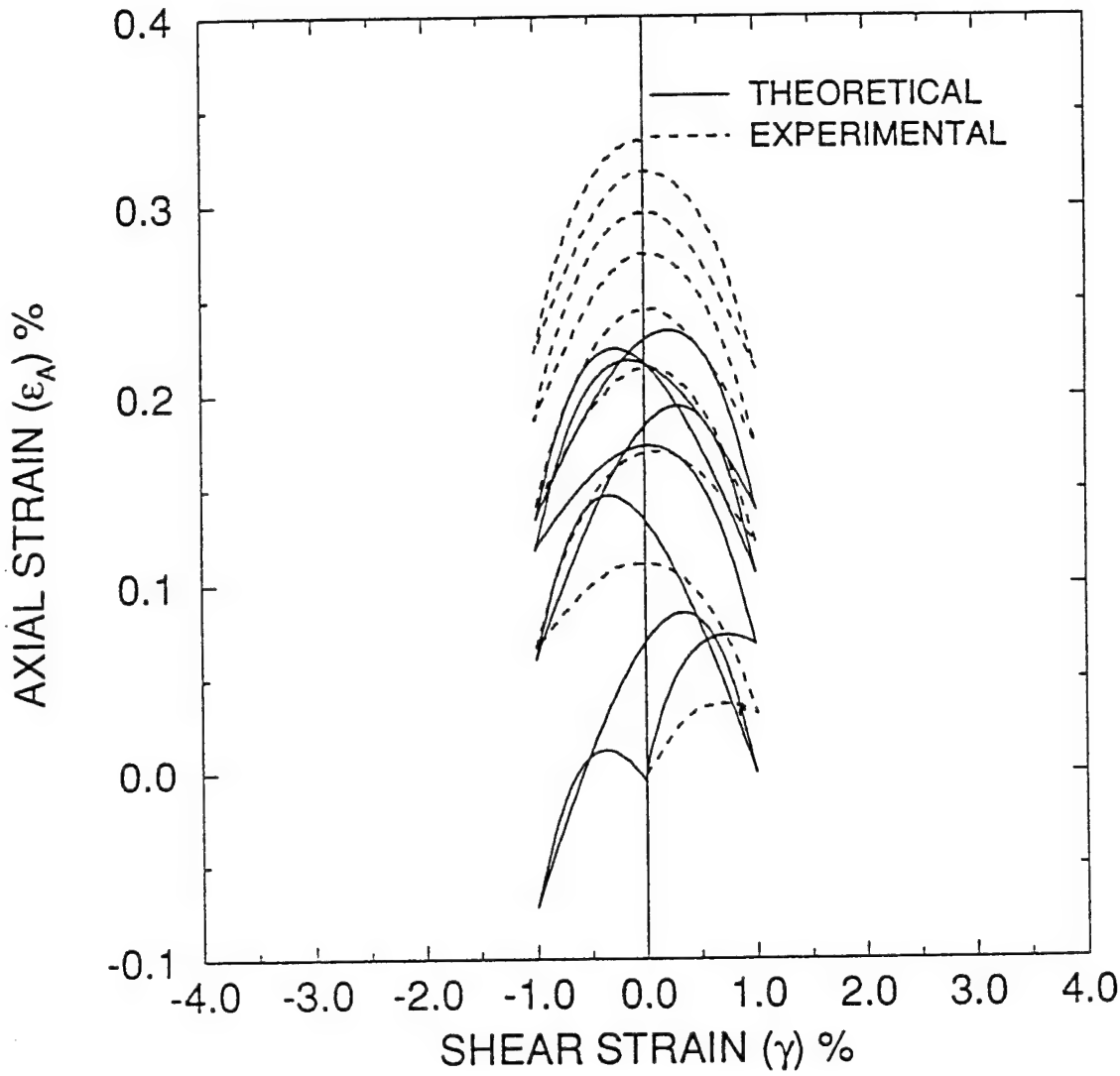

Figure I.12c Comparison of theoretical simulation with experimental results in continuous cyclic shearing; relation between axial strain and shear strain (amplitude of the shear strain = 1%).

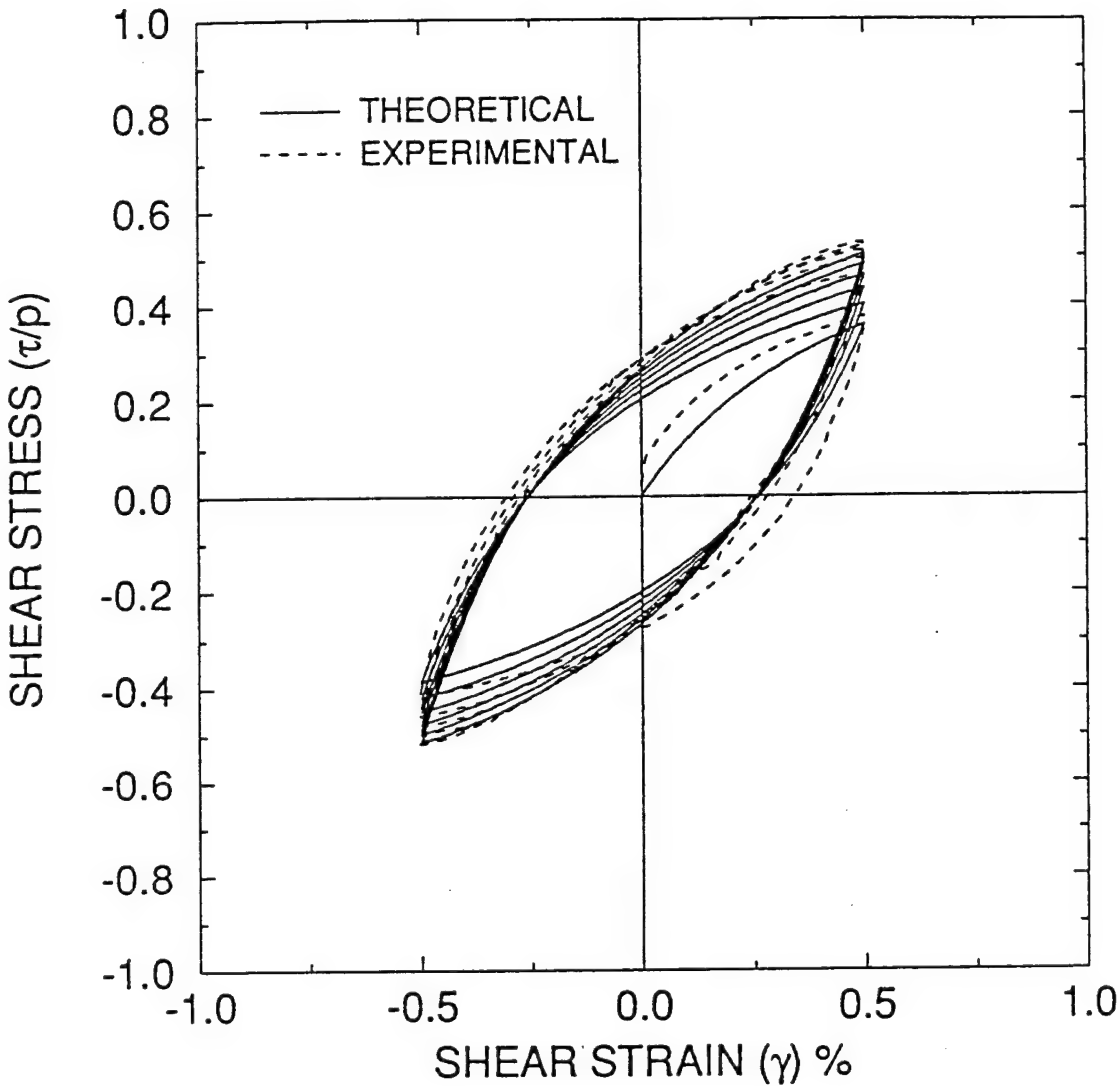

Figure I.13a Comparison of theoretical simulation with experimental results in continuous cyclic shearing; relation between stress ratio and shear strain (amplitude of the shear strain = 0.5%).

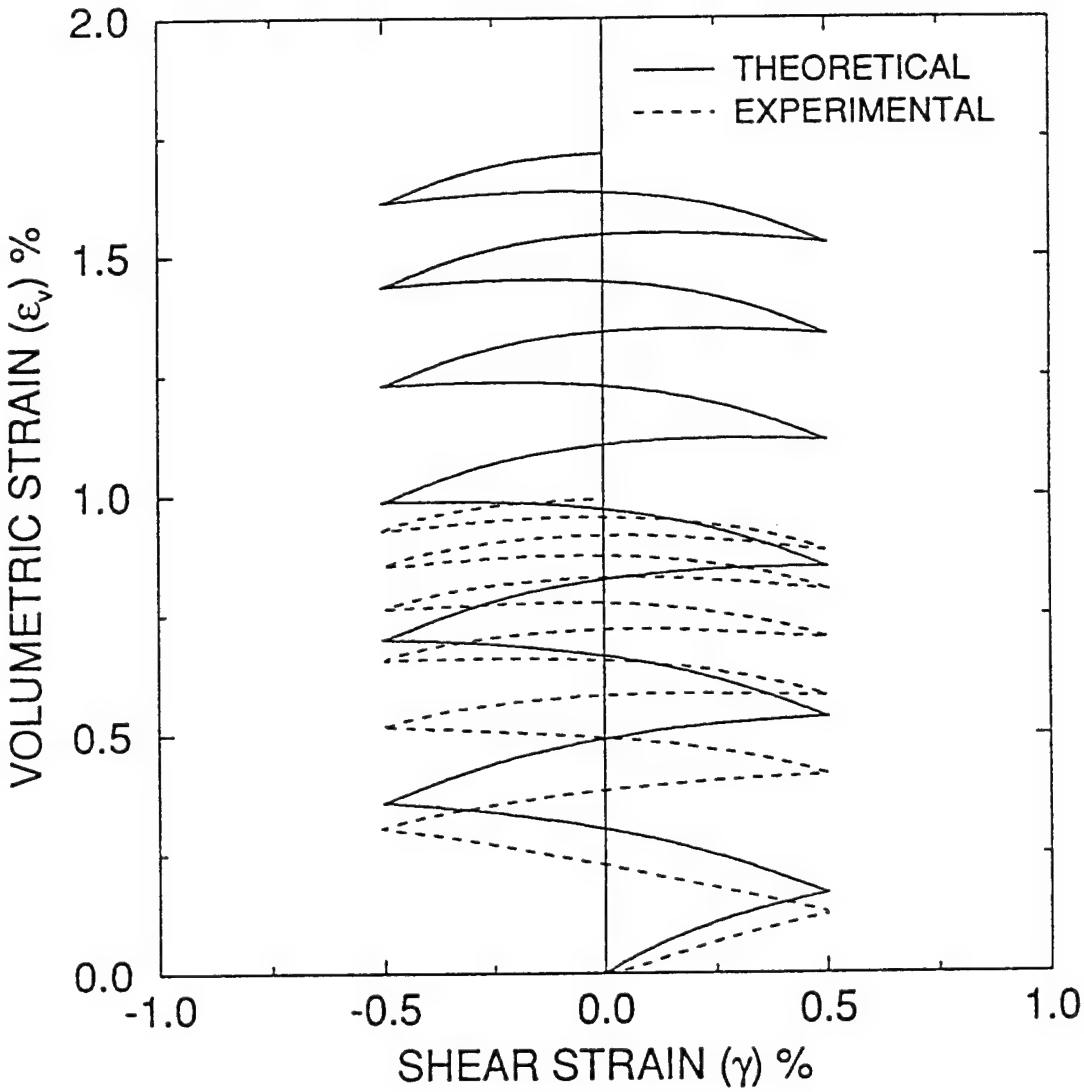

Figure I.13b Comparison of theoretical simulation with experimental results in continuous cyclic shearing; relation between volumetric strain and shear strain (amplitude of the shear strain = 0.5%).

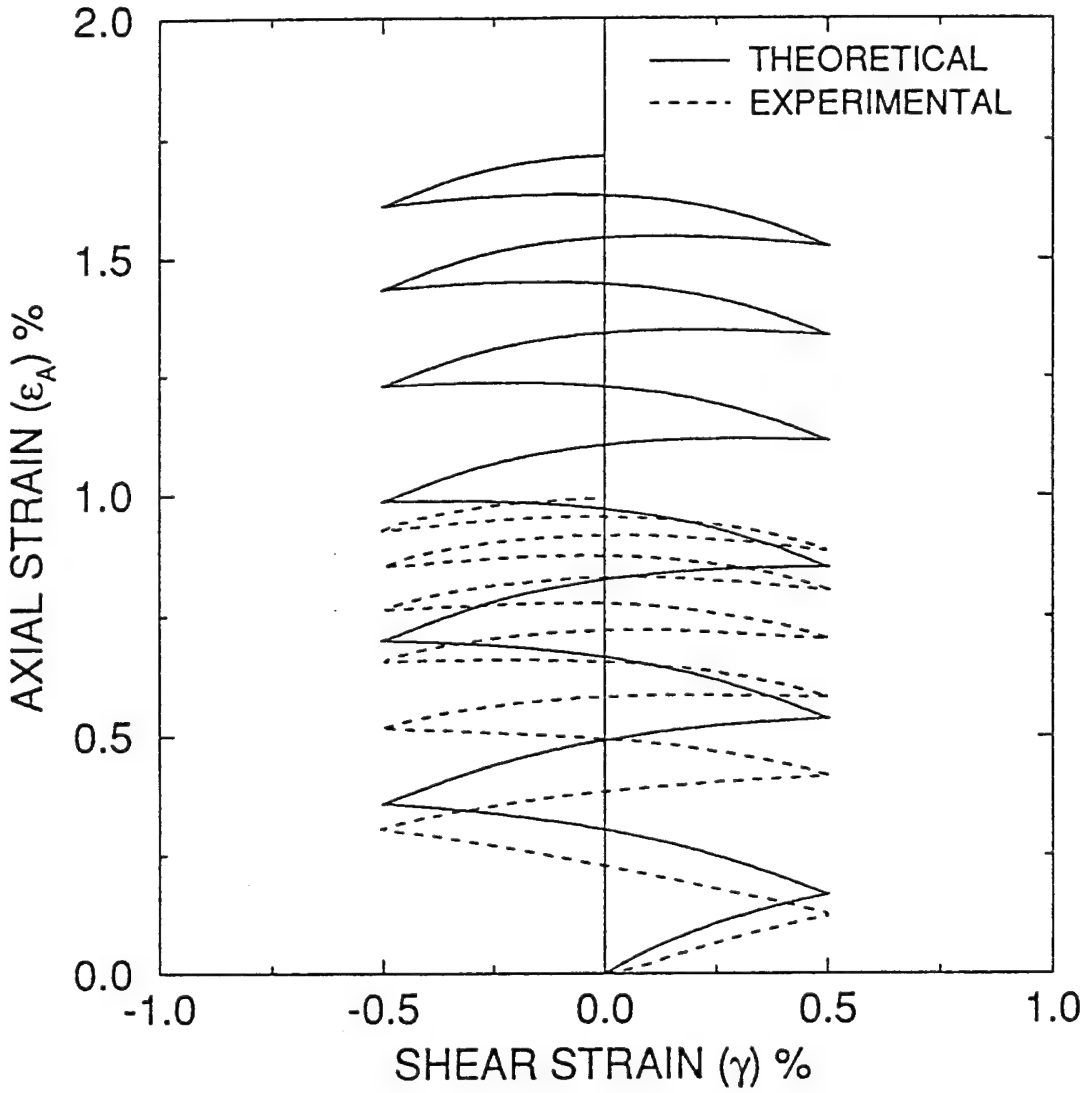

Figure I.13c Comparison of theoretical simulation with experimental results in continuous cyclic shearing; relation between axial strain and shear strain (amplitude of the shear strain = 0.5%).

APPENDIX II

CONSTITUTIVE MODEL FOR THREE DIMENSIONAL FLOW

Principal Investigator: Sia Namet-Nasser

Postdoctoral Fellow: Bala Balendra

II.1 INTRODUCTION

A constitutive model for the rate–independent planar deformation of granular materials is developed by Balendra and Nemat-Nasser (1993a). This model is extended to rate–dependent planar deformation of granular materials by Balendra and Nemat-Nasser (1993b). In these models, the fabric anisotropy is taken into account by a deviatoric tensor. The fabric anisotropy is shown to result in a pressure–dependent back stress. The final constitutive equations are written in a tensor form. Simulations of simple shear and biaxial compression tests are shown to duplicate qualitatively the experimental results from direct shear and triaxial tests, respectively. This suggests that the constitutive equations in the tensor form may be generalized to three dimensional flow of granular materials.

II.2 CONSTITUTIVE EQUATIONS

Consider the constitutive equations for the three dimensional flow of granular materials implied by those for planar deformation. For three dimensional flow of granular materials, the fabric anisotropy can be expressed by a three dimensional deviatoric tensor which would result in a pressure–dependent back stress. Let the fabric

tensor be denoted by $\boldsymbol{\beta}$ such that the back stress is $p\,\boldsymbol{\beta}$. We denote the Cauchy stress by $\boldsymbol{\sigma}$. The stress difference $\boldsymbol{\tau}$ is related to the Cauchy stress and back stress by,

$$\boldsymbol{\tau} = \boldsymbol{\sigma}' - p\,\boldsymbol{\beta}\,. \tag{II.2.1}$$

From the double sliding model for planar deformation, the plastic part of the deformation rate is given by,

$$\mathbf{D}^{p\prime} = \alpha(\mathbf{1} - \boldsymbol{\mu}\otimes\boldsymbol{\mu}):\mathbf{D}' + \dot{\gamma}\frac{\boldsymbol{\mu}}{\sqrt{2}}\,, \quad D^p_{kk} = \dot{\gamma}B\,, \tag{II.2.2a,b}$$

$$\boldsymbol{\mu} = \frac{\boldsymbol{\tau}}{\sqrt{2}q}\,, \quad q = (\tfrac{1}{2}\boldsymbol{\tau}:\boldsymbol{\tau})^{1/2}\,, \tag{II.2.3a,b}$$

where $\dot{\gamma}$ is the coaxial plastic shearing rate, B is the dilatancy parameter, α is the noncoaxiality coefficient, and $\boldsymbol{\mu}$ is the unit stress difference. To describe the elastic response, the objective Jaumann rate of Cauchy stress,

$$\overset{\circ}{\boldsymbol{\sigma}} = \dot{\boldsymbol{\sigma}} - \mathbf{W}\boldsymbol{\sigma} + \boldsymbol{\sigma}\mathbf{W}\,, \tag{II.2.4}$$

is considered and is related to the elastic deformation rate by

$$\overset{\circ}{\boldsymbol{\sigma}} = \mathbf{C}:\mathbf{D}^* = \mathbf{C}(\mathbf{D} - \mathbf{D}^p)\,, \tag{II.2.5}$$

where $\mathbf{C}$ is the instantaneous elasticity tensor. If isotropic elasticity is assumed, by substituting (II.2.2) into (II.2.5), we obtain

$$\overset{\circ}{\sigma}_{kk} = 3K(D_{kk} - \dot{\gamma}B)\,,$$

$$\overset{\circ}{\boldsymbol{\sigma}}' = 2G\left[\mathbf{D}' - \alpha(\mathbf{1} - \boldsymbol{\mu}\otimes\boldsymbol{\mu}):\mathbf{D}' - \dot{\gamma}\frac{\boldsymbol{\mu}}{\sqrt{2}}\right], \tag{II.2.6a,b}$$

where G and K are the shear and bulk moduli respectively. The rate of change of the fabric tensor is decomposed into two parts, one which is coaxial with the stress difference and the other which is normal to the stress difference. The noncoaxial part

is related to the noncoaxial plastic deformation by,

$$\overset{\circ}{\boldsymbol{\beta}} - \overset{\circ}{\boldsymbol{\beta}}:\boldsymbol{\mu}\,\boldsymbol{\mu} = \rho\,(\mathbf{1} - \boldsymbol{\mu}\otimes\boldsymbol{\mu}):\mathbf{D}'\,. \tag{II.2.7}$$

Evolution of the fabric due to coaxial plastic deformation is given by a hardening law,

$$\dot{\mu}_f = \Lambda\dot{\gamma}, \quad \mu_f = \frac{\boldsymbol{\beta}:\boldsymbol{\mu}}{\sqrt{2}}\,, \tag{II.2.8}$$

where μ_f is the effective anisotropic frictional resistance and Λ is the anisotropic hardening parameter. The resistance to shearing is not only due to fabric anisotropy but also due to interparticle friction and interaction of particles. The latter is an isotropic effect. Denote the effective isotropic angle of friction by ϕ and the microscopic angle of friction by ϕ_μ. The dilatancy parameter and the noncoaxiality coefficient are related to the macroscopic and microscopic frictional resistance by

$$B = \frac{\sin\delta}{\cos(\phi-\delta)}\,, \quad \alpha = \frac{\sin(\phi-\delta)}{\cos\delta}\,,$$

$$\delta = \phi_f + \phi - \phi_\mu\,, \quad \phi_f = \tan^{-1}(\mu_f)\,. \tag{II.2.9a-d}$$

II.2.1 Rate–Independent Plasticity

The frictional shearing criterion for the rate–independent plasticity is given by,

$$q \le M\,p\,, \quad M = \sin\phi\,. \tag{II.2.10}$$

Shearing occurs when $q = M\,p$. The rate form of the shearing criterion (II.2.10) is

$$\dot{q} - M\,\dot{p} = \dot{\gamma}\,h\,p\,, \quad h = \frac{\partial M}{\partial\gamma}\,, \tag{II.2.11a,b}$$

where h is the isotropic hardening parameter. Substituting (II.2.6)-(II.2.8) and in view of (II.2.1), we get

$$\dot{\gamma} = \frac{\sqrt{2}\,G\,\mathbf{D}':\boldsymbol{\mu} + K\,D_{kk}\,\mu_\beta\,\boldsymbol{\mu}_\beta:\boldsymbol{\mu} + p\,\mu_\beta\,\boldsymbol{\mu}_\beta:\overset{\circ}{\boldsymbol{\mu}} + M\,K\,D_{kk}}{(h+\Lambda)p + M\,K\,B + G + K\,B\,\mu_\beta\,\boldsymbol{\mu}_\beta:\boldsymbol{\mu}}\,, \tag{II.2.12}$$

where μ_β and $\boldsymbol{\mu}_\beta$ are the magnitude and the orientation of the fabric anisotropy given by

$$\boldsymbol{\mu}_\beta = \frac{\boldsymbol{\beta}}{\sqrt{2}\mu_\beta}, \quad \mu_\beta = (\tfrac{1}{2}\boldsymbol{\beta}:\boldsymbol{\beta})^{1/2}. \tag{II.2.13a,b}$$

II.2.2 Rate–Dependent Plasticity

For the rate–dependent plasticity, the inelastic strain rate is related to the Cauchy stress and fabric anisotropy $\boldsymbol{\beta}$ by

$$\frac{\dot{\gamma}}{\dot{\gamma}_0} = \left[\frac{\boldsymbol{\sigma}:\boldsymbol{\mu}/\sqrt{2} - B\,p}{p + \alpha\,\boldsymbol{\sigma}:\boldsymbol{\mu}/\sqrt{2}}\right]^m, \tag{II.2.14}$$

where m is the rate dependent exponent and $\dot{\gamma}_0$ is the reference shearing rate.

II.2.3 Hardening and Softening

Consider now the evolution of the isotropic and anisotropic frictional resistance. A very simple model is considered for the evolution of the anisotropic frictional resistance where the rate of change of the effective frictional coefficient, with respect to the rate of shearing, is linearly related to its deviation from the maximum saturation value, μ_s. The isotropic frictional resistance is assumed to increase from zero (which is associated with the maximum void ratio, e_M), as the void ratio decreases. In this manner, the evolution equations for μ_f and M are written as follows:

$$\frac{\partial \mu_f}{\partial \gamma} = a(\mu_s - \mu_f), \quad M = b\,(e_M - e)^n. \tag{II.2.15a,b}$$

It is further assumed that the saturation value μ_s of the anisotropic frictional resistance decreases linearly with increasing void ratio, as follows:

$$\mu_s(e) = \mu_{sc} + \frac{e_c - e}{e_c - e_m}(\mu_{sm} - \mu_{sc}), \tag{II.2.16}$$

where μ_{sc}, μ_{sm}, e_c, and e_m are material constants.

II.3 NUMERICAL INTEGRATION

For application to complex problems, finite element techniques are often necessary. An important step in such a case is to embed the constitutive relations into a computer code by means of suitable computational algorithms. We examine this issue for our constitutive relations. Consider the numerical integration of the constitutive equations (II.2.1) for a constant velocity gradient **L**, over a timestep Δt.

The radial return method is extensively used in finite element codes to integrate the J_2-elastoplastic constitutive equations; Wilkins (1964), Taylor and Flanagan (1987, 1989), and Hallquist and Whirley (1987, 1989). The main advantages of this method are, first, it does not calculate the fraction of the timestep required to reach the yield surface and, second, if the stress state is outside the yield surface due to the error in the preceding timestep, it corrects back to the yield surface in the current timestep. In the radial return method, the final deviatoric stress is assumed to be collinear with *trial* deviatoric stress which is obtained by assuming the total strain increment to be entirely due to elastic deformation,

$$\boldsymbol{\sigma}^{TR} = \boldsymbol{\sigma}'(t) + 2G\,\mathbf{D}'\Delta t\ . \tag{II.3.1}$$

This assumption constrains the final deviatoric stress to be in the plane of $\boldsymbol{D}'$ and $\boldsymbol{\sigma}'(t)$, in the deviatoric stress space. This is valid only if there is no spin (*i.e.* $\mathbf{W} = \mathbf{0}$), in which case the resulting error (a tensorial quantity) falls in the plane of $\mathbf{D}'$ and $\boldsymbol{\sigma}'(t)$. This has been well researched for coaxial plastic flow. Krieg and Krieg (1977) compare this method with the analytical solution and show that this method has reasonable single-step accuracy. There is no similar approach in the literature for

noncoaxial plastic flow with nonzero spin, and pressure-dependent kinematic hardening.

We now consider a new method where the orientation of the final deviatoric stress includes the effects of noncoaxiality, spin, and the variation of back stress due to changes in pressure, but we seek to retain the simplicity of the radial return method. To this end we denote the rotation of the material due to the spin $\mathbf{W}$ at time $t + \xi$ by $\mathbf{R}(\xi)$,

$$\mathbf{R}(\xi) = \exp(\mathbf{W}\,\xi)\,, \quad 0 \le \xi \le \Delta t\,. \tag{II.3.2}$$

We denote the current configuration by Π_ξ and the deformed configuration at the beginning of the time step by Π_t. Therefore, the Cauchy stress with respect to the configuration Π_t is given by

$$\hat{\boldsymbol{\sigma}}(\xi) = \mathbf{R}^T(\xi)\,\boldsymbol{\sigma}(\xi)\,\mathbf{R}(\xi)\,. \tag{II.3.3}$$

Differentiating (II.3.3), we get

$$\dot{\hat{\boldsymbol{\sigma}}} = \mathbf{R}^T\,\overset{\circ}{\boldsymbol{\sigma}}\mathbf{R}\,. \tag{II.3.4}$$

We use a superposed ^ to denote the tensors with respect to the configuration Π_t. With this notation, constitutive equations (II.2.6) and evolution equation (II.2.7) are rewritten with respect to the configuration Π_t as follows:

$$\dot{\hat{\sigma}}_{kk} = 3K(\hat{D}_{kk} - \dot{\gamma}B)\,,$$

$$\dot{\hat{\boldsymbol{\sigma}}}' = 2G\left[\hat{\mathbf{D}}' - \alpha(\mathbf{1} - \hat{\boldsymbol{\mu}}\otimes\hat{\boldsymbol{\mu}}):\hat{\mathbf{D}}' - \dot{\gamma}\frac{\hat{\boldsymbol{\mu}}}{\sqrt{2}}\right],$$

$$\dot{\hat{\boldsymbol{\beta}}} - \dot{\hat{\boldsymbol{\beta}}}:\hat{\boldsymbol{\mu}}\,\hat{\boldsymbol{\mu}} = \rho\,(\mathbf{1} - \hat{\boldsymbol{\mu}}\otimes\hat{\boldsymbol{\mu}}):\hat{\mathbf{D}}'\,. \tag{II.3.5a-c}$$

It should be noted that

$$\hat{\mathbf{D}}'(\xi) = \mathbf{R}^T(\xi)\,\mathbf{D}'\,\mathbf{R}(\xi) \tag{II.3.6}$$

is not constant, even though $\mathbf{D}'$ and $\mathbf{W}$ are constant. Therefore, the integration of the constitutive equations are complicated even for isotropic hardening; *i.e,* even when $\hat{\boldsymbol{\beta}} = \mathbf{0}$. In order to simplify the integration, we replace the variable $\hat{\mathbf{D}}'$ by its integral average

$$\overline{\mathbf{D}} = \frac{1}{\Delta t}\int_0^{\Delta t} \mathbf{R}^T(\xi)\,\mathbf{D}'\,\mathbf{R}(\xi)\,d\xi\,. \tag{II.3.7}$$

For a small timestep, (II.3.5) can be approximately integrated as follows:

$$p(t+\Delta t) = p^{TR} + K\,\Delta V^p\,, \quad p^{TR} = p(t) - K\,D_{kk}\,\Delta t\,,$$

$$\hat{\boldsymbol{\sigma}}'(t+\Delta t) = \hat{\boldsymbol{\sigma}}(t) + 2G\left[(1-\alpha)\overline{D}'\Delta t + \alpha\,\hat{\boldsymbol{\mu}}^{TR}:\overline{\mathbf{D}}\,\hat{\boldsymbol{\mu}}^{TR}\,\Delta t - \Delta\gamma\frac{\hat{\boldsymbol{\mu}}^{TR}}{\sqrt{2}}\right]$$

$$\hat{\boldsymbol{\beta}}(t+\Delta t) = \hat{\boldsymbol{\beta}}(t) + \Delta\hat{\boldsymbol{\beta}}(t):\hat{\boldsymbol{\mu}}^{TR}\,\hat{\boldsymbol{\mu}}^{TR} + \rho\left[\overline{\mathbf{D}}' - \hat{\boldsymbol{\mu}}^{TR}:\overline{\mathbf{D}}\,\hat{\boldsymbol{\mu}}^{TR}\right]\Delta t$$

$$\Delta\hat{\boldsymbol{\beta}}:\hat{\boldsymbol{\mu}}^{TR} = \hat{\boldsymbol{\beta}}(t+\Delta t):\hat{\boldsymbol{\mu}}^{TR} - \hat{\boldsymbol{\beta}}(t):\hat{\boldsymbol{\mu}}^{TR}\,, \tag{II.3.8a-e}$$

where ΔV^p is the inelastic volumetric strain increment and $\boldsymbol{\mu}^{TR}$ is the *trial* value of the unit stress difference tensor,

$$\hat{\boldsymbol{\mu}}^{TR} = \frac{\hat{\boldsymbol{\tau}}^{TR}}{(\tfrac{1}{2}\hat{\boldsymbol{\tau}}^{TR}:\hat{\boldsymbol{\tau}}^{TR})^{1/2}}\,. \tag{II.3.9}$$

The final values of the Cauchy stress and the back stress are given by

$$\boldsymbol{\sigma}(t+\Delta t) = \mathbf{R}(\Delta t)\,\hat{\boldsymbol{\sigma}}(t+\Delta t)\,\mathbf{R}^T(\Delta t)\,,$$

$$\boldsymbol{\beta}(t+\Delta t) = \mathbf{R}(\Delta t)\,\hat{\boldsymbol{\beta}}(t+\Delta t)\,\mathbf{R}^T(\Delta t)\,. \tag{II.3.10a,b}$$

The stress difference tensor at the end of the timestep is then given by

$$\hat{\boldsymbol{\tau}}(t+\Delta t) = \hat{\boldsymbol{\sigma}}(t+\Delta t) - p\,(t+\Delta t)\,\hat{\boldsymbol{\beta}}(t+\Delta t)$$

$$\simeq \hat{\boldsymbol{\sigma}}'(t+\Delta t) - p^{TR}\,\hat{\boldsymbol{\beta}}(t+\Delta t) - K\,\Delta V^{p}\,\hat{\boldsymbol{\beta}}(t)\,. \tag{II.3.11}$$

We now assume the trial value of the stress difference to be

$$\hat{\boldsymbol{\tau}}^{TR} = \hat{\boldsymbol{\sigma}}(t) - (p^{TR} + K\,\Delta V^{p})\,\hat{\boldsymbol{\beta}}(t) + 2\,G\,(1-\alpha)\,\overline{\mathbf{D}}'\,\Delta t - \rho\,p^{TR}\,\overline{\mathbf{D}}'\,\Delta t\,. \tag{II.3.12}$$

Substituting (II.3.12) into (II.3.11) in view of (II.3.8), we get

$$\hat{\boldsymbol{\tau}}(t+\Delta t) = \hat{\boldsymbol{\tau}}^{TR} + (2\,G\,\alpha + \rho\,p^{TR})\,(\hat{\boldsymbol{\mu}}^{TR}:\overline{\mathbf{D}})\,\Delta t\,\hat{\boldsymbol{\mu}}^{TR}$$

$$- 2\,G\,\Delta\gamma\,\frac{\hat{\boldsymbol{\mu}}^{TR}}{\sqrt{2}} - p^{TR}\,\Delta\hat{\boldsymbol{\beta}}:\hat{\boldsymbol{\mu}}^{TR}\,\hat{\boldsymbol{\mu}}^{TR}\,. \tag{II.3.13}$$

It can be seen from (II.3.13) that the assumptions (II.3.12) for the trial value of the stress difference tensor yields

$$\hat{\boldsymbol{\mu}}(t+\Delta t) = \hat{\boldsymbol{\mu}}^{TR}\,. \tag{II.3.14}$$

The final value of the stress difference tensor can be written as,

$$\hat{\boldsymbol{\tau}}(t+\Delta t) = \sqrt{2}q\,(t+\Delta t)\,\hat{\boldsymbol{\mu}}^{TR}\,, \tag{II.3.15}$$

where $q\,(t+\Delta t)$ is the effective shear stress-difference at the end of the timestep. Taking the double contraction product of both sides of (II.3.8c) with $\boldsymbol{\mu}^{TR}$, we obtain

$$\tau(t+\Delta t) = \tau^{TR} - G\,\Delta\gamma, \tag{II.3.16}$$

where

$$\tau(t+\Delta t) = \hat{\boldsymbol{\sigma}}'(t+\Delta t):\hat{\boldsymbol{\mu}}(t+\Delta t)\,/\sqrt{2}\,,$$

$$\tau^{TR} = \hat{\boldsymbol{\sigma}}'(t):\hat{\boldsymbol{\mu}}^{TR}\,/\sqrt{2} + \sqrt{2}\,G\,\overline{\mathbf{D}}':\hat{\boldsymbol{\mu}}^{TR}\,\Delta t\,. \tag{II.3.17a,b}$$

This is a scalar incremental equation. Now the task is to find the final value of the

resolved shear stress, $\tau(t+\Delta t)$, and the plastic strain increment, $\Delta\gamma$, satisfying this scalar incremental equation and the sliding criterion at the end of the timestep.

II.3.1 Rate–Independent Plasticity

In this subsection we consider the integration of the constitutive equations (II.2.1), for rate-independent plastic flow for which the sliding criterion is given by (II.2.3a). For continued plastic flow, the sliding criterion at the end of the timestep is given by

$$\tau(t+\Delta t) = p(t+\Delta t)\left[M(t+\Delta t) + \hat{\boldsymbol{\beta}}(t+\Delta t):\hat{\boldsymbol{\mu}}(t+\Delta t)/\sqrt{2}\right]. \tag{II.3.18}$$

From the forward gradient method, the frictional strength at the end of the timestep are given by

$$M(t+\Delta t) = M(t) + h\,\Delta\gamma, \quad h = \frac{\partial M}{\partial \gamma}\Big|_t = B(1+e)\frac{\partial M}{\partial e}\Big|_t, \tag{II.3.19a,b}$$

$$\hat{\boldsymbol{\beta}}(t+\Delta t):\hat{\boldsymbol{\mu}}(t+\Delta t) = \hat{\boldsymbol{\beta}}(t):\hat{\boldsymbol{\mu}}^{TR} + \Lambda\,\Delta\gamma/\sqrt{2}. \tag{II.3.19c}$$

Substituting (II.3.18) into (II.3.17) in view of (II.3.19) and (II.3.8a,b), we get

$$\Delta\gamma = \frac{\tau^{TR} - p^{TR}(M + \hat{\boldsymbol{\beta}}(t):\hat{\boldsymbol{\mu}}^{TR}/\sqrt{2})}{G + p^{TR}(h + \Lambda/2) + K\,B\,(M + \hat{\boldsymbol{\beta}}(t):\hat{\boldsymbol{\mu}}^{TR}/2)}. \tag{II.3.20}$$

In implementing this method, first we calculate the *trial* values of the pressure and deviatoric stress from (II.3.8a) and (II.3.12), assuming $\Delta V^p = \alpha = \rho = 0$. Then $\Delta\gamma$ is calculated from (II.3.20). If $\Delta\gamma$ is less than zero, then it is set to zero. If $\Delta\gamma$ is greater than zero, then ΔV^p is set to $B\,\Delta\gamma$, *trial* values are again calculated from (II.3.8a) and (II.3.12) and $\Delta\gamma$ is calculated from (II.3.20). The total stress and back stress are updated from (II.3.8). The void ratio is updated from

$$e(t+\Delta t) = e(t) + B\,(1+e)\,\Delta\gamma. \tag{II.3.21}$$

It should be noted that in the *forward gradient* method, the derivative of the hardening laws are evaluated only at the beginning of the timestep. Hence the procedure is not exact even if the loading is unidirectional (*i.e.*, even if there is no error due to orientation). Nemat-Nasser and co-workers have introduced an efficient algorithm for time integration of elastoplasticity constitutive relations with nonlinear hardening laws, in which the total applied strain rate at the start of each timestep is assumed to be entirely due to plastic flow. Then the error introduced by this assumption is calculated explicitly and corrected; see Nemat-Nasser (1991), Nemat-Nasser and Chung (1992), and Nemat-Nasser and Li (1992). These authors show that this "*plastic-predictor-and-elastic-corrector*" gives remarkably accurate results for incompressible materials, even for very large timesteps. We follow and extend their procedure to integrate the reduced-scalar rate equation (II.3.16) for dilatant and pressure-sensitive materials.

In this integration method, we assume that the deformation is elastic, until the current yield surface is reached and then it is entirely due to plastic flow. In this assumption, we do not need to calculate the fraction of the timestep required to reach the yield surface. Instead, in estimating the approximate value of $\Delta\gamma$ from (II.3.21), we impose the condition that the stress state is on the yield surface. Let the approximate initial estimate of $\Delta\gamma$ be $\Delta\gamma_A$, and the associated error be denoted by $\Delta\gamma_e$. Then the exact value of the plastic strain increment is

$$\Delta\gamma = \Delta\gamma_A - \Delta\gamma_e\,, \qquad \Delta\gamma_A = \frac{\tau^{TR} - p^{TR}\,[X(t) + M(t)]}{G}\,, \tag{II.3.22a,b}$$

where

$$X(t) = \hat{\boldsymbol{\beta}}(t):\hat{\boldsymbol{\mu}}(t)/\sqrt{2}\,. \tag{II.3.23}$$

Substituting (II.3.22) into (II.3.16), we get

$$\tau(t+\Delta t) = p^{TR}\,[X(t) + M(t)] + G\,\Delta\gamma_e\,,$$

$$p(t+\Delta t) = p_A - K\,B_A\,\Delta\gamma_e\,,$$

$$p_A = p^{TR} + K\,\Delta V_A^p\,, \qquad \text{(II.3.24a-c)}$$

where ΔV_A^p is the inelastic volumetric strain increment due to the increment in the shear strain $\Delta\gamma_A$,

$$\Delta V_A^p = \int_0^{\Delta\gamma_A} B\,d\gamma. \qquad \text{(II.3.25)}$$

The hardening law for the back stress can be approximately integrated as follows:

$$X(t+\Delta t) = X_A - \Lambda_A\,\Delta\gamma_e/2\,, \quad X_A = \int_0^{\Delta\gamma_A} \frac{\partial X}{\partial\gamma}\,d\gamma. \qquad \text{(II.3.26a,b)}$$

Integrating of the evolution equation for the void ratio, we get

$$e(t+\Delta t) = e_A + B_A(1+e_A)\,\Delta\gamma_e\,,$$

$$e_A = [1 + e(t)]\exp(\Delta V_A^p) - 1\,. \qquad \text{(II.3.27a,b)}$$

The hardening law for the isotropic frictional frictional strength is integrated to get

$$M(t+\Delta t) = M_A - h\,\Delta\gamma_e\,, \quad h = B_A\,(1+e_A)\,\frac{\partial M}{\partial e}\Big|_A\,,$$

$$M_A = \int_{e(t)}^{e_A} \frac{\partial M}{\partial e}\,de\,. \qquad \text{(II.3.28a-c)}$$

Substituting (II.3.24), (II.3.26), and (II.3.28) into (II.3.18) we estimate the error $\Delta\gamma_e$,

$$\Delta\gamma_e = \frac{\tau_A - p^{TR}\,[X(t) + M(t)]}{G + p_A\,(h + \Lambda_A/2) + K\,B_A\,(X_A + M_A)}\,. \qquad \text{(II.3.29)}$$

where

$$\tau_A = p_A\,(X_A + M_A)\,. \tag{II.3.30}$$

Substituting (II.3.29) into (II.3.8) in view of (II.3.23) and (II.3.26), the final values of the total stress and back stress are obtained. The final value of the void ratio is obtained from (II.3.27).

II.3.2 Rate–Dependent Plasticity

In this subsection we consider the integration of the constitutive equations (II.2.1), for rate-dependent plastic flow of granular materials for which the sliding rates are related to the stress state, back stress and the isotropic frictional strength by (II.2.4). We note that the forward gradient method is inefficient for the integration of stiff equations. However, it has already been shown by Nemat-Nasser and co-workers that the *plastic–predictor–and–elastic corrector* method gives remarkably accurate results for stiff equations, even for very large timesteps. Therefore, we consider only the *plastic–predictor–and–elastic–corrector* method to integrate the constitutive equations in this sub-section. To this end, we rewrite the flow rule (II.2.4) as follows:

$$\tau = F(B\,,\alpha\,,Y)\,p\,, \quad Y = (\dot{\gamma}/\dot{\gamma}_0)^{1/m}\,. \tag{II.3.31a,b}$$

Let the approximate initial estimate of $\dot{\gamma}$ be $\dot{\gamma}_A$, and the associated error be denoted by $\dot{\gamma}_e$. Then the exact value of the plastic strain rate is

$$\dot{\gamma} = \dot{\gamma}_A - \dot{\gamma}_e\,, \quad \dot{\gamma}_A = \frac{\tau^{TR} - p^{TR}\,[X(t) + M(t)]}{G}\,. \tag{II.3.32a,b}$$

The total plastic strain increment is approximated as follows:

$$\Delta\gamma = \dot{\gamma}_A\,\Delta t - \dot{\gamma}_e\,\Delta t = \Delta\gamma_A - \Delta\gamma_e\,. \tag{II.3.33}$$

Substituting (II.3.32) and (II.3.33) into (II.3.16), we get

$$\tau(t + \Delta t) = p^{TR}\,[X(t) + M(t)] + G\,\Delta\gamma_e\,. \tag{II.3.34}$$

Let the approximate values of B and α after the integration of the evolution equations for the increment of $\Delta\gamma_A$ in the plastic strain be denoted by B_A and α_A. Therefore, the effective resolved shear stress can be estimated as

$$\tau_A = F_A\, p_A\,, \quad F_A = F(B_A\,, \alpha_A\,, Y_A)\,. \tag{II.3.35a,b}$$

Differentiating (II.3.35), and substituting into (II.3.34), we obtain

$$\Delta\gamma_e = \frac{\tau_A - p^{TR}\,[X(t) + M(t)]}{p_A\,\eta + K\,B_A\,F_A + G}\,, \tag{II.3.36}$$

where

$$\eta = \frac{\partial F}{\partial B}\frac{\partial B}{\partial \gamma} + \frac{\partial F}{\partial \alpha}\frac{\partial \alpha}{\partial \gamma} + \frac{1}{\Delta t}\frac{\partial F}{\partial Y}\frac{\partial Y}{\partial \dot{\gamma}} \tag{II.3.37}$$

We now consider the performance evaluation of the proposed integration scheme. For the demonstration we use the following material parameters for granular materials with small void ratios: $G = 150p_0$, $K = 175p_0$, $a = 50$, $b = 10$, $\mu_s = \tan 20°$, $\phi_\mu = 20°$, and $e_M = 0.5$. We consider a sample which is initially deformed biaxially to a biaxial strain of $\varepsilon'_{11} = -\varepsilon'_{22} = 10\%$ and the subjected to a simple shearing to $\varepsilon_{12} = 10\%$. For rate–dependent constitutive model, the effective deformation rate is set at $10\dot{\gamma}_0$ for the first 5% of the biaxial deformation and at $1000\dot{\gamma}_0$ for the rest of the deformation. Integration of the constitutive equations with *plastic-predictor–and –elastic–corrector* method are shown in Fig. II.1 for rate–independent case and in Fig. II.2 for rate–dependent case. The results obtained using 200 and 100 increments for entire deformation coincide almost exactly. This indicates that the integration scheme is convergent. The results obtained using 10 increments also almost coincide with those with the 200 increments in biaxial loading. However they tend to deviate for simple shearing as the strain increases. This shows that replacing $\hat{\mathbf{D}}$ by $\overline{\mathbf{D}}$ in (II.3.5) is

not good for large rotations. However, the proposed method is convergent and within a reasonable accuracy for use in explicit finite element codes where the timesteps are very small. Particularly, in rate dependent model, even with large strain increments, the small jumps in the stress-strain relations due to sudden change in the deformation rate are accurately predicted.

II.4 SHEAR INDUCED PRESSURE WAVES IN GRANULAR MATERIALS

Granular materials, due to their inherent porosity are dilatant and pressure sensitive. Shear deformation in granular materials always accompanies a change in volume. As a results, the shear and the pressure waves in granular materials cannot be decoupled.

Consider the propagation of shear and pressure waves in a semi-infinite granular media with small void ratio when the free surface is subjected to a dynamic shearing. A schematic diagram of the semi–infinite media is shown in Fig. II.3 with a rectangular Cartesian coordinate system. The free surface, x_2,x_3–plane is subjected to a shear traction $\tau(t)$. Due to symmetry and confinement, the nonvanishing components of the deformation gradient are F_{11} and F_{21}. Therefore this problem can be considered as a plane strain problem. The nonvanishing stress components are σ_{11}, σ_{22}, σ_{33}, and σ_{12}. However, all these stress components vary only with time and x_1. Therefore, the equations of motion take on the form,

$$\frac{\partial \sigma_{11}}{\partial x_1} + \rho b_1 = \rho \ddot{u}_1,$$

$$\frac{\partial \sigma_{21}}{\partial x_1} + \rho b_2 = \rho \ddot{u}_2, \qquad \text{(II.4.1a,b)}$$

where ρ is the density of the material, and b_i and $\ddot{u}_i$ are the body force and acceleration in the x_i–direction, $i = 1,2$.

A one–dimensional explicit finite element code is developed to integrate the equations of motion (II.4.1) in time and space with the constitutive equations (II.2.6). In order to study the dynamic loading and unloading in granular materials, we consider a trapezoidal input pulse as shown in Fig. II.4. The initial pressure and the void ratio in the granular media are assumed to be uniform at p_0 and $e_0 = 0.1$, respectively. For simplicity we assume that the saturation value of the anisotropic frictional resistance is constant for all void ratios, *i.e* $\mu_s = \mu_{sc} = \mu_{sm}$ in (II.2.16). We use the following material parameters: $G = 150p_0$, $K = 175p_0$, $a = 50$, $b = 10$, $\mu_s = \tan 20°$, $\phi_\mu = 20°$, and $e_M = 0.5$. In order to investigate the effect of noncoaxiality, the results using α given by (II.2.9b) are compared with the results using $\alpha = 0$. Pressure and the nonvanishing components of the deviatoric stress at various distances from the free surface are plotted against time in Fig. II.5. These quantities at various times are plotted against the distance from the free surface in Fig. II.6.

II.5 DYNAMIC FINITE ELEMENT ANALYSIS OF STRAIN LOCALIZATION IN GRANULAR MATERIALS

It is a common feature of granular materials to form zones of localized deformation, in the form of narrow shear bands, when subjected to large deformations. Rudnicki and Rice (1975) suggested that localization is an instability in the macroscopic constitutive description of inelastic deformation of the material. Constitutive relations may allow the homogeneous deformation of an initially uniform material to lead to a bifurcation point, at which non-uniform deformation can be incipient in a planar band under conditions of continuing equilibrium and continuing homogeneous deformation.

Granular materials due to their inherent porosity are dilatant. Since the shearing are frictional in nature, the criterion for plastic deformation in strongly pressure sensitive. In general the pressure dependence of the shearing criterion and the inelastic dilatancy do not match, resulting in nonnormality. The deviatoric plastic deformation rate is not coaxial with the stress, due to the preferred sliding planes. These features are destabilizing, and affect significantly the onset of localization.

The explicit finite element code PRONTO2D with the constitutive model developed in Section II.2, are used to study the strain localization in granular materials with large void ratios when subjected to plane strain compression. The geometry consisted of a 10cm × 20cm rectangular block discretized into 3200 elements, as shown in Fig. II.7. The lateral pressure is kept constant at the initial value $p_0 = 500\,kPa$. The top and bottom edges of the specimen are subjected to an imposed compression velocity V_0 in the vertical direction and zero tractions in the horizontal direction. Because of the symmetry of the problem, only one quadrant of the grid shown in Fig. II.7 is actually involved in the calculation, with appropriate boundary conditions at the symmetry planes. We use the following parameters in the finite element simulation for granular materials with large void ratios: $G = 80MPa$, $3K = 400MPa$, $a = 50$, $b = 1$, $n = 2$, $\phi_\mu = 20°$, $\mu_{sc} = \tan 25°$, $\mu_{sm} = \tan 35°$, $e_c = 0.6$, $e_m = 0.5$, and $e_M = 0.7$. The density of the material is specified as $2.5g/cm^3$. Here we present a few example problems to study the effect of initial void ratio and the strain rate.

In most of the examples, simulations are carried out up to a vertical strain of 10%. However, the simulations are terminated if the pressure in an element becomes zero. As the deformation localized to a narrow shear band, the elements in the shear band undergo constant volume shearing. Therefore, the pressure in the shear band

increases if the angle of dilatancy is positive and decreases if it is negative. Deformed grids for three different imposed end velocity V_0 (5cm/s, 10cm/s, 100cm/s) values with the initial void ratio 0.6 are shown in Fig. II.8-II.10. Comparison of these grids shows the effect of inertia on the pattern of localization. For higher imposed velocity, the inertia effects are greater in the material. The deformed grids indicates that inertia plays a significant role in delaying the onset of shear localization. Stress–strain relations from these finite element analysis are compared with those for the homogeneous deformation in Fig. II.11. It is seen from this figure that the localization starts earlier for lowest strain rate in comparison to the higher strain rates. Deformed grids for two other initial void ratios (0.5, 0.65) with the imposed velocity 10cm/s are shown in Fig. II.12-II.13. Comparison of these grids with that in Fig. II.9 shows the effect of initial void ratio on the pattern of localization. These grids indicate that the dense samples have the higher tendency to localize than the loose samples. Stress–strain relations from the finite element analysis for these three initial void ratios are compared along with those for the corresponding homogeneous deformations in Fig. II.14. It is seen from this figure that the localization starts right after the peak stress is reached.

REFERENCES

Balendran, B., & Nemat-Nasser, S. (1993a). Double sliding model for cyclic deformation of granular materials, including dilatancy effects. *Journal of Mechanics and Physics of Solids,* **41**, No. 3, pp. 573-612.

Balendran, B., & Nemat-Nasser, S. (1993b). Viscoplastic flow of planar granular materials. *Mechanics of Materials*, **16**, pp. 1-12.

Hallquist, J.O., and Whirley, R.G. (1987). User's Manual for DYNA2D: An Explicit Two–Dimensional Hydrodynamic Finite Element Code with Interactive Rezoning and Graphical Display. *Lawrance Livermore National Laboratory Report,* UCID–18756, Rev. 3.

Hallquist, J.O., and Whirley, R.G. (1989). DYNA3D User's Manual: Nonlinear Dynamic Analysis of Structures in Three Dimensions. *Lawrence Livermore National Laboratory Report,* UCID–19592.

Krieg, R.D., and Krieg, D.B. (1977). Accuracies of Numerical Solution Methods for the Elastic-Perfectly Plastic Model. *Journal of Pressure Vessel Technology,* **99**, pp. 510-515.

Nemat-Nasser, S. (1991). Rate-Independent Finite-Deformation Elastoplasticity: A New Explicit Constitutive Algorithm. *Mechanics of Materials,* **11**, pp. 235-249.

Nemat-Nasser, S., and Chung, D.-T. (1992). An Explicit Constitutive Algorithm for Large Strain Large Strain–Rate Elastic–Viscoplasticity. *Computer Methods in Appl. Mechanics & Engineering,* **95**, pp. 205-219.

Nemat-Nasser, S., and Li, Y.-F. (1992). A New Explicit Algorithm for Finite-Deformation Elastoplasticity and Elastoviscoplasticity: Performance Evaluation. *Computers and Structures,* **44**, No. 5, pp. 937-963

Taylor, L.M., and Flanagan, D.P. (1987). PRONTO 2D: A Two Dimensional Transient Solid Dynamics Program. Sandia Report, SAND 86–0594.

Taylor, L.M., and Flanagan, D.P. (1989). PRONTO 3D: A Three Dimensional Transient Solid Dynamics Program. Sandia Report, SAND 87–1912.

Wilkins, M.L. (1964). Calculation of Elastic–Plastic Flow. *Meth. Comput. Physics* **3B**, pp. 211-262

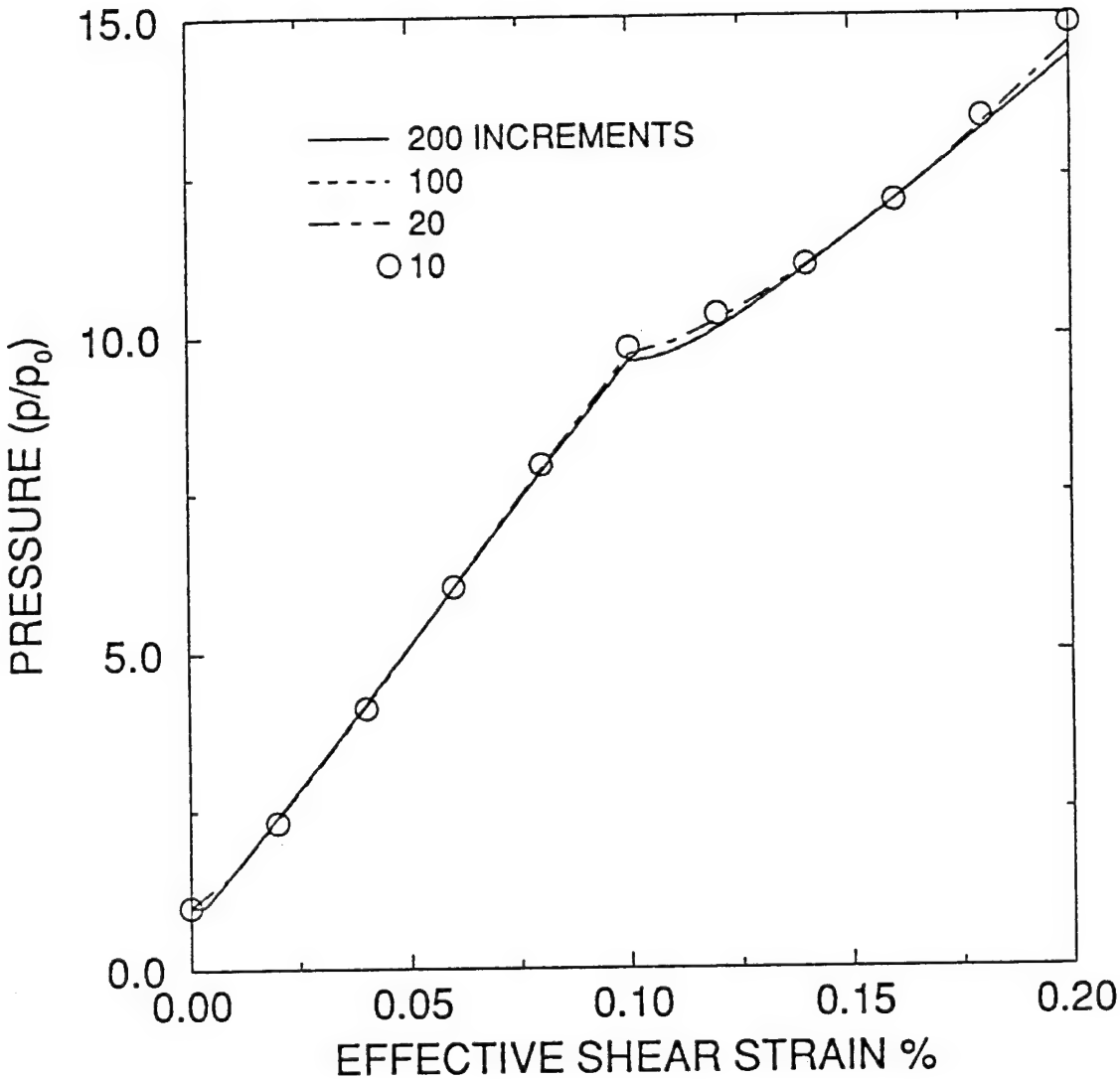

Figure II.1a Performance evaluation of the integration scheme for rate–independent equations; relation between pressure and shear strain.

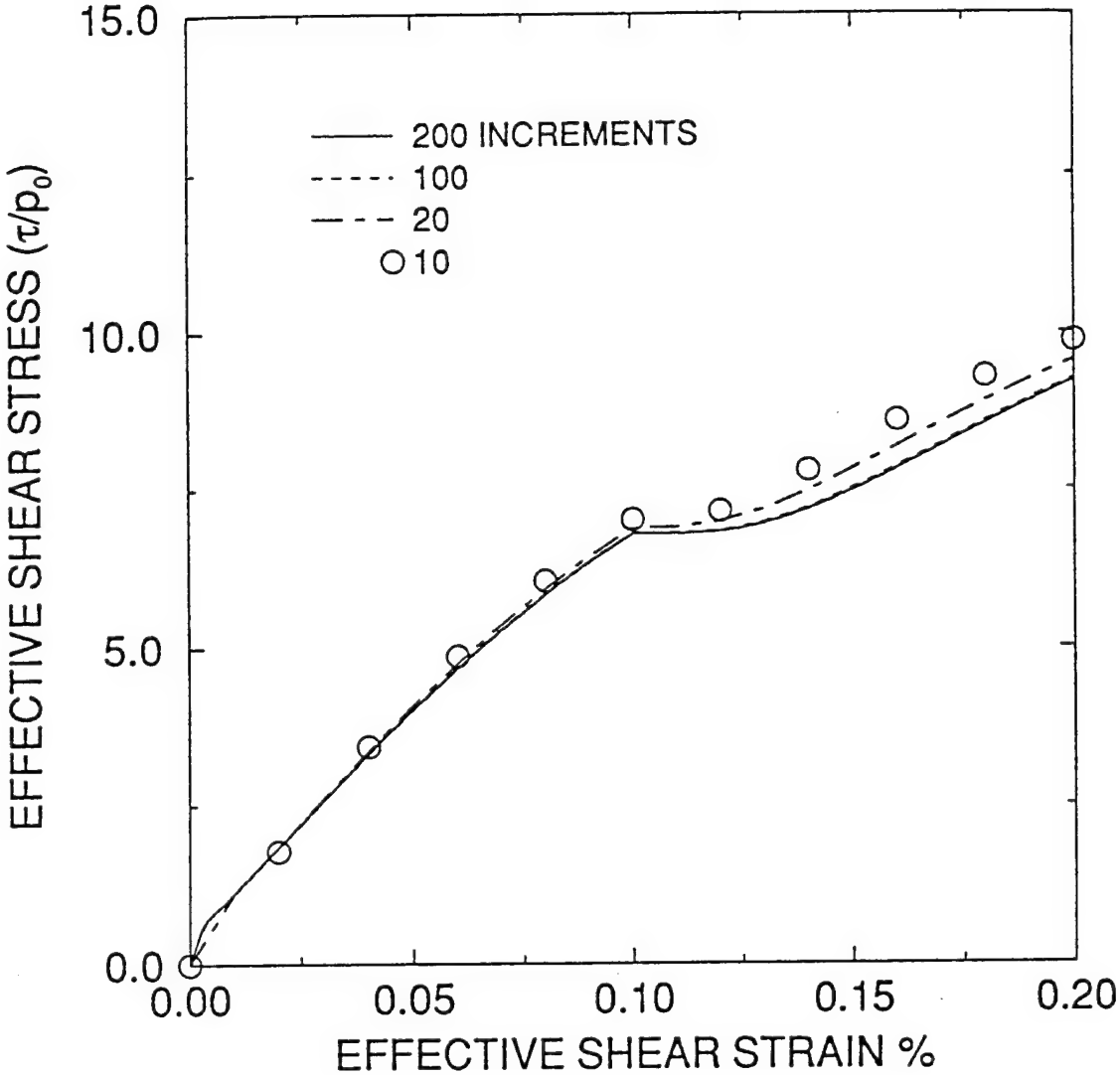

Figure II.1b Performance evaluation of the integration scheme for rate–independent equations; relation between effective shear stress and shear strain.

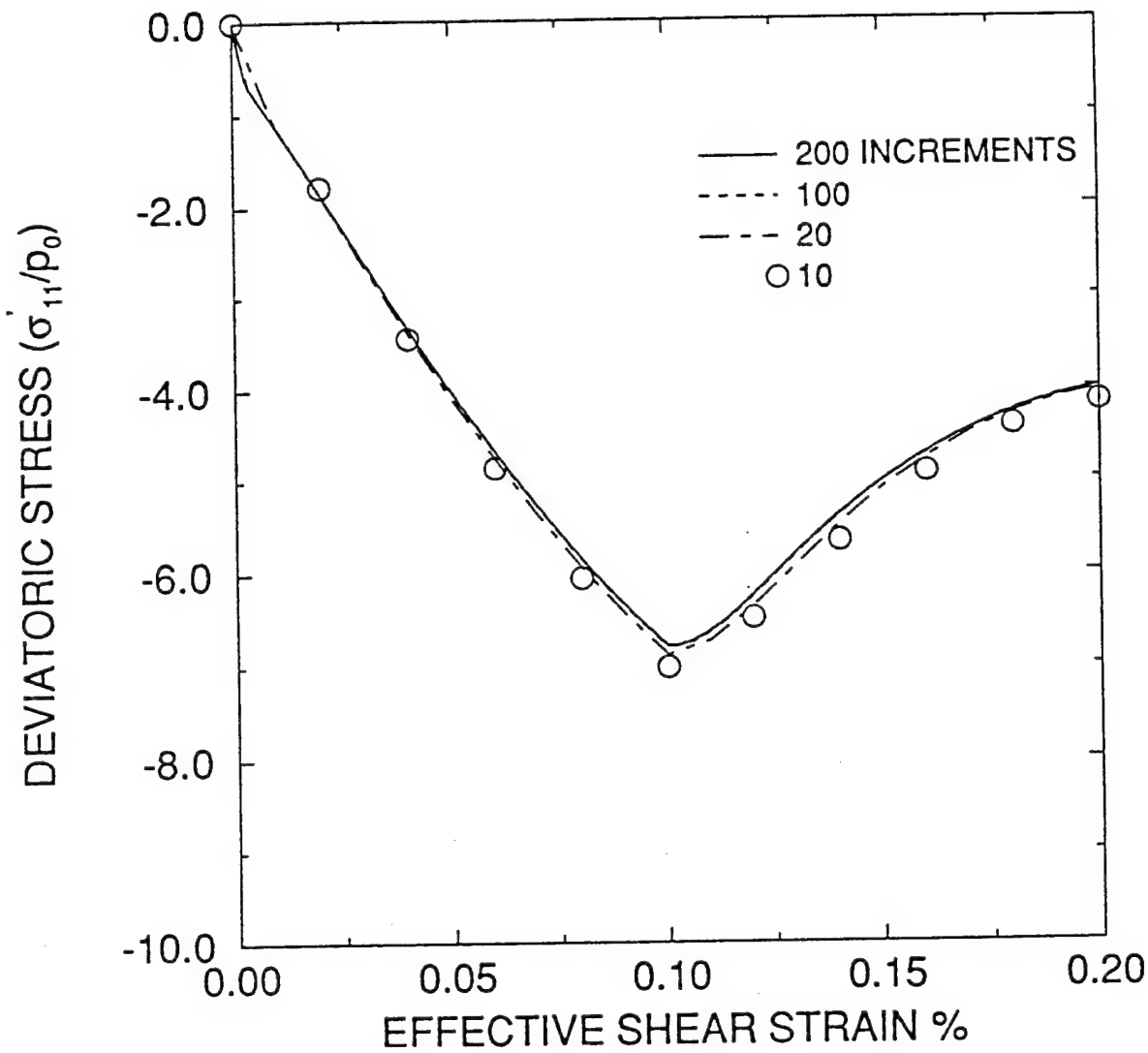

Figure II.1c Performance evaluation of the integration scheme for rate–independent equations; relation between deviatoric stress σ'_{11} and shear strain.

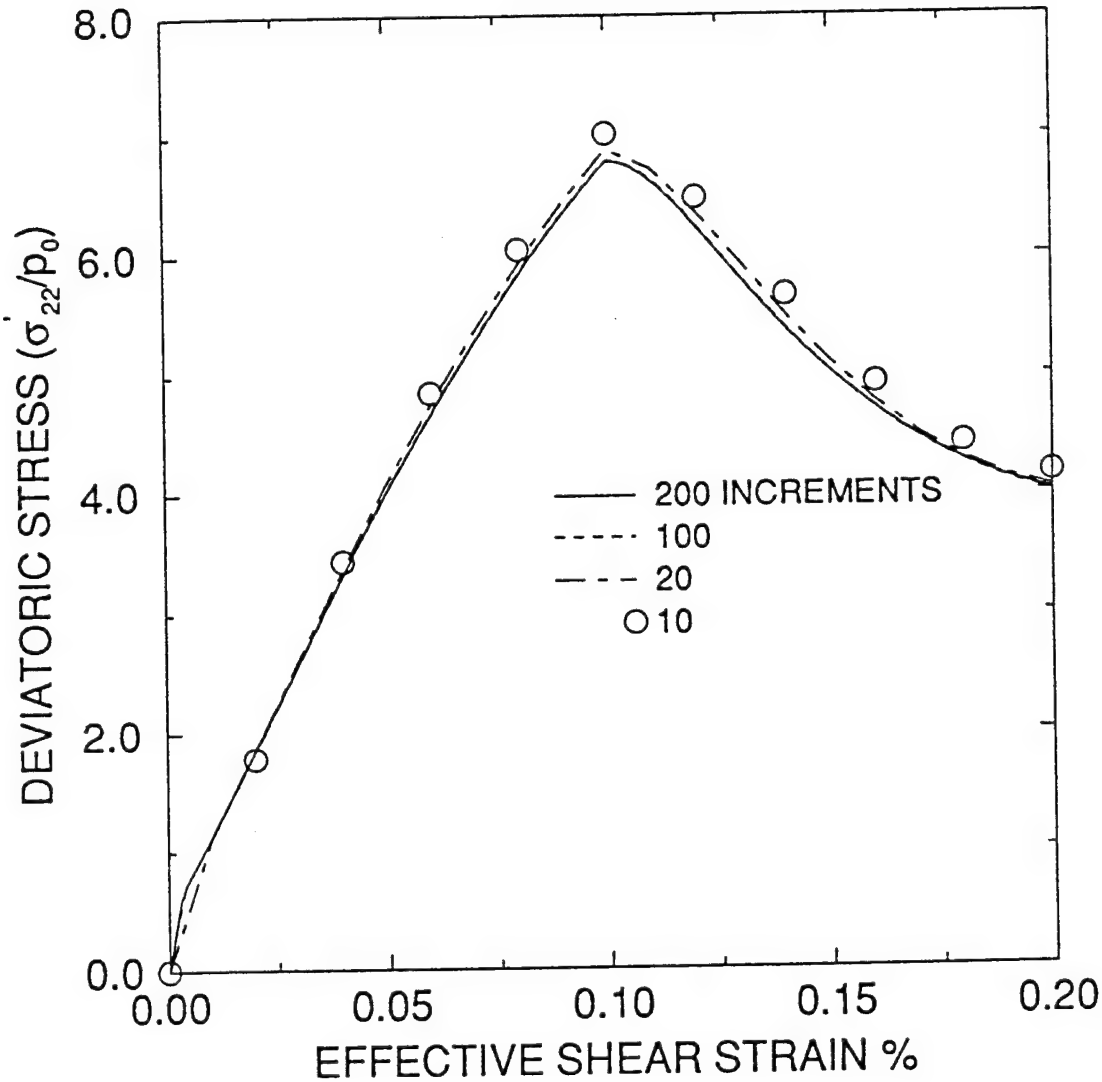

Figure II.1d Performance evaluation of the integration scheme for rate–independent equations; relation between deviatoric stress σ'_{22} and shear strain.

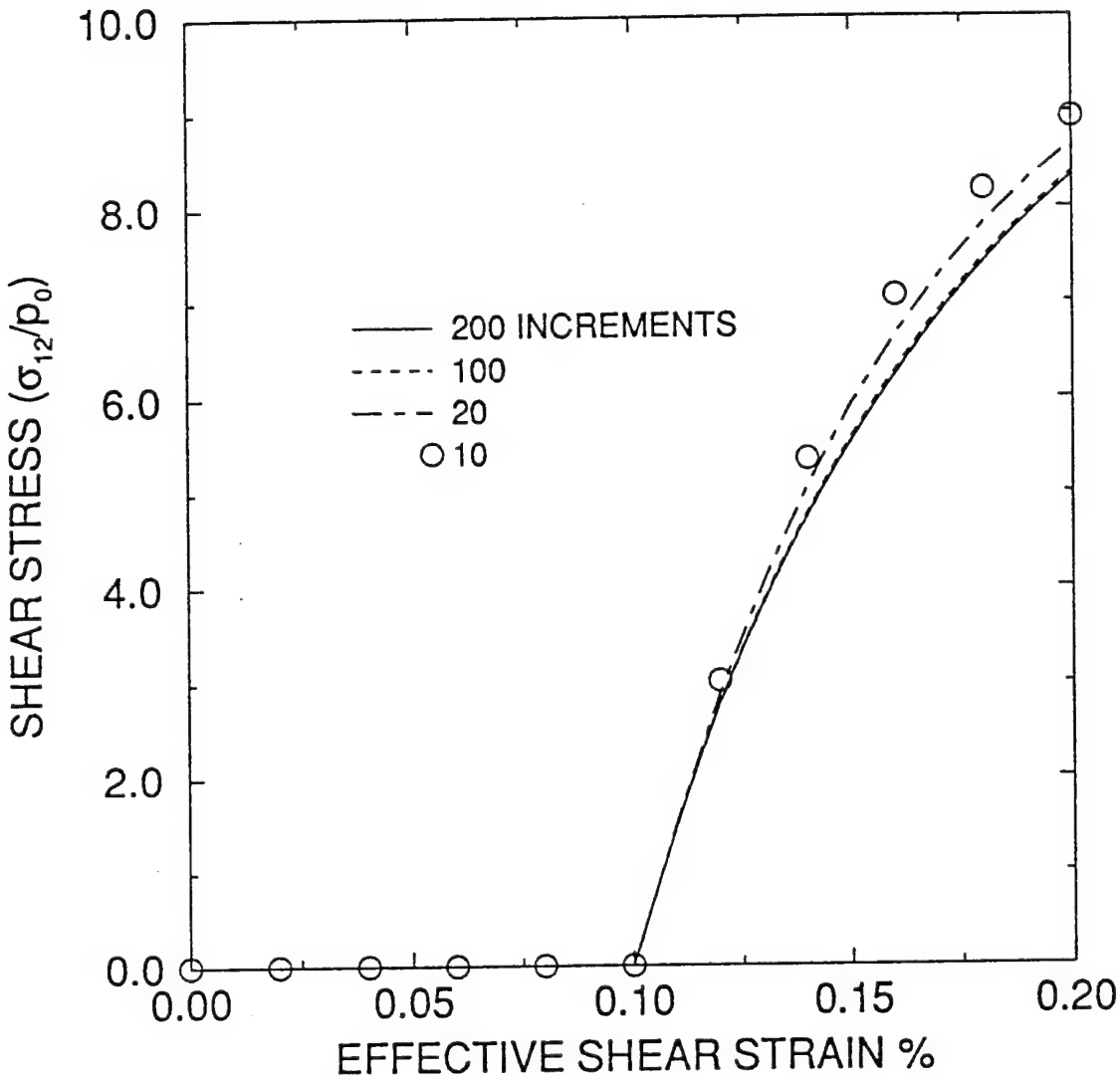

Figure II.1e Performance evaluation of the integration scheme for rate–independent equations; relation between shear stress σ'_{12} and shear strain.

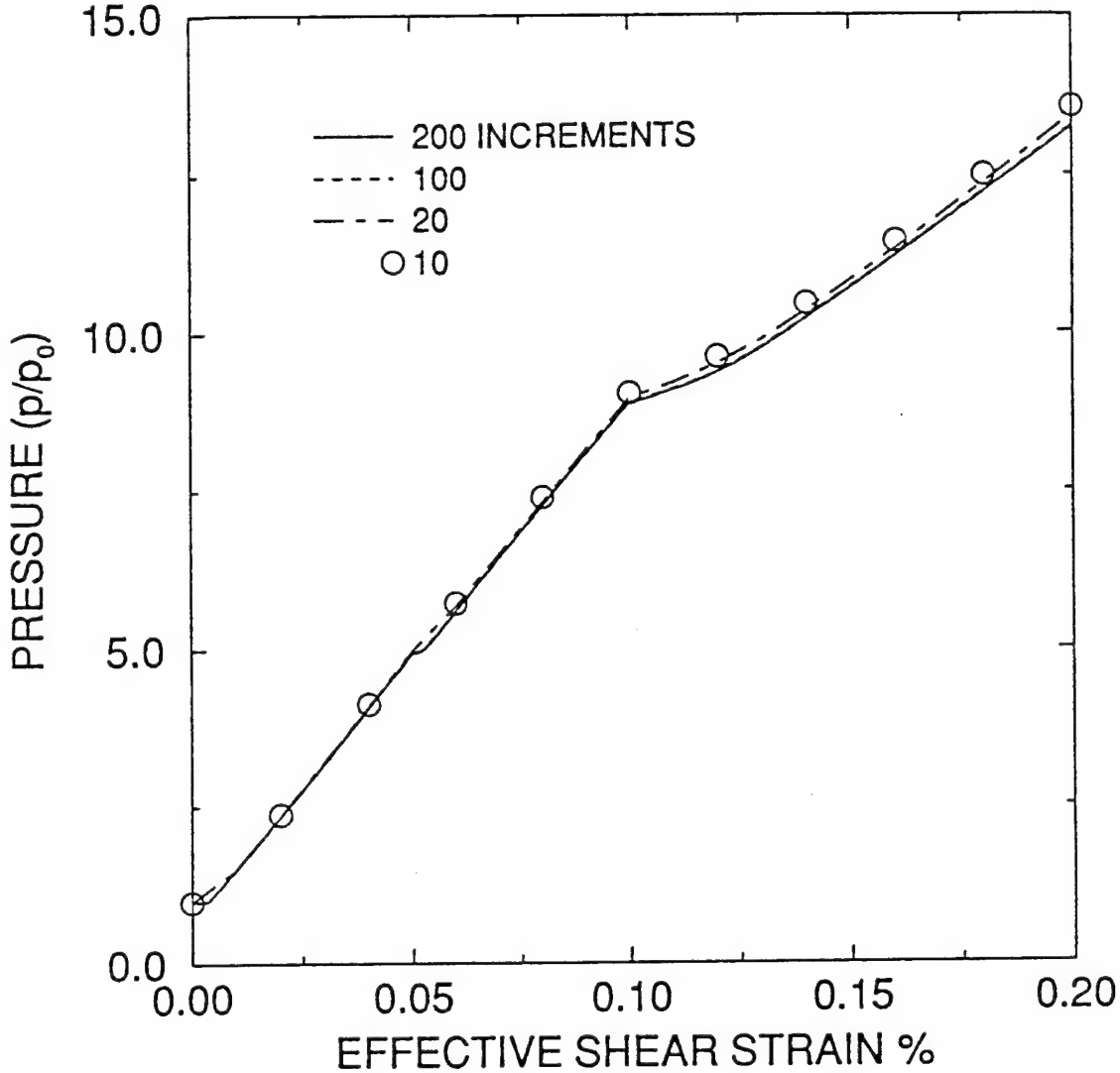

Figure II.2a Performance evaluation of the integration scheme for rate–dependent equations; relation between pressure and shear strain.

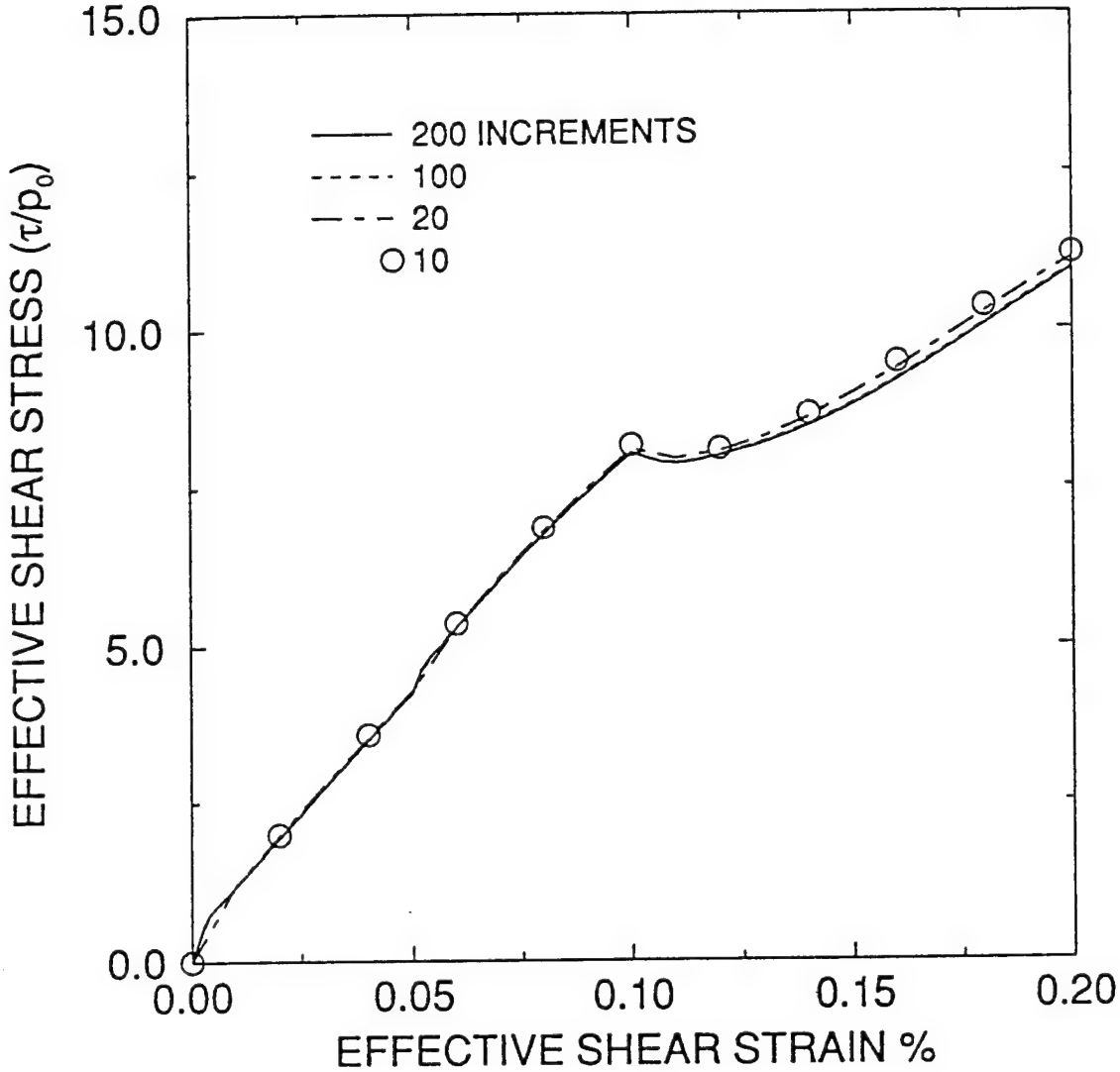

Figure II.2b Performance evaluation of the integration scheme for rate–dependent equations; relation between effective shear stress and shear strain.

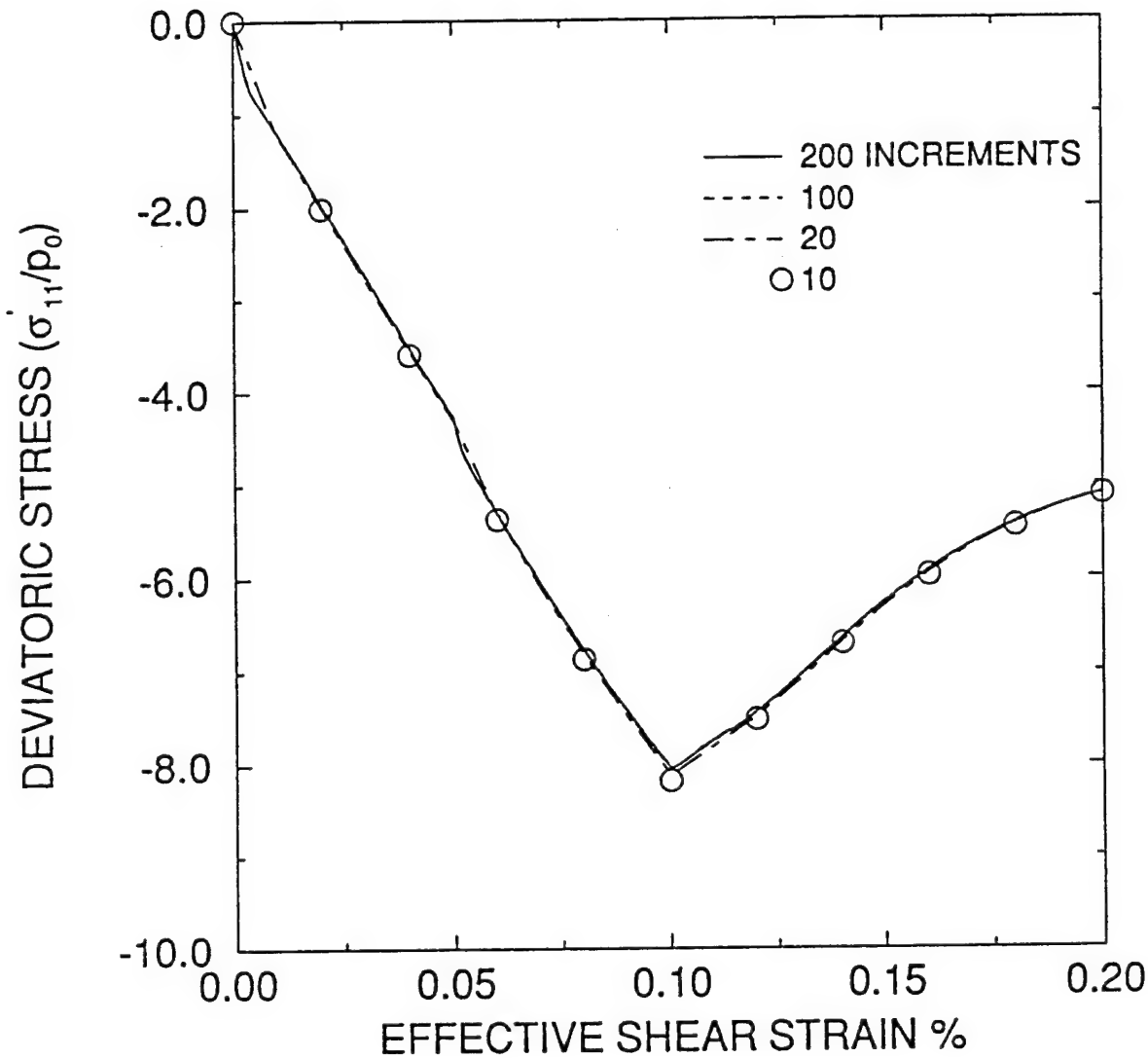

Figure II.2c Performance evaluation of the integration scheme for rate–dependent equations; relation between deviatoric stress σ'_{11} and shear strain.

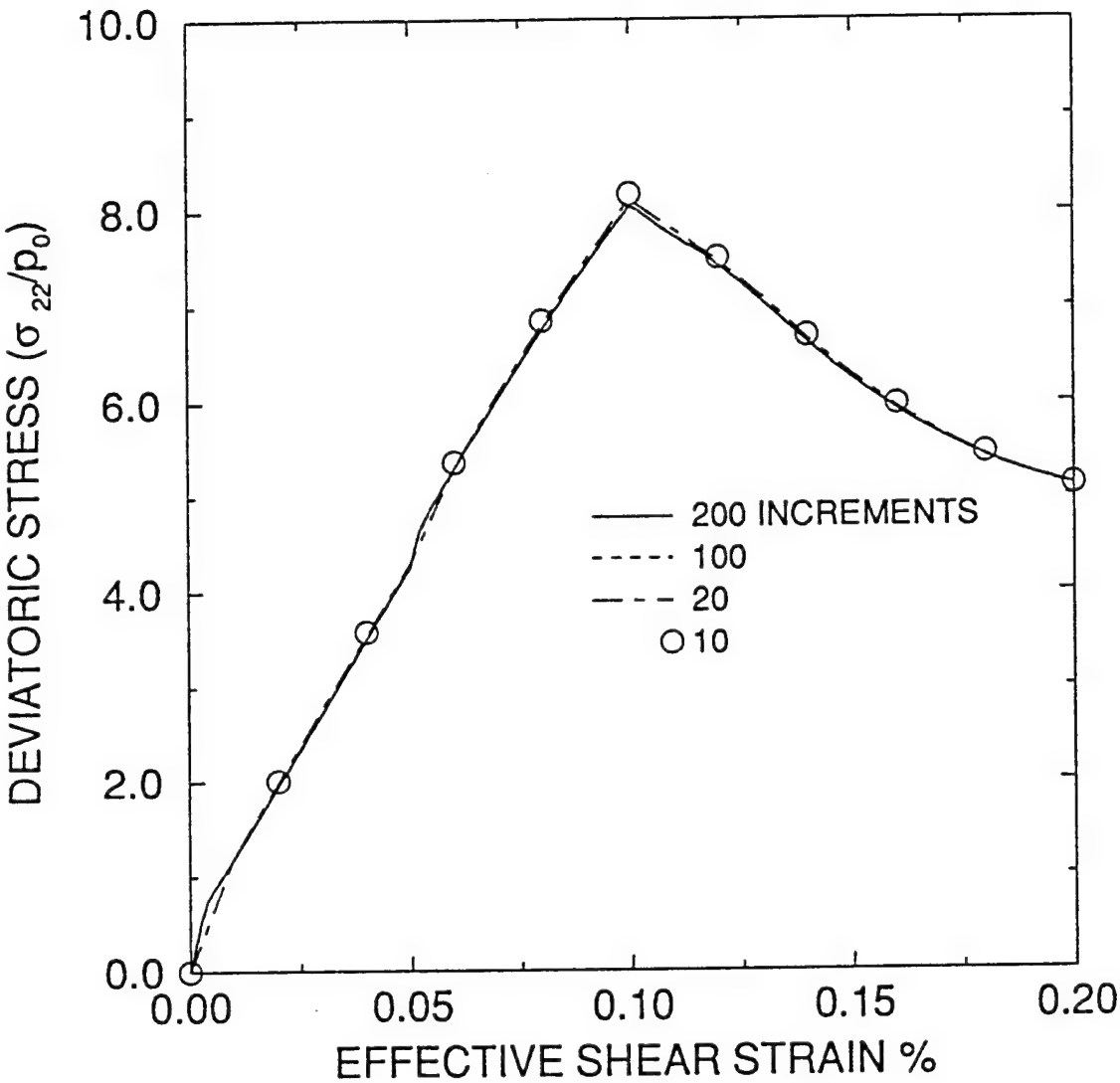

Figure II.2d Performance evaluation of the integration scheme for rate–dependent equations; relation between deviatoric stress σ'_{22} and shear strain.

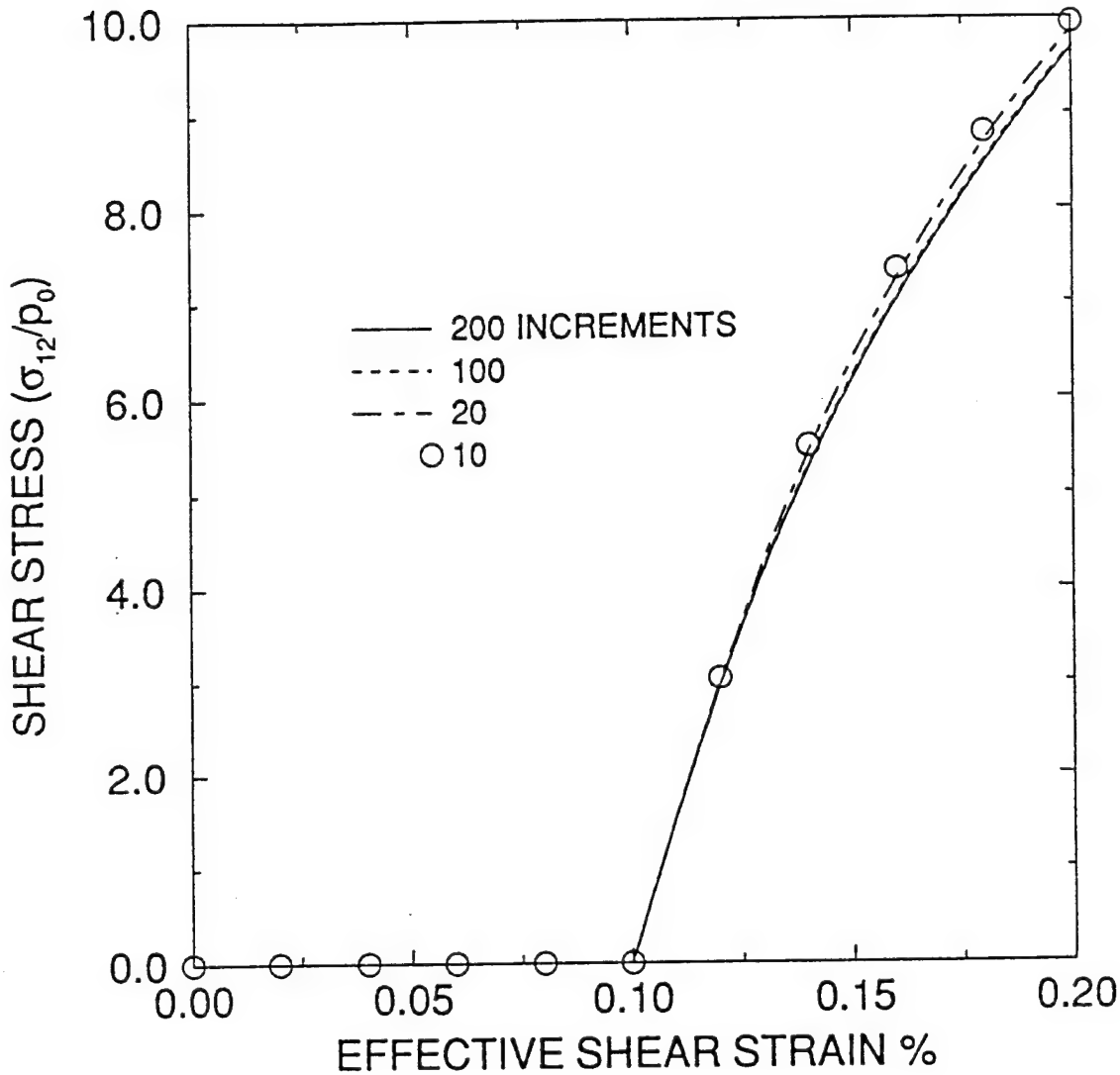

Figure II.2e Performance evaluation of the integration scheme for rate–dependent equations; relation between shear stress σ'_{12} and shear strain.

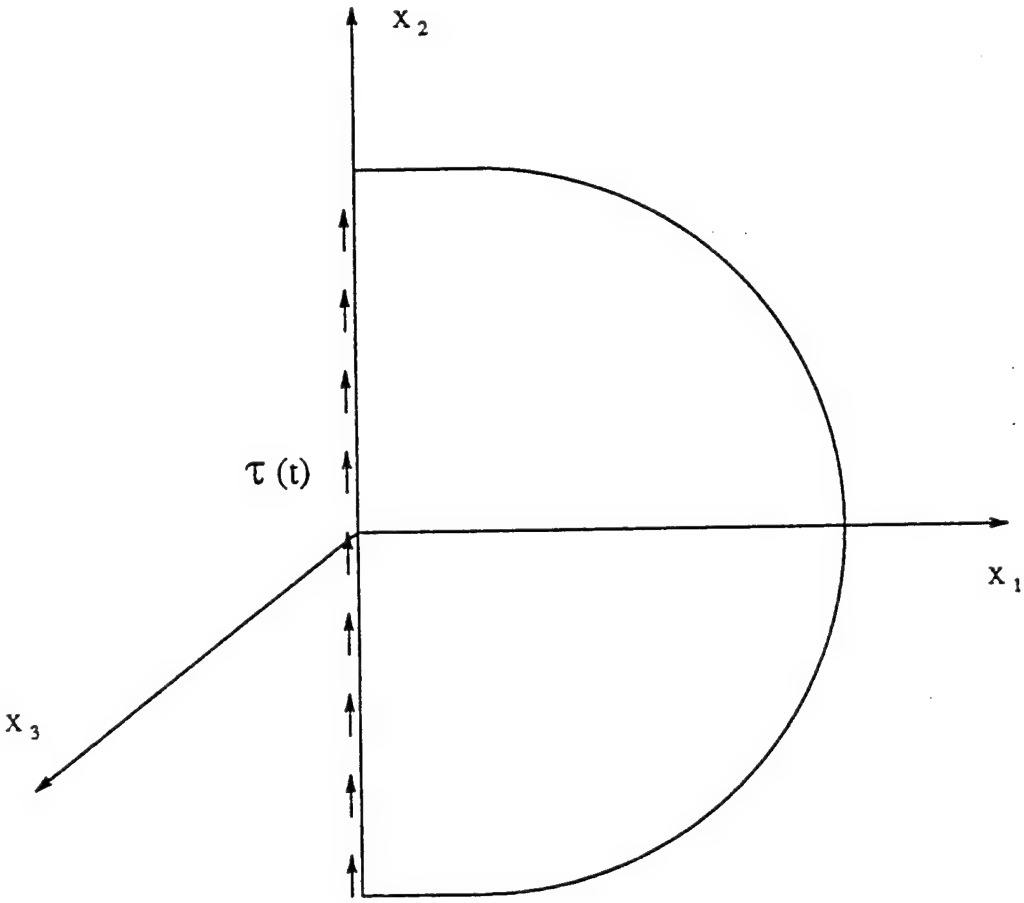

Figure II.3 Schematic diagram of a semi infinite media subjected to shear traction at the free surface.

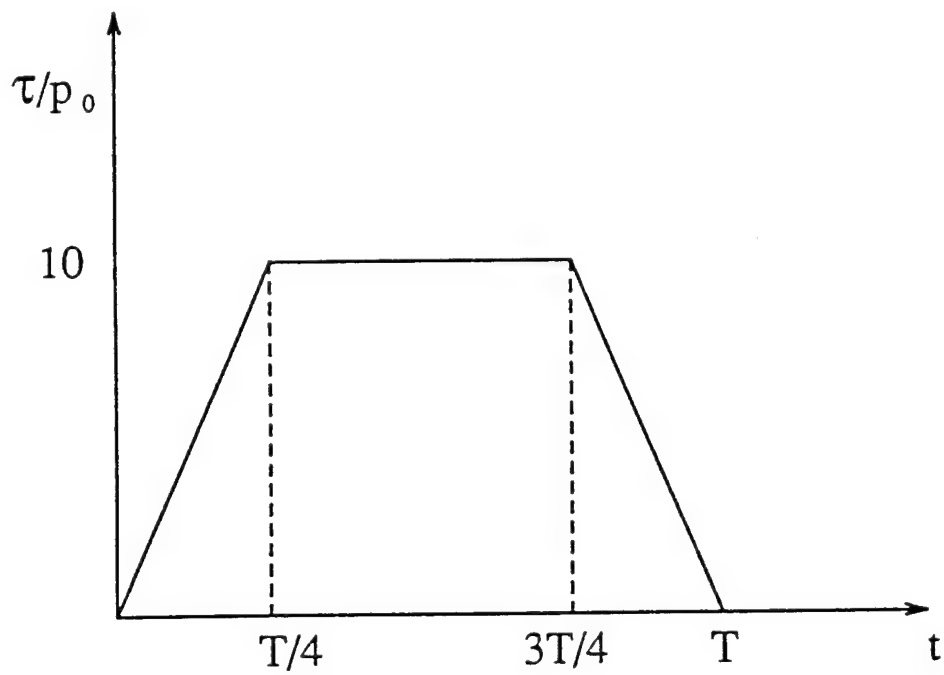

Figure II.4 Input shear stress pulse at the free surface.

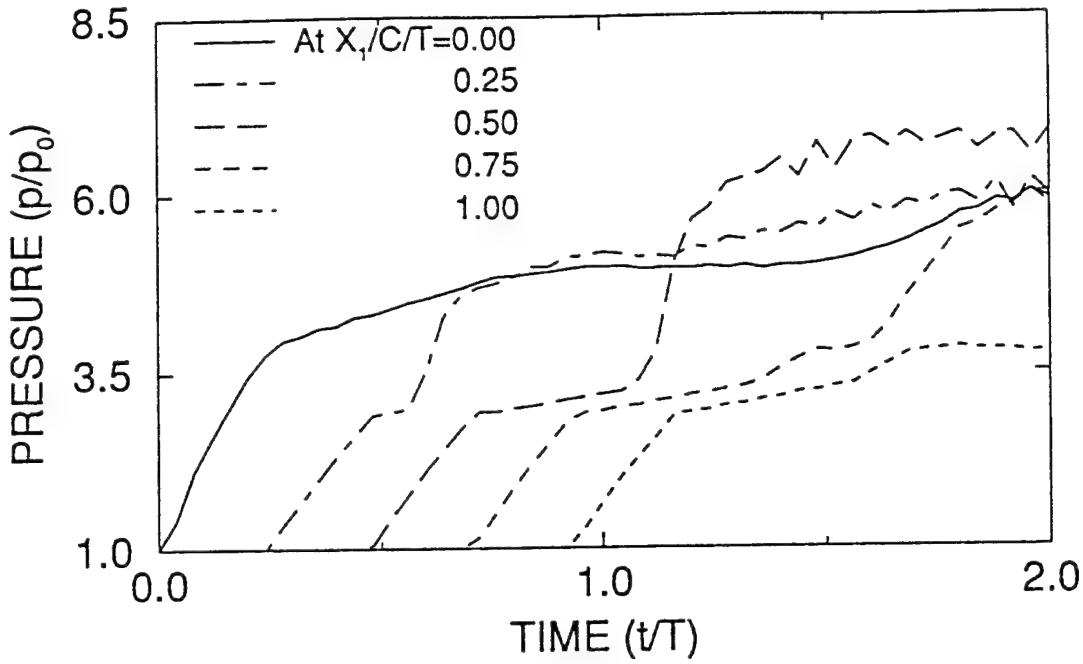

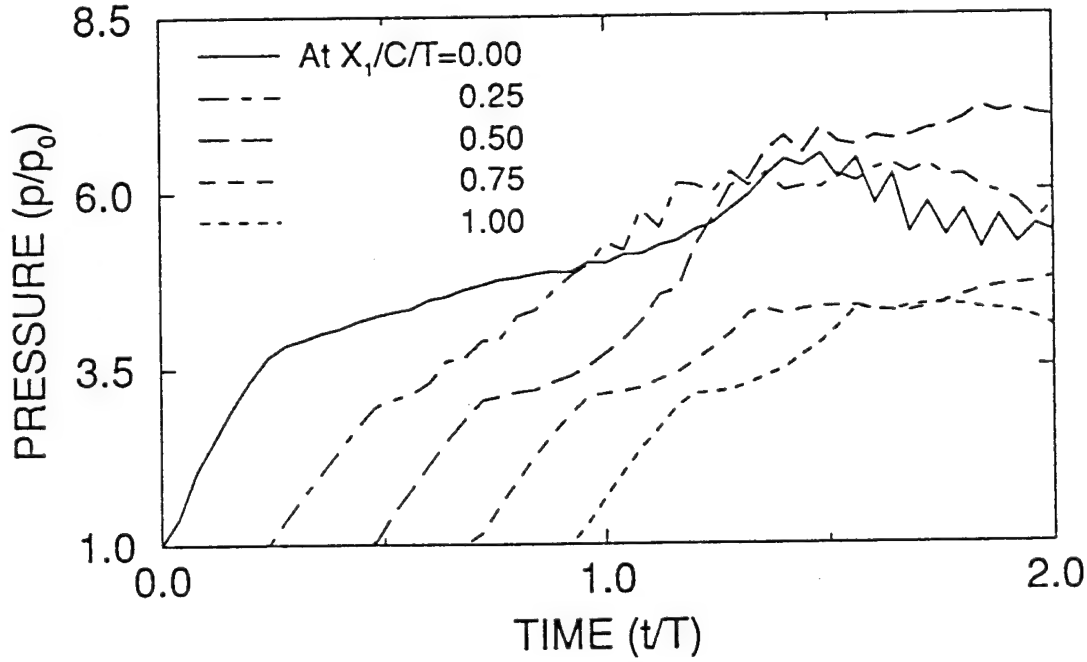

Figure II.5a Time history of pressure at various distances from the free surface; (i) with out noncoaxiality, (ii) with noncoaxiality

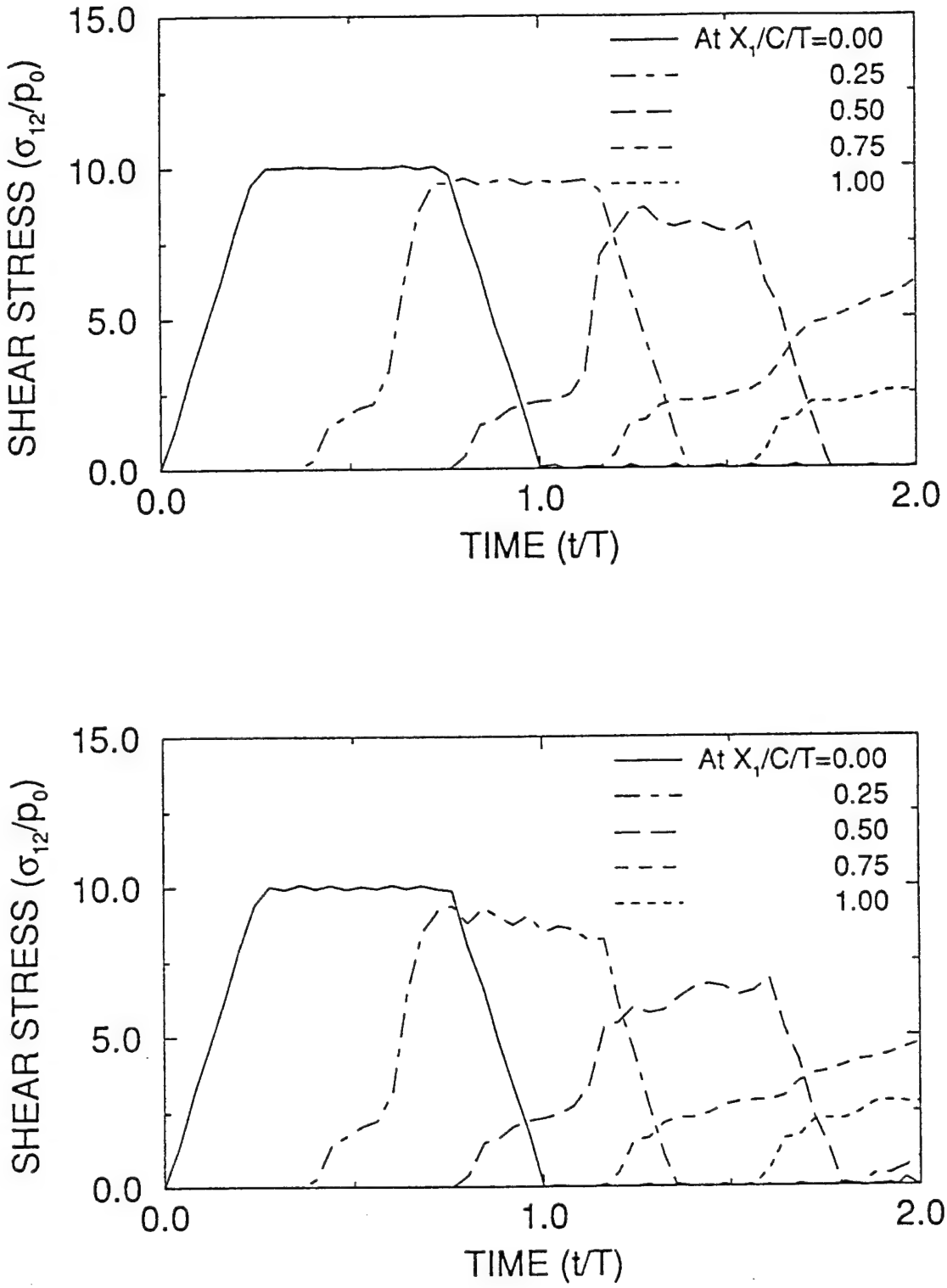

Figure II.5b Time history of shear stress σ_{12} at various distances from the free surface; (i) with out noncoaxiality, (ii) with noncoaxiality

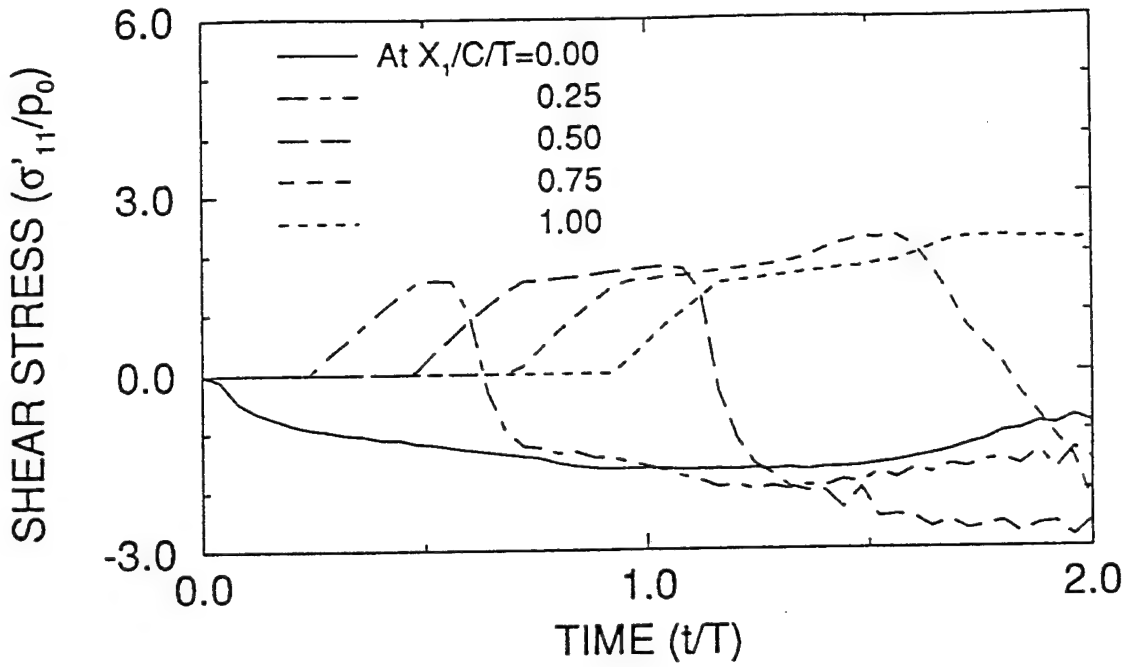

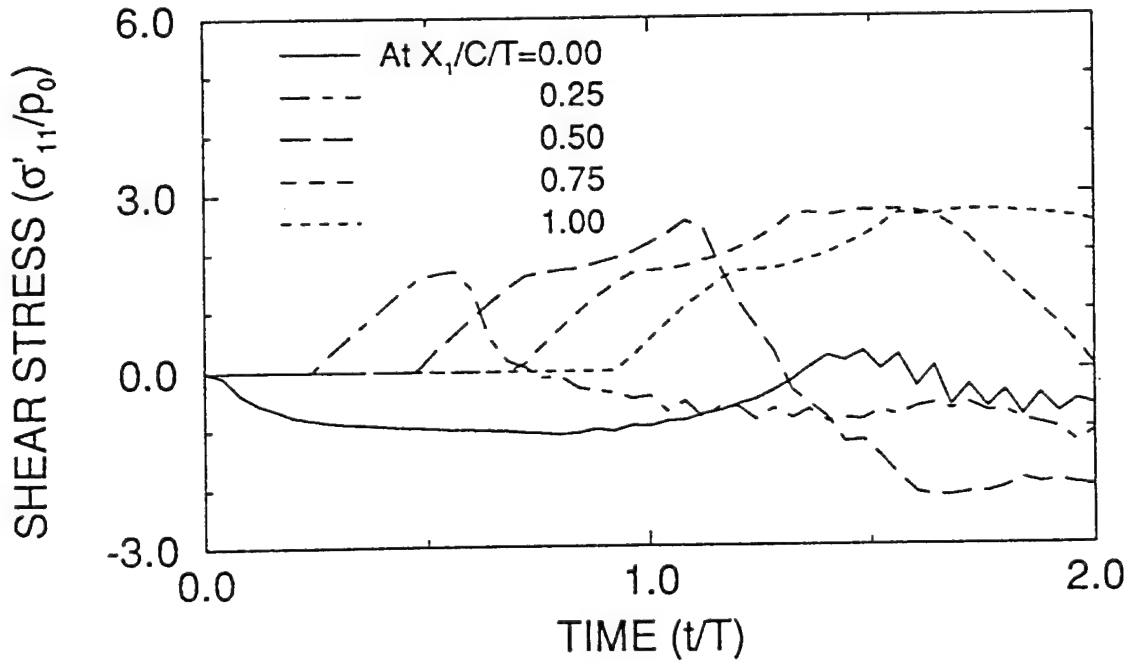

Figure II.5c Time history of deviatoric stress σ'_{11} at various distances from the free surface; (i) with out noncoaxiality, (ii) with noncoaxiality

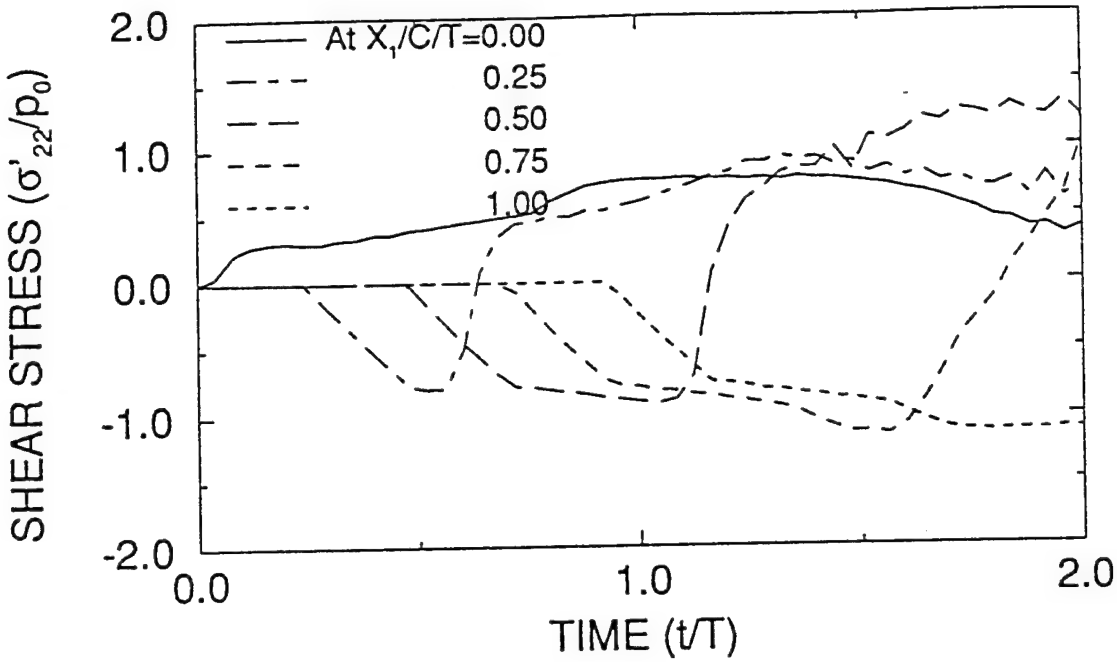

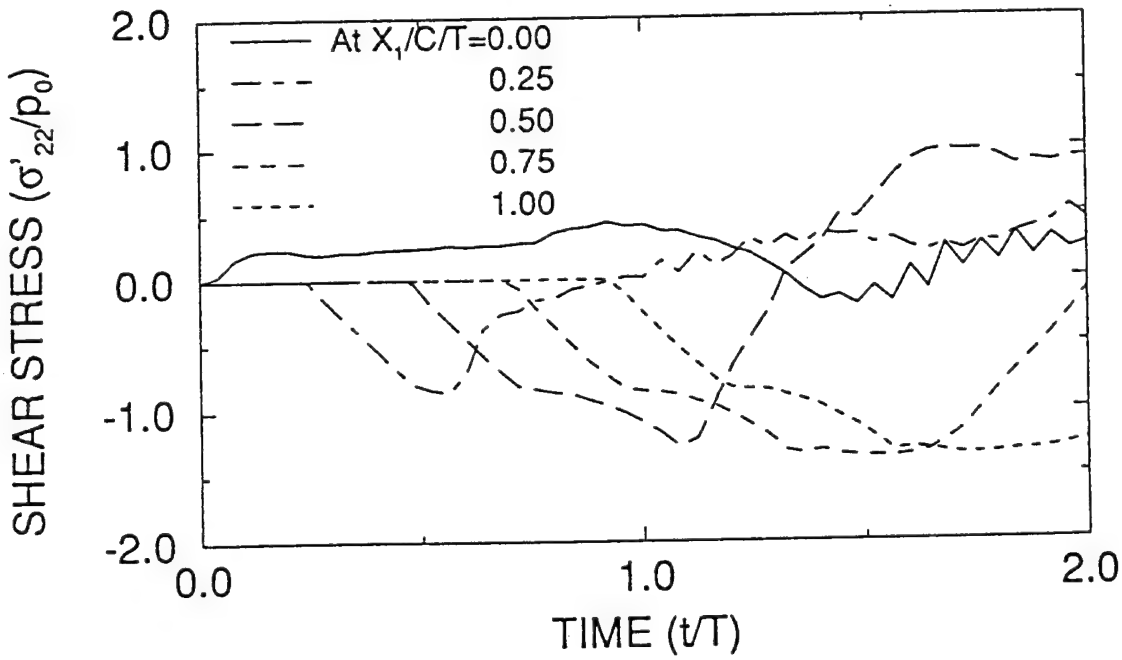

Figure II.5d Time history of deviatoric stress σ'_{22} at various distances from the free surface; (i) with out noncoaxiality, (ii) with noncoaxiality

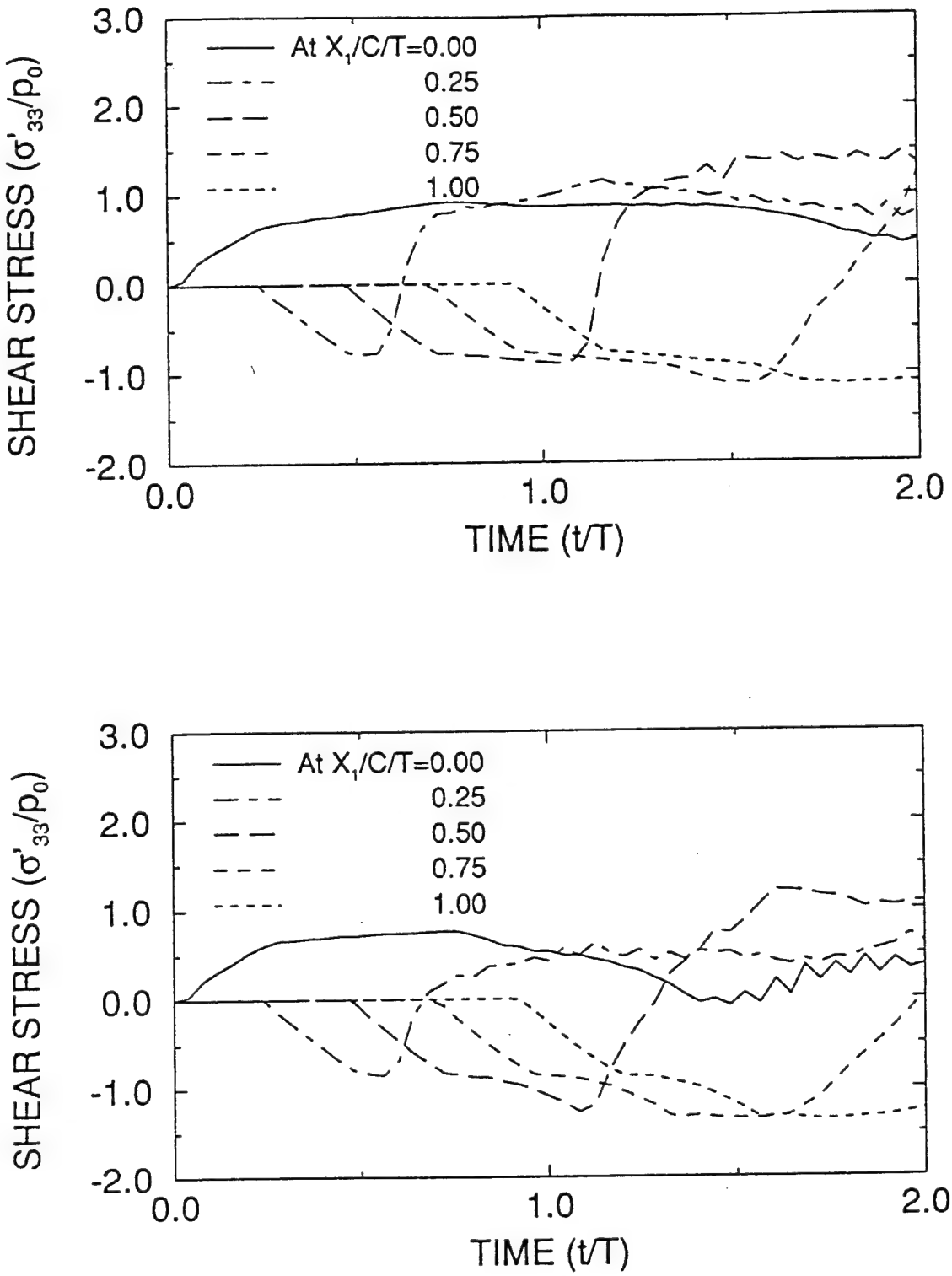

Figure II.5e Time history of deviatoric stress σ'_{33} at various distances from the free surface; (i) with out noncoaxiality, (ii) with noncoaxiality

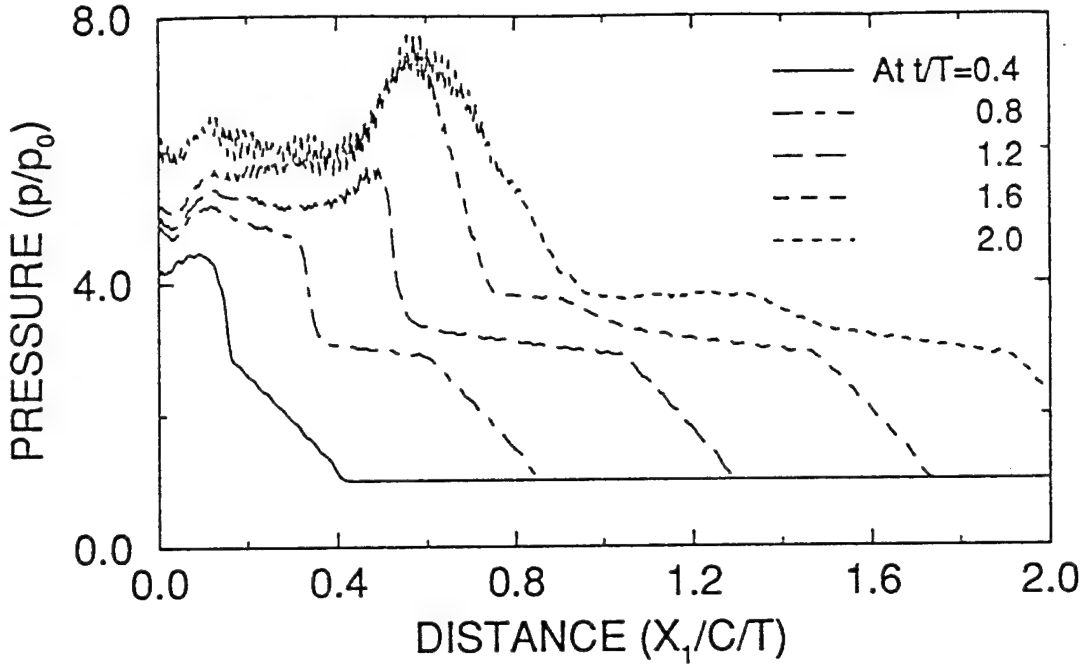

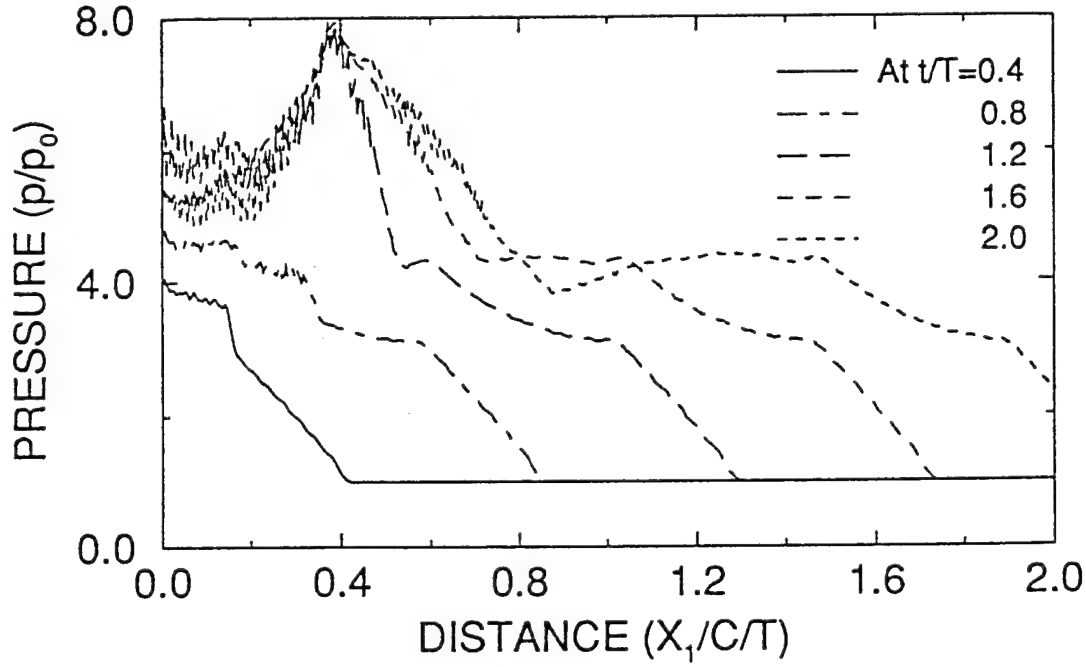

Figure II.6a Profile of pressure at various times; (i) with out noncoaxiality, (ii) with noncoaxiality

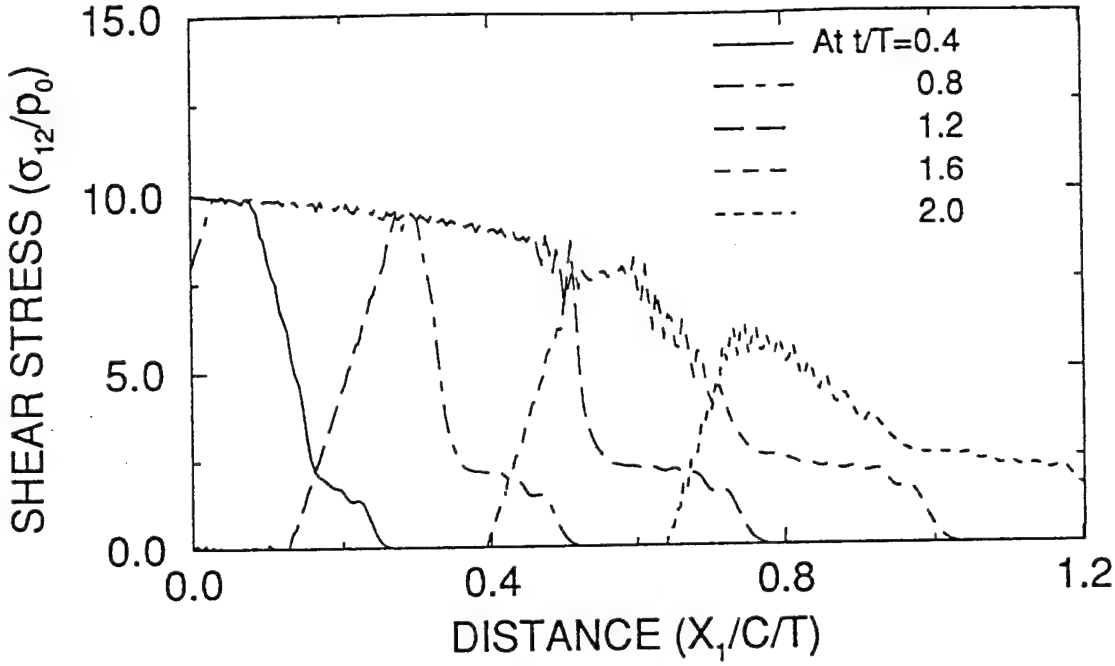

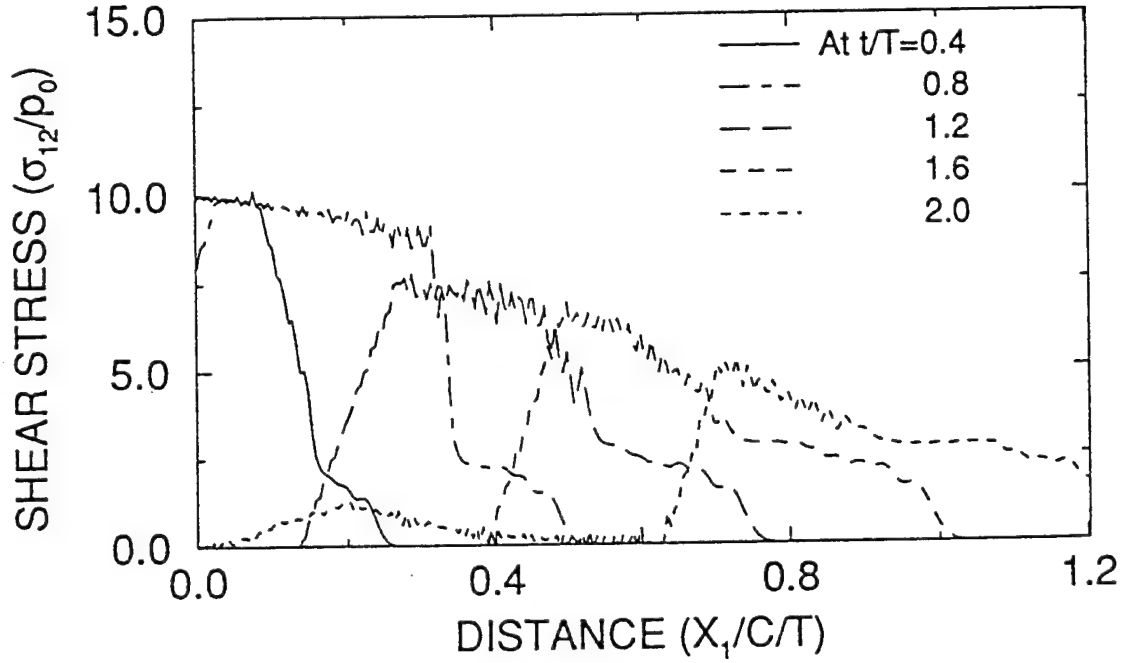

Figure II.6b Profile of shear stress σ_{12} at various times; (i) with out noncoaxiality, (ii) with noncoaxiality

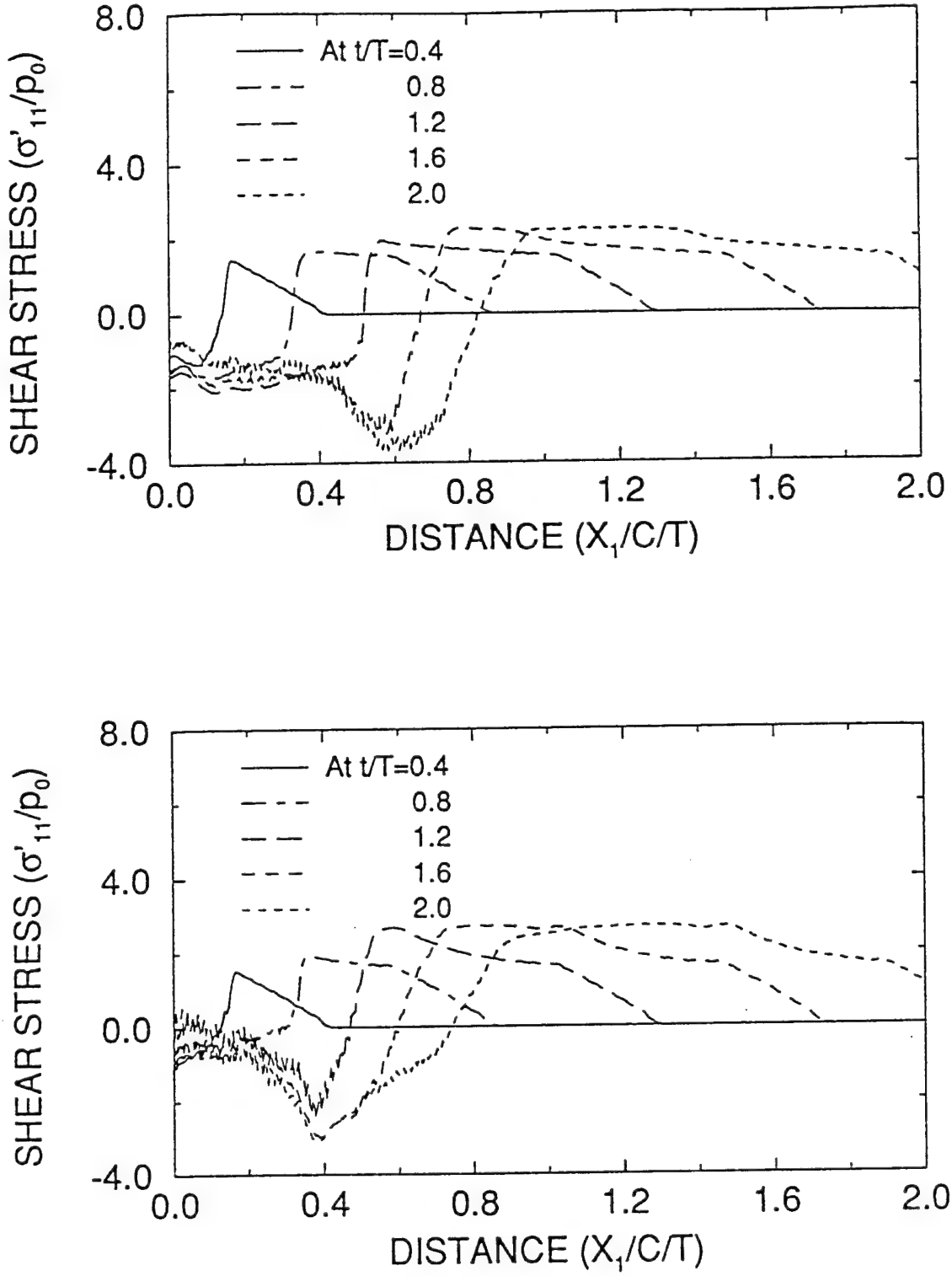

Figure II.6c Profile of deviatoric stress σ'_{11} at various times; (i) with out noncoaxiality, (ii) with noncoaxiality

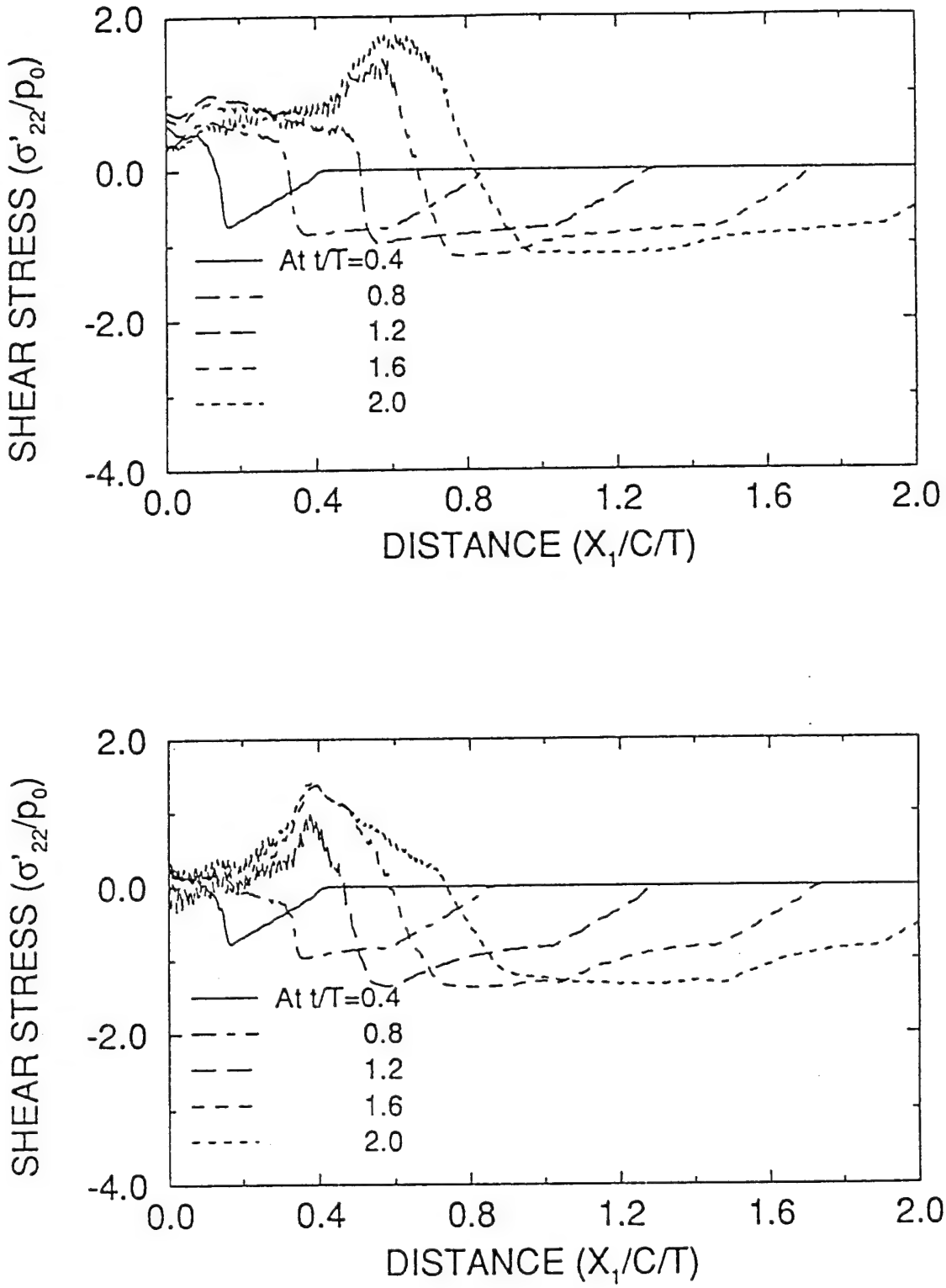

Figure II.6d Profile of deviatoric stress σ'_{22} at various times; (i) with out noncoaxiality, (ii) with noncoaxiality

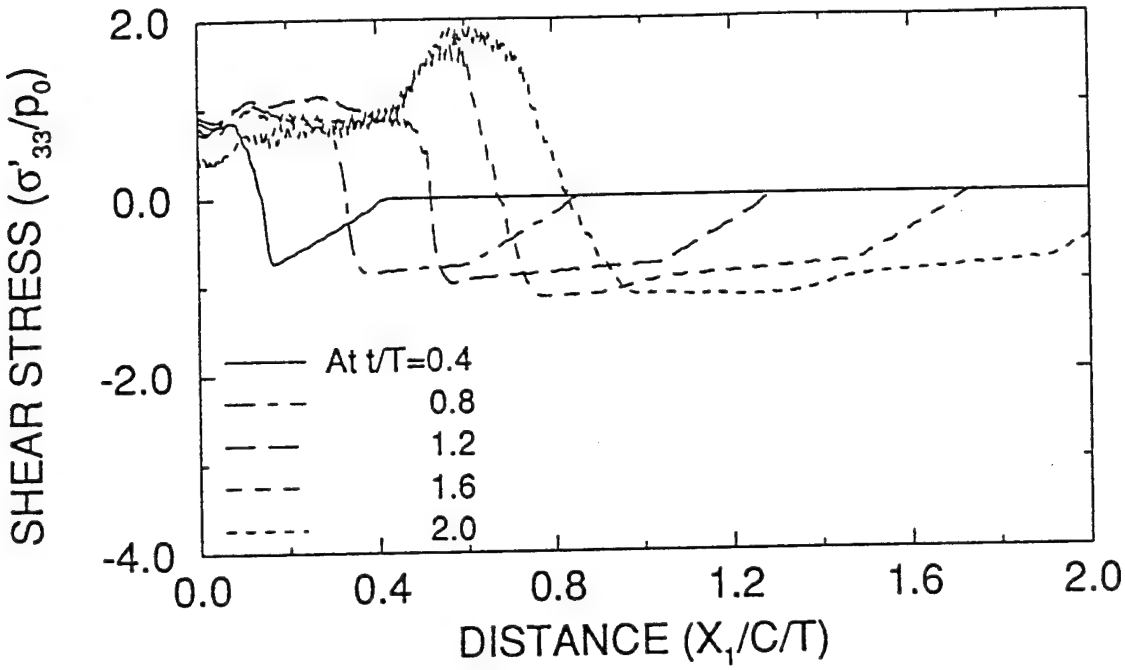

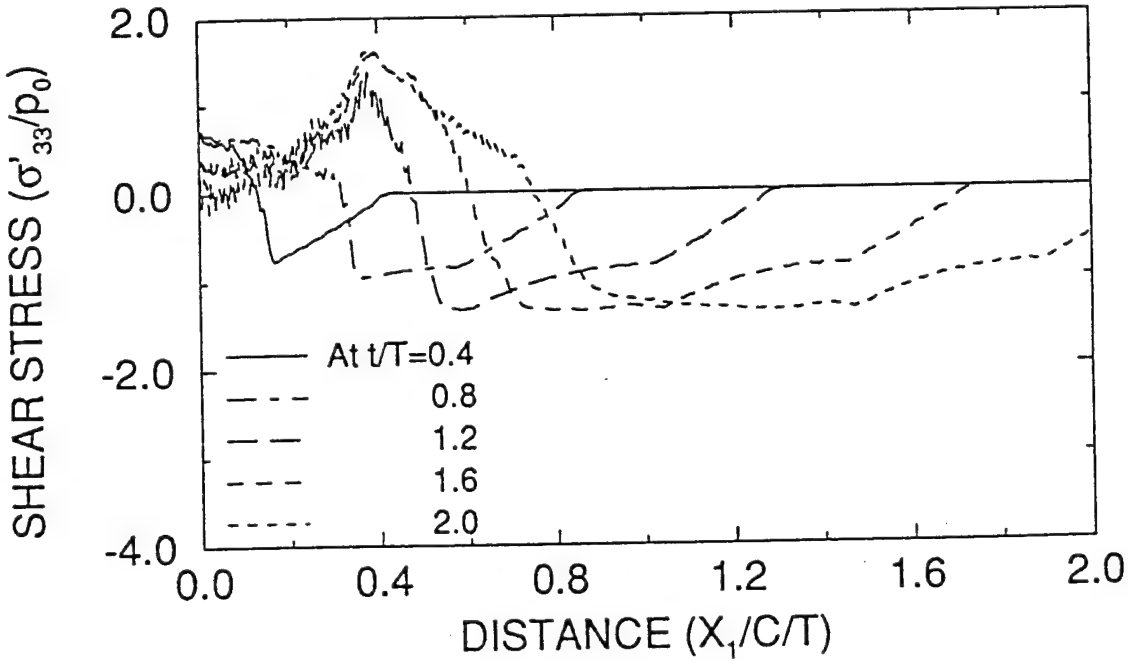

Figure II.6e Profile of deviatoric stress σ'_{33} at various times; (i) with out noncoaxiality, (ii) with noncoaxiality

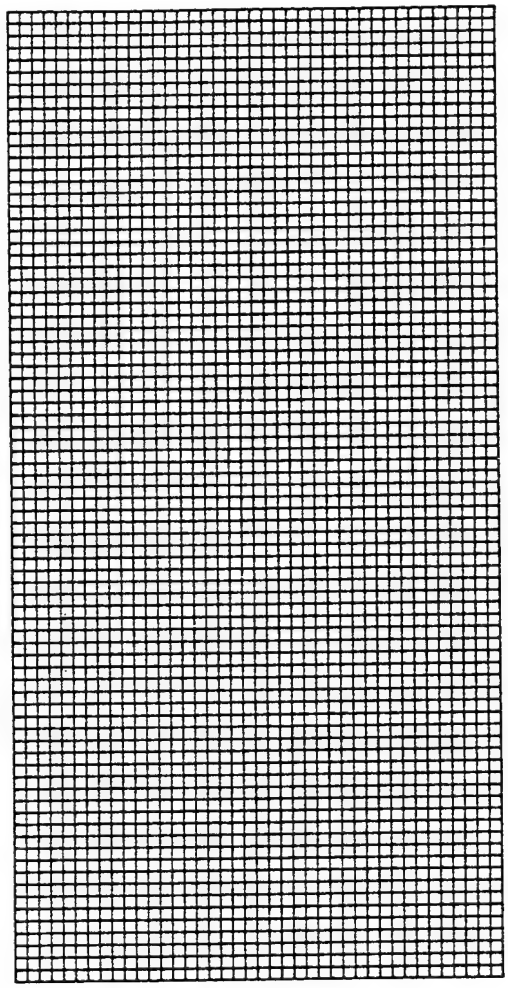

Figure II.7 Undeformed mesh for the plane strain compression problem.

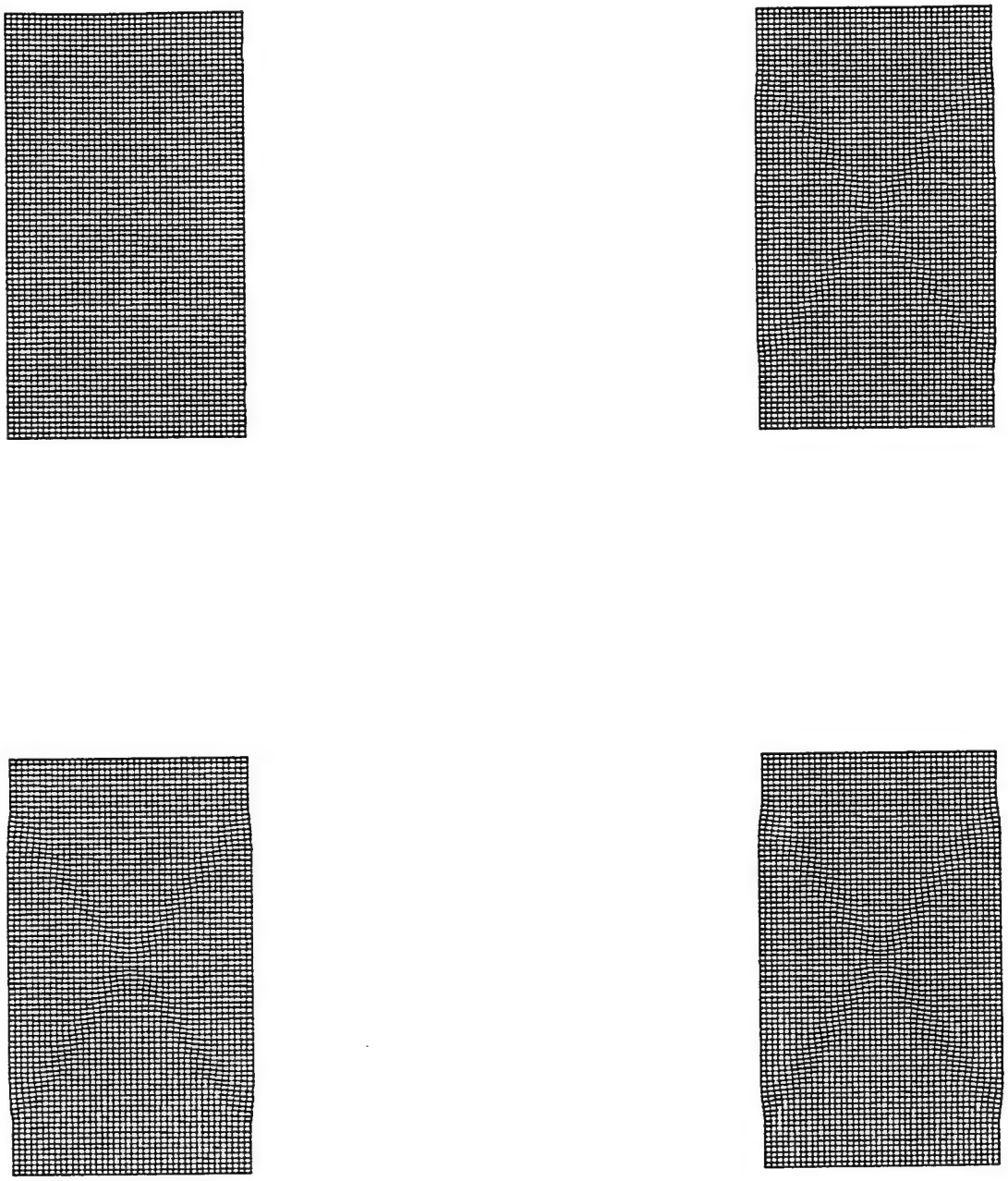

Figure II.8 Deformed mesh plots for $e_0 = 0.6$ and $V_0 = 5\,cm/s$ at (a) 4, (b) 5, (c) 6, (d) 7, percent axial strain levels.

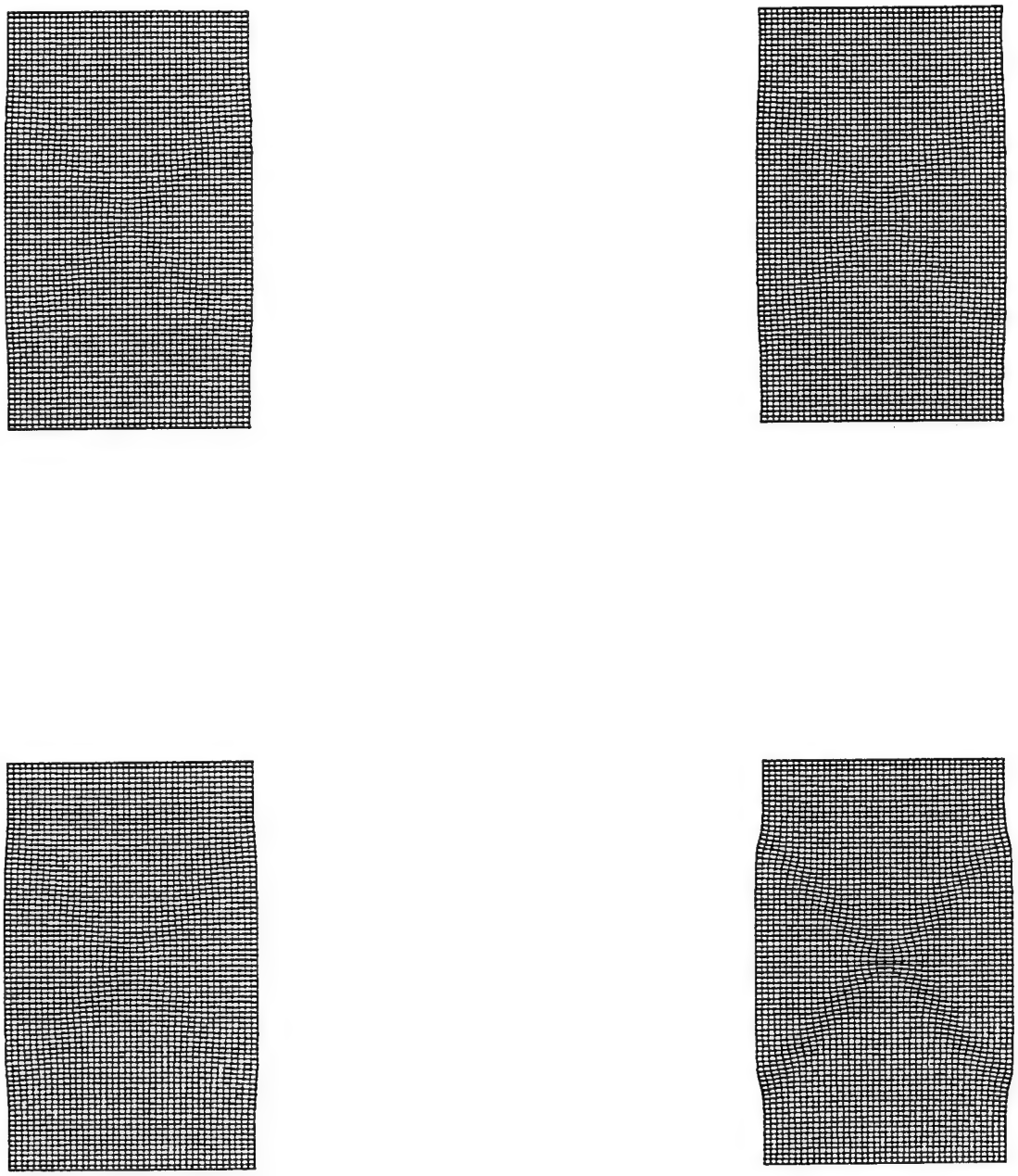

Figure II.9 Deformed mesh plots for $e_0 = 0.6$ and $V_0 = 10\,cm/s$ at (a) 4, (b) 6, (c) 8, (d) 10, percent axial strain levels.

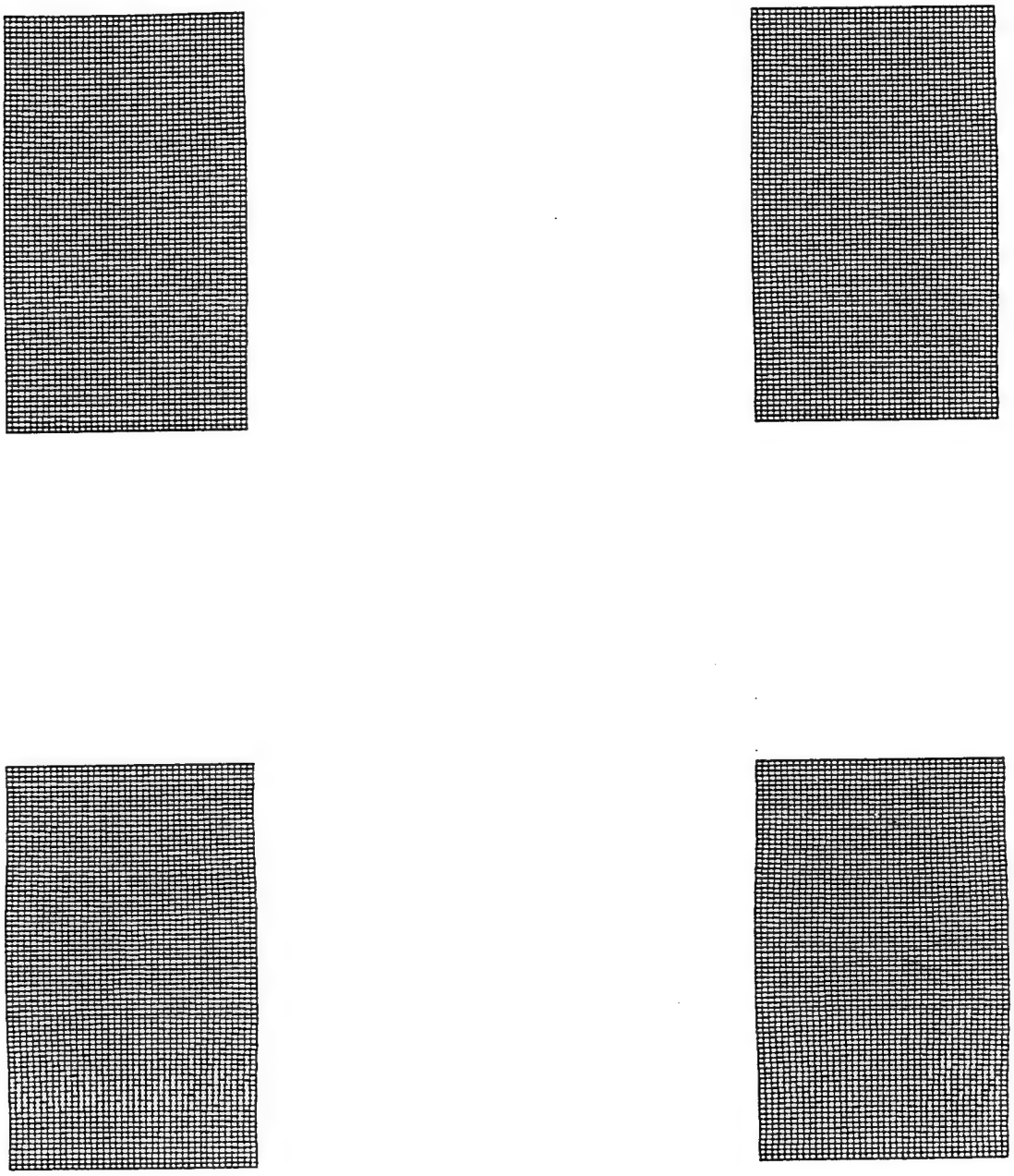

Figure II.10 Deformed mesh plots for $e_0 = 0.6$ and $V_0 = 100\,cm/s$ at (a) 4, (b) 6, (c) 8, (d) 10, percent axial strain levels.

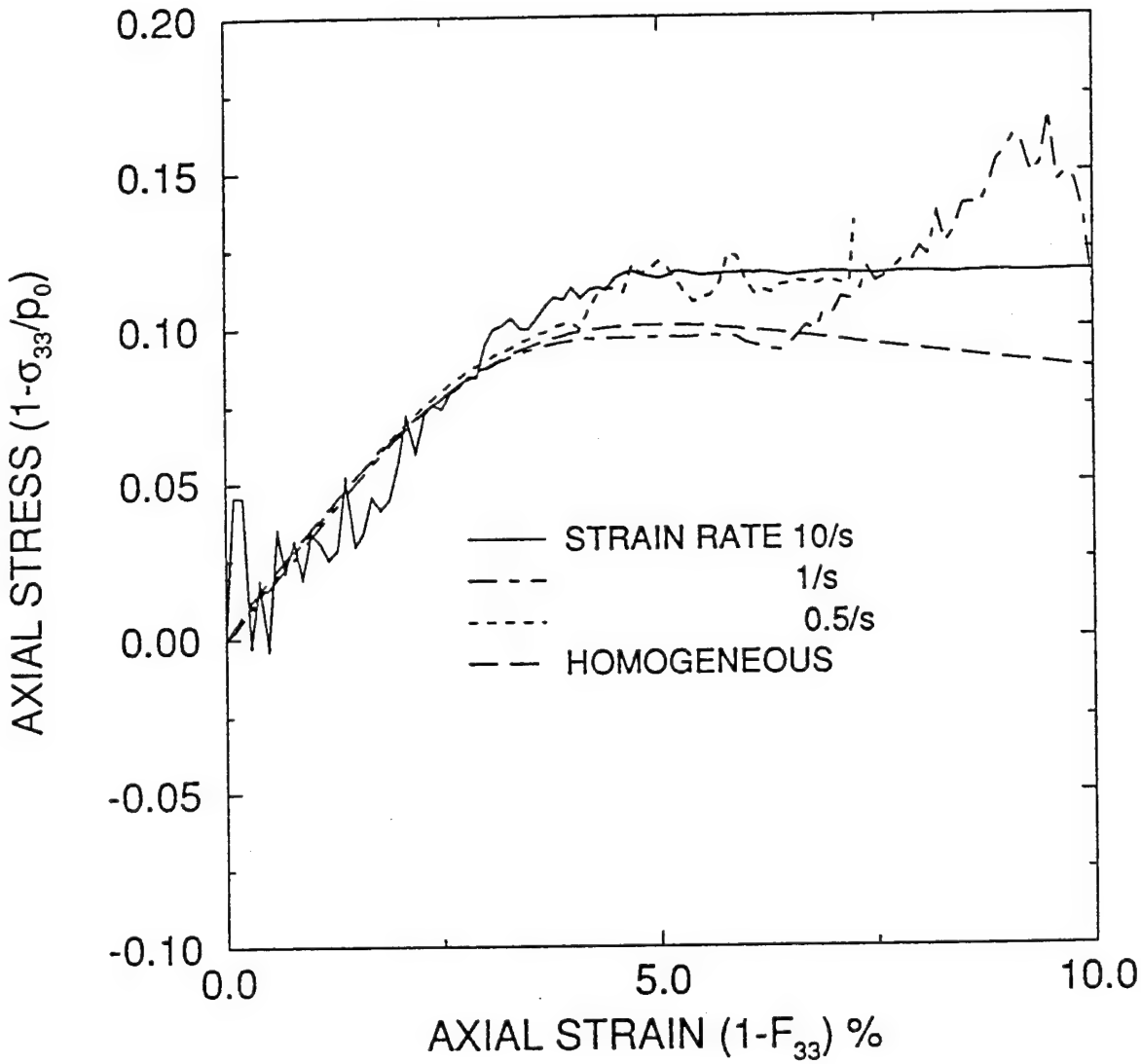

Figure II.11 Comparison of stress–strain relations from the finite element analysis with that for homogeneous deformation for three different velocities.

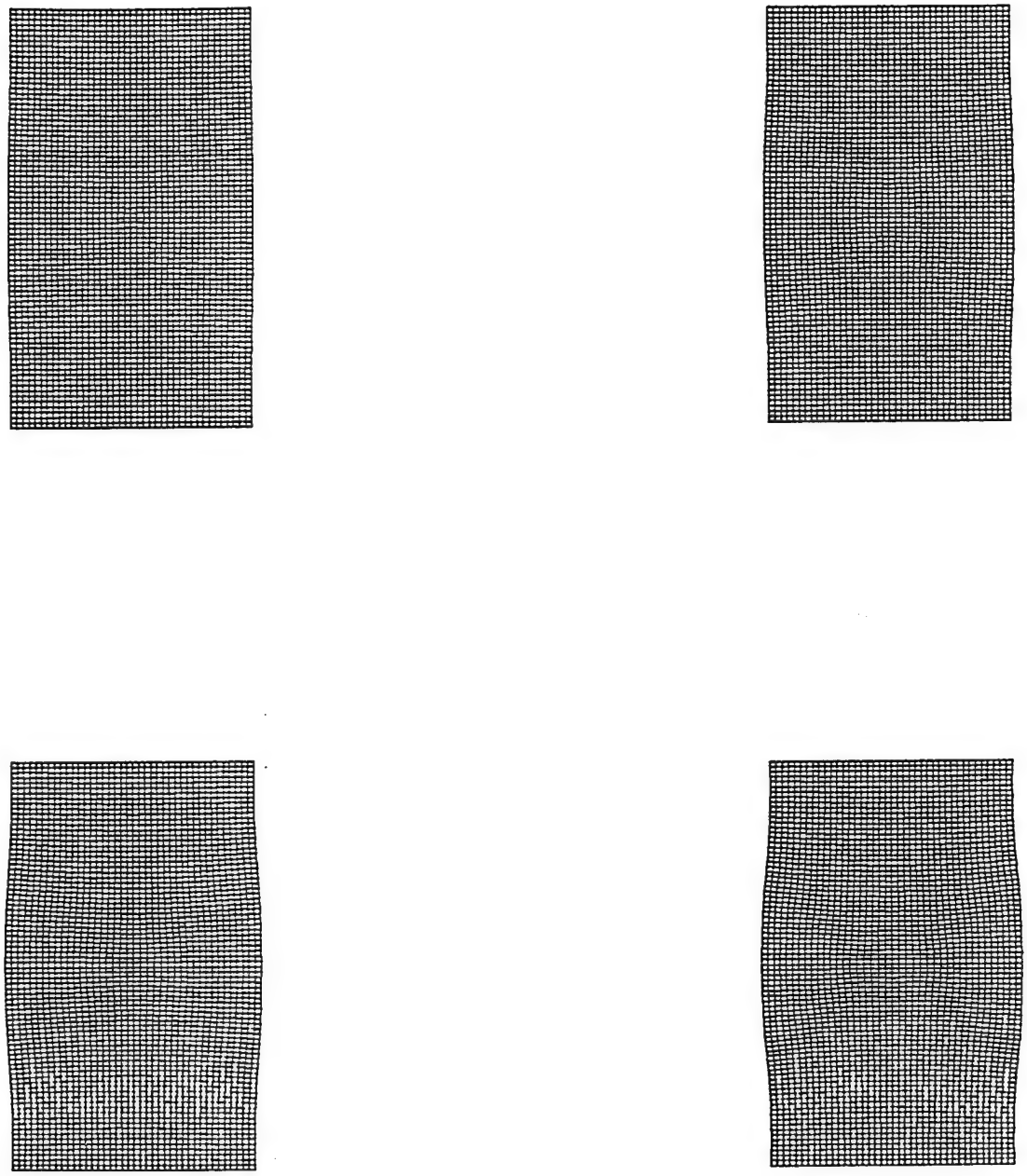

Figure II.12 Deformed mesh plots for $e_0 = 0.65$ and $V_0 = 10\,cm/s$ at (a) 4, (b) 6, (c) 8, (d) 10, percent axial strain levels.

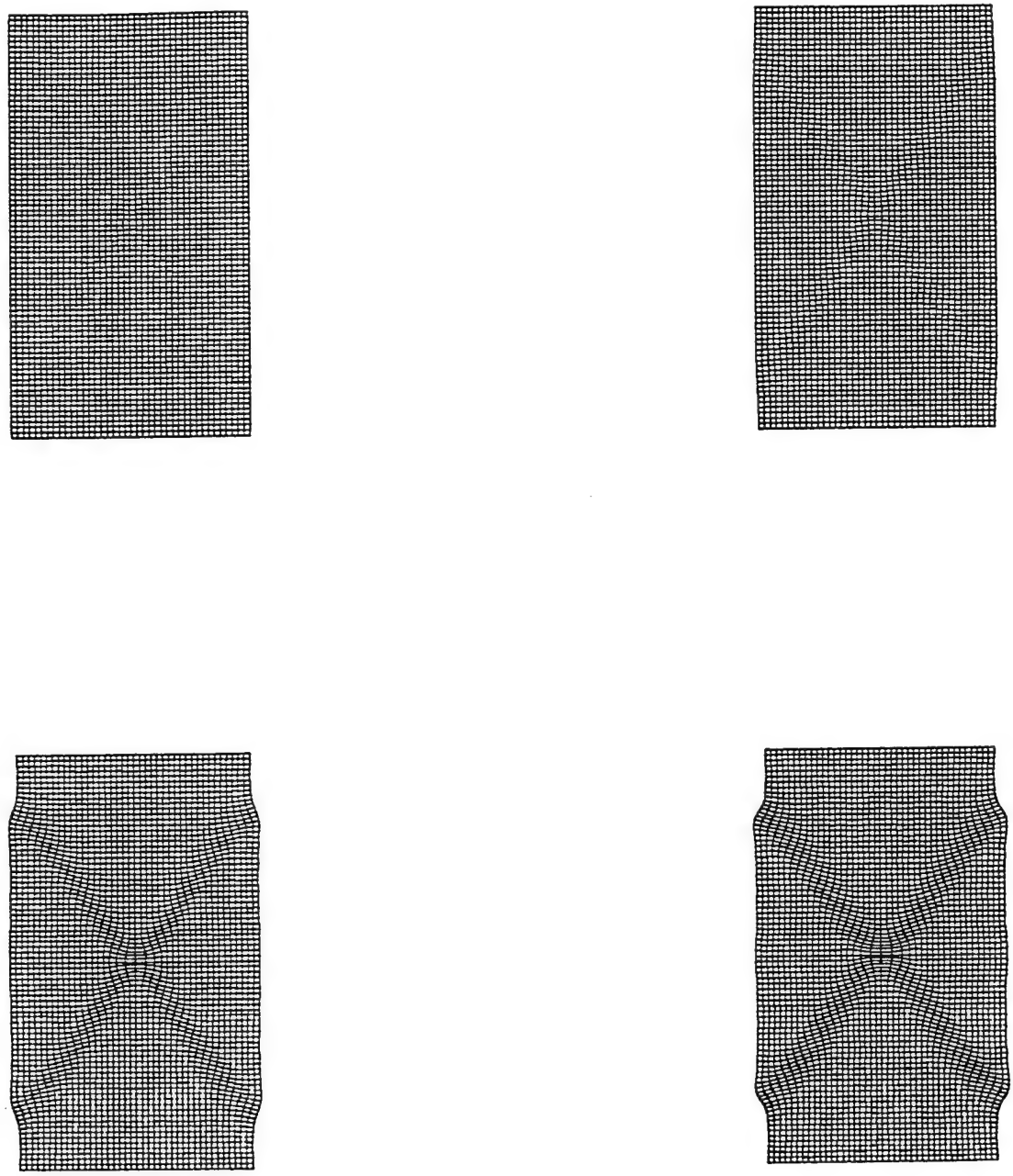

Figure II.13 Deformed mesh plots for $e_0 = 0.50$ and $V_0 = 10\,cm/s$ at (a) 4, (b) 5, (c) 6, (d) 6.5, percent axial strain levels.

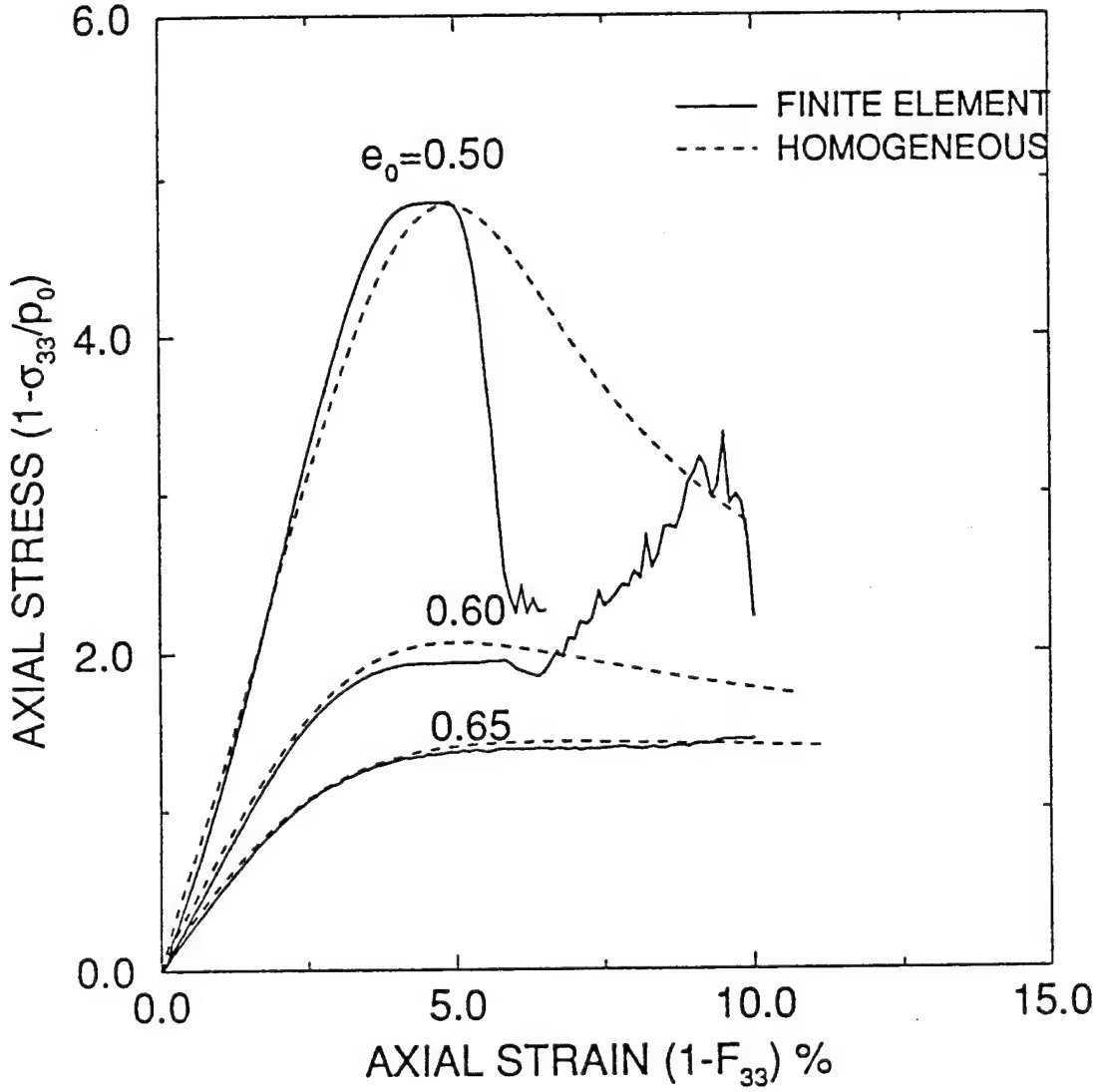

Figure II.14 Comparison of stress–strain relations from the finite element analysis with those for homogeneous deformation for three different initial void ratios.

APPENDIX III

DIRECT OBSERVATION OF DEFORMATION OF GRANULAR MATERIALS THROUGH X-RAY PHOTOGRAPHY

Principal Investigator: Sia Namet-Nasser

Postdoctoral Fellow: Naoyuki Okada

ABSTRACT

Lines of lead granules are embedded in a large hollow cylindrical specimen of granular materials, and a series of X-ray photographs is taken to capture the micromechanical response during shear deformation.

The X-ray film is placed just behind the inner wall of the hollow cylindrical specimen in order to minimize the film-to-object distance which significantly affects the quality of the X-ray image. The film is attached to the surface of a plexiglass tube whose diameter is slightly less than the inner diameter of the hollow cylindrical specimen. The plexiglass tube with the film is lapped with a rubber membrane and sealed with silicon grease and o-rings so that the film is kept dry in the water-filled chamber. Lead foils are placed between the film and the specimen and spaced apart, such that a limited area of the film is exposed. After each exposure, the stepping motor placed in the chamber rotates the plexiglass tube so that a part of the unexposed portion of the film faces the X-ray source. In this way, several different stages of shear deformation can be captured on a single radiographic film placed inside the hollow cylindrical specimen.

Two series of experiments, drained and undrained tests, are conducted. After the experiment, the film is processed. The movement of the lead-granules embedded in the specimen is traced. The local strain distribution and the micromechanical response during shear deformation can be delineated in this manner. In drained tests, shear localizations produced by large deformation of the specimen are directly observed by this technique. In undrained test, the shear localization is not observed until the excess pore water pressure is recovered in the specimen.

Table of Contents

ABSTRACT ..... III-i

Table of Contents ..... III-ii

List of Figures ..... III-iii

1. INTRODUCTION III-1

2. X-RAY TECHNIQUE: EQUIPMENT AND PROCEDURE III-3

   2.1 Triaxial Torsional Apparatus III-3

   2.2 Lead Silicate Granules and Sample Preparation III-4

   2.3 Experimental Setup III-4

   2.4 Flash X-Ray System, Film, and Fluorescent Screen III-6

   2.5 Experiment and Analysis Technique III-7

3. SHEAR LOCALIZATION PHENOMENON III-9

4. LIQUEFACTION PHENOMENON III-12

REFERENCES III-14

FIGURES III-17

List of Figures

Figure 1. Triaxial torsional apparatus

Figure 2. Experimental setup

Figure 3. Plexiglass tube with attached film and lapped membrane, placed inside the hollow cylindrical specimen

Figure 4. Film-location control unit; stepping motor and its control system

Figure 5. Flash X-ray system

Figure 6. Particle size distribution curve

Figure 7. Relation between shear stress and shear strain for Silica No. 60

Figure 8. Relation between volumetric strain and shear strain for Silica No. 60

Figure 9. Relation between shear stress and shear strain for Monterey No. 0

Figure 10. Relation between volumetric strain and shear strain for Monterey No. 0

Figure 11. Series of radiographs for Silica No. 60

Figure 12. Series of radiographs for Monterey No. 0

Figure 13. Displacement in each stage of deformation for Monterey No. 0

Figure 14. Relation between shear stress and effective pressure in undrained test

Figure 15. Relation between shear stress and shear strain

Figure 16. Series of radiographs for undrained test

1. INTRODUCTION

Radiography has been widely used to investigate the internal structure of materials since the discovery of X-rays in 1895 by Roentgen. Radiography appears to be an important, perhaps an indispensable tool for investigation of the behavior of particulate materials. A number of investigators have applied this method to study various aspects of particulates response: see Roscoe, Arthur, and James (1963), Arthur, James and Roscoe (1964), Kirkpatric and Belshaw (1968), Scarpelli and Wood (1982), and Vardoulakis and Graf (1982). Notwithstanding these investigations, the method has not been exploited to its full potential, because of the existence of several difficulties as discussed in the sequel. With new initiatives, further development in this area is expected.

First, in a conventional triaxial apparatus, the sample is placed in a pressurized, water-filled chamber. Therefore, the film must be placed outside the outer cell. The resulting distance between the film and the lead shot in the sample reduces the resolution of the radiographs. When the outer cell is removed and a vacuum is applied to produce confining pressure, the volumetric strain cannot be measured during the test.

Second, when the specimen has a thick wall, it hinders the X-ray penetration, and the resulting scattered radiation in the sample reduces the definition of the radiographs. Therefore, relatively large-sized lead shot (compared with the size of the samples) must be employed. This affects the material response and may lead to unreliable results.

To overcome the above-mentioned problems, a large hollow cylindrical apparatus having a thin wall is developed. The specimen geometry is 25cm high, with inner and outer diameters of 20cm and 25cm, respectively. X-ray films are attached to a plexiglass tube of a slightly smaller diameter than the inner diameter of the specimen. The film is lapped by a membrane and sealed by silicon grease and o-rings so that it is kept dry in the water-filled chamber. The plexiglass with film is placed inside the hollow cylindrical

specimen. This setup reduces the film-to-object distance, to a minimum, improving the sharpness of the radiograph. Since the thickness of the specimen wall is only 2.5cm, the scattered radiation in sand is relatively small. The plexiglass, the film, and related accessories do not have any physical contact with the specimen, and, hence, no influence on its deformation.

The film is placed inside the hollow cylindrical specimen before the experiment, and several stages of shear deformation are captured on a single film. To this end, lead foils are placed in front of the film and spaced apart such that a limited area of suitable width of the film is exposed at each step. The position of the plexiglass tube is controlled by a computer-controlled stepping motor placed in the chamber. After the experiment, the radiograph is processed and analyzed using a digital image analysis system to trace the movement of the string of lead silicate granules embedded in the specimen. The equipment developed and the experimental technique are presented in Section 2. With the aid of the X-ray technique presented in Section 2, the shear localization phenomenon of particulate materials is investigated and the results are presented in Section 3.

2. X-RAY TECHNIQUE: EQUIPMENT AND PROCEDURE

2.1 Triaxial Torsional Apparatus

Cohesionless granular materials support the general external loads through contact friction. An experimental program must include compression and shearing of reproducible samples in a controlled manner with reliable data. This requires extensive experimental facilities with a closed-loop feedback system, to control the experiment and to monitor the specimen deformation. The specimen geometry used for the present investigation is a large hollow cylinder, 25cm high, with inner and outer diameters of 20cm and 25cm, respectively. This geometry is chosen so that there is enough space inside the hollow cylindrical specimen in order to place the film and related equipment inside the hollow cylinder, without any interference with the sample deformation. Since the specimen is thin, easy X-ray penetration gives clear radiographs. The geometry of the sample is such that in torsion, the shear stress remains (approximately) homogeneous throughout the thickness of the specimen; see Hight *et al.* (1983) for a detailed examination of this and related issues. The specimen is supported by a triaxial load frame; see Figure 1. The axial and torsional deformations are controlled through an MTS servohydraulic loading system. In addition, the specimen is subjected to lateral hydrostatic pressure, on both its inside and outside cylindrical surfaces. In this manner, triaxial states of stress can be imposed on the material under controlled conditions with complete data acquisition capability. This load frame, to our knowledge, is one of four that have been constructed to date. Our load frame is fully computer-controlled, where either the stress- or the strain-path can be preprogrammed with automatic mode-switching capability. Any function of measurable parameters can be used to control the test.

2.2 Lead Silicate Granules and Sample Preparation

Tribasic-lead-silicate granules provided by Hammon Lead Products, Inc. are used in this study to trace their movements in the sand specimen by X-ray photography. Tribasic lead silicate is used primarily by glass and frit manufacturers, and has high lead oxide content: 92% of PbO and 8% of SiO_2. The hardness of this material is nearly the same as that of the sand particles. The specific gravity of this material is 7.510. The size distribution of lead silicate granules is adjusted so that it is the same as that of the sand used in the experiment. In the 150 kV range of the X-ray, the absorption of lead is 14 times greater than that of steel and more than 100 times greater than that of silica.

The particulate material is first prepared in wet form (5% water content). The vertical and horizontal strings of lead silicate granules are embedded in the sample. In order to embed the vertical strings, rectangular bars with 3.2mm (1/8") width are first placed at the center of the specimen wall. The rodding method is used to prepare the sample. The horizontal strings of lead silicate granules are also embedded at a certain heights in the sample. After filling up the cylinder with particulates, the amount of overfilled material is 'cut' away. Then, the rectangular bars are slowly removed from the wet particulates, and dry lead silicate granules are poured in to fill resulting rectangular holes.

2.3 Experimental Setup

Figure 2 shows the experimental setup. It is very important for obtaining a clear image on the X-ray film to minimize the film-to-object distance. In order to do so, the X-ray film is placed inside the hollow cylindrical sample. After attaching the film to the outer surface of the plexiglass tube (outer diameter 18.4cm (7.25") and height 38.1cm (15")), the plexiglass tube with film is lapped with a rubber membrane and sealed at both ends by silicon grease and o-rings to keep the film dry in the water-filled chamber; see

Figure 3.

The plexiglass tube with film is placed on a ring-shaped base, as shown in Figure 4. There are three spur gears on this ring-shaped base. They match the internal gears placed on the lower part of the plexiglass tube, and hold the plexiglass tube in place.

One of the spur gears is connected to the stepping motor which controls the position of the film attached to the plexiglass tube in the chamber. The stepping motor used here is a VEXTA Stepping Motor made by ORIENTAL MOTOR CO. LTD. The motor has two control modes; the full-step mode is 200 steps per revolution (1.8 degree per step), and the half-step mode is 400 steps per revolution (0.9 degree per step). The motor is controlled by a CY545 Stepper System Controller made by CYBERNETIC MICRO SYSTEM, INC, with an IBM-PC. The mode of the stepping motor, the number of steps, the speed, and the direction of rotation can be controlled through a computer. The entire unit is placed inside the hollow cylindrical specimen, and it is attached to the bottom plate of the triaxial apparatus by screws, without affecting other aspects of the experiments.

In Figure 3, the plastic plate, placed in front of the film, has a lead position marker consisting of one vertical string and several horizontal strings spaced 1cm apart. These lead position markers will give the reference position on each stage of the X-ray film for later analysis. Two lead foils, 1mm thickness, are placed and spaced apart in front of the film so that a limited area of film is exposed in each exposure. The space between the two lead foils depends on the design of the experiment: a wide space is needed for large deformations, and a narrow space is sufficient for small deformations.

In Figure 2, a lead plate is placed behind the film in order to absorb the X-rays passing through the film and the plexiglass tube to eliminate scattered X-rays. Two lead plates, 5mm thickness, are placed and spaced apart in front of the specimen, so that the

X-rays can penetrate only the space made by the two lead foils placed in front of the film. The space made by the two lead plates having 5mm thickness is, therefore, slightly wider than the one made by the lead foils. A hollow plastic box is placed between the specimen and the cell. Since water absorbs significant amounts of X-ray, it is replaced by air in a plastic box, so that the X-rays can penetrate the specimen more easily. This setup does not interfere with the water pressure on the sample.

2.4 Flash X-Ray System, Film, and Fluorescent Screen

The Model 43731A Flash X-ray System made by Hewlett Packard is used for the X-ray source; see Figure 5. The tubehead is placed 45cm (1.5') from the radiographic film, as shown in Figure 2. This system provides a 70 nanosecond "burst" of 150 kV X-rays.

The X-ray tube is operated in the high voltage pulse generator (pulser) or in a small, remote tubehead connected to the HV pulse generator by coaxial cable. The remote tube-head enables the positioning of the X-ray tube in an area too confined or potentially hazardous to permit access to the HV pulser. The system characteristics of this flash X-ray unit are as follows:

Output voltage: 150 kV
Pulser current: 2 kA
Dose at 20 cm/exposure: 40 mR
Effective Source Size: 3 mm

The radiographic film used in this study is a Polaroid Instant Film Type TPX which produces a positive image on a transparent 20cm × 25cm (8"×10") sheet. Type TPX film consists of negatives (each in a light-tight envelope) and positive sheets (each with a pod of processing chemicals attached). At the time of processing, the film must be loaded in

a Polaroid 8×10 Radiographic Film Cassette for processing in a Polaroid Film Processor.

A fluorescent intensifying screen is used to reduce exposure time. This screen has the ability to absorb X-rays and immediately emit light. For the exposure, the film is attached firmly to the fluorescent screen. The photographic effect on the film, then, is the sum of the effects of the X-rays and of the light emitted by the screen. The required exposure is 1/50 of that without the fluorescent intensifying screen.

In order to attach the film to the surface of the plexiglass tube, the film cassette must be flexible. Therefore, the negative film with the light-tight envelope is directly used as the film cassette instead of loading it in a rigid film cassette provided by Polaroid. The procedure is as follows. In total darkness, the fluorescent screen is inserted into the envelope containing the film such that it attaches to the negative film in the envelope. Then the envelope is closed. The envelope containing the film with the fluorescent screen is flexible, and can be attached to the outer surface of the plexiglass tube. It is necessary for a good image, to obtain firm contact between the negative and the fluorescent screen. This contact is provided by the pressure in the experimental chamber, which is 392kN/m^2 during the experiment.

The number of exposures depends on the film size and the space provided between the lead foils. When the lead foils are spaced 2.5cm (1") apart, 9 exposures are possible on an 8×10 film. It is possible to attach 2 films to the plexiglass tube. Therefore, a total of 18 exposures can be captured in this case, which is sufficient for our purposes.

2.5 Experiment and Analysis Technique

The specimen is then water-saturated, using CO_2-circulation and de-aired water circulation techniques, with back pressure. The last step of specimen preparation is to increase the effective pressure. Finally, the specimen is left undisturbed in this condition,

to consolidate isotropically.

After the specimen is consolidated, the experiment is started. The initial positions of the lead silicate granules in the silica specimen define the reference configuration prior to loading. First, the plexiglass tube is rotated by the computerized stepping motor to face the unexposed film in line with the X-ray tubehead. Second, the specimen is deformed to a desired configuration. Then, the radiograph is taken. This procedure is then continued.

After the experiment, the equipment is disassembled. The film is removed from the plexiglass and loaded into the Radiographic Film Cassette for processing. The envelope and fluorescent screen are now removed from the radiographic film cassette with the film remaining in the cassette. The film is finally processed by the Polaroid 8×10 Radiographic Film Processor.

The radiograph obtained from the experiment is analyzed using a digital image analysis system consisting of ScanJet Plus made by Hewlett Packard and Macintosh with a software called Scanner. After digitizing the radiographs obtained at each stage of loading, a computer program is employed to obtain the displacement of the string of lead granules relative to their original positions. The strain distribution in the specimen is calculated based on these results, and the micromechanical response of the sand during shearing or any other general deformation path is identified.

3. SHEAR LOCALIZATION PHENOMENON

Shear localization is an important mode of failure in granular media. The relation between the angle and the thickness of a shear band and the internal frictional and dilatancy angles, and the thickness has been the subject of several investigations; see Roscoe (1970), Vardoulakis (1980, 1981), Scarpelli and Wood (1982), Vardoulakis and Graf (1982, 1985), Tatsuoka *et al.* (1990), and Saada *et al.* (1994). With the aid of the X-ray technique presented in the preceding sections, the shear localization phenomenon in granular media is examined in this section.

Two types of sands, Silica No. 60 and Monterey No. 0, are used in this study in order to examine the particle-size effect on shear localization. The particle size distribution curves of both sands are shown in Figure 6. The mean particle diameters of Silica No. 60 and Monterey No. 0 are 220μm and 480μm, respectively. For Silica 60, the minimum and maximum void ratios are 0.631 and 1.095, respectively. For Monterey No. 0, the minimum and maximum void ratios are 0.550 and 0.839, respectively. The specific gravities of Silica No. 60 and Monterey No. 0 are 2.645 and 2.642, respectively.

The rodding method is used for making specimens, as described in Section 2. Two vertical strings of lead silicate, approximately 2cm apart, and three horizontal lines of lead silicate granules, spaced 5cm apart, are embedded in the specimen.

The hollow cylindrical specimen is isotropically consolidated under 294kN/m^2 of effective pressure. The simple shear experiments are performed under drained conditions. The shear strain is controlled and is monotonically increased with a constant strain rate, 0.1%/min. The relation between the shear stress and shear strain, and the relation between the shear strain and volumetric strain of Silica No. 60 are shown in Figures 7 and 8. The same relations in Monterey No. 0 sand are shown in Figures 9 and 10. It takes approximately 3 minutes to take the X-ray photo in each stage. The shearing is, therefore,

temporarily stopped. This causes a certain stress relaxation, as seen in the stress-strain relation of Figures 7 and 9.

The width of the window between the lead foils is 4cm (1.6"). This allows 5 stages of deformation to be photographed on each film. A total of 9 stages of deformation, 0% overall shear strain (the undeformed stage), and 2%, 4%, 5%, 6%, 7%, 8%, 9%, and 10% overall shear strains are captured by two X-ray films in one experiment.

The X-ray results for Silica No. 60 specimen, are shown in Figure 11. Stage 1 is the image of the undeformed specimen. It is seen that one vertical string and three horizontal strings of lead silicate granules are captured by the X-ray. However, the second vertical string, embedded 2cm to the left of the first string, is out of range in this stage and, therefore, is not seen on the radiograph. As is seen, the position markers, placed just in front of the film, are clearly captured on the radiographs. These position markers on the radiograph are used to analyze the movement of the lead strings. There are 2 numerals, 1 and 2, seen on the radiographs. These are the lead position markers indicating the 10cm and 20cm of height of the specimen, respectively.

Stage 2 is associated with 2% overall shear strain. It is seen that the first vertical string of lead silicate granules has started to tilt. The second vertical string of lead silicate granules is seen on the upper-left corner. Up to stage 3 associated with 4% overall shear strain, the shear deformation appears uniform, and no shear localization can be detected.

Stage 5 corresponds to 5% overall shear strain. It is seen that the shear localization has started on the upper portion of the figure. In stage 6, with the corresponding 7% shear strain, the shear strain is localized in two different locations, at the top and in the middle. In stage 9, with the corresponding 10% shear strain, shear localization is clearly observed. The vertical strings are kinked at three different locations.

The X-ray results for Monterey No. 0 specimen are shown in Figure 12. In stage 1, the undeformed stage, two vertical strings and three horizontal strings of lead silicate granules are clearly seen. Up to stage 3 associated with 4% overall shear stain, the shear deformation appears uniform. However, after stage 4 associated with 5% overall shear strain, the shear localization starts at a point between 12cm and 13cm of the specimen height. In stage 7 with 8% strain, the shear localization is clearly seen.

The displacements in each stage are measured from the X-ray photographs. For Monterey No. 0, this is shown in Figure 13. It is seen that the deformations up to 4% overall shear strain, are nearly homogeneous. However, at 5% overall shear strain, the shear localization seems to start at between 12cm and 13cm of specimen height. It is clearly seen in Figure 13 that the displacements after 6% shear strain, are accommodated by the deformation of the shear-band zone between 12cm and 13cm of specimen height, and the remaining part of the specimen has a significantly small strain.

It is clearly seen from these two figures that the shear band in Monterey No. 0, 7.0mm, is wider than the one in Silica No. 60, 2.5mm. The mean particle diameters of Monterey No. 0 and Silica No. 60 are 0.48mm and 0.22mm, respectively. Therefore, the mean particle diameter affects the shear-band width, which is approximately 10 to 15 times as large as the mean particle diameter. This is the same conclusion has been reached by Roscoe (1970), Vardoulakis, Goldscheider, and Gudehus (1978), Vardoulakis (1980, 1981), Vardoulakis and Graf (1982, 1985), Vardoulakis, Goldscheider, and Gudehus (1978), and Tatsuoka *et al.* (1990).

4. LIQUEFACTION PHENOMENON

Liquefaction is a complex phenomenon in which fluid-saturated granular media may momentarily behave like fluids. It is an important aspect of earthquake-resistant foundation design of many structures, especially those located in coastal areas, which are often built on sand with high underground water levels. As liquefaction takes place under seismic loading, saturated sand behaves more like a fluid, and therefore fails to support the applied loads of the building. Severe damage to the structure is often the result. Damage resulting from liquefaction has been observed in the aftermath of many earthquakes; the Loma Prieta earthquake (1989), the Niigata earthquake (1964), and the Alaska earthquake (1964) are a few examples.

Liquefaction has been experimentally treated extensively by a number of researchers; see, for example, Silver and Seed (1971), Castro (1975), and Ishihara and Yasuda (1975). Parameters influencing the onset of liquefaction of the sand within a controlled volume are identified and measured. These parameters typically include overall density, initial packing conditions, and granule size distribution; see Seed (1979), Miura and Toki (1982), and Tatsuoka *et al.* (1982). In addition to these internal characteristics, the applied loading also affects the onset and nature of liquefaction; see Ishihara and Towhata (1983, 1985), and Symes *et al.* (1984).

In undrained test, the specimen is isotropically consolidated under 196kN/m^2 of effective pressure. A cyclic shear stress is applied under undrained conditions. Stress amplitudes of 36.8kN/m^2 is used with a period of 2 minutes per cycle. The relation between shear stress and effective pressure, and the relation between shear stress and shear strain are shown in Figures 14 and 15.

A total of 5 stages of deformation including undeformed stage are captured by two X-ray films. The stages captured by radiograph are shown in Figure 14, and the images

of the radiographs are shown in Figure 16.

Stage 1 is the image of the undeformed specimen. It is seen that two vertical line and three horizontal lines of lead silicate granules are captured by X-ray. Stage 2 is the state which the excess pore water pressure is accumulated to almost half of the initial effective pressure. It seems there is no significant difference between Stage 1 and 2.

Stage 3 corresponds to the shear strain 4.94% at peak shear stress 36.8kN/m^2. The specimen is once liquefied, and later the effective pressure is recovered as the shear stress is increased. It is seen that the vertical lines are straight and the shear localization is not observed. A large deformation occurred in the granular mass which is liquefied state. It is well-known that under the low confining pressure, the granular mass does not show clear shear band even after the large deformation. Stage 4 corresponds to the stage after reloading to zero shear stress where shear strain is 2.70%. The shear localization is not seen in this stage.

Stage 5 corresponds to the shear strain approximately -10%, where the effective pressure is recovered by approximately half of its initial value at the end of loading. The shear localization is observed at the middle of the specimen. It is believed that this shear localization was formed after the granular mass recovered its effective pressure.

It is clearly seen that the shear deformation of granular media is directly observed by this method developed here in University of California, San Diego. This technique gives not only overall deformation characteristics but also local deformation characteristics.

REFERENCES

American Society for Nondestructive Testing (1985): "Nondestructive Testing Handbook, Second Edition, Volume 3, Radiography and Radiation Testing," Technical Editor; Bryant, L.E., Editor; McIntire, P.

Arthur, J.R.F., James, R.G. and Roscoe, K.H. (1964): "The determination of stress fields during plane strain of a sand mass," *Géotechnique,* **14,** pp. 283-308.

Bergfelt, A. (1956): "Loading tests on clay," *Géotechnique,* **6,** pp. 15-31.

Desrues, J. and Chambon, R. (1989): "Shear band analysis for granular materials: The question of incremental non-linearity," *Ingenjeur-Archiv* **59,** pp. 187-196.

Halmshaw, R. (1982): "Industrial radiology," Applied Science Publishers, London.

Hight, D. W., Gens, A. and Symes, M. J. (1983): "The development of a new hollow cylinder apparatus for investigating the effects of principal stress rotation in soils," *Géotechnique* **33,** No. 4, pp. 355-383.

Ishihara, K., and Yasuda, S. (1975): "Sand liquefaction in hollow cylinder torsion under irregular excitation," *Soils and Foundations* **15,** No. 1, pp. 45-59.

Ishihara, K. and Towhata, I. (1983): "Sand response to cyclic rotation of principal stress directions as induced by wave loads," *Soils and Foundations* **23,** No. 4, pp. 11-26.

Ishihara, K. and Towhata, I. (1985): "Sand response to cyclic rotation of principal stress directions as induced by wave loads (closure)," *Soils and Foundations* **25,** No. 1, pp. 117-120.

Kirkpatrick, W.M. and Belshaw, D.J. (1968): "On the interpretation of the triaxial test," *Géotechnique,* **18,** pp. 336-350.

Krinitzsky, E.L. (1970): "Radiography in the Earth Sciences and Soil Mechanics," Plenum Press, New York.

Kolymbas, D. and Rombach, G. (1989): "Shear band formation in generalized hypoelasticity," *Ingenjeur-Archiv* **59,** pp. 177-186.

Miura, S., and Toki, S. (1982): "A sample preparation method and its effect on static and cyclic deformation-strength properties of sand," *Soils and Foundations* **22,** No. 1, 61-77.

Molenkamp, F. (1985): "Comparison of frictional material models with respect to shear band initiation," *Géotechnique,* **35,** No. 2, pp. 127-143.

Mühlhaus, H.-B. and Vardoulakis, I. (1987): "The thickness of shear bands in granular materials," *Géotechnique,* **37,** No. 3, pp. 271-283.

Roscoe, K.H. (1970): "The influence of strains in soil mechanics," 10th Rankine Lecture, *Géotechnique,* **20,** No. 2, pp. 129-179.

Roscoe, K.H., Arthur, J.R.F. and James, R.G. (July, 1963, and August, 1963): "The determination of strains in soils by an x-ray method," *Civil Engineering and Public Works Review* **58,** pp. 873-876, pp. 1009-1012.

Scarpelli, G. and Wood, D.M. (1982): "Experimental observations of shear band patterns in direct shear tests," *IUTAM Conference on Deformation and Failure of Granular Materials, Delft,* pp. 473-484.

Seed, H. B. (1979): "Soil liquefaction and cyclic mobility evaluation for level ground during earthquakes" *J. Geotech. Engng. Div. Am. Soc. Civ. Engrs* **105,** GT2, pp. 201-255.

Silver, M. L., and Seed, H. B. (1971): "Deformation characteristics of sands under cyclic loading," *J. Soil Mech. Fdns. Div. Am. Soc. Civ. Engrs* **97,** SM8, pp. 1081-1098.

Symes, M. J. P. R., Gens, A. and Hight, D. W. (1984): "Undrained anisotropy and principal stress rotation in saturated sand," *Géotechnique* **34,** No. 1, pp. 11-27.

Tatsuoka, F, Nakamura, S., Huang, C.-C. and Tani, K. (1990): "Strength anisotropy and shear band direction in plane strain tests of sand," *Soils and Foundations,* **30,** No. 1, pp. 35-54

Vardoulakis, I. (1980): "Shear band inclination and shear modulus on sand in biaxial tests," *International Journal for numerical and analytical methods in geomechanics,* **4,** pp. 103-119.

Vardoulakis, I. (1981): "Bifurcation analysis of the plane rectilinear deformation on dry sand samples," *Int. J. Solids and Structures,* **17,** No. 11, pp. 1085-1101.

Vardoulakis, I. and Graf, B. (1982): "Imperfection sensitivity of the biaxial test on dry sand," *IUTAM Conference on Deformation and Failure of Granular Materials, Delft,* pp. 485-491.

Vardoulakis, I. and Graf, B. (1985): "Calibration of constitutive models for granular materials using data from biaxial experiments," *Géotechnique,* **35,** No. 3, pp. 299-317.

Vardoulakis, I. Goldscheider, M., and Gudehus, G. (1978): "Formation of shear bands in sand bodies as a bifurcation problem," *International Journal for Numerical and Analytical Methods in Geomechanics,* **2,** pp. 99-128.

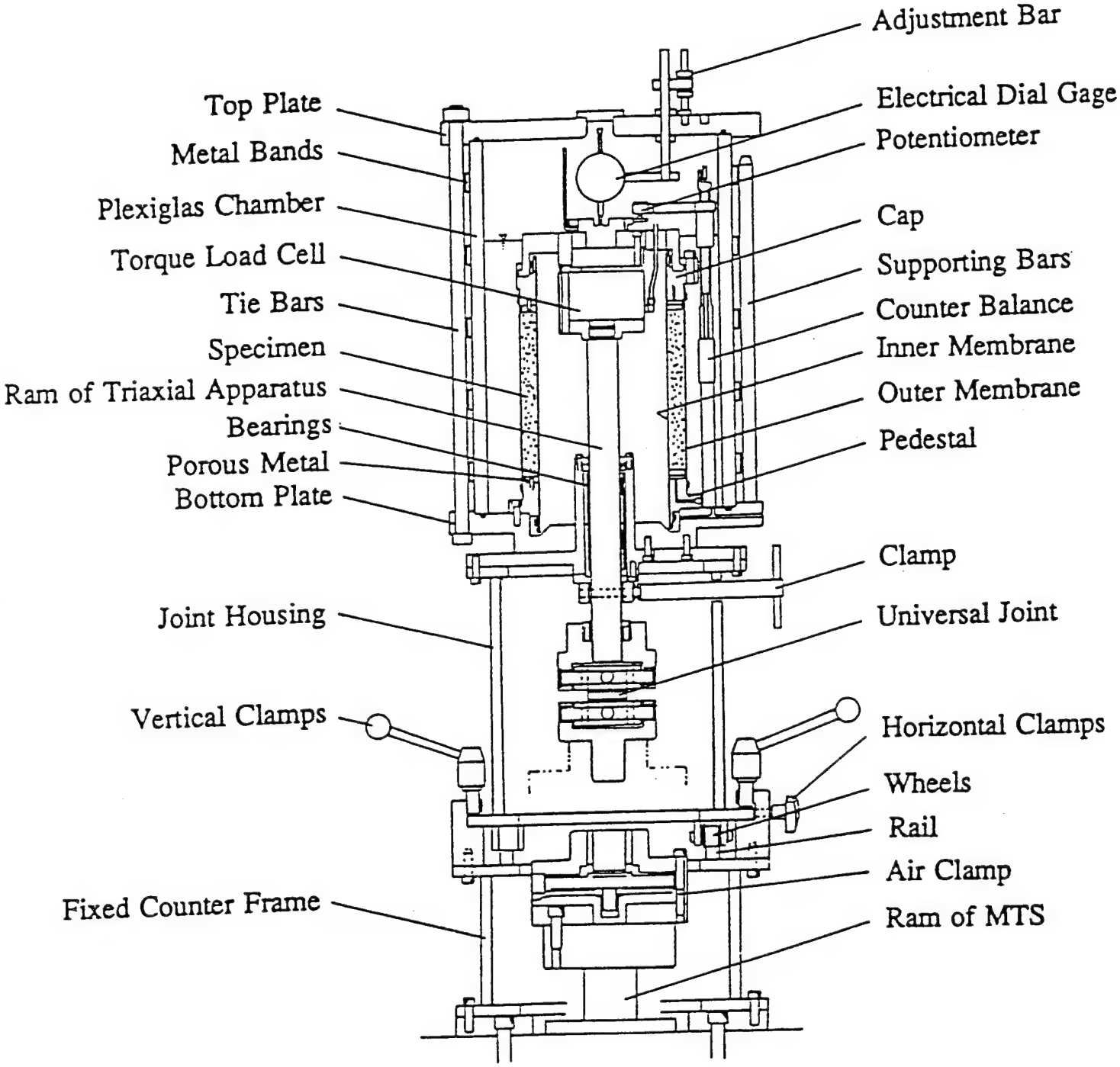

Figure 1. Triaxial torsional apparatus

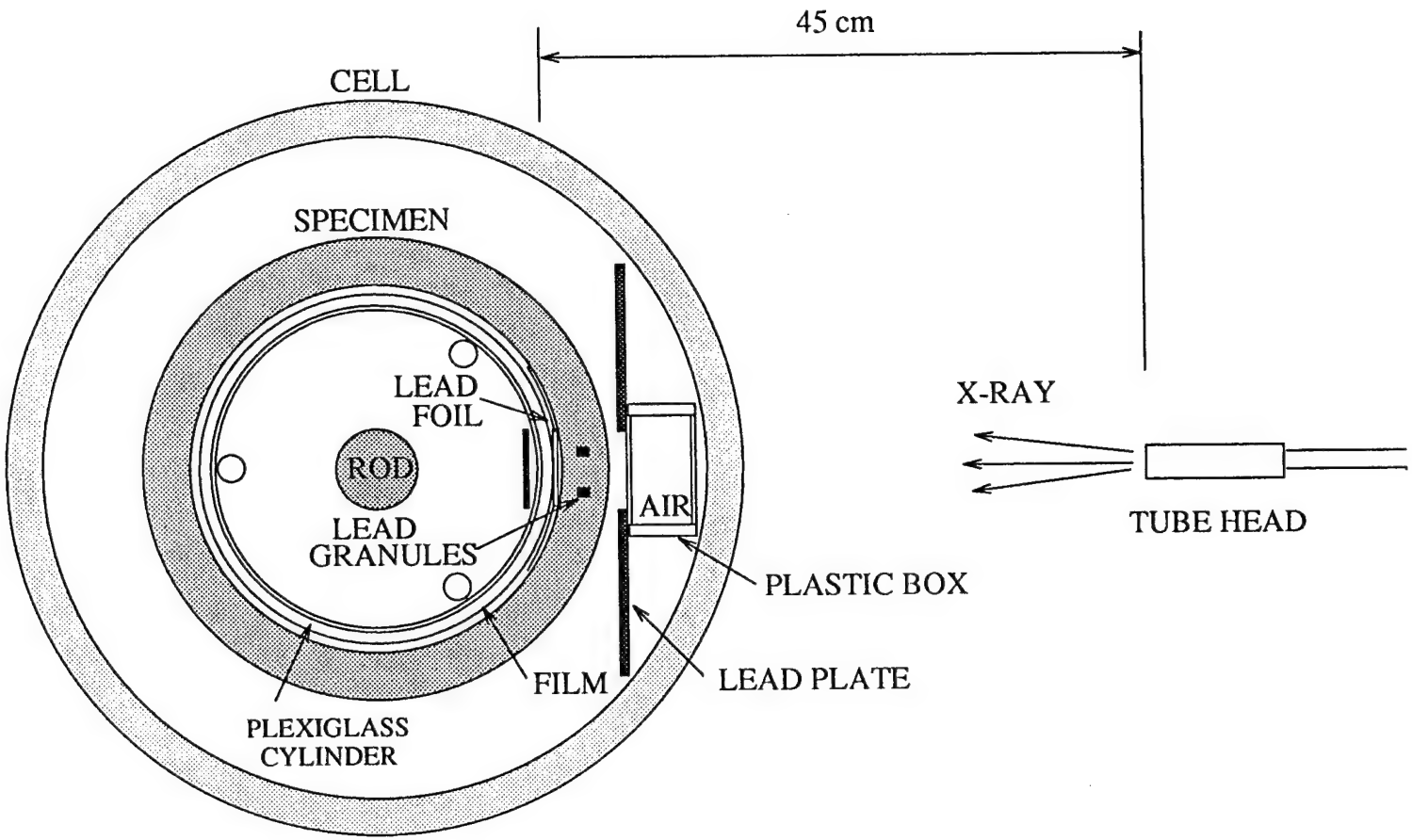

Figure 2. Experimental setup

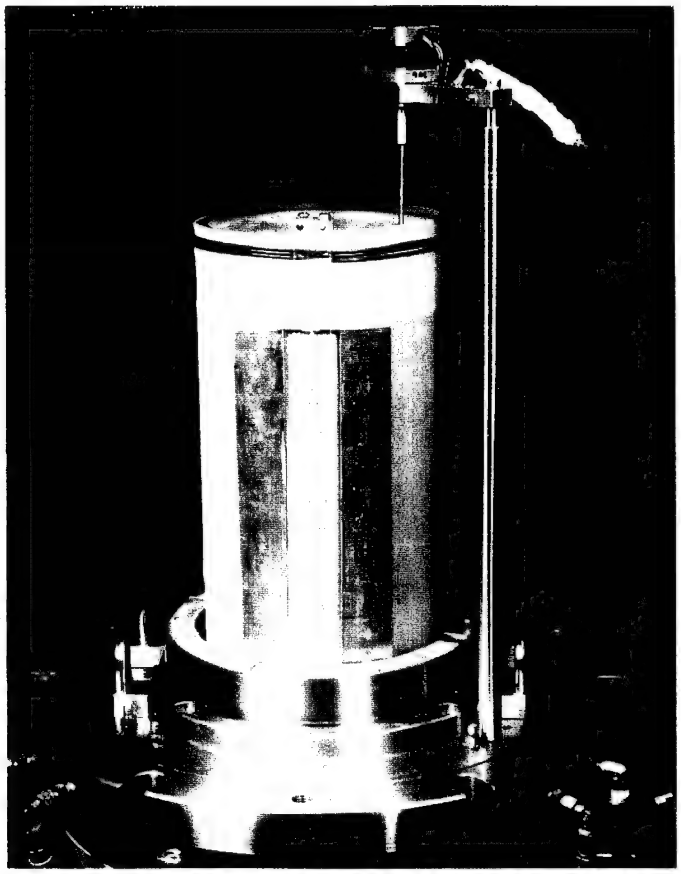

Figure 3. Plexiglass tube with attached film and lapped membrane, placed inside the hollow cylindrical specimen

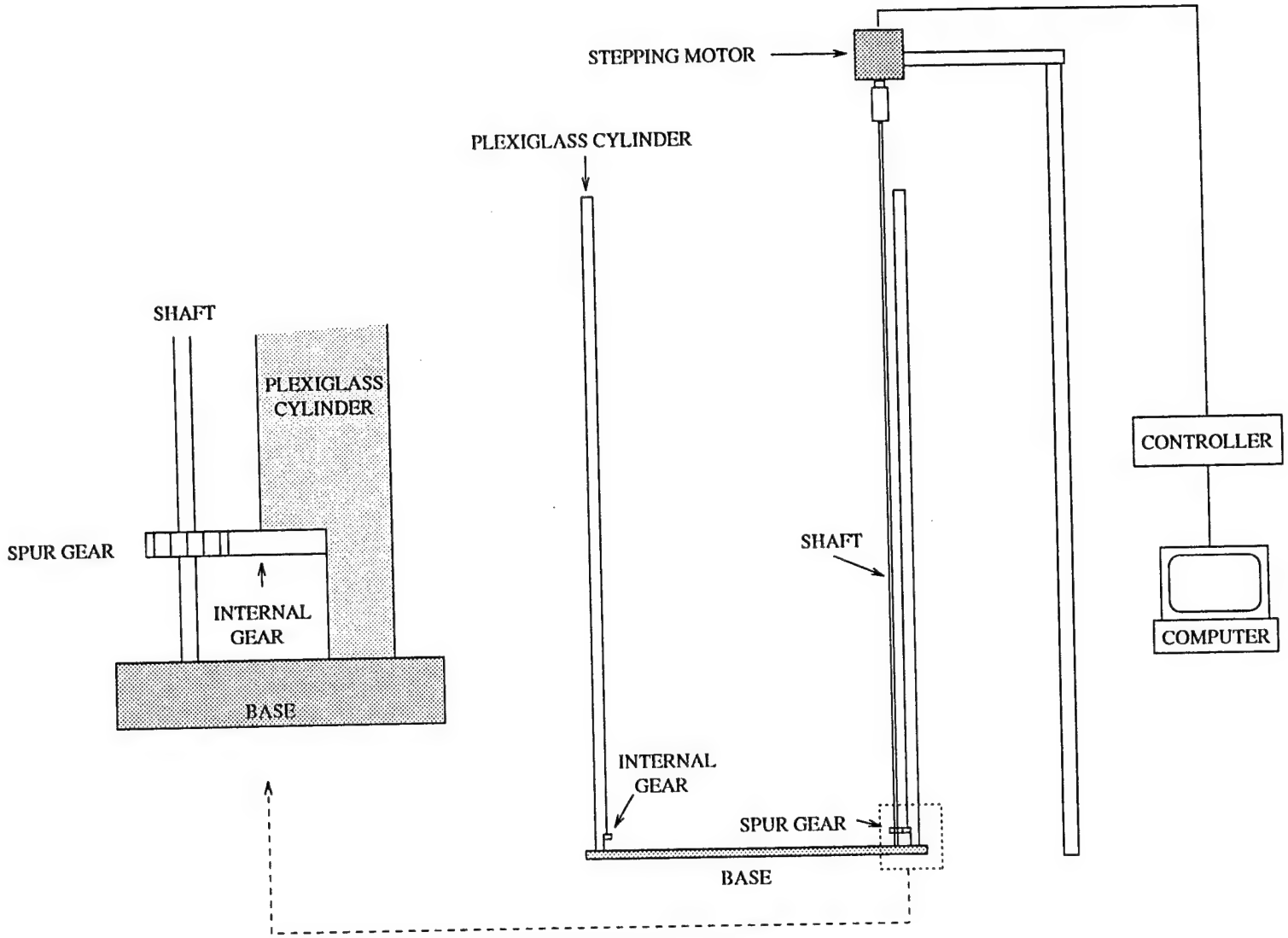

Figure 4. Film-location control unit; stepping motor and its control system

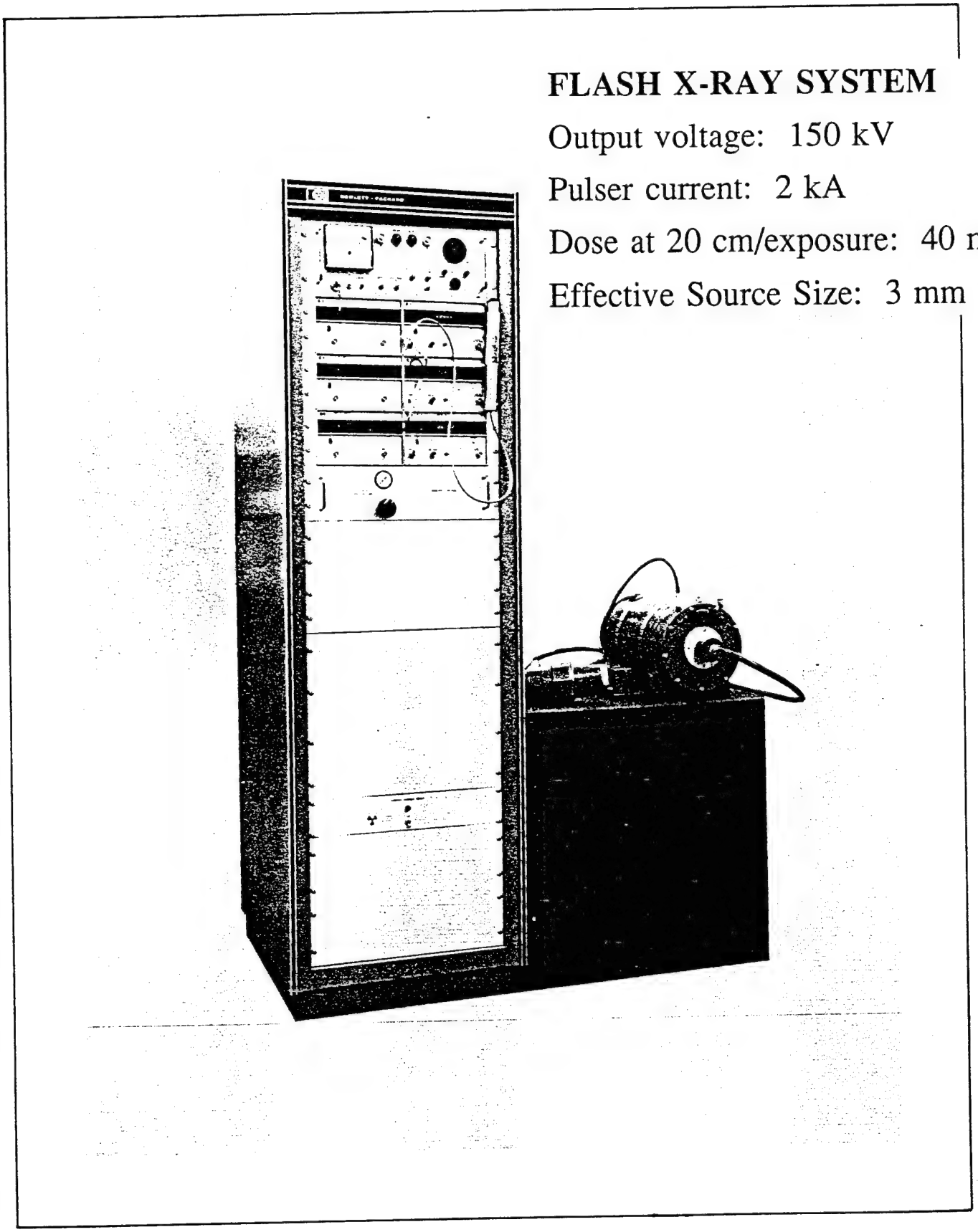

Figure 5. Flash X-ray system

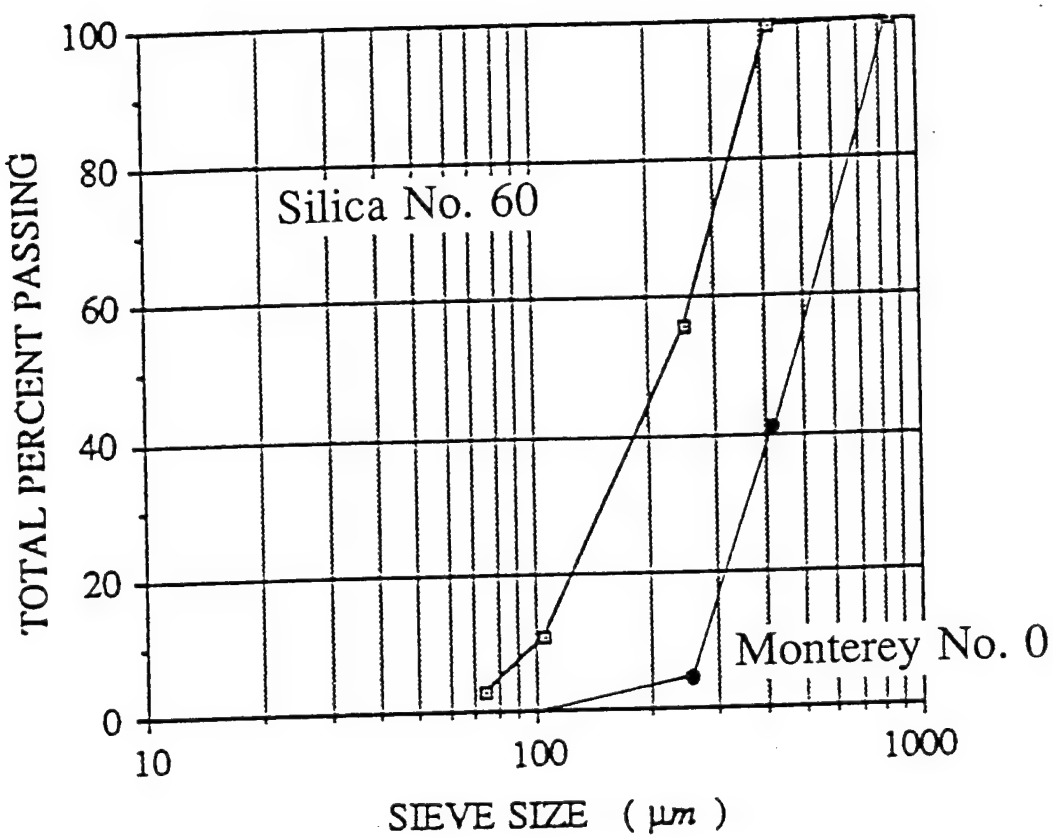

Figure 6. Particle size distribution curve

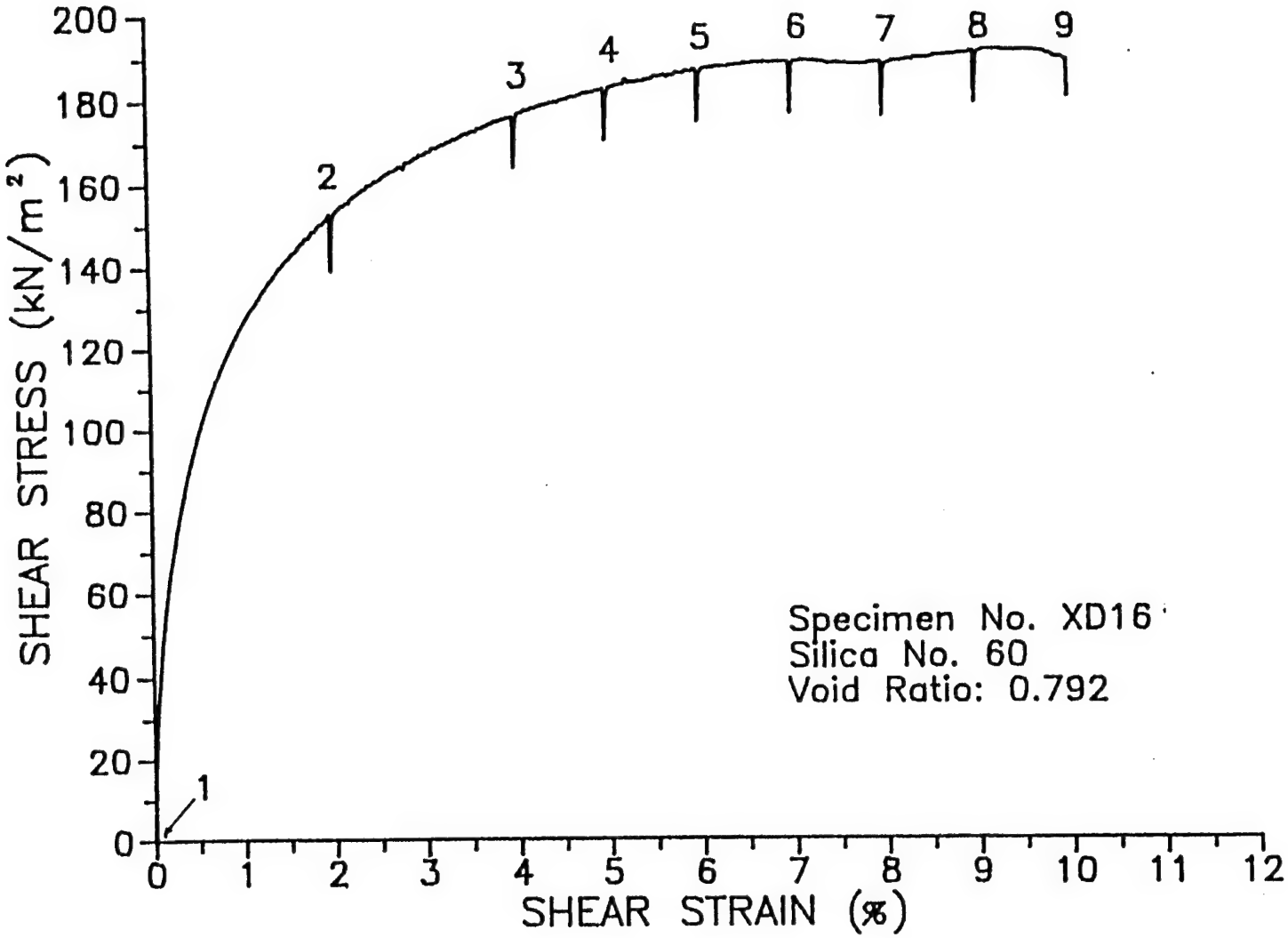

Figure 7. Relation between shear stress and shear strain for Silica No. 60

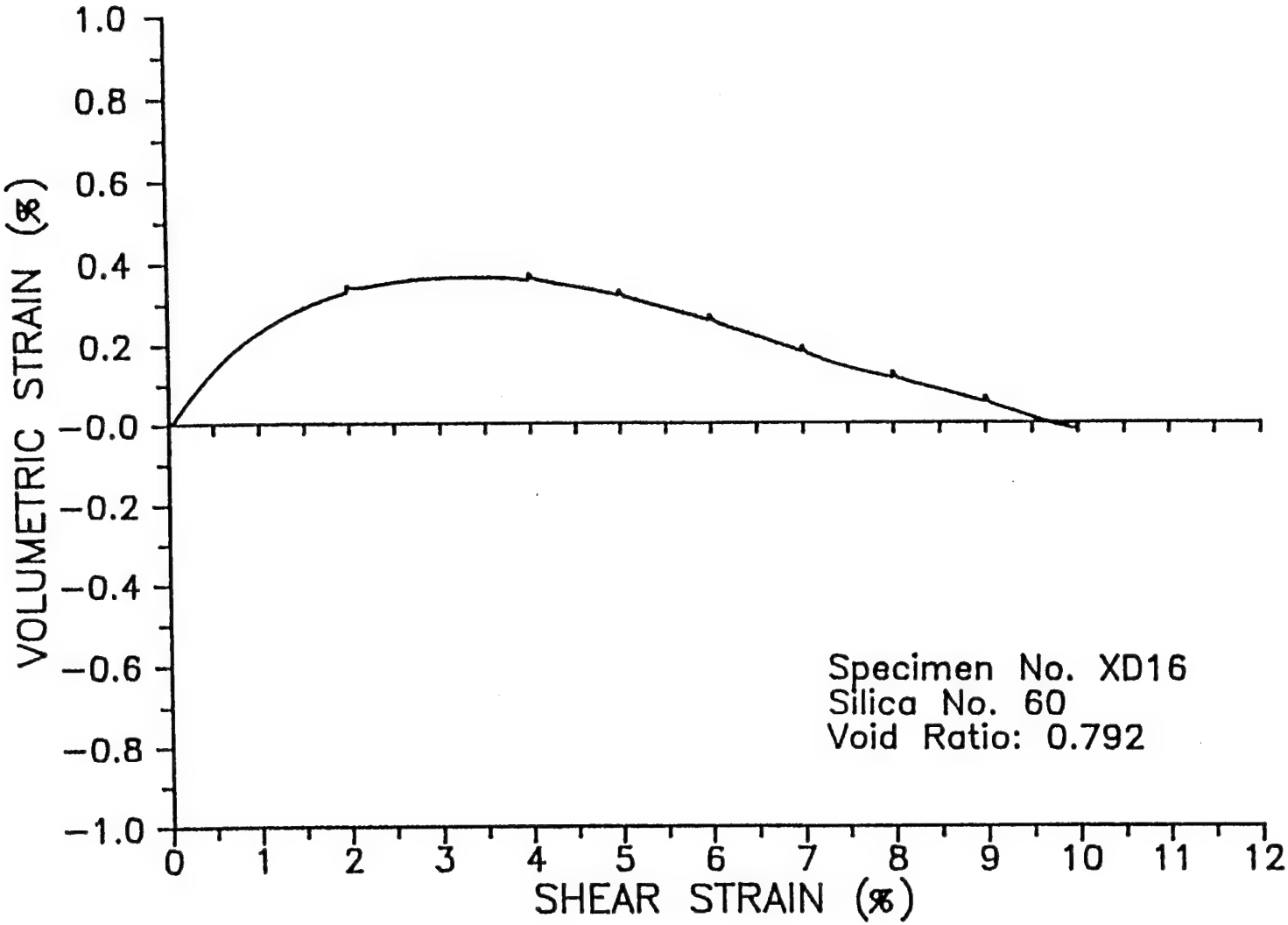

Figure 8. Relation between volumetric strain and shear strain for Silica No. 60

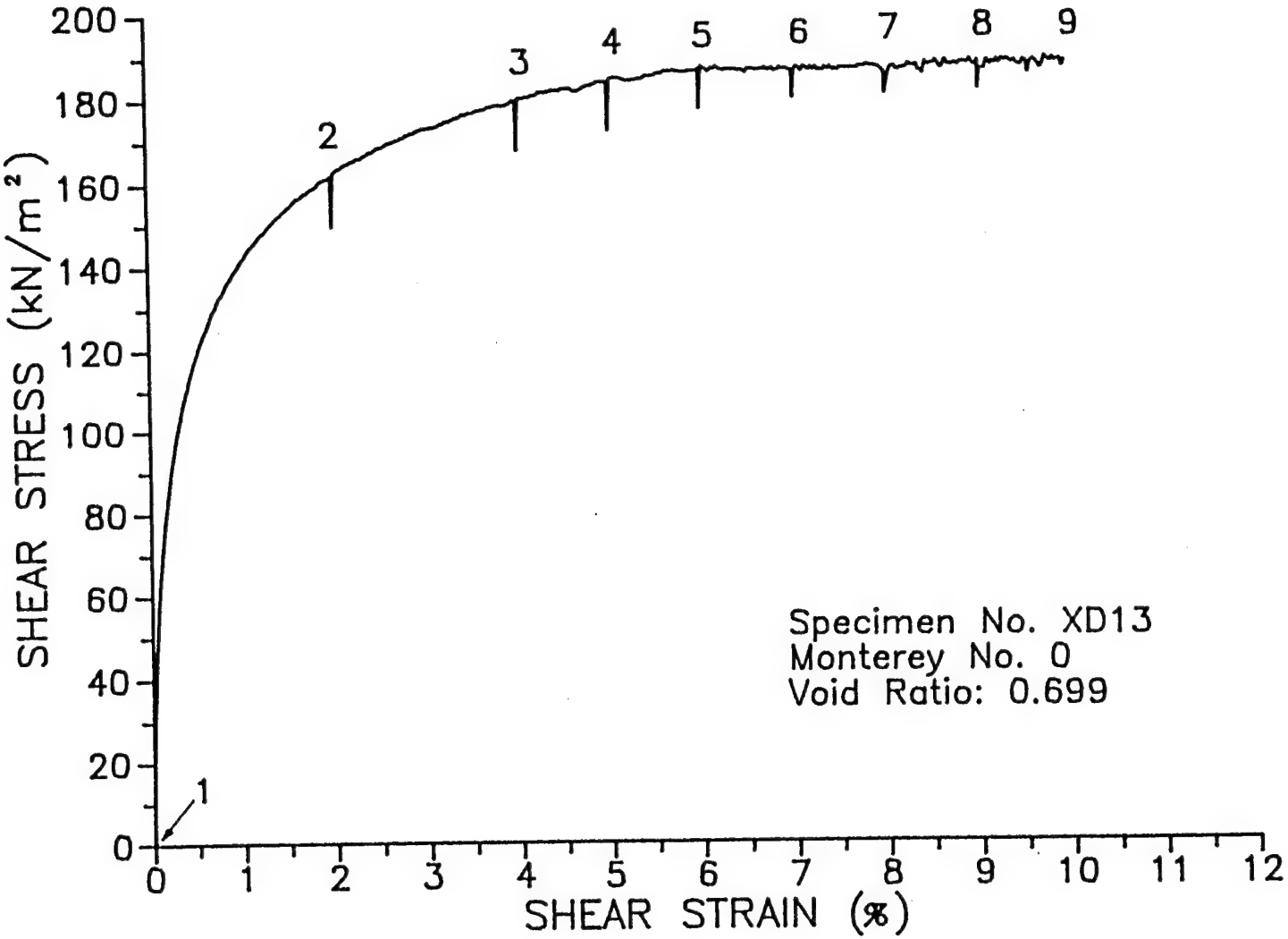

Figure 9. Relation between shear stress and shear strain for Monterey No. 0

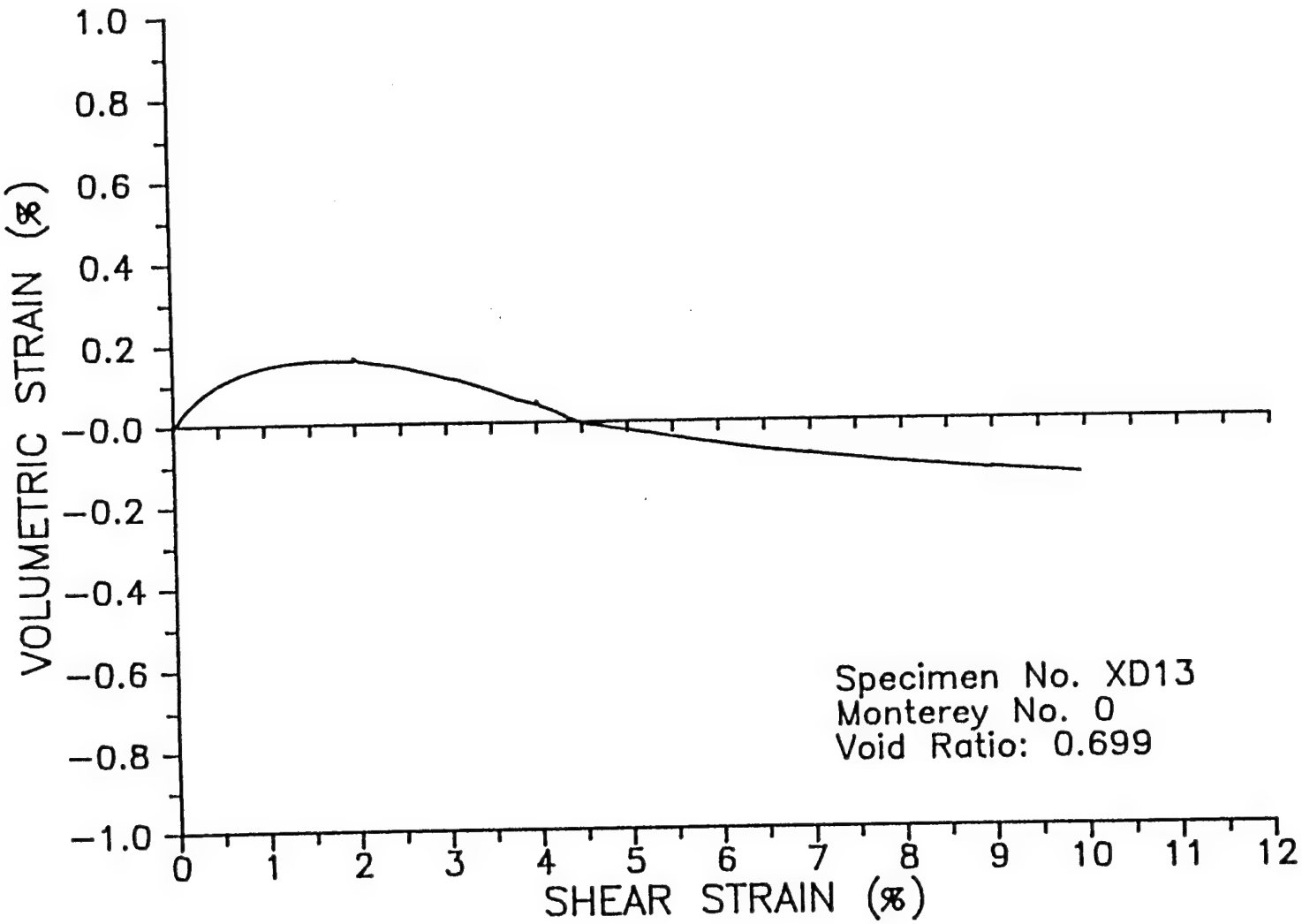

Figure 10. Relation between volumetric strain and shear strain for Monterey No. 0

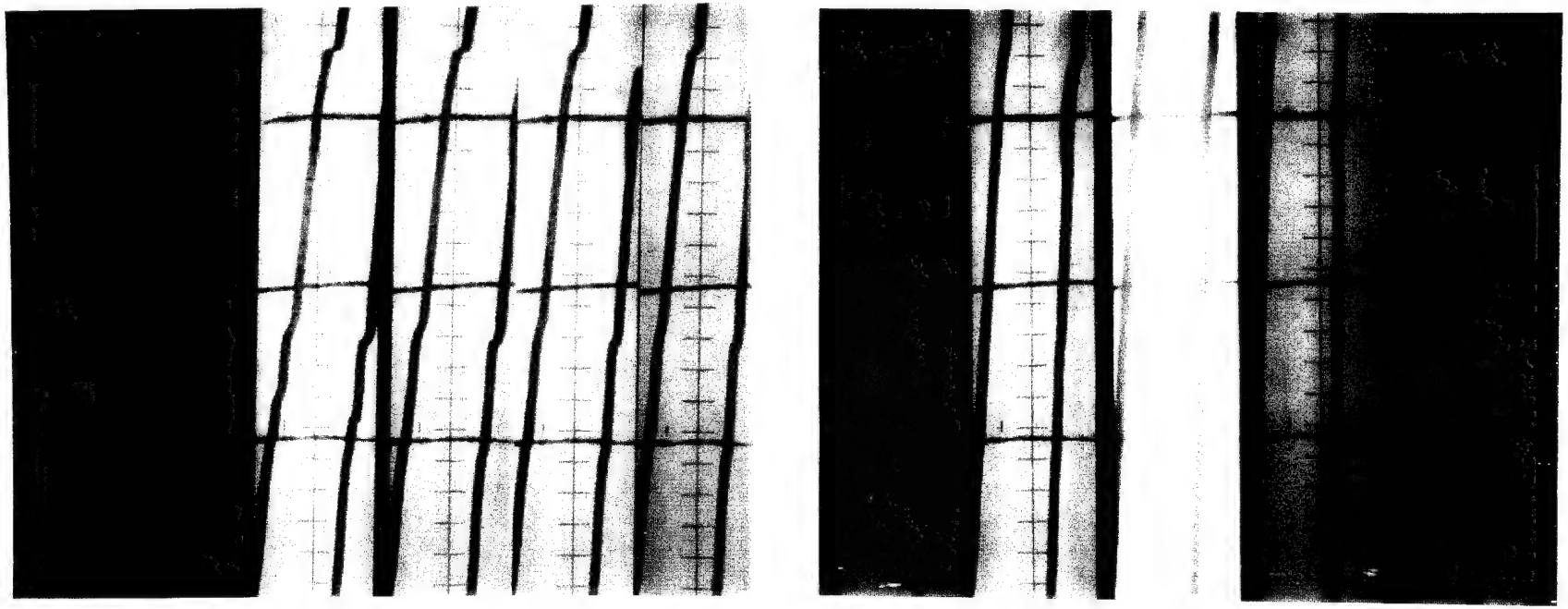

9 (10%) 8 (9%) 7 (8%) 6 (7%) 5 (6%) 4 (5%) 3 (4%) 2 (2%) 1 (0%)

Figure 11. Series of radiographs for Silica No. 60

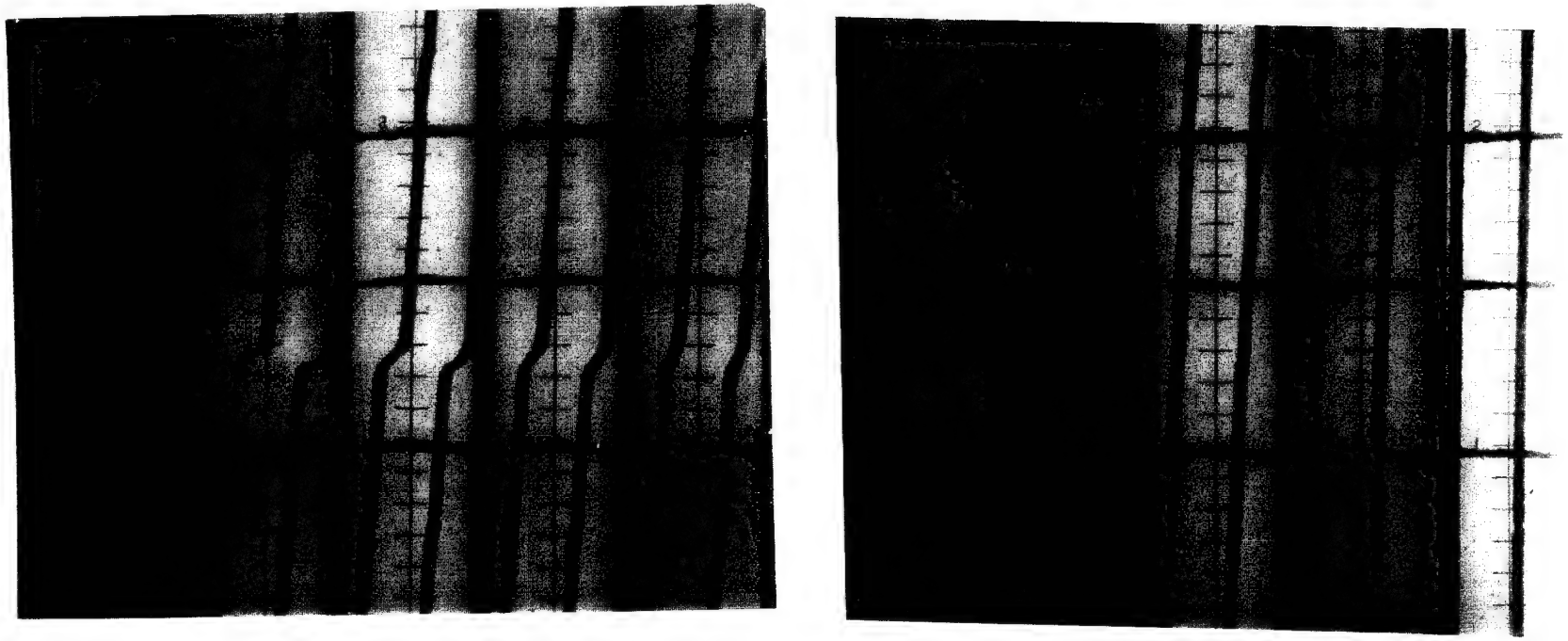

9 (10%) 8 (9%) 7 (8%) 6 (7%) 5 (6%) 4 (5%) 3 (4%) 2 (2%) 1 (0%)

Figure 12. Series of radiographs for Monterey No. 0

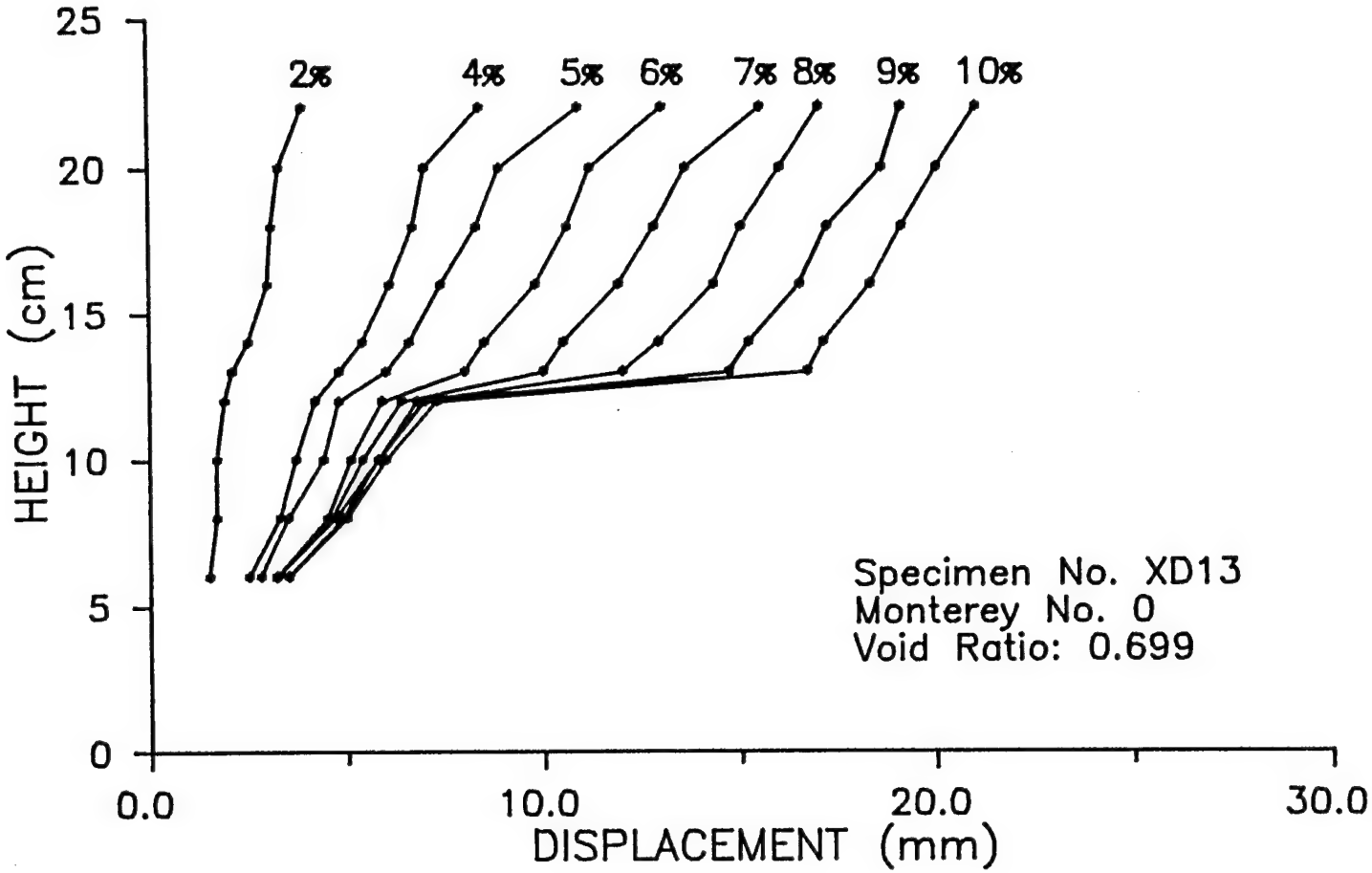

Figure 13. Displacement in each stage of deformation for Monterey No. 0

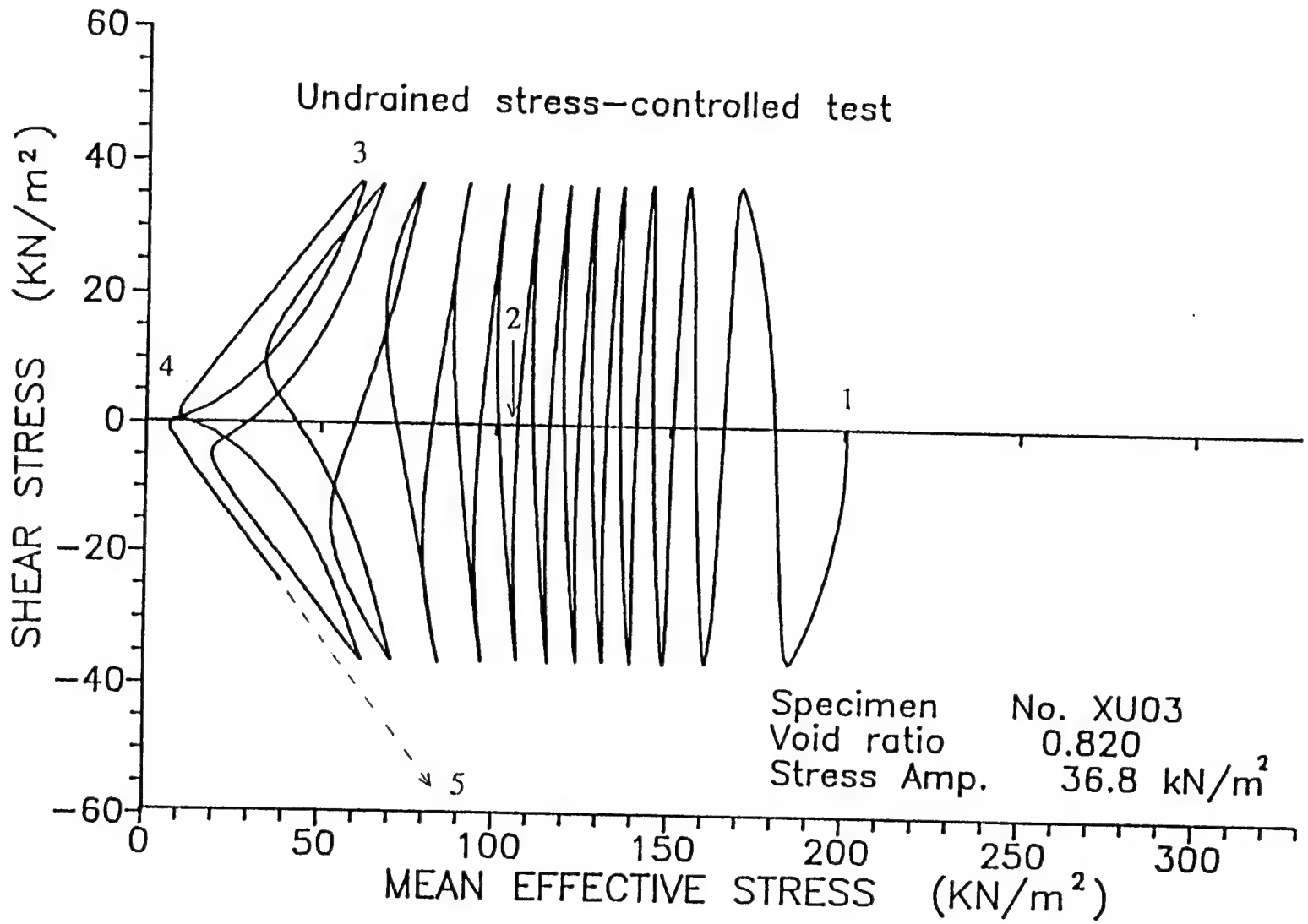

Figure 14. Relation between shear stress and effective pressure

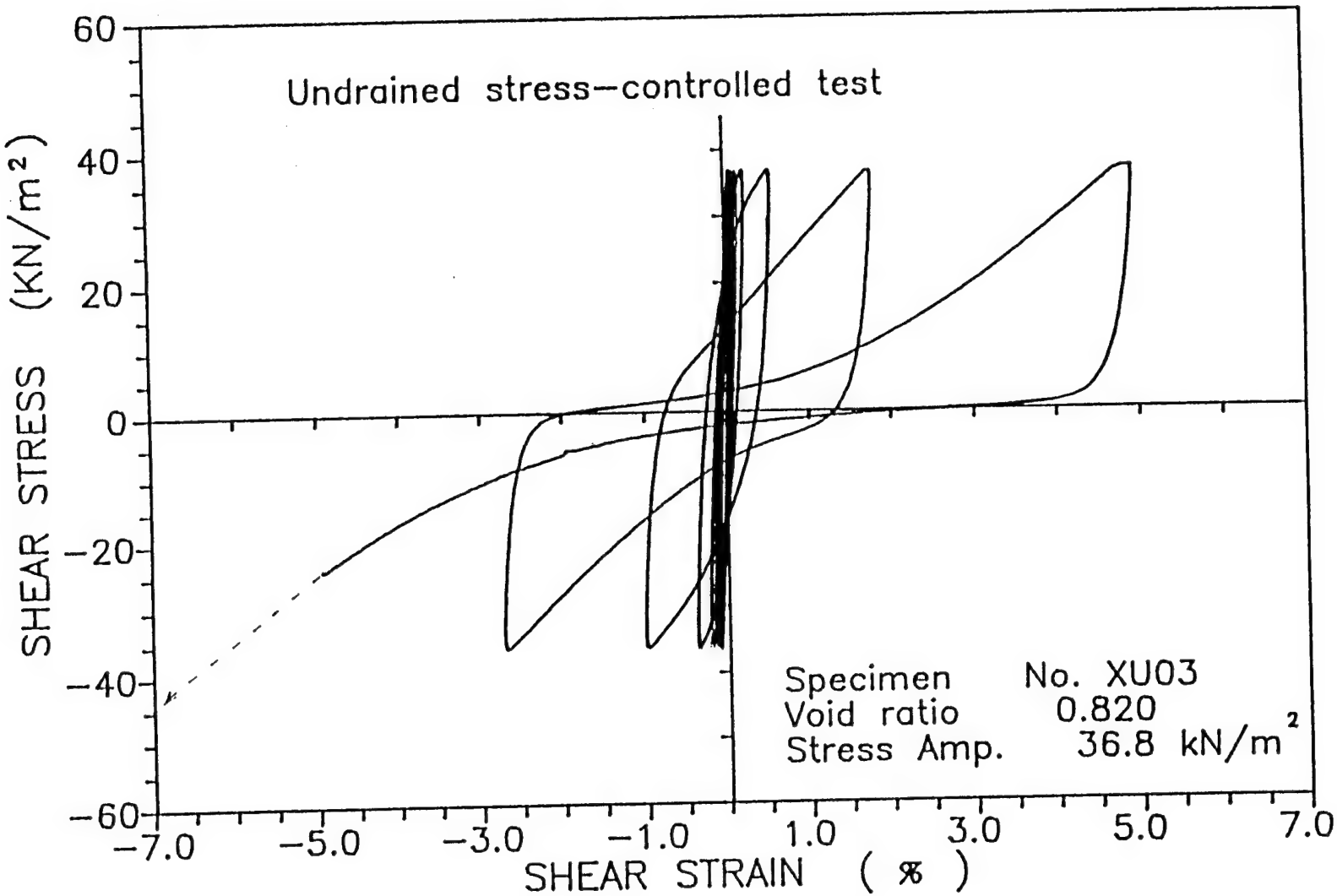

Figure 15. Relation between shear stress and shear strain

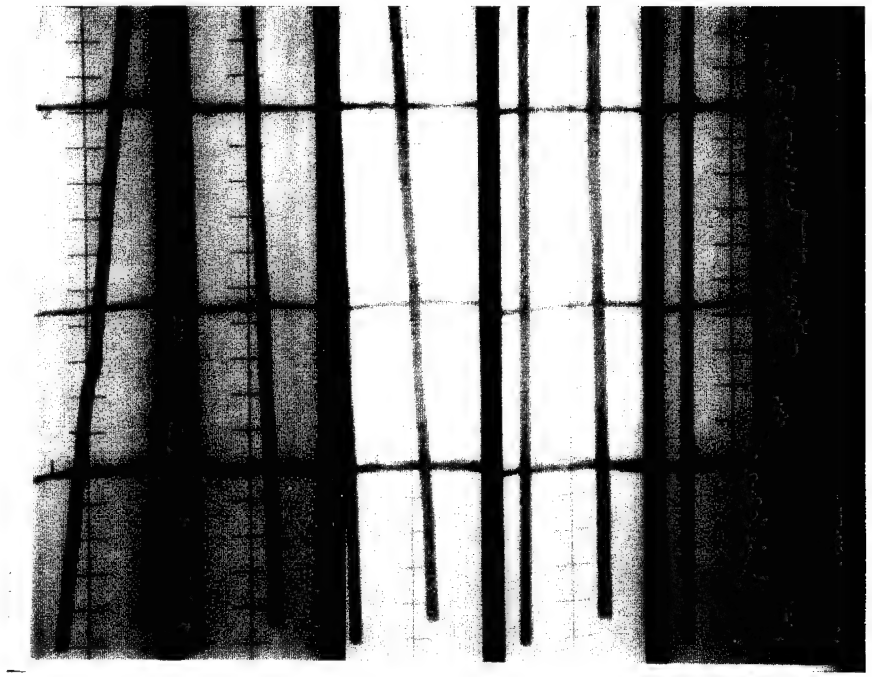

5 (-10%) 4 (2.70%) 3 (4.94%) 2 (0.04%) 1 (0%)

Figure 16. Series of radiographs for undrained test

APPENDIX IV

RESIDUAL SHEAR STRAIN EFFECT ON UNDRAINED RESPONSE OF SATURATED COHESIONLESS GRANULES

Principal Investigator: Sia Namet-Nasser

Postdoctoral Fellow: Naoyuki Okada

ABSTRACT

The effect of residual shear strains on the undrained cyclic shear deformation characteristics and the shear strength of sand is experimentally studied using a large hollow cylindrical torsional apparatus. Experiments are conducted under both *strain-* and *stress*-controlled conditions, and the corresponding effects are investigated and compared. In the strain-controlled tests, specimens are presheared under drained conditions and the deformation is stopped after a desired residual shear strain is attained. The specimens are then subjected to cyclic shear strain with *constant strain amplitude* under undrained conditions. It is seen that the magnitude of the residual shear strain affects the deformation characteristics, but does not affect the resistance. In the *stress*-controlled tests, cyclic loads at a constant stress amplitude are applied to both dense and loose specimens under undrained conditions. After a suitable shear strain amplitude is attained, the loading is stopped, with a desired residual shear strain remaining. After reconsolidation, the specimens are subjected to the original cyclic loads. For the preliquefied dense specimens, the shear resistance increases, especially when a small residual shear strain remains. For the preliquefied loose specimens, there is no significant reduction of the shear resistance when a small residual shear strain remains, but a significant reduction is observed when a large residual shear strain remains.

Table of Contents

ABSTRACT ..... IV-i

Table of Contents ..... IV-ii

List of Figures ..... IV-iii

1. INTRODUCTION IV-1

2. EXPERIMENTAL SETUP IV-5

   2.1 EQUIPMENT IV-5

   2.2 SPECIMEN PREPARATION AND INSTALLATION IV-6

3. STRAIN-CONTROLLED TESTS IV-8

4. STRESS-CONTROLLED TESTS IV-13

5. CONCLUSION IV-17

REFERENCES IV-19

FIGURES IV-21

List of Figures

Figure 1. Triaxial load frame

Figure 2. Particle size distribution curve

Figure 3. Relation between shear stress and shear strain for three specimens

Figure 4. Relation between volumetric strain and shear strain for three specimens

Figure 5. Relation between shear strain and effective pressure for specimen having -3.19% residual shear strain

Figure 6. Relation between shear stress and effective pressure for specimen having -3.19% residual shear strain

Figure 7. Relation between shear strain and effective pressure for specimen having 0.00% residual shear strain

Figure 8. Relation between shear stress and effective pressure for specimen having 0.00% residual shear strain

Figure 9. Relation between shear strain and effective pressure for specimen having -1.50% residual shear strain

Figure 10. Relation between shear stress and effective pressure for specimen having -1.50% residual shear strain

Figure 11. Relation between shear strain and effective pressure for virgin specimen

Figure 12. Relation between shear stress and effective pressure for virgin specimen

Figure 13. Relation between external work per unit volume and excess pore water pressure for presheared specimens and virgin specimen

Figure 14. Relation between shear stress and effective pressure in second loading of dense specimen having a large residual shear strain

Figure 15. Relation between shear stress and effective pressure in second loading of dense specimen having a small residual shear strain

Figure 16. Relation between shear stress and shear strain in second loading of dense specimen having a large residual shear strain

Figure 17. Relation between shear stress and shear strain in second loading of dense specimen having a small residual shear strain

Figure 18. Relation between shear stress and effective pressure in second loading of loose specimen having a large residual shear strain

Figure 19. Relation between shear stress and effective pressure in second loading of loose specimen having a small residual shear strain

Figure 20. Relation between shear stress and shear strain in second loading of loose specimen having a large residual shear strain

Figure 21. Relation between shear stress and shear strain in second loading of loose specimen having a small residual shear strain

Figure 22. Relation between normalized number of cycles and residual shear strain for dense and loose specimens

Figure 23. Relation between external work per unit volume and excess pore water pressure in second loading of dense specimens

Figure 24. Relation between external work per unit volume and excess pore water pressure in second loading of loose specimens

1. INTRODUCTION

It is well known that preshearing affects the subsequent monotonic or cyclic shear-deformation characteristics of granular media; see, for example, Finn *et al.* (1970), Arthur *et al.* (1977), Seed *et al.* (1977), Ishihara and Okada (1978, 1982), Nemat-Nasser and Tobita (1982), Nemat-Nasser and Takahashi (1984), Suzuki and Toki (1984), and Vaid *et al.* (1989). The overall shear-deformation characteristics of granular media are governed by their microstructure as well as the friction properties of contacting granules. The overall shearing causes slip and rolling of contacting granules, leading to microstructural changes. The discrete nature of the granular mass causes the deformation-history-dependency of the overall shear behavior.

The effect of preshearing on the cyclic shear resistance of sand specimens was studied by Finn *et al.* (1970). They observed that the reliquefaction resistance of sand with a small amount of preshearing had increased, whereas this resistance had decreased when the specimen had undergone a large amount of preshearing. In a series of experiments, Arthur *et al.* (1977) have shown in monotonic shearing that the behavior of presheared specimens depends on the principal stress directions in subsequent monotonic shearing. This directional dependency is called *induced anisotropy*. Seed *et al.* (1977) investigated the effects of a small amount of preshearing on the liquefaction resistance of sand, using a large-scale simple-shear apparatus mounted on a shake table. They observed that the liquefaction resistance of sand subjected to a small amount of preshearing increased considerably, in spite of no significant change in the density. Similar observations were made by Ishihara and Okada (1978). In two series of cyclic triaxial tests, one with a small and the other with a large amount of preshearing, Ishihara and Okada observed that the specimens in the first case developed less pore water pressure, having a symmetric response in compression and extension. On the other hand, the specimens with a large

amount of preshearing had a nonsymmetric response, being stiffer in the direction of preshearing. Ishihara and Okada (1982) also investigated the cyclic shear behavior of specimens which were presheared to a large shear strain and then restored to a state of zero residual shear strain. They showed that the resistance to subsequent liquefaction of a sand which had previously been liquefied and reconsolidated to the original effective stress state depends not only on the magnitude of the preshear strain, but, more significantly, on the direction of the preshearing. Nemat-Nasser and Tobita (1982) studied preshearing effects on the liquefaction and densification potentials of saturated cohesionless granular materials, both theoretically and experimentally. It was shown that preshearing with zero residual stress can reduce the resistance to liquefaction, although sample density was increased and other conditions were kept the same. Nemat-Nasser and Takahashi (1984) studied reliquefaction and densification potentials of sand under both strain- and stress-controlled conditions. They observed that the reliquefaction and densification potentials do not necessarily decrease because of preliquefaction or because of large-amplitude prestraining, but rather, the response depends on the anisotropy which is induced during the first loading of the specimen. In particular, these authors showed that in cyclic simple shearing, *the resistance to reliquefaction or densification of a preliquefied sample actually increases, because of the concomitant densification, if the preliquefaction is terminated at zero residual shear strain, but this resistance becomes very small, if the preliquefaction is terminated at zero residual shear stress*. Vaid *et al.* (1989) carried out a series of experiments to study the effects of preshearing on the subsequent monotonic and cyclic undrained reloading behavior of saturated sand. They showed that large preshearing may or may not eliminate the entire contractive tendency for reloading without strain reversal.

In the past, most experiments have been performed under *stress*-controlled condition, where specimens are subjected to cyclic loading at constant *stress* amplitude. Few

experiments have been performed under *strain*-controlled conditions. This is because most loading devices that have been used are pneumatic rather than servohydraulic, allowing for only *stress*-controlled tests. Some experiments have been carried out using the conventional triaxial apparatus; see for example Ishihara and Okada (1978, 1982), Suzuki and Toki (1984), and Vaid *et al.* (1989). The specimen in such tests experiences different stress conditions in the compression portion of the loading cycle, as compared with its tension portion. Thus, the mean value of the externally applied stress varies during each cycle, as well as the intermediate principal stress and, hence, the b-value.

In this paper, the results of a study of the effects of preshearing on the cyclic, undrained shear-deformation characteristics of sand are presented. Experiments are performed under both *stress*-controlled tests and *strain*-controlled conditions, using a large hollow cylindrical torsional apparatus. The experimental system is fully computer-controlled. The experiments can be controlled through a closed-loop system, by monitoring the values of the stress, strain, or the pore water pressure, terminating the test through programmed instructions, when any of these three variables attain a desired value. In these experiments, the shear stress or strain is cyclically applied to the isotropically pressurized specimen, and, therefore, the mean applied external stress, the intermediate principal stress, and the b-value, are kept constant throughout the course of the experiment. Special attention is paid to the magnitude of the residual shear strain remaining in the presheared specimens after reconsolidation, and its effects on the subsequent response of the specimen is experimentally studied. This paper is organized as follows: In Section 2, the experimental setup, the material, and the sample preparation technique are described. In Section 3, the results of a unique set of *strain*-controlled experiments are presented. It is seen that the shear deformation characteristics are greatly influenced by the magnitude of the residual shear strain, but not the shear resistance. Section 4 reports the results of our *stress*-controlled tests, and Section 5 gives the basic conclusions, summarizing the

differences observed between *strain*- and *stress*-controlled response of undrained cohesionless sands.

2. EXPERIMENTAL SETUP

2.1 EQUIPMENT

The experimental facility has been discussed by Okada and Nemat-Nasser (1994). It includes a closed-loop feedback system to control and monitor the specimen deformation. The specimen is a large hollow cylinder, 25cm high, with inner and outer diameters of 20cm and 25cm, respectively. With this geometry, the shear stress remains (approximately) homogeneous throughout the thickness of the specimen, as discussed by Hight *et al.* (1983); these authors provide a detailed examination of this and related issues. The specimen is supported by a triaxial load frame; see Figure 1.

The axial and torsional deformations are controlled through an MTS servohydraulic loading system. The load frame is fully computer-controlled, where either the stress- or the strain-path can be preprogrammed with smooth mode switching capability. The computer operates three independent controllers, each with three independent feedback channels. Controller 1 is associated with the vertical movement of the MTS/triaxial load frame ram assembly. Controller 2 is associated with the pressure measurements. Controller 3 is associated with the twist of the ram assembly. During the experiment, the vertical load in Controller 1 is controlled to keep the specimen in a state of hydrostatic compression in accord with the external pressure, P_o. Both strain- and stress-controlled tests are performed. For strain-controlled tests, the angular displacement in Controller 3 is assigned by the computer to cyclically twist the specimen to a desired shear strain amplitude at a desired shear strain rate. For stress-controlled tests, the torque in Controller 3 is controlled. The active control mode can be switched in the middle of experiment without disturbing the sample. Moreover, the experiment can be automatically stopped or started when the stress, or the strain, or the pore water pressure attain a desired state.

2.2 SPECIMEN PREPARATION AND INSTALLATION

The granular material is Silica 60 manufactured by U.S. Silica, having fine particle size, so as to minimize the membrane penetration phenomenon. The particle size distribution is shown in Figure 2. The mean particle diameter is 220μm and the specific gravity is 2.645. Depending on the packing conditions, different void ratios are obtained. For Silica 60, the minimum and maximum void ratios are 0.631 and 1.095, respectively, and are measured by the JSSMFE method; Committee of JSSMFE on the Test Method of Relative Density of Sand (1979).

It is well known that the initial packing condition of the sand has an important effect on the subsequent material response; Arthur and Menzies (1972), Oda (1972a), and Miura and Toki (1982). To achieve a consistent initial packing condition, the rodding method is used with 10 layers to obtain loose packing conditions and 14 layers for dense packing conditions. Experiments performed under loose conditions use the sand in a wet form. Here the sand has been air-dried and then mixed with 8 weight percent water before pouring into the mold. (The water is needed to prevent non-homogeneous initial packing conditions in the loose form.) The void ratio for this condition varies between 0.843 and 0.855. Experiments performed with dense conditions use only air-dried sand with the void ratio varying between 0.708 and 0.727.

The entire specimen assembly is raised to the level of the MTS load frame via a special forklift with a work frame built onto the MTS load frame, which allows attachment of all connections to the specimen assembly and provides a railway for installation and removal of the specimen.

The specimen is water-saturated in a conventional manner. CO_2 is used to remove the air from the specimen. Then, de-aired water is used to saturate the specimen. To remove small amounts of air and CO_2 gas remaining in the specimen, the pore water

pressure is increased to 196kN/m^2 as back pressure, while at the same time the external hydrostatic pressure is increased to 225.4kN/m^2 to keep the effective pressure constant (29.4kN/m^2) during this procedure. In this manner, B-values in excess of 0.99 have been achieved for all experiments. The effective pressure is then increased to 196kN/m^2, and the sample is isotropically consolidated for a period of 3 hours.

3. STRAIN-CONTROLLED TESTS

Stress-controlled tests have been widely performed to investigate the preshearing effect on the subsequent response of saturated sands; see Finn *et al.* (1970), Seed *et al.* (1977), and Ishihara and Okada (1978, 1982), among others. On the other hand, *strain*-controlled tests have been rarely performed; Nemat-Nasser and Takahashi (1984), Ishibashi *et al.* (1985), and Okada and Nemat-Nasser (1994). In the present work, specimens having different residual shear strains are subjected to cyclic shear straining in undrained conditions. In this section, the procedure for strain-controlled tests is first described and then the test results are discussed.

Consider the cylindrical coordinates, (θ, r, z). The shear strain, $\gamma_{z\theta}$, is controlled throughout this series of experiments. Preshearing is applied monotonically to the isotropically consolidated dense specimens under drained conditions, so that a suitable residual shear strain remains; Figure 3. A shear strain rate of 1/6% per minute is used for the preshearing. Three specimens are presheared, where the preshearing is stopped at different shear strains in each specimen. As shown in Figures 3 and 4, one specimen (No. 30) is presheared to point A with a strain amplitude of -4.0%, and then this is reversed and stopped at point B where the shear strain is -3.25% with zero shear stress. A second specimen (No. 31) is sheared to the same maximum strain amplitude (-4.0%) and then reversed and stopped at point D where the shear strain is zero but a shear stress of 112kN/m^2 remains. A third specimen (No. 35) is subjected to the same preshearing, but this is stopped at point C where the shear strain is -1.50% and a shear stress of 78kN/m^2 remains.

The specimens are reconsolidated for 3 hours after preshearing. The residual shear strain is defined as the shear strain remaining in the presheared specimen after reconsolidation. The shear stress in specimen No. 30 is kept zero during reconsolidation, and a

residual shear strain of -3.19% is measured after reconsolidation. The shear strain is kept constant in specimens Nos. 31 and 35 during reconsolidation. The shear stress, therefore, is nonzero in both specimens during and after reconsolidation. The residual shear strains in samples 30 and 35 are 0.00% and -1.50%, respectively.

These three specimens are then subjected to *undrained* cyclic *strain*-controlled shearing. The imposed cyclic displacement has a triangular time variation with constant strain rate, 2/3% per minute, over each quarter-cycle. The cyclic shearing (0.5% amplitude) starts in the (positive) shear direction which continues the preshearing direction towards zero shear strain; Figure 3. The cyclic shearing is stopped at the end of the cycle for which the excess pore water pressure reaches 95% of the initial effective pressure, *i.e.*, 186.2 kN/m^2.

First, the effect of the residual shear strain on the shear deformation characteristics of presheared specimens is discussed. The relation between the shear strain and the effective pressure and the relation between the shear stress and the excess pore water pressure in each specimen are shown in Figures 5-10. It is seen from Figure 5 that considerable excess pore water pressure in the specimen having -3.19% residual shear strain is generated during shearing in the positive shear direction. The pore pressure then decreases during shearing in the negative shear direction. It is also seen from Figure 6 that this specimen has a small resistance in the positive shear direction and a large resistance in the negative shear direction. On the other hand, it is seen from Figures 7 and 8 that the behavior of the specimen with zero residual shear strain is opposite of that of the specimen with -3.19% residual shear strain: a substantial excess pore water pressure is created when shearing in the negative shear direction, with the shear resistance being greater in the positive shear direction. The response of the specimen with -1.50% residual shear strain is shown in Figures 9 and 10. The characteristics of this specimen are somewhere

between those of the other two specimens, being almost symmetric in both the positive and negative shear directions. These results show that the shear deformation characteristics of presheared samples strongly depend on the magnitude of the residual shear strain. Hence, the microstructure which governs the overall shear behavior is greatly affected by the magnitude of the residual shear strain, as well as by the deformation history. The change of the microstructure at several stages of the shear deformation has been examined by Oda (1972b), Konishi *et al.* (1983), and Subhash *et al.* (1991). The magnitude of the residual shear strain is one of the parameters with strong influence on the microstructure.

Second, the effect of the residual shear strain on the shear strength is considered. There is no significant (strain-controlled tests) difference among the presheared specimens in the number of cycles required for the excess pore water pressure to reach 95% of the initial effective pressure. It takes 22, 24, and 20 cycles for the specimens having 0.0%, -1.50%, and -3.19% residual shear strain, respectively. As Nemat-Nasser and Tobita (1982) mentioned, this is because in a strain-controlled test, the deformation of the specimen is limited by the prescribed strain amplitude and this prevents extensive particle rearrangement which often occurs in stress-controlled tests, once sufficiently high pore water pressure is attained.

As a comparison with the presheared specimens, a virgin specimen is subjected to the same cyclic shearing under undrained conditions. The relation between shear strain and effective pressure and the relation between shear stress and effective pressure are shown in Figures 11 and 12, respectively. It takes just 9 cycles for the virgin specimen to reach 95% of the initial effective pressure, which is much fewer than those in presheared specimens. The results show that the preshearing itself may increase the number of cycles to 95% of the initial effective pressure, and the magnitude of the residual shear

strain does not affect this for the experiments conducted in this work.

Finally, we consider the effect of the residual shear strain on the shear resistance in the second loading from an energy viewpoint. The external work applied to the specimen is mainly consumed by the slip between contacting granules, causing the rearrangement of granules. It is, therefore, meaningful for the study of shear strength to use external work per unit volume as a scalar parameter which indicates the fabric change in the granular mass; see Nemat-Nasser and Shokooh (1979), Nemat-Nasser (1980), Towhata and Ishihara (1985), and Okada and Nemat-Nasser (1994). From the experimental results, the external work per unit volume is calculated at the end of each cycle, and the relation between excess pore water pressure and external work per unit volume during the experiment is examined.

The rate of external work per unit volume, $< \dot{w}_E >$, can be evaluated in terms of the applied boundary tractions, $\boldsymbol{\tau}$, and the boundary velocity field, $\dot{\mathbf{u}}$,

$$< \dot{w}_E > \equiv \frac{1}{V} \int_{\partial D} \boldsymbol{\tau} \cdot \dot{\mathbf{u}} \, dS \ , \tag{3.1}$$

where dot denotes the inner-product, and ∂D is the boundary of the sample domain D. If we assume that the boundary tractions are *uniform*, then (3.1) can be expressed in terms of the overall stresses and strain rates, as (Hill, 1963, 1967)

$$< \dot{w}_E > = < \sigma_{zz} > < \dot{\varepsilon}_{zz} > + < \sigma_{rr} > < \dot{\varepsilon}_{rr} > + < \sigma_{\theta\theta} > < \dot{\varepsilon}_{\theta\theta} > + < \sigma_{z\theta} > < \dot{\gamma}_{z\theta} >. \tag{3.2}$$

Since the specimen is isotropically pressurized by the external pressure, P_o, throughout the experiment, all three normal stresses equal P_o. Denoting the average volumetric strain rate by $\frac{\dot{V}}{V}$, (3.2) can be rewritten as

$$\begin{aligned} < \dot{w}_E > &= P_o \, (< \dot{\varepsilon}_{zz} > + < \dot{\varepsilon}_{rr} > + < \dot{\varepsilon}_{\theta\theta} >) + < \sigma_{z\theta} > < \dot{\gamma}_{z\theta} > , \\ &= P_o \, \frac{\dot{V}}{V} + < \sigma_{z\theta} > < \dot{\gamma}_{z\theta} > . \end{aligned} \tag{3.3}$$

Since, for the pressure levels used here, sand particles and water can be assumed to be incompressible, $\frac{\dot{V}}{V}$ is zero during the undrained experiment, if the sample is completely saturated. The rate of external work per unit volume then becomes

$$< \dot{w}_E > = < \sigma_{z\theta} > < \dot{\gamma}_{z\theta} > . \tag{3.4}$$

The external work per unit volume, $< w_E >$, up to time t can then be evaluated by the time-integration of (3.4),

$$< w_E > = \int_{t_0}^{t} < \sigma_{z\theta} > < \dot{\gamma}_{z\theta} > dt \ , \tag{3.5}$$

where t_0 denotes the time at which the experiment is started.

Figures 13 shows the relation between excess pore water pressure and external work per unit volume at the end of each cycle, for presheared and virgin specimens, respectively. It is seen that there is no significant difference among presheared specimens. However, there is a large difference between the presheared specimens and the virgin specimen. The presheared specimens require more energy than the virgin specimen in order to reach a certain excess pore water pressure. While preshearing itself greatly affects the external work required to attain a certain pore water pressure in the subsequent cyclic shearing, the magnitude of the residual shear strain seems to have relatively small effect on this phenomenon.

4. STRESS-CONTROLLED TESTS

The results of the stress-controlled tests under undrained conditions are presented in this section. The shear stress, $\tau_{z\theta}$, is controlled throughout this series of experiments. First, the experimental procedure for stress-controlled tests is described and then the results are presented.

Both dense and loose specimens are examined. The specimens are prepared as described in Section 2.2. A cyclic shear stress is applied under undrained conditions and the test is terminated such that a shear strain remains in the specimen. Stress amplitudes of 41.2kN/m^2 and 33.3kN/m^2 are used for dense and loose specimens, respectively, with a period of 2 minutes per cycle. Once the range of the shear strain amplitude (which is the shear-strain difference between two consecutive peaks) reaches 6%, the cyclic loading is stopped at a desired shear strain. Since the shear strain in the loose specimens becomes suddenly large during the cyclic loading, the loading is removed before the completion of the last cycle, whenever necessary.

After the first loading, the valve between the buret and the pore water inside the specimen is opened slightly so that the excess pore water pressure is released very slowly. Once the excess pore water pressure reaches zero and the initial effective pressure is recovered, the small residual shear *stress* remaining in the specimen is released. The specimens are then isotropically reconsolidated for 3 hours. Since the shear stress is controlled during reconsolidation, the changes of shear strain remaining in the preliquefied specimen are observed. The residual shear strain is defined as the shear strain remaining after reconsolidation. Then, the same cyclic loading as the first loading is applied to the reconsolidated specimens. The second cyclic loading was always started in a direction which continued the last half-cycle of the first loading. Once the range of the shear strain amplitudes (peak to peak) reached 6%, the cyclic loading was stopped.

This entire process is called the second loading.

First, the effects of the residual shear strain on the cyclic shear deformation characteristics in the second loading are discussed. Figures 14 and 15 show the relation between the shear stress and the effective pressure in the second loading, for dense specimens having large and small residual shear strains, respectively. It is clearly seen that in the specimen having a large residual shear strain, a large excess pore water pressure appears in the first half-cycle. However, the increase in the excess pore water pressure in the subsequent half-cycle is much less than that in the first half-cycle. On the other hand, in the specimen having a small residual shear strain, the excess pore water pressure developed at the end of the first cycle of the second loading is almost the same as that in the first loading. However, the excess pore water pressure developed during the first half-cycle is less than that in the subsequent half-cycle. Figures 16 and 17 show the stress-strain relation for the same specimens used in Figures 14 and 15. It is also seen (Figure 16) in the specimen having a large residual shear strain, that a large shear strain suddenly appears in the first half-cycle, and is not recovered during the subsequent half-cycle. Finally, unlike for the first loading, the stress-strain profile is not symmetric. The stress-strain relation for the specimen with a small residual shear strain (Figure 17) is entirely different than that of the specimen with a large residual strain. The shape of the stress-strain relation in Figure 17 is almost symmetric. This difference in the response of specimens having large and small residual shear strains is also observed for loose specimens. Figures 18 and 19 show the relation between the shear stress and the effective pressure in the second loading for loose specimens having large (Figure 18) and small residual shear strains (Figure 19), respectively. Figures 20 and 21 show the corresponding stress-strain relations for these specimens. It is seen that the response in the second loading is again influenced by the nature of the first loading. It is clearly observed from the results of this and related series of experiments that the shear deformation

characteristics in the second loading are significantly influenced by the magnitude of the residual shear strain.

Nemat-Nasser and Tobita (1982) showed that a sample with large residual shear strain remaining, shows a large anisotropic response in the cyclic undrained test, although a sample with zero residual shear strain remaining shows a relatively isotropic response in the subsequent cyclic undrained test. They concluded from a micromechanical point of view that, if the fabric as it is described by the distribution of the contact normals, is the key ingredient in introducing dramatic changes in sample behavior because of prestraining, then prestraining over a cycle of relatively large strain amplitude which *terminates with zero residual shear strain*, should result in a considerably different subsequent response as compared with the one which *terminates with zero residual shear stress*. Nemat-Nasser and Takahashi (1984) carried out a series of tests, and showed that in cyclic shearing, the resistance to reliquefaction (undrained) or densification (drained) of a preliquefied sample actually increases, because of the concomitant densification, if the preliquefaction is terminated at zero residual shear strain, but this resistance becomes very small, if the preliquefaction is terminated at zero residual shear stress with a relatively large residual shear strain remaining. The experimental results obtained here also support the results of Nemat-Nasser and Tobita (1982), and Nemat-Nasser and Takahashi (1984). These anisotropic responses during cyclic undrained tests can be explained by the anisotropic fabric induced in the sample by preshearing.

We now discuss the effect of the residual shear strain on the shear resistance in the second loading, *i.e.*, on the reliquefaction strength. For this, we use the "normalized number of cycles" as the ratio of the number of cycles to liquefaction in the second loading and the number of cycles to liquefaction in the first loading; Finn (1970). This parameter may be regarded as expressing the shear resistance in the second loading or the

reliquefaction potential. The relation between the normalized number of cycles and the magnitude of the residual shear strain for both dense and loose specimens is shown in Figure 22. It is seen that the specimens having a small residual shear strain show a greater strength than specimens having a large residual shear strain, in both dense and loose specimens. It is also seen that, for dense specimens, the shear resistance in the second loading increases, especially for specimens having a small residual shear strain. On the other hand, for loose specimens, the shear resistance in the second loading decreases for the specimens having a large residual shear strain, whereas it remains almost the same as that in the first loading, for a small residual shear strain.

Finally, we consider the effect of the residual shear strain on the shear resistance in the second loading from an energy viewpoint. Figures 23 and 24 show the relation between excess pore water pressure and external work per unit volume at the end of each cycle, for dense and loose specimens, respectively. As a comparison, the results of the first loading are also plotted in the same figures. It is seen from Figure 23 that there are some differences among the dense specimens, depending on the magnitude of the residual shear strain; specimens having smaller residual shear strains need more energy than specimens having larger residual shear strains, in order to reach the same excess pore water pressure at the end of a cycle. It is also seen from Figure 23 that until the excess pore water pressure reaches $100 kN/m^2$ for the same specimens, there is no difference between the response in the first loading and that in the second loading which starts with a large residual shear strain. On the other hand, it is seen from Figure 24 that for loose specimens, there is an almost unique relation between the excess pore water pressure and the external work per unit volume, independently of the corresponding number of cycles and the magnitude of the residual shear strain, and that there is no difference between the response in the first loading and that in the second loading.

5. CONCLUSIONS

The effect of preshearing on the cyclic undrained shear deformation characteristics of water-saturated sand is studied experimentally, using a large hollow cylindrical torsion apparatus. Two series of experiments, strain-controlled and stress-controlled tests, are conducted on specimens with different residual shear strains. In both series of tests, the second loading is started in the direction which continues the last half-cycle of the preshearing. The following experimental results are obtained.

In strain-controlled tests, the shear deformation characteristics are greatly influenced by the magnitude of the residual shear strain. The number of cycles to 95% of the effective pressure in strain-controlled tests is, however, not affected by the magnitude of the residual shear strain. The results for a virgin specimen show that preshearing greatly affects the number of cycles to 95% of the effective pressure, as well as the relation between pore water pressure and the external work per unit volume in the subsequent cyclic shearing under undrained conditions.

In stress-controlled tests, the shear deformation characteristics are also greatly influenced by the magnitude of the residual shear strain. The specimen with a large residual shear strain produces a larger shear strain and a larger pore water pressure in the first cycle, as compared with the specimen with a small residual shear strain. Moreover, the magnitude of the residual shear strain affects the shear resistance in the stress-controlled tests. The specimen having a large residual shear strain shows a lower shear resistance than that having a small residual shear strain. For dense specimens, preshearing does not reduce the shear resistance in the second loading; the shear resistance in the second loading is greater than that in the first loading, especially for the specimens having a small residual shear strain. On the other hand, preshearing reduces the shear resistance for the loose specimens, especially for the specimens possessing a large residual shear strain.

However, even for loose specimens, a reduction of the shear resistance is not observed in the specimen having a small residual shear strain.

REFERENCES

Arthur, J.R.F., and Menzies, B.K. (1972): "Inherent anisotropy in a sand," *Géotechnique,* **22,** No. 1, pp. 115-128.

Arthur, J.R.F., Chua, K.S., and Dunstan, T. (1977): "Induced anisotropy in a sand," *Géotechnique,* **27,** No. 1, pp. 13-30.

Committee of JSSMFE on the Test Method of Relative Density of Sand. 1979. Maximum-minimum density test method of sand. Procedure for Testing Soils, Second Revised Edition, JSSMFE, Part 2, pp. 172-188 (in Japanese).

Finn, W.D.L., Bransby, P.L., and Pickering, D.J. (1970): "Effect of strain history on liquefaction of sand," *Journal of Soil Mechanics and Foundations Division, ASCE,* **96,** No. SM6, pp. 1917-1934.

Hight, D.W., Gens, A., and Symes, M.J. (1983): "The development of a new hollow cylinder apparatus for investigating the effects of principal stress rotation in soils," *Géotechnique,* **33,** No. 4, pp. 355-383.

Hill, R. (1963): "Elastic properties of reinforced solids: some theoretical principles," *J. Mech. Phys. Solids* **11,** pp. 357-372.

Hill, R. (1967): "The essential structure of constitutive laws for metal composites and polycrystals," *J. Mech. Phys. Solids* **15,** pp. 79-95.

Ishibashi, I., Kawamura, M., and Bhatia, S. (1985): "Effect of initial shear on cyclic behavior of sand," *Journal of Geotechnical Engineering, ASCE,* **111,** No. 12, pp. 1395-1410.

Ishihara, K., and Okada, S. (1978): "Effects of stress history on cyclic behavior of sand," *Soils and Foundations,* **18,** No. 4, pp. 31-45.

Ishihara, K., and Okada, S. (1982): "Effects of large preshearing on cyclic behavior of sand," *Soils and Foundations,* **22,** No. 3, pp. 109-125.

Konishi, J., Oda, M., and Nemat-Nasser, S. (1983): "Induced anisotropy in assemblies of oval cross section rods in biaxial compression," *Mechanics of Granular Materials; New Models and Constitutive Relations, (ed. Jenkins, J.T. and Satake, M.)* pp. 31-39.

Miura, S., and Toki, S. (1982): "A sample preparation method and its effect on static and cyclic deformation-strength properties of sand," *Soils and Foundations* **22,** No. 1, pp. 61-77.

Nemat-Nasser, S. (1980): "On behavior of granular materials in simple shear," *Soils and Foundations,* **20,** No. 3, pp. 59-73.

Nemat-Nasser, S., and Shokooh, A. (1979): "A unified approach to densification and liquefaction of cohesionless sand in cyclic shearing," *Can. Geotech. J.,* **16,** pp. 659-678.

Nemat-Nasser, S., and Takahashi, K. (1984): "Liquefaction and fabric of sand," *Journal of Geotechnical Engineering, ASCE,* **110,** No. 9, pp. 1291-1306.

Nemat-Nasser, S., and Tobita, Y. (1982): "Influence of fabric on liquefaction and densification potential of cohesionless sand," *Mechanics of Materials,* **1,** No. 1, pp. 43-62.

Oda, M. (1972a): "Initial fabric and their relations to mechanical properties of granular materials," *Soils and Foundations,* **12,** No. 1, pp 17-36.

Oda, M. (1972b): "The mechanism of fabric changes during compressional deformation of sand," *Soils and Foundations,* **12,** No. 2, pp. 1-18.

Okada, N., and Nemat-Nasser, S. (1994): "Energy dissipation in inelastic flow of saturated cohesionless granular media," *Géotechnique,* **44,** No. 1, pp. 1-19.

Seed, H.B., Mori, K., and Chan, C.K. (1977): "Influence of seismic history on liquefaction of sands," *Journal of Geotechnical Engineering Division, ASCE,* **103,** No. GT4, pp. 257-270.

Subhash, G., Nemat-Nasser, S., Mehrabadi, M.M., and Shodja, H.M. (1991): "Experimental investigation of fabric-stress relations in granular materials," *Mechanics and Materials,* **11,** pp. 87-106.

Suzuki, T., and Toki, S. (1984): "Effects of preshearing on liquefaction characteristics of saturated sand subjected to cyclic loading," *Soils and Foundations,* **24,** No. 2, pp. 16-28.

Towhata, I., and Ishihara, K. (1985): "Shear work and pore water pressure in undrained shear," *Soils and Foundations,* **25,** No. 3, pp. 73-84.

Vaid, Y.P., Chung, E.K.F., and Kuerbis, R.H. (1989): "Preshearing and undrained response of sand," *Soils and Foundations,* **29,** No. 4, pp. 49-61.

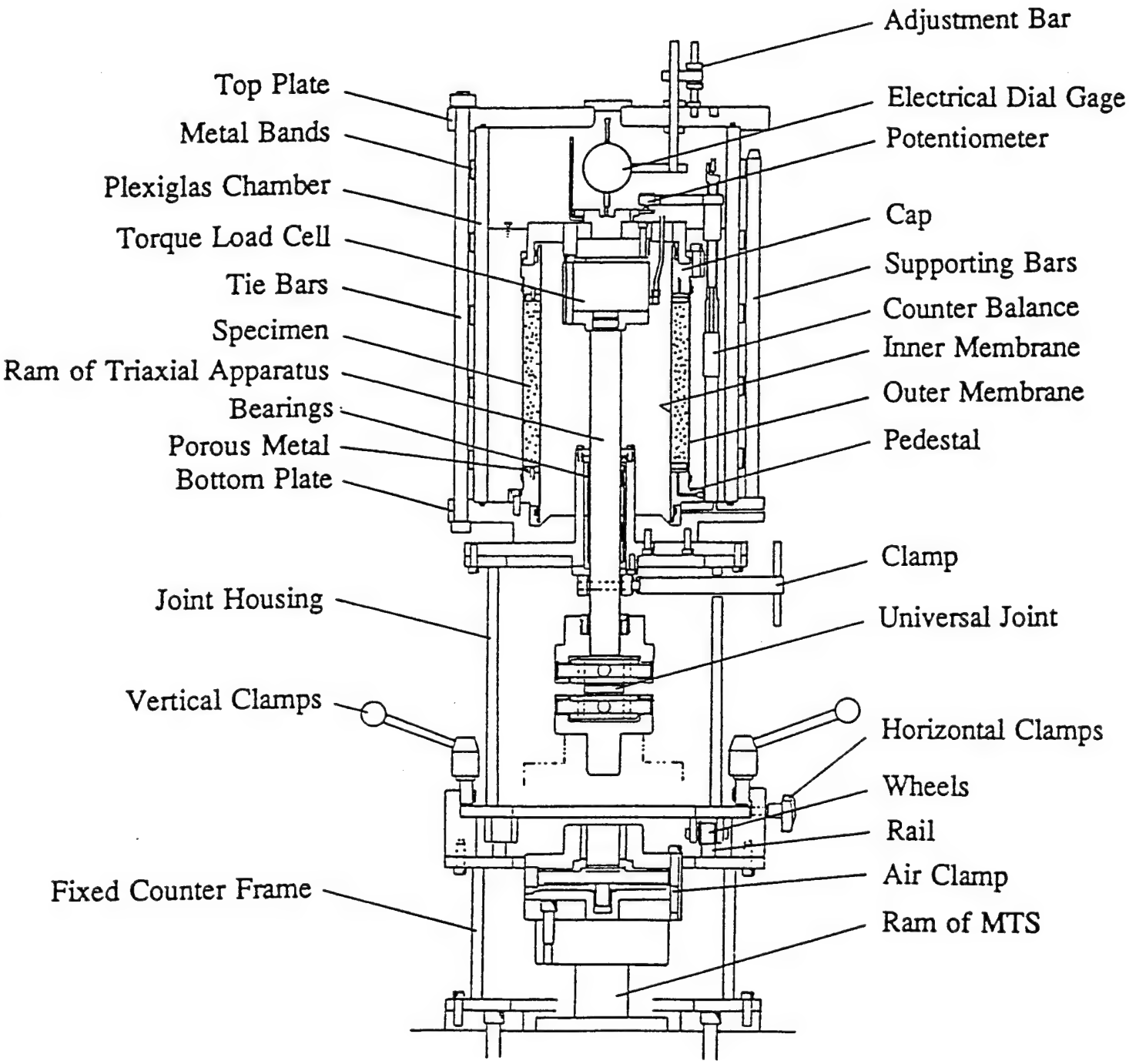

Figure 1. Triaxial load frame

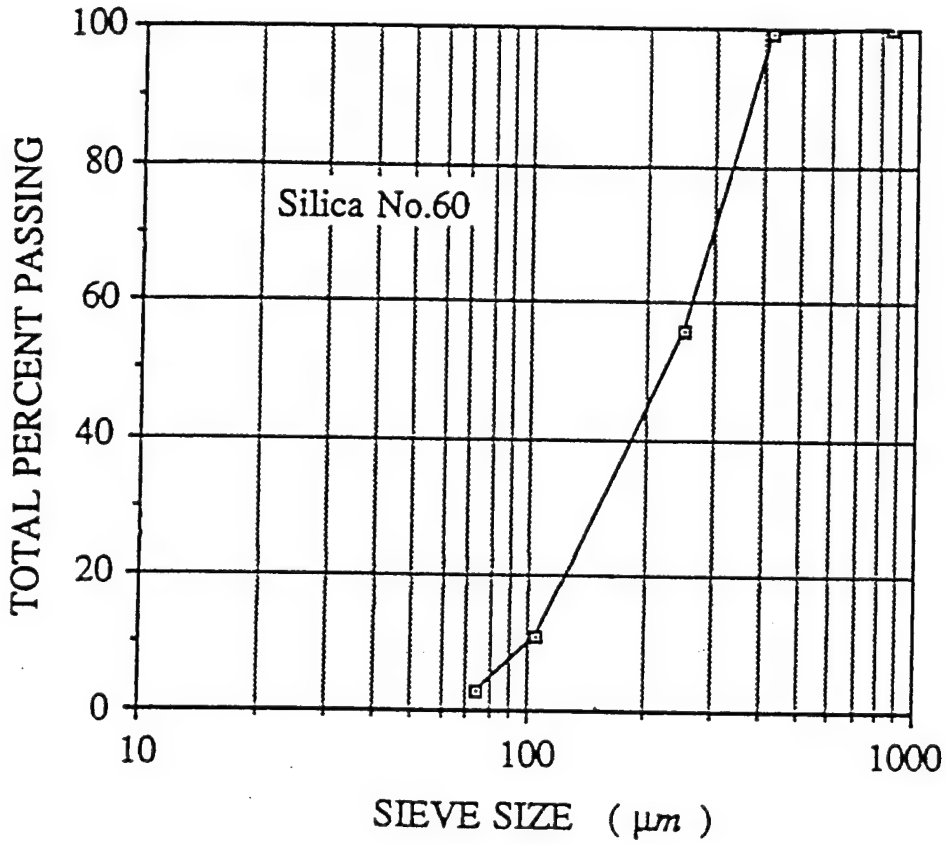

Figure 2. Particle size distribution curve

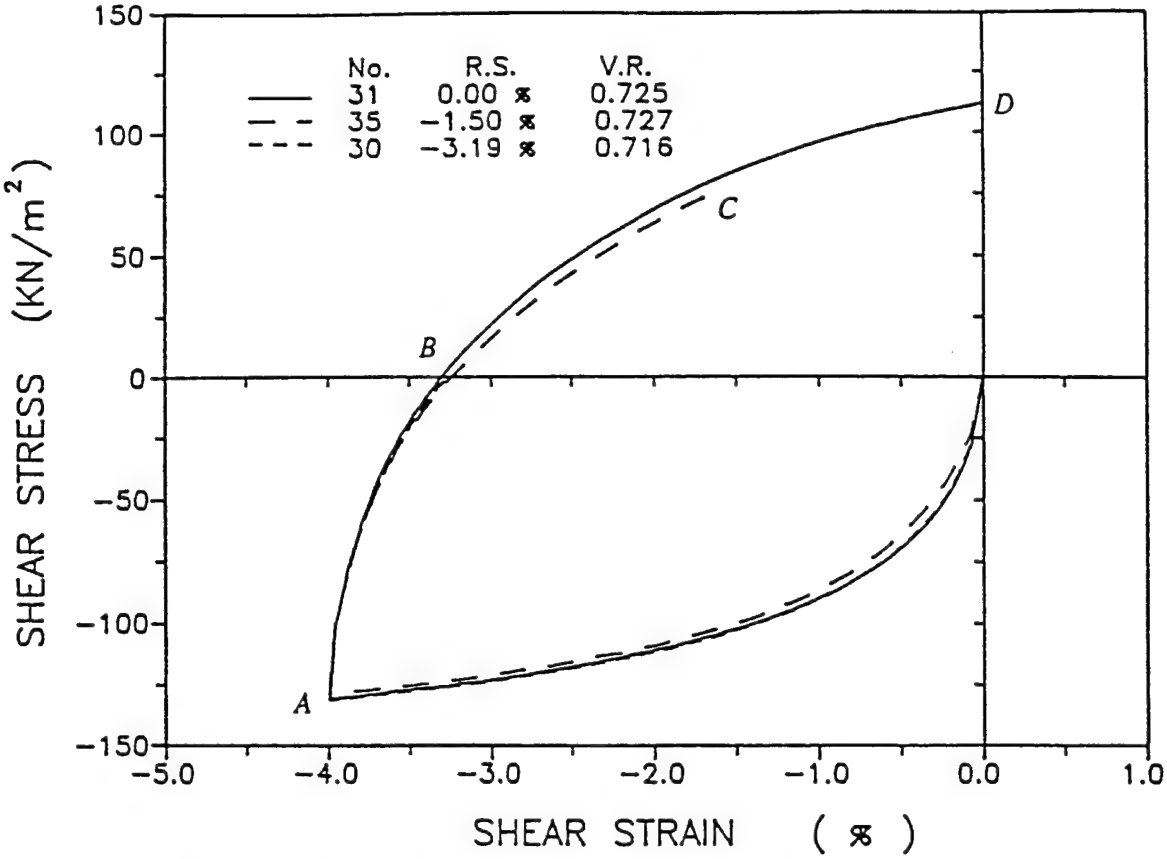

Figure 3. Relation between shear stress and shear strain for three specimens

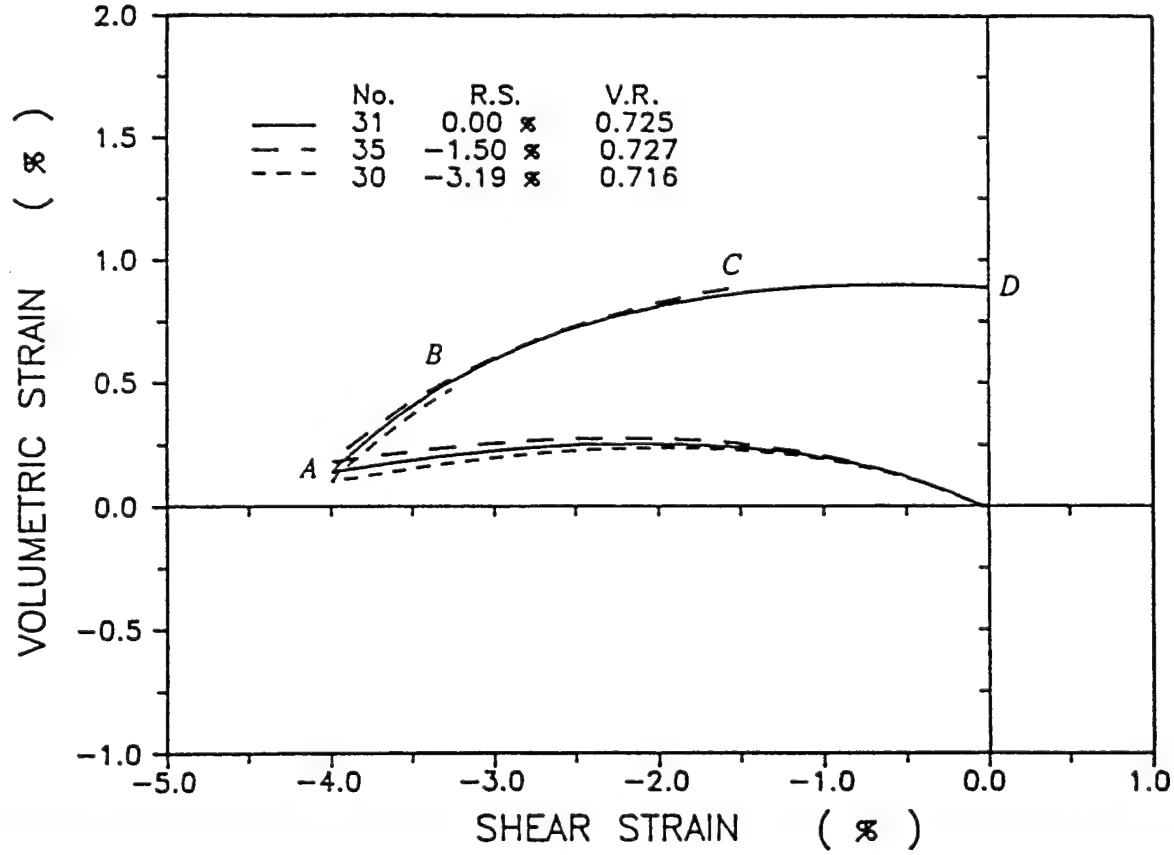

Figure 4. Relation between volumetric strain and shear strain for three specimens

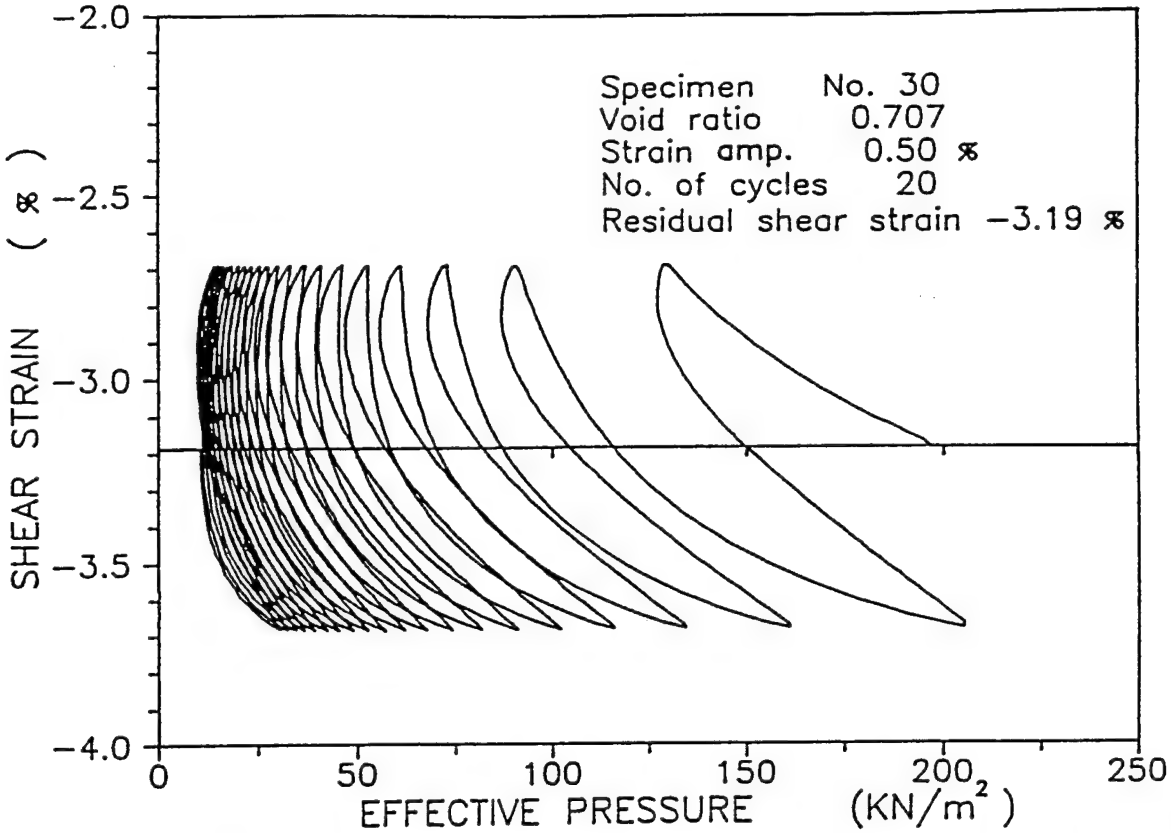

Figure 5. Relation between shear strain and effective pressure for specimen having -3.19% residual shear strain

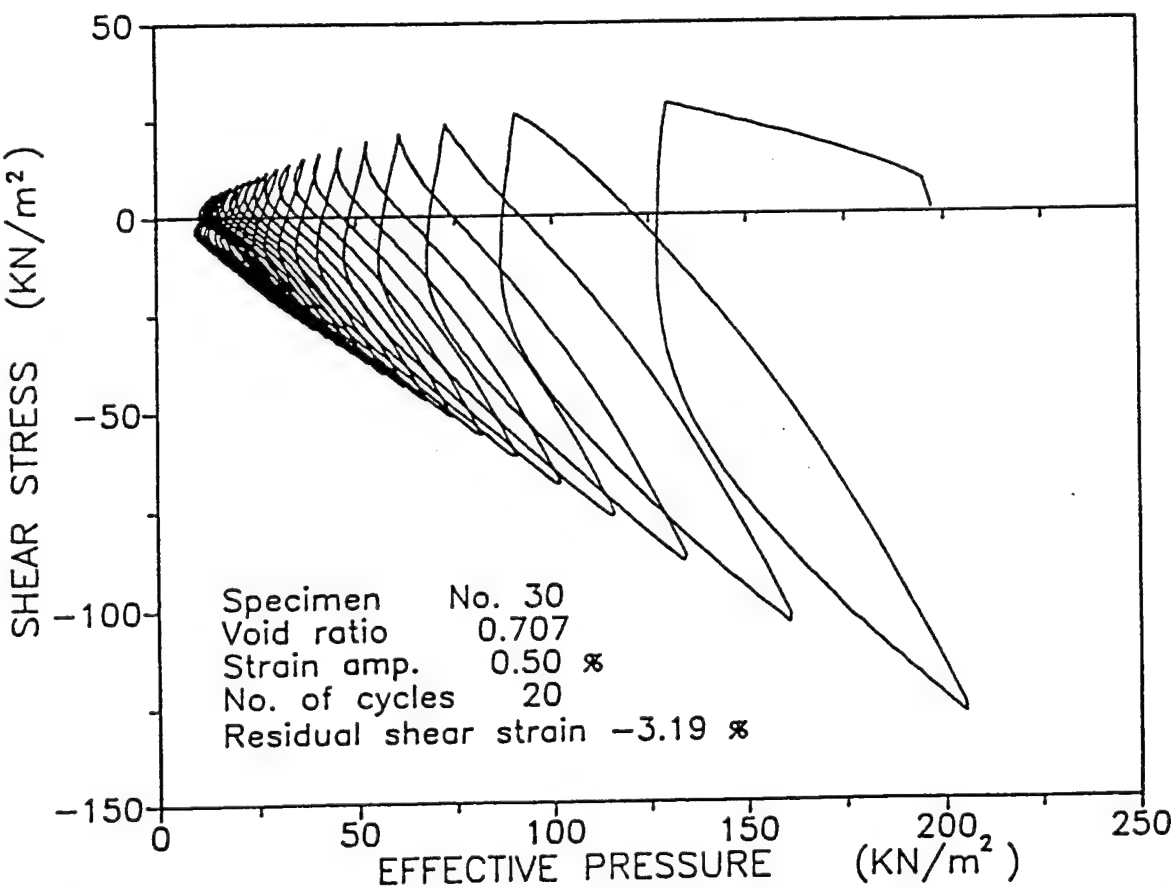

Figure 6. Relation between shear stress and effective pressure for specimen having -3.19% residual shear strain

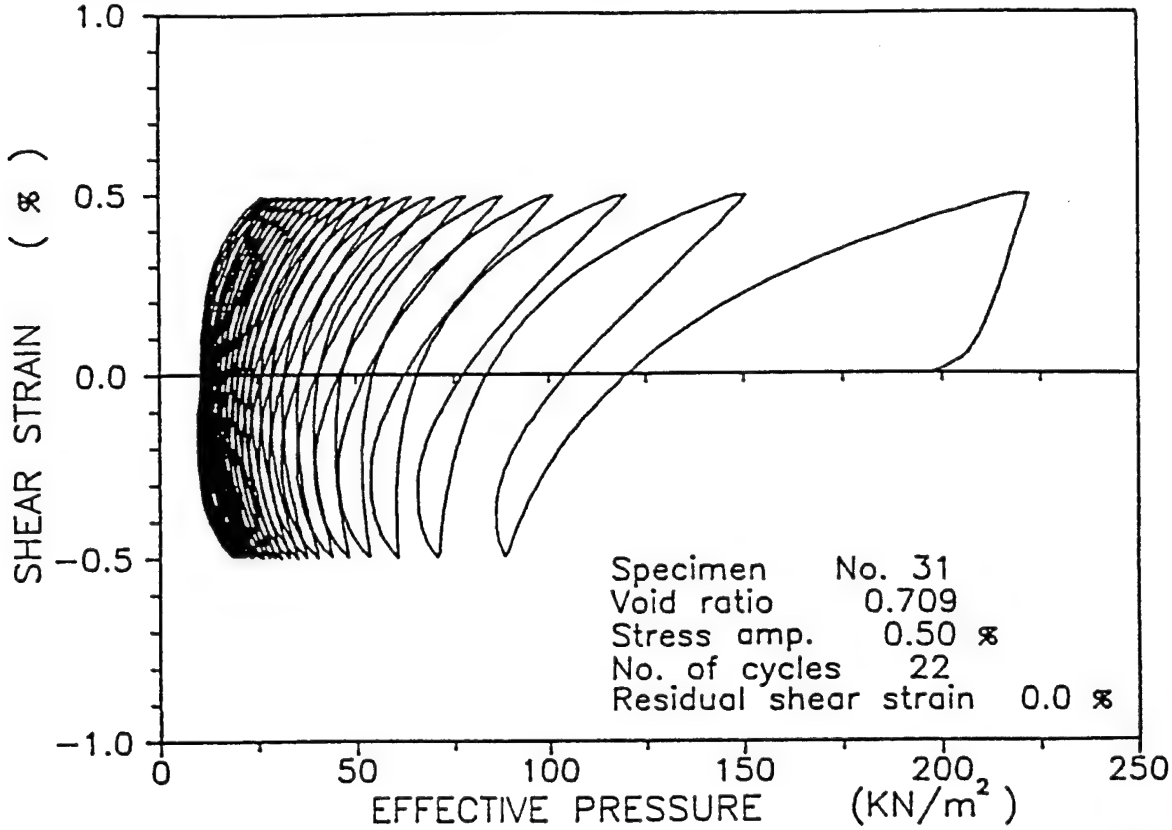

Figure 7. Relation between shear strain and effective pressure for specimen having 0.00% residual shear strain

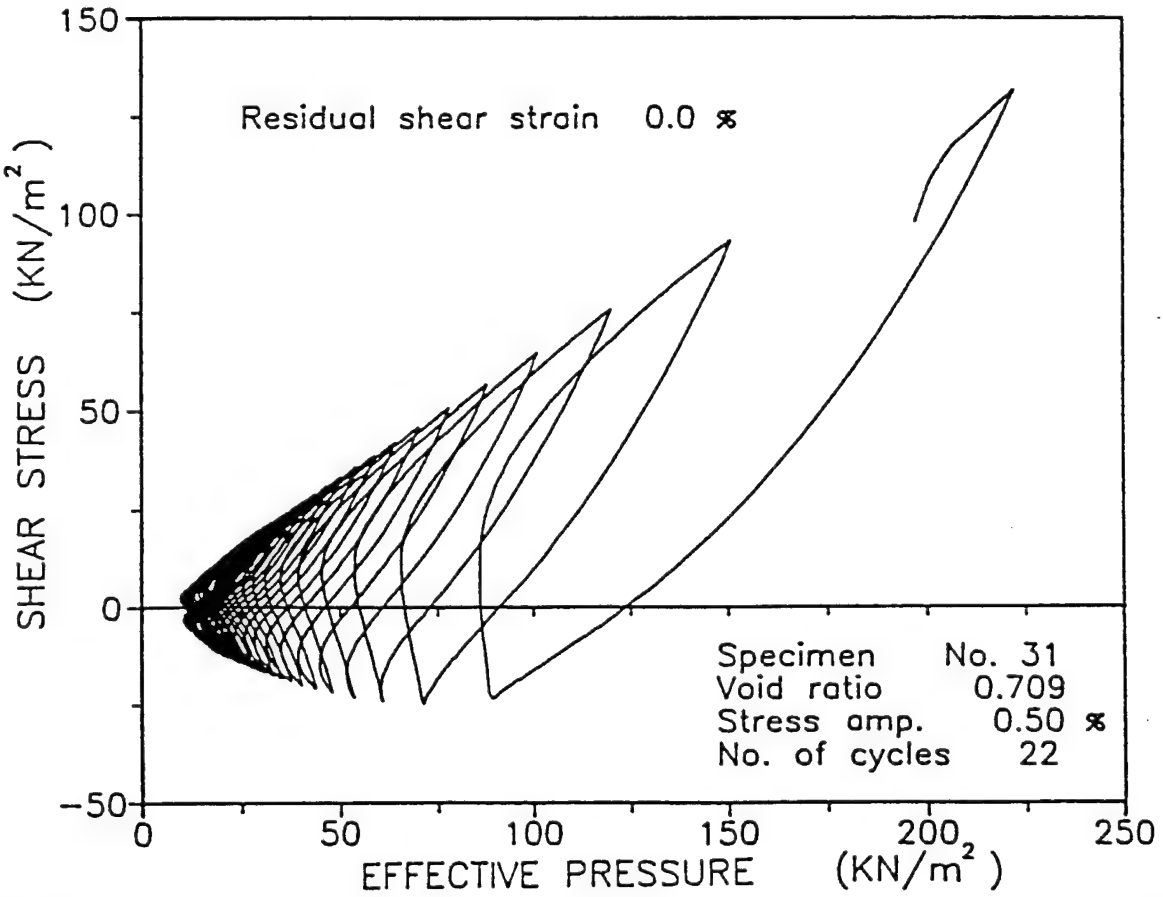

Figure 8. Relation between shear stress and effective pressure for specimen having 0.00% residual shear strain

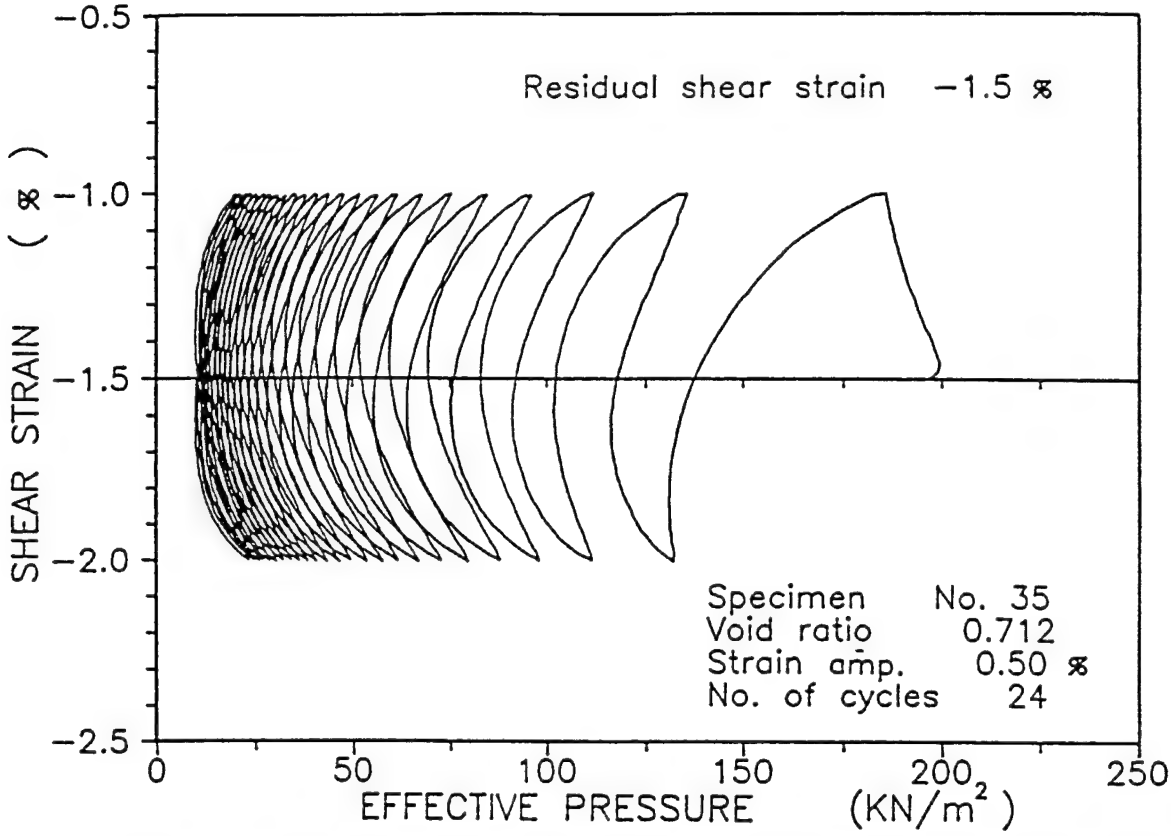

Figure 9. Relation between shear strain and effective pressure for specimen having -1.50% residual shear strain

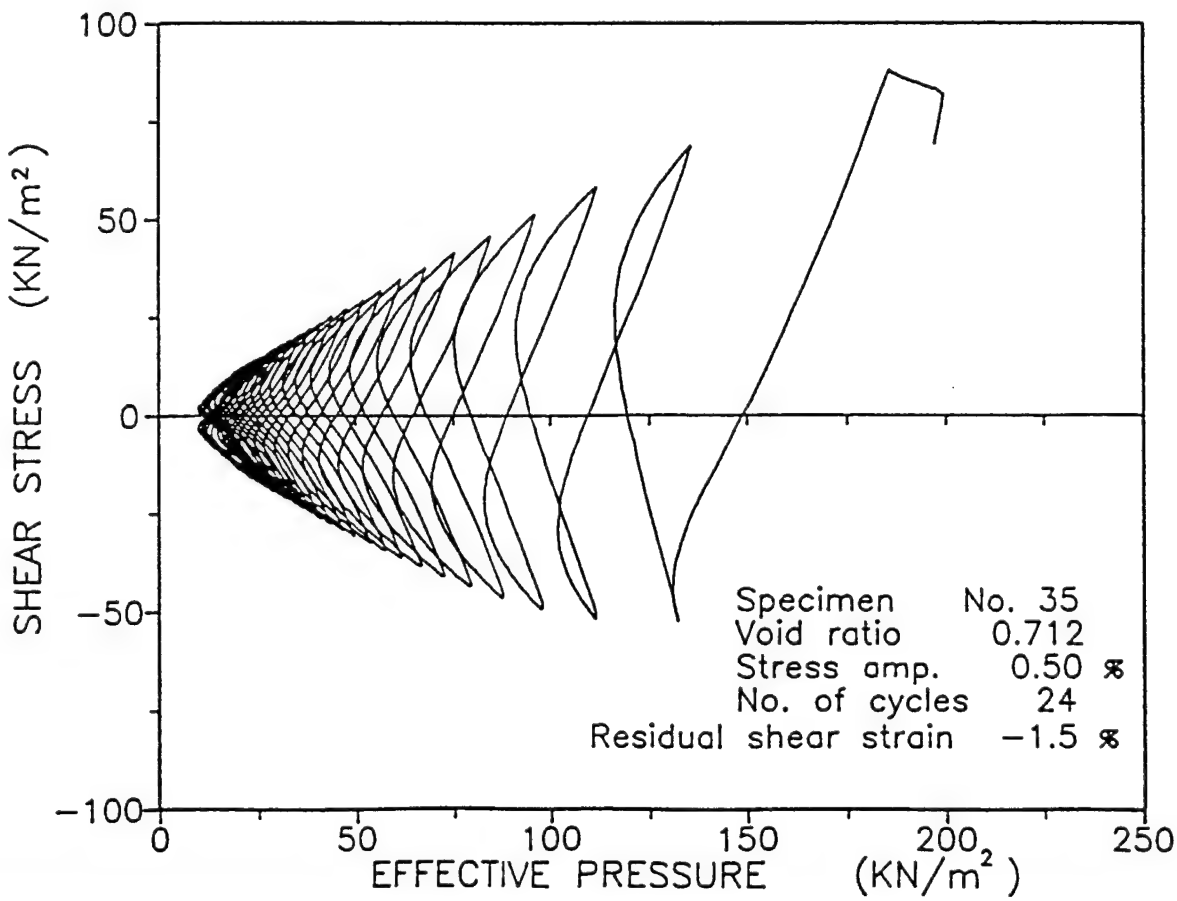

Figure 10. Relation between shear stress and effective pressure for specimen having -1.50% residual shear strain

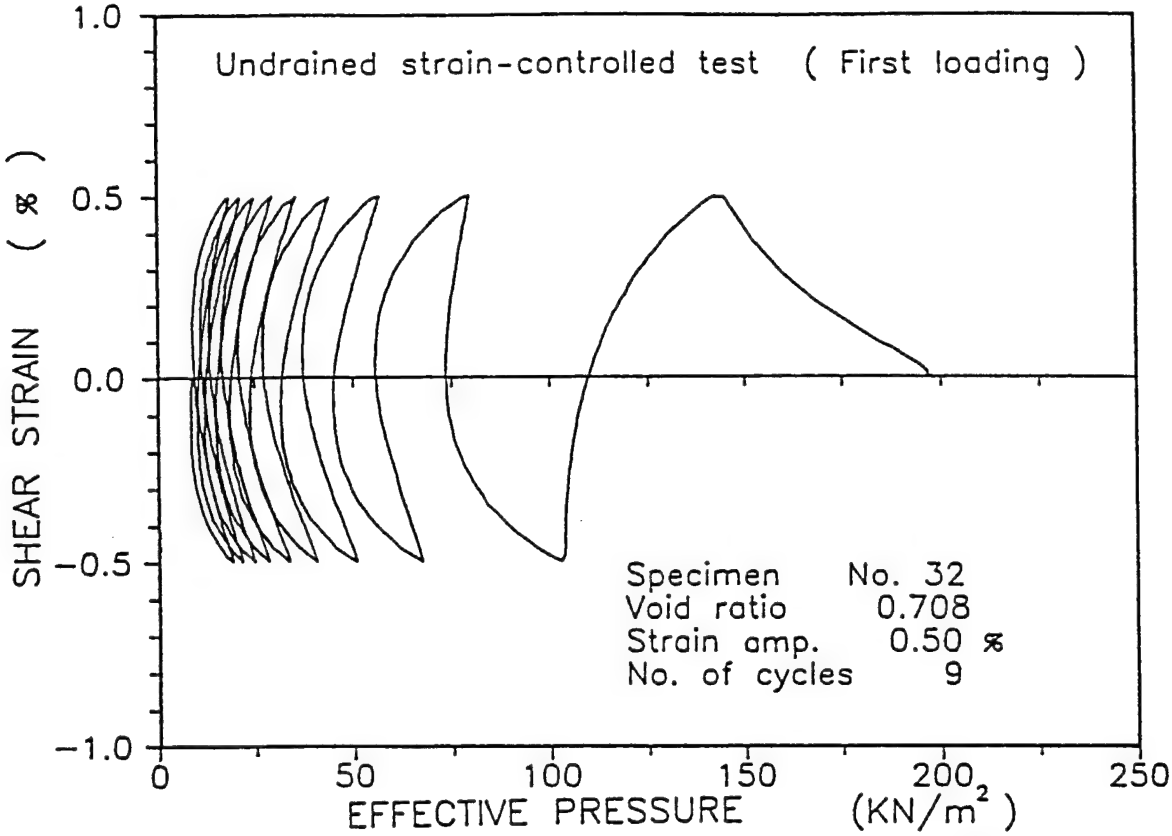

Figure 11. Relation between shear strain and effective pressure for virgin specimen

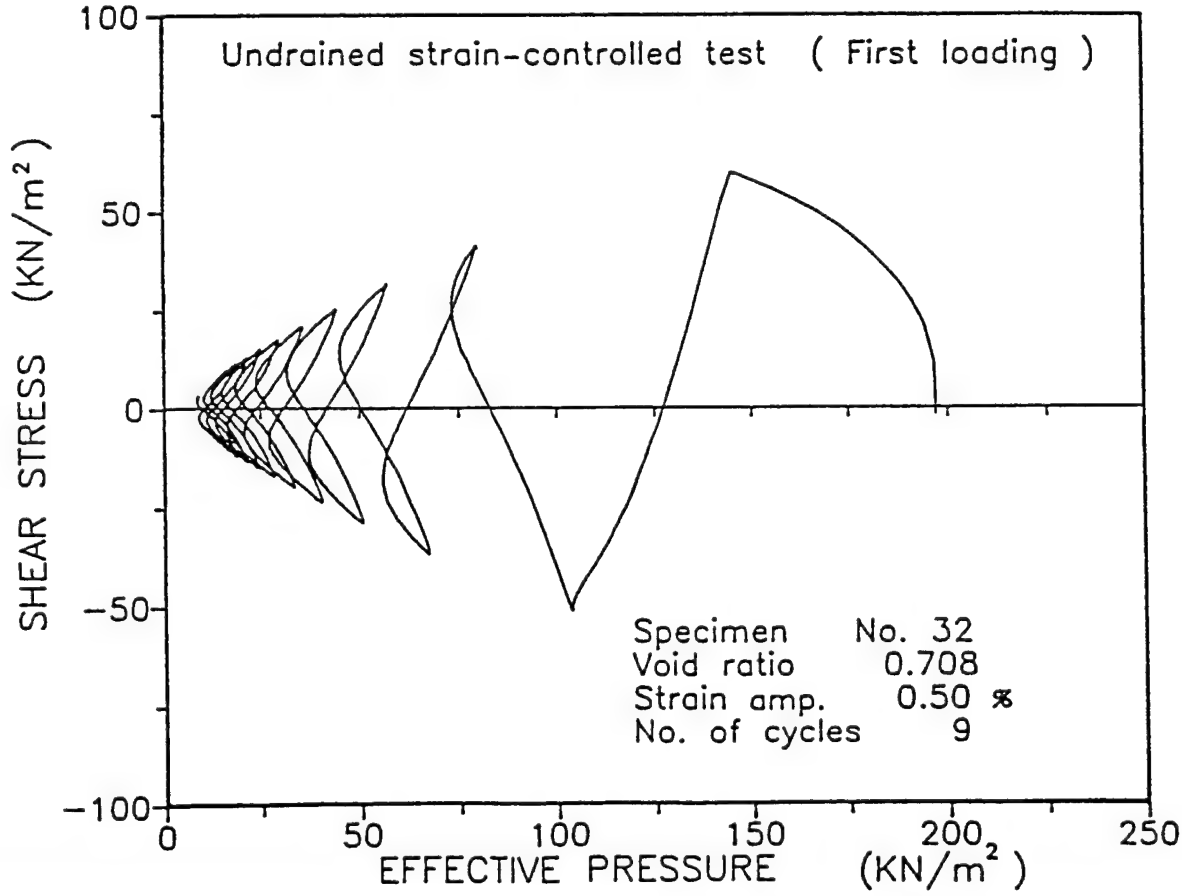

Figure 12. Relation between shear stress and effective pressure for virgin specimen

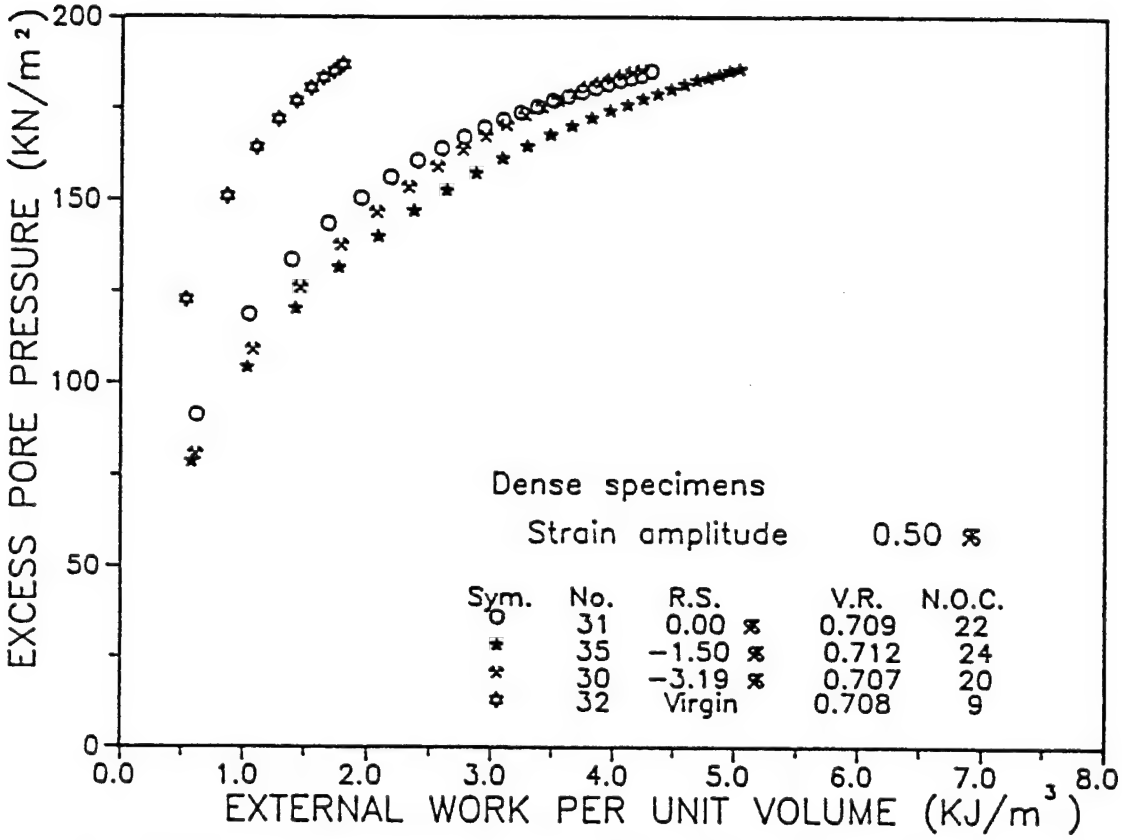

Figure 13. Relation between external work per unit volume and excess pore water pressure for presheared specimens and virgin specimen

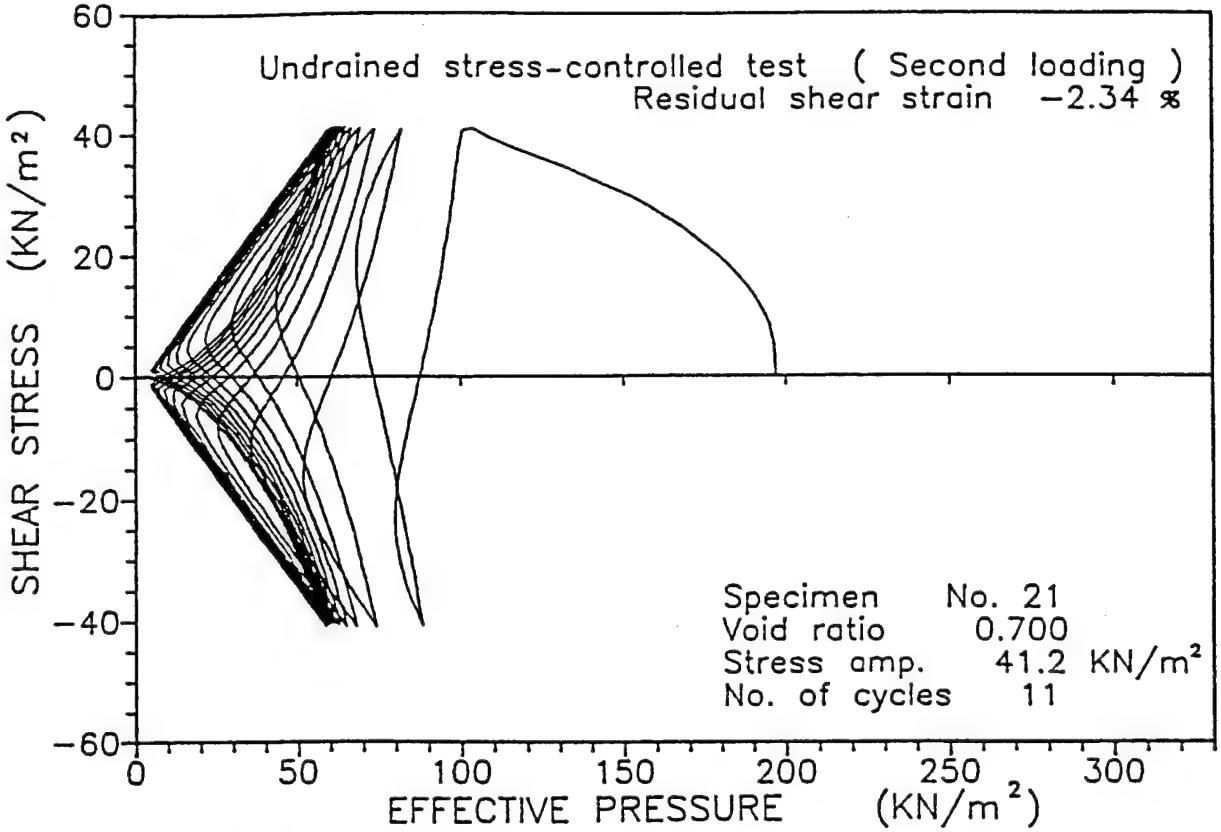

Figure 14. Relation between shear stress and effective pressure in second loading of dense specimen having a large residual shear strain

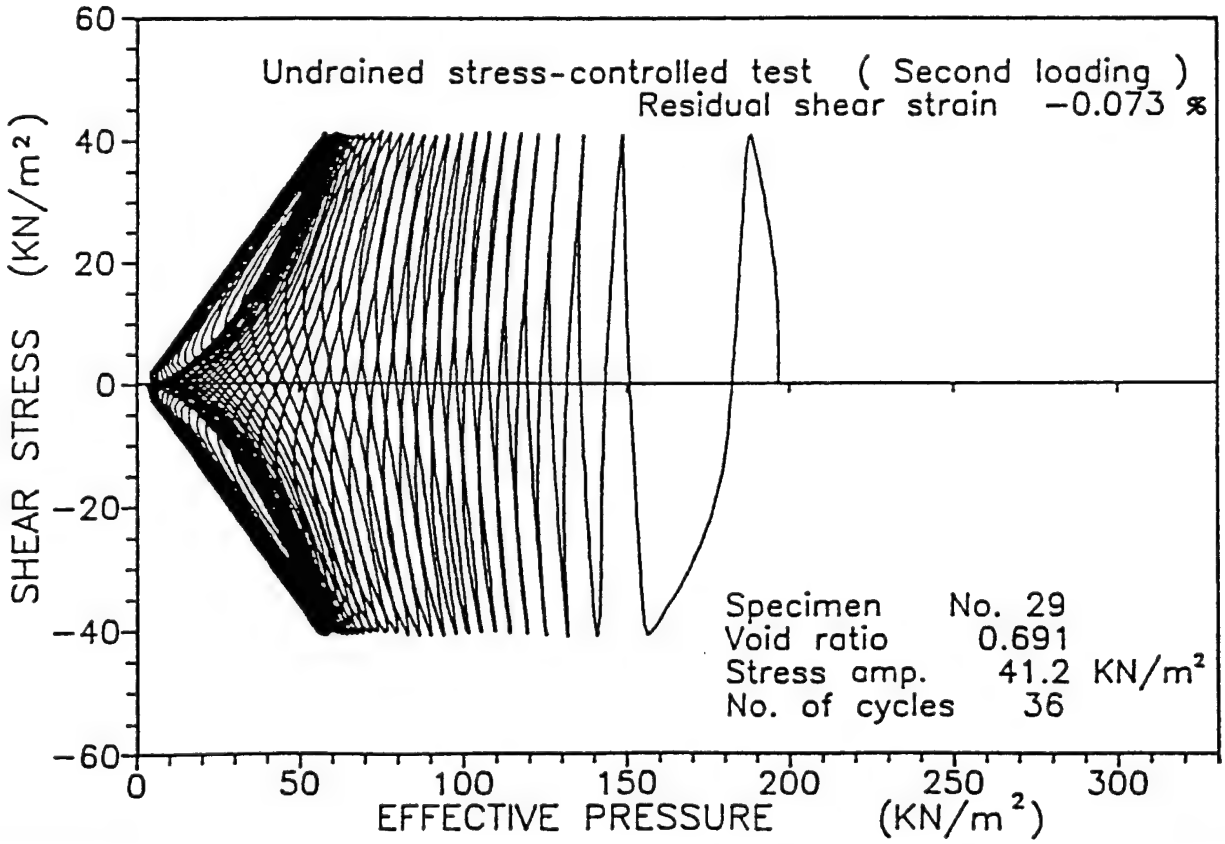

Figure 15. Relation between shear stress and effective pressure in second loading of dense specimen having a small residual shear strain

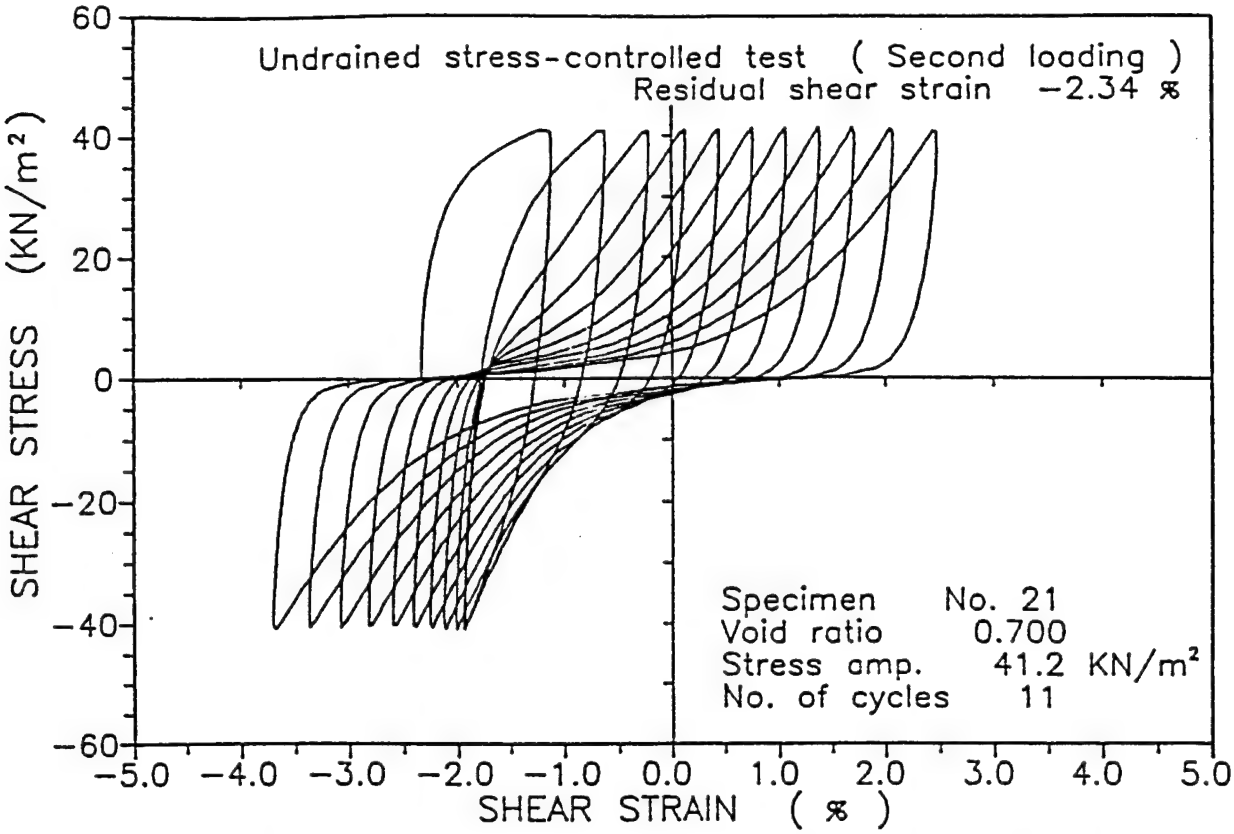

Figure 16. Relation between shear stress and shear strain in second loading of dense specimen having a large residual shear strain

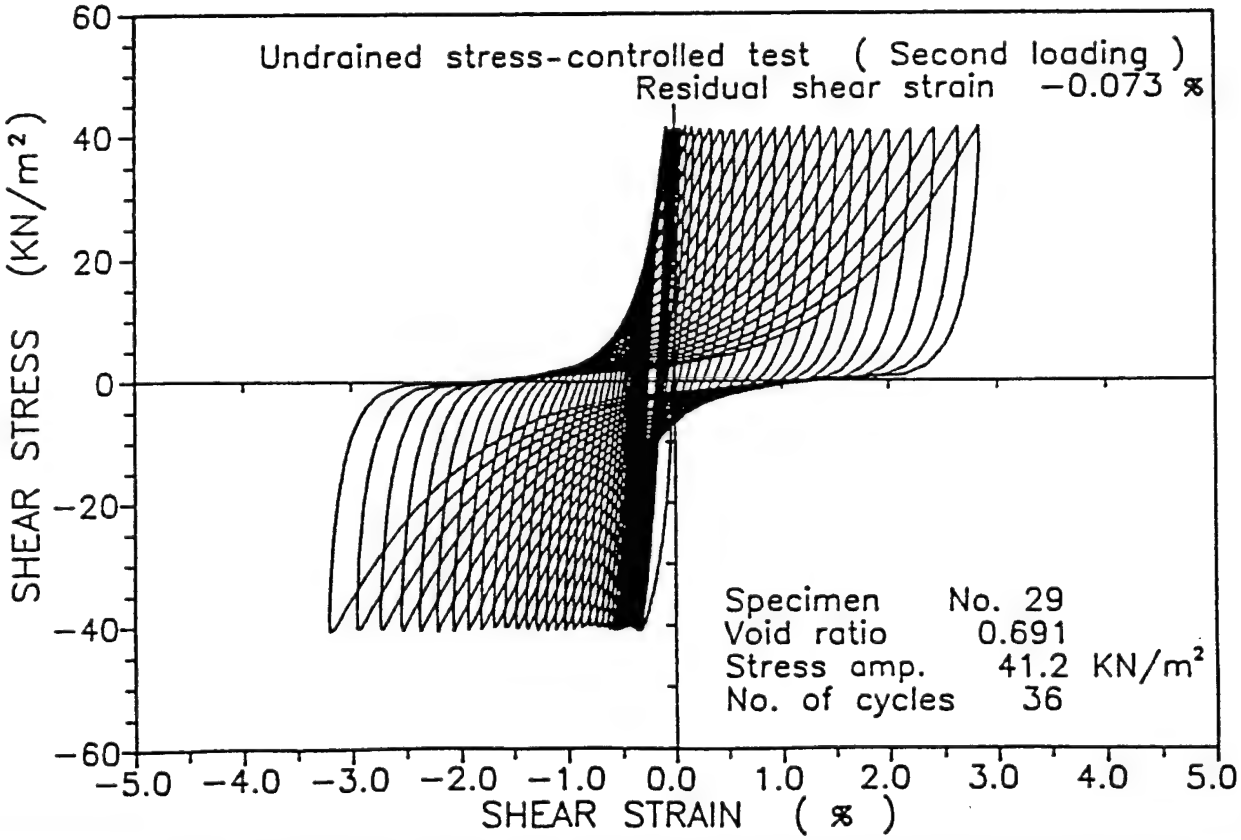

Figure 17. Relation between shear stress and shear strain in second loading of dense specimen having a small residual shear strain

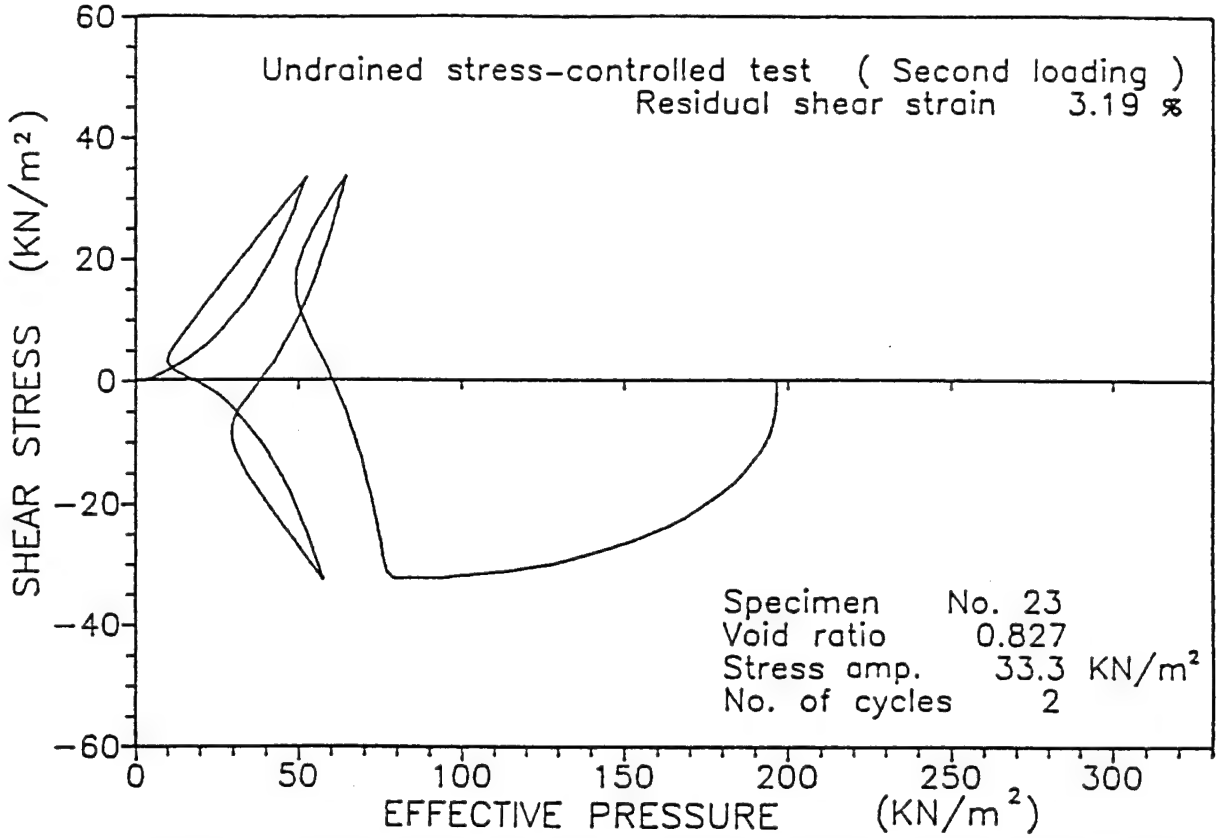

Figure 18. Relation between shear stress and effective pressure in second loading of loose specimen having a large residual shear strain

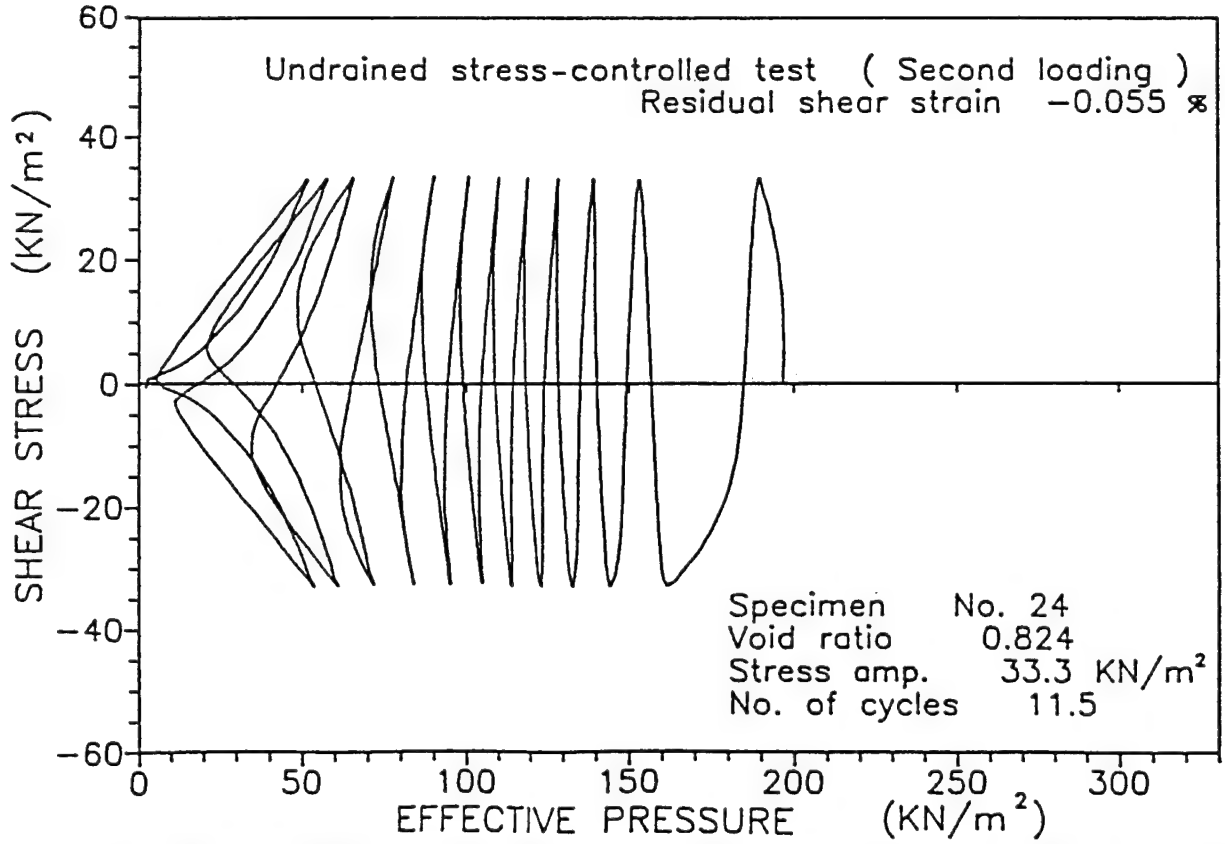

Figure 19. Relation between shear stress and effective pressure in second loading of loose specimen having a small residual shear strain

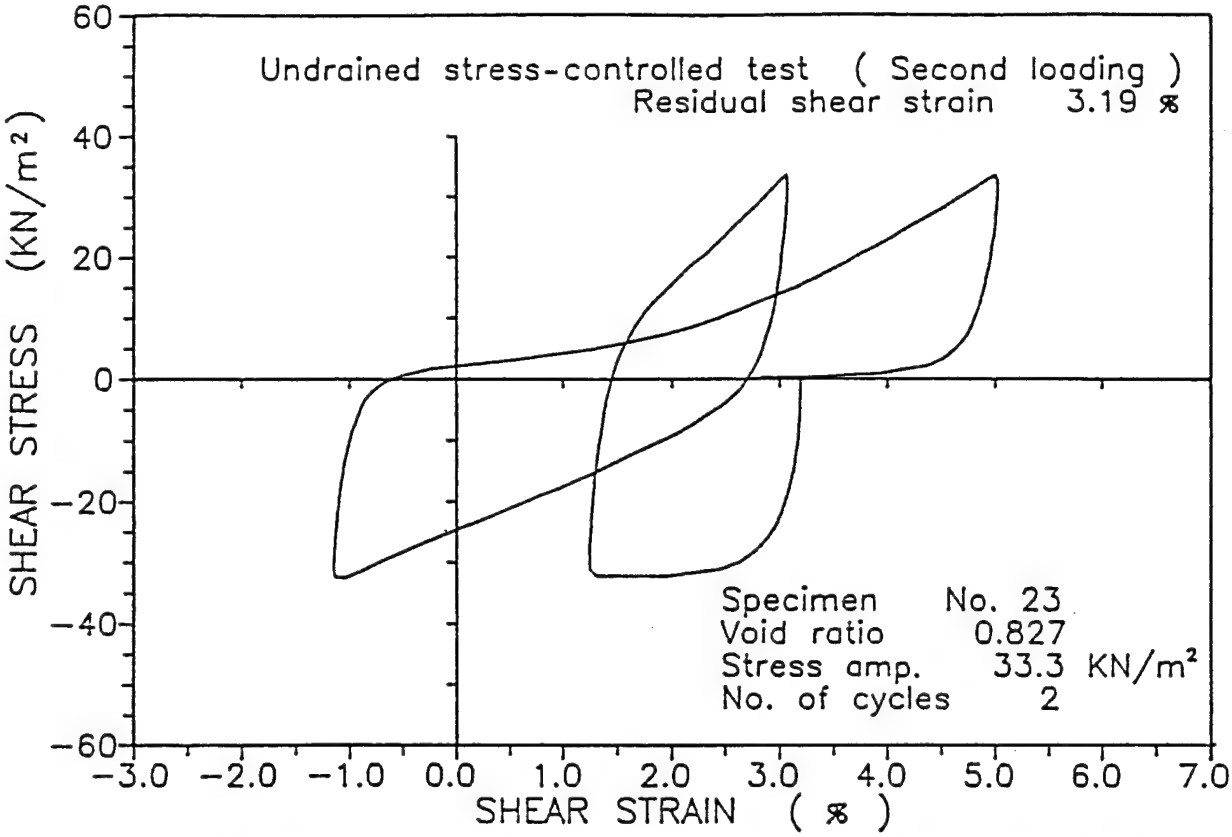

Figure 20. Relation between shear stress and shear strain in second loading of loose specimen having a large residual shear strain

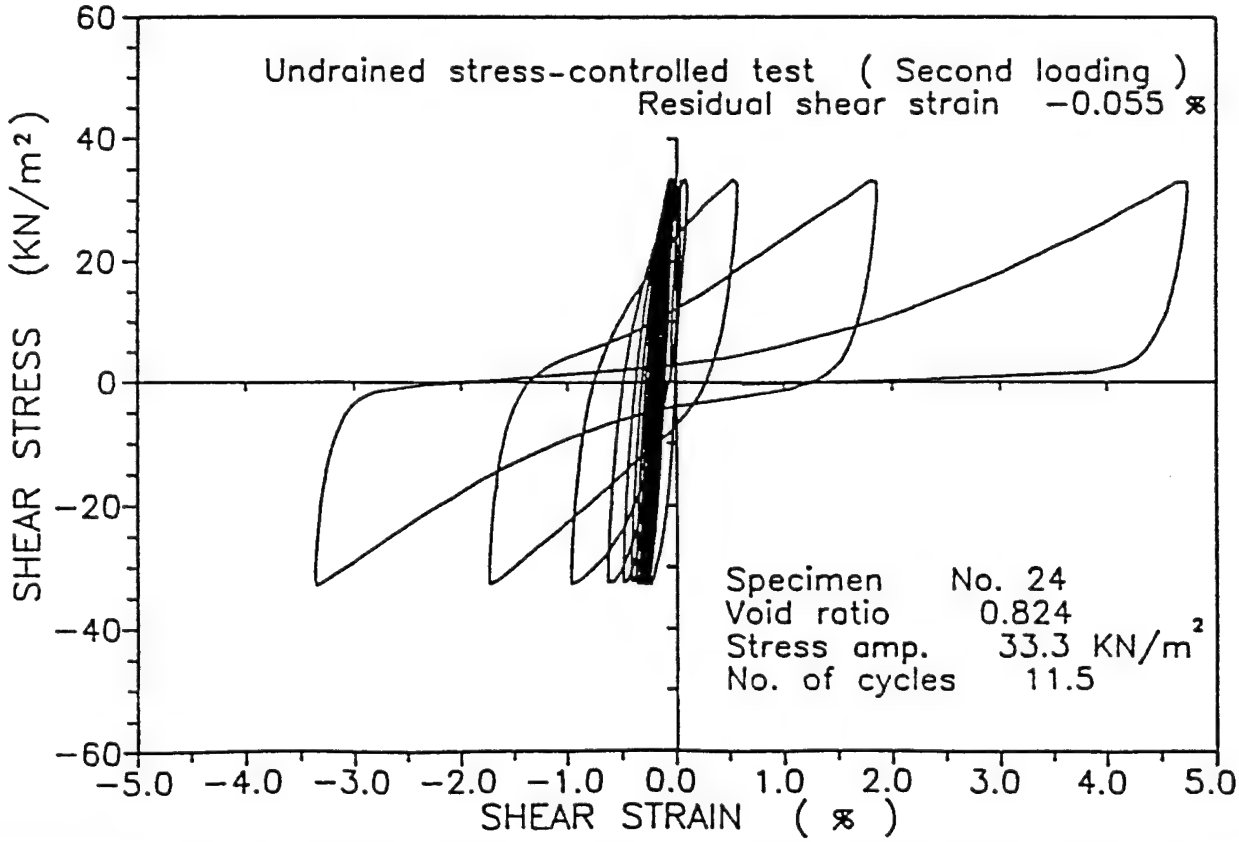

Figure 21. Relation between shear stress and shear strain in second loading of loose specimen having a small residual shear strain

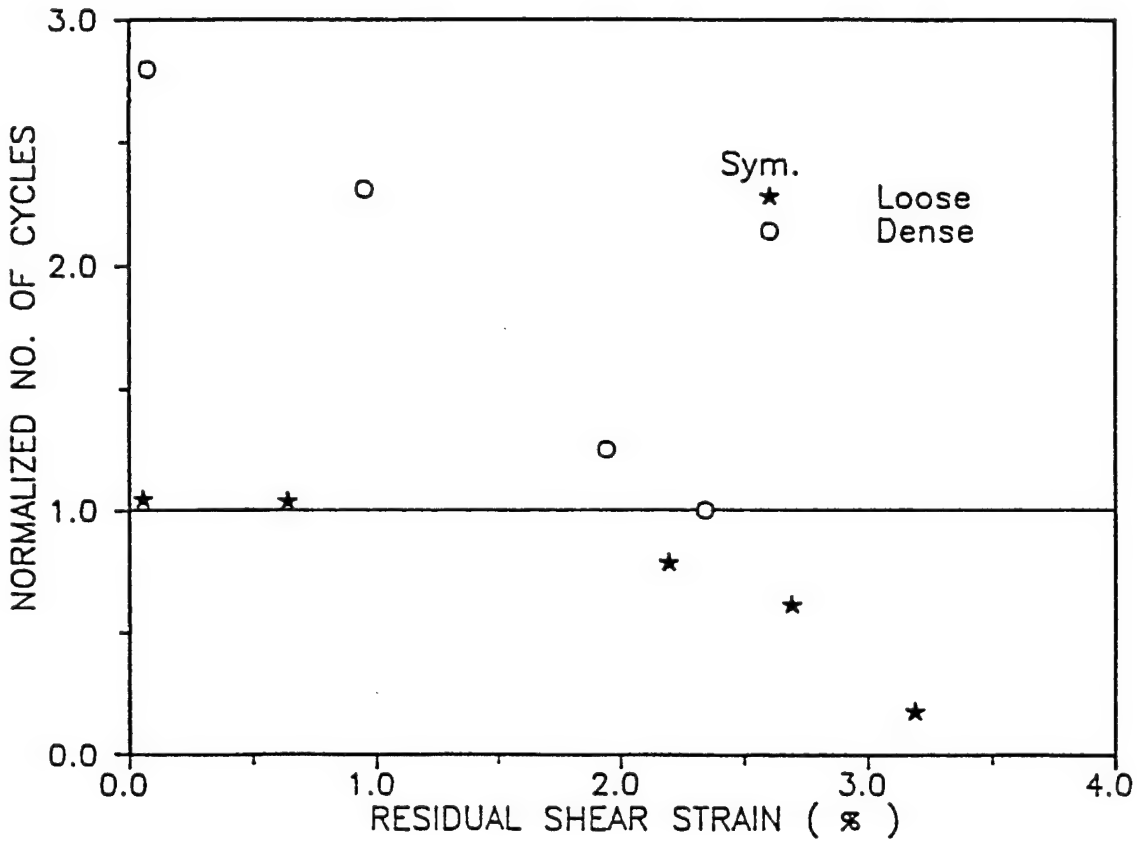

Figure 22. Relation between normalized number of cycles and residual shear strain for dense and loose specimens

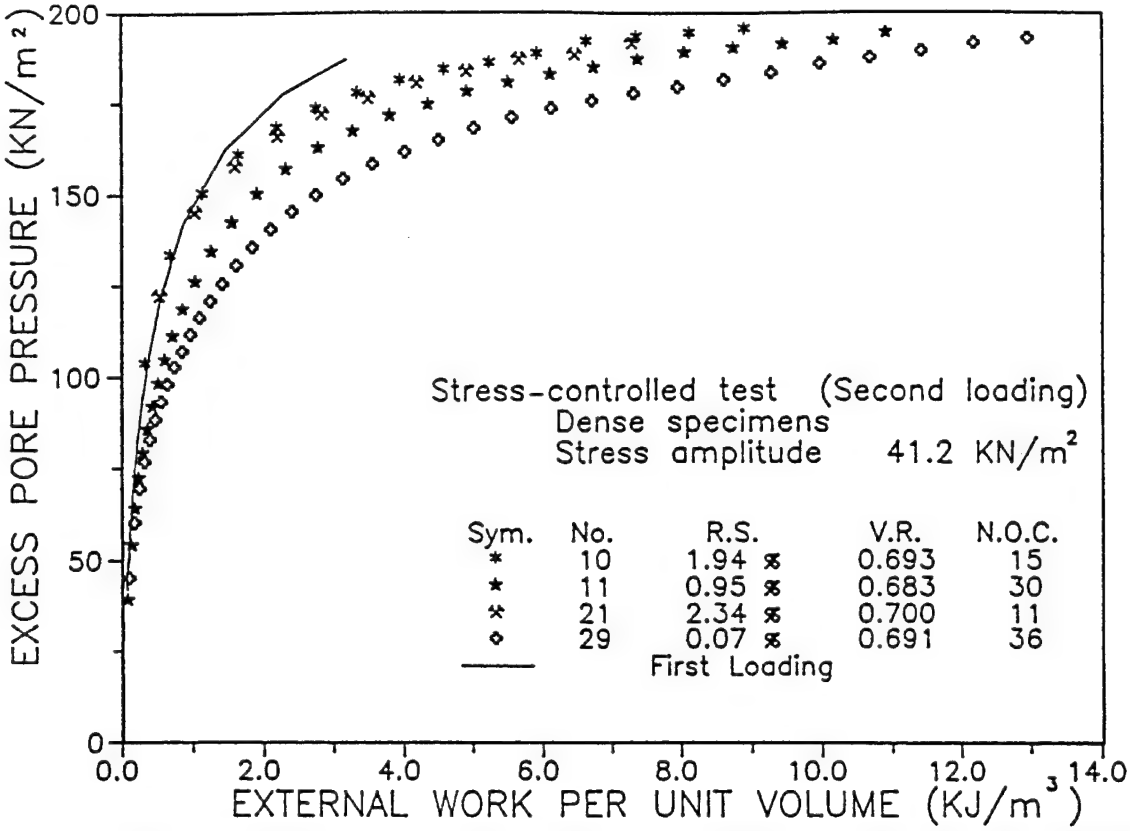

Figure 23. Relation between external work per unit volume and excess pore water pressure in second loading of dense specimens

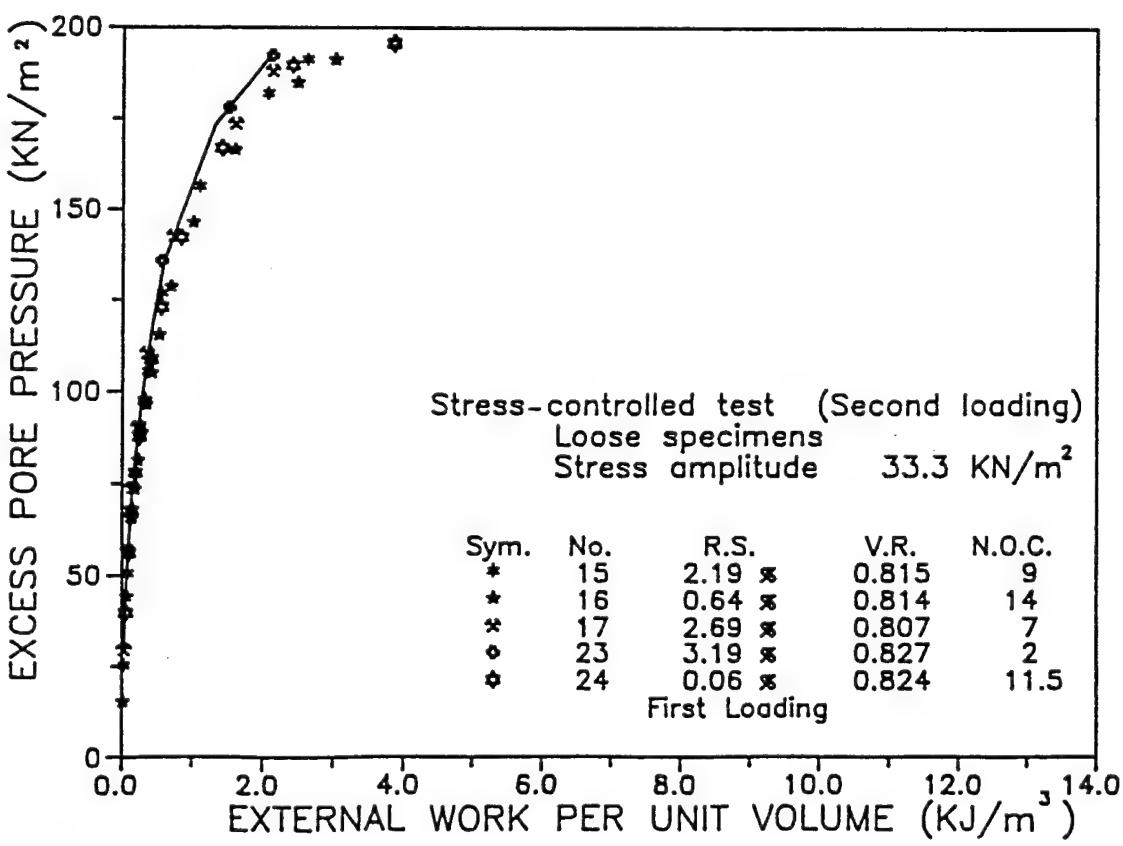

Figure 24. Relation between external work per unit volume and excess pore water pressure in second loading of loose specimens

APPENDIX V

FABRIC AND CHARACTERISTICS OF VOID SHAPE AND DISTRIBUTION IN GRANULAR MASSES

Principal Investigator: Sia Nemat-Nasser

Visiting Assistant Researcher: Zong-Lian. Qiu

ABSTRACT

The results of a series of experiments on photo-elastic rod-like granules undergoing simple shearing under constant confining pressure, are examined in order to identify the evolution of the shape, size, and orientation of voids within the granules. It is observed that the voids rotate towards, and elongate in the direction of the maximum principal compressive stress. The morphology of the voids is characterized by the void polygon and its distribution. Various related parameters are examined, together with their variations over three cycles of shearing.

V.1. INTRODUCTION

Following the work reported by Subhash *et al.* (1991) and using the same fixture and rod-like photo-elastic granules with oval cross sections, we have performed a series of simple cyclic shearing experiments under constant confining pressure, recording in addition to the overall stress-strain relation, the photo-elastic pictures of the granules at various states of deformation. Based on the results of these experiments, we have sought to identify the evolution of the microstructure in terms of the granular fabric, as well as the evolution of the morphology of the intergranular voids and their relation to the overall response of the granular mass. The potential significance of the evolution of the voids in granular masses which carry the applied loads through contact friction, has been pointed out by Oda, Nemat-Nasser, and Konishi (1985), in connection with the results of the biaxial deformation of the same photo-elastic granules that are used in our experiments. These authors observe that the voids tend to elongate parallel to the direction of

maximum axial compression. They introduce a second-order tensor to characterize the morphology of the voids. Using some of the same data, Konishi and Naruse (1988) further elaborate on the importance of the void morphology in characterizing the fabric of a granular mass. Introducing a second-order tensor which they call "local void tensor", these authors identify the direction of its maximum principal value with the direction of a void vector whose magnitude is the corresponding principal value. Through averaging, they then consider a "mean void tensor" as a fabric measure. All these results have been for monotonic loading.

It is experimentally observed that the response of a granular mass which has been subjected to a monotonic loading, changes drastically if the loading ceases and unloading commences. During the course of monotonic loading, extensive anisotropy is induced, as the particles roll and slide on each other in response to the external loads. This strong, induced anisotropy then affects the subsequent response, once unloading ensues. One of the objectives of the present investigation is to examine the microstructural changes which take place in such a sequence of loading and unloading, using three complete cycles of shearing.

V.2. APPARATUS AND EXPERIMENTAL PROCEDURE

The equipment and the experimental procedure have been described by Mehrabadi *et al.* (1988) and Subhash *et al.* (1991).

The granules are cylindrical rods of oval cross section. Three different sizes are used; see Table 1. These granules have been cast using photo-elastic sensitive polyurethane rubber material.

The testing equipment consists of a rigid outer frame, within which an inner frame can deform in simple shear under a constant confining pressure; see Fig. 1a. The granules are packed within the inner frame. On the inner frame, two horizontal and two vertical

bars which can be moved in parallel, are mounted. These are denoted by HB1, HB2, VB1, and VB2, respectively, in Fig. 1b. The confining.

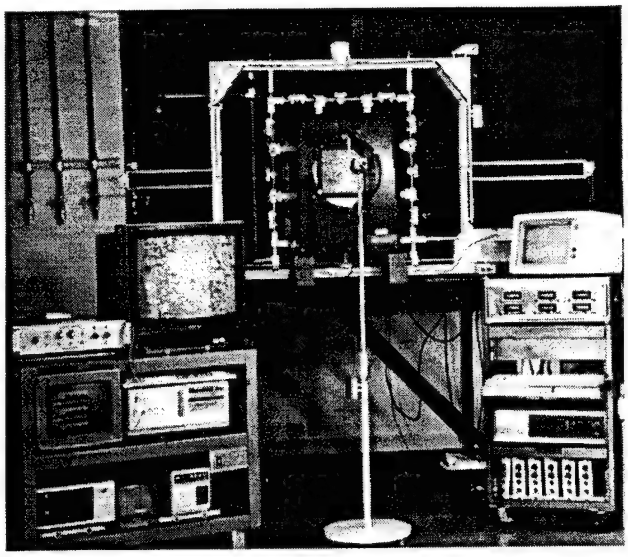

Fig. 1a. Experimental Setup

pressure is applied on the sample by means of weights p and a system of wheels. In order to balance the weights of the bars and the granules, the upper bar HB1 is lifted up by springs, and additional weights w are applied on HB1 and HB2.

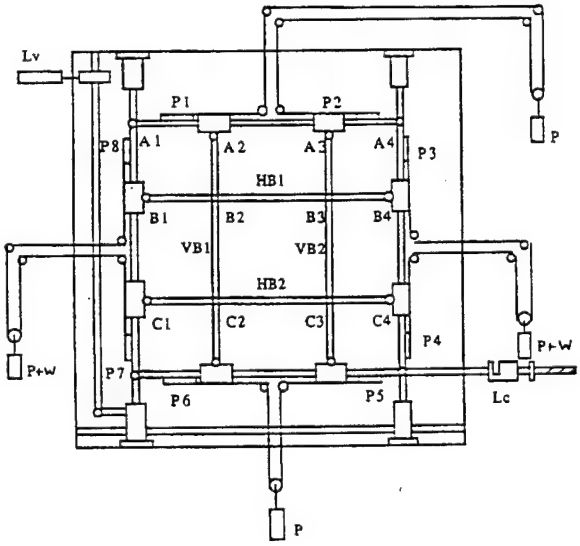

Fig. 1b. Schematic of Experimental Setup

To asses the influence of the friction of the apparatus on the measured forces, the friction test, in which the frictional resistance of the frame is measured over each cycle, is performed. The friction test is completed under the same conditions as for the actual test. A linear least-square approximation is fitted

through the data points obtained from the friction test, and these values are subtracted from the corresponding horizontal shear forces applied to the granules.

The granules are packed in the internal frame 20x20 cm^2 in a random fashion in size, direction, and position under a constant confining pressure, and then the horizontal shear force is applied to the granular mass by incremental horizontal displacements, and measured by a load cell, Lc. The horizontal and vertical movements of the bars are measured by the transducers P1 to P8. The shear strain is recorded by an LVDT, Lv.

The loading frame is placed in the field of a circular polariscope consisting of a monochromatic light source, a polarizer, two quarter-wave plates, and an analyzer. After the packing is complete, under a confining load, three cycles of shearing are performed. The shear stress, shear strain, and the volumetric strain are measured. At appropriate stages of deformation, photographs of the isochromatic fringe pattern are taken with a digital video camera and input in a computer for analysis.

Computer programs for processing the pictures and test data were developed. With these programs, one can measure the length and direction of the void polygon vectors and obtain their distribution density functions, and can plot the actual distribution density function and its second-order and fourth-order approximations.

Variations of the stress ratio, and the volumetric strain with the shear strain are computed from the recorded data. The actual, second-order, and fourth-order distribution density functions of the void polygon vector, weighted by their length, are computed and drawn from the recorded data and the photographs. The relation of the distribution density function to the overall deformation and loading measures is examined, so is the relation of a measure of the anisotropy of the distribution density function to the test stage. To avoid the effect of the boundaries, a sample from the middle part of the granular mass is used for analysis.

V.3. SOME THEORETICAL OBSERVATIONS

A granular mass consists of two phases: the particles and the associated voids. The solid particles transmit internal forces through contact friction at contact points, to support the externally applied loads. The evolution of the voids is important in characterizing the overall response in granular masses. The shape, size, and direction of the voids are changed in the course of deformation. The

evolution of the morphology of the voids can be represented by different parameters such as the void ratio (or porosity) and by certain tensorial quantities associated with the voids. The void ratio is scalar. It cannot represent the characteristics of the shape and the direction of the voids. The change of the shape and direction of the voids in granular masses is obviously an important factor, as has been observed in simple shear experiments. The voids elongate, and the direction of elongated voids changes with the direction of the principal compressive stress. These quantities are distributed randomly, while the shear stress is zero, Fig. 2a.

Fig. 2a. Distribution of Voids for $\tau=0$

When the shear stress is increased, as a consequence the direction of the principal compressive stress changes. The orientation of a large number of voids are changed, as they tend to point towards the direction of the maximum principal compressive stress, as can be seen from Fig. 2b.

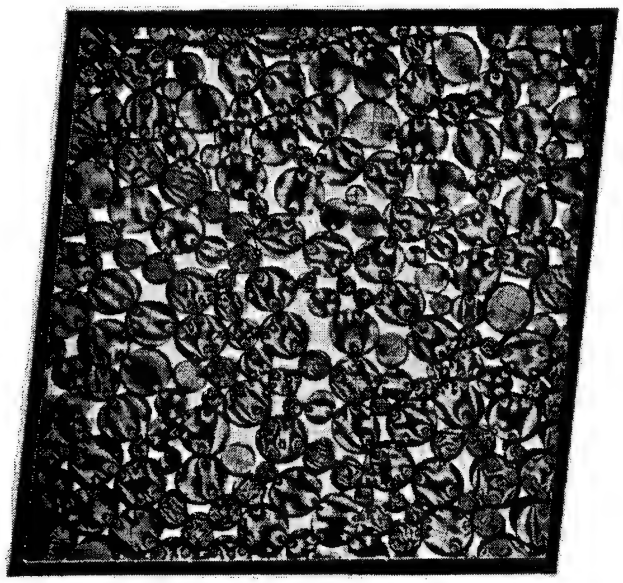

Fig. 2b. Distribution of Voids for σ_{min} at 135°

Vectorial and the tensorial quantities are required in characterizing the shape and direction of the voids in granular masses. Several measures have been introduced by Oda, Nemat-Nasser, Konishi (1985), and others, as will be discussed in the sequel.

3.1 Scanning Lines

To characterize the relation of the solid and the void, we may use a scanning line defined by its unit vector **q**; (Fig. 3); Oda, Nemat-Nasser, Konishi (1985). This line passes through both solid

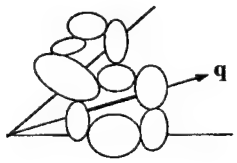

Fig. 3. Scanning Line and Void

particles and voids. Let $\overline{\ell}(\mathbf{q})$ be the mean path length through the voids. This mean path length, in general, depends on the orientation of the unit vector **q**. A dimensionless measure, $\ell(\mathbf{q})$, is introduced as follows:

$$\ell(\mathbf{q}) = \frac{1}{L}\bar{\ell}(\mathbf{q}), \tag{1}$$

where

$$L = \int_{\Omega} \bar{\ell}(\mathbf{q}) \cdot d\Omega$$

and, because of the definition of $\ell(\mathbf{q})$, we have

$$\int_{\Omega} \ell(\mathbf{q}) \cdot d\Omega = 1, \tag{2}$$

where Ω is a unit sphere. The distribution density function of the mean path length through the voids can be expressed as,

$$\ell(\mathbf{q}) = \frac{1}{4\pi} V_{ij}\, q_i\, q_j\,, \tag{3}$$

where

$$V_{ij} = \frac{15}{2}\left[\frac{1}{L}\sum_{k=1}^{m} \bar{\ell}^{k} q_i^k q_j^k - \frac{1}{5}\delta_{ij}\right]$$

for three dimensions, and

$$\ell(\mathbf{q}) = \frac{1}{2\pi} V_{ij}\, q_i\, q_j\,, \tag{4}$$

with

$$V_{ij} = 4\left[\frac{1}{L}\sum_{k=1}^{m} \bar{\ell}^{k} q_i^k q_j^k - \frac{1}{4}\delta_{ij}\right]$$

for two dimensions. Here, the summation is taken over all scanning lines. Expressions (3) and (4) are the second-order approximations of the experimental data. In our work, we consider (3) for our two-dimensional experiments.

V.3.2 Local Void Tensor

Imagine a void surrounded by several contacting particles. For two-dimensional cases (rod-like granules), the boundary of the void consists of several curved segments linked at contact points of the associated particles. To characterize

the size, shape, and direction of this void, the curved segments are replaced by vectors $\mathbf{v}^\ell$, connecting the contact points; Fig. 4. The polygon formed by the vectors $\mathbf{v}^\ell$'s will be called the void polygon and each vector $\mathbf{v}^\ell$ of this polygon will be called the void-polygon vector. We calculate the sum of the *tensor* product $\mathbf{v}^\ell * \mathbf{v}^\ell$ to define

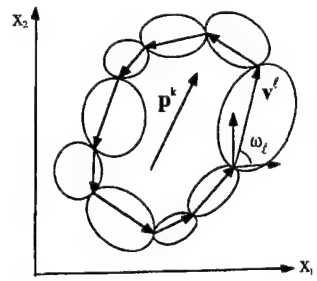

Fig. 4. Local Void Vector and Void-Polygon Vectors

$$P_{ij}^k \equiv \sum_{\ell=1}^{n} v_i^\ell \, v_j^\ell, \tag{5}$$

where n is the number of the associated vectors which form the polygon k. This tensor is called a "local void tensor" by Konishi and Naruse (1988). Its principal values are

$$p_1^k, p_2^k = \frac{1}{2}\sum_{\ell=1}^{n}(d^\ell)^2 \pm \frac{1}{2}\sqrt{\left[\sum_{\ell=1}^{n}(d^\ell)^2 \cos 2\omega_\ell\right]^2 + \left[\sum_{\ell=1}^{n}(d^\ell)^2 \sin 2\omega_\ell\right]^2} \tag{6}$$

where $d^\ell = |\mathbf{v}^\ell|$, and ω_ℓ is the angle of vector $\mathbf{v}^\ell$ with the x_1-axis. The difference of the principal values is denoted by D^k,

$$D^k = p_1^k - p_2^k \tag{7}$$

The major principal direction is

$$\zeta^k = \frac{1}{2}\arctan\left\{\left[\sum_{\ell=1}^{n}(d^\ell)^2 \sin 2\omega_\ell\right] \Big/ \left[\sum_{\ell=1}^{n}(d^\ell)^2 \cos 2\omega_\ell\right]\right\} \tag{8}$$

The size and direction of a local void k are characterized by a local void vector $\mathbf{p}^k$ for which the magnitude is D^k and the direction is ζ^k.

A void system consisting of a number of local voids can be characterized by a mean void tensor, M_{ij}, in the following form:

$$M_{ij} = \frac{1}{N} \frac{1}{\sum_{k=1}^{N} D^k} \sum_{k=1}^{N} D^k \, n_i^k \, n_j^k, \tag{9}$$

where N is the number of local voids and $\mathbf{n}^k$ is a unit vector along $\mathbf{p}^k$.

V.3.3 Distribution of Void-Polygon Vectors

Consider now a direct characterization of the distribution of the void-polygon vectors, $\mathbf{v}^\ell$, shown in Fig. 4. Let $W(\mathbf{n})$ be the distribution density function of the orientation of the void- polygon vectors, $\mathbf{v}^\ell$, weighted by their lengths, as shown in Fig. 5. Assume that $W(\mathbf{n})$ is symmetric:

$$W(\mathbf{n}) = W(-\mathbf{n}). \tag{10}$$

It satisfies

$$\int_{\Omega} W(\mathbf{n}) \cdot d\Omega = 1. \tag{11}$$

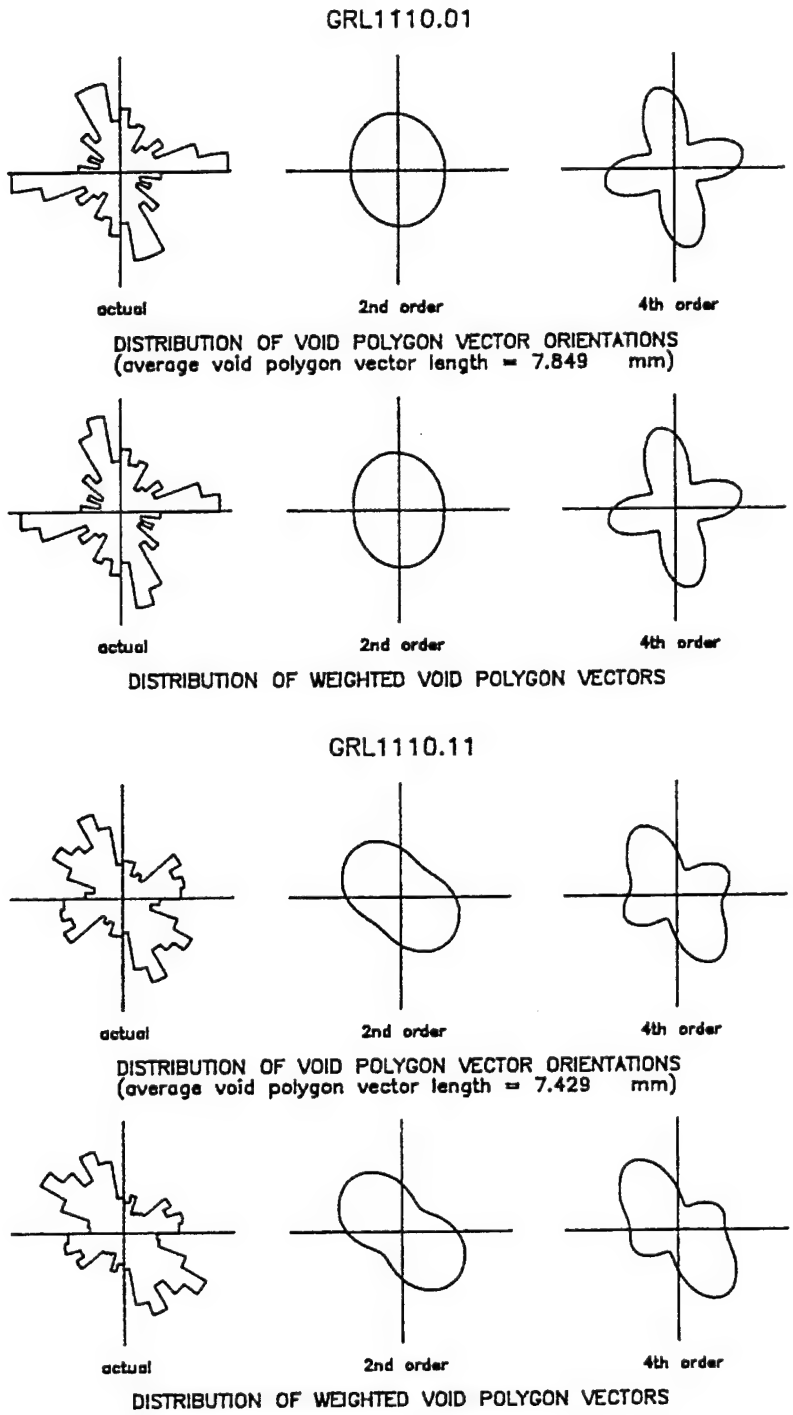

Fig. 5. Distribution of Void Polygon Vectors

Then W(**n**) may be represented by

$$W(\mathbf{n}) = \frac{1}{2\pi} \left[1 + J_{ij}\, n_i n_j + J_{ijkl}\, n_i n_j n_k n_l + \cdots \right], \qquad (12)$$

Here, Jij and Jijkl are deviators, given by

$$J_{ij} = 4 \left[< n_i n_j > - \frac{1}{2} \delta_{ij} \right], \qquad (13)$$

and

$$J_{ijkl} = 16 \left[< n_i n_j n_k n_l > - \delta_{(ij} < n_k n_l) > + \frac{1}{8} \delta_{(ij} \delta_{kl)} \right], \qquad (14)$$

where the angular brackets denote averages taken over all orientations. Jij and Jijkl are symmetric and traceless.

The distribution density function W(**n**) characterizes the void system; see Fig. 5. When weighted by the lengths of the void-polygon vectors, it becomes a better representation than the unweighted one. In the plane problem, if all voids are like a series of small cracks with a common direction, the distribution density function becomes a delta function. If all voids are circular holes, the distribution density function is a circle. If all voids are small quadrangles of a common direction, the distribution density function becomes two $\frac{1}{2}$ delta functions at orthogonal directions in the **n**-space.

Generally, the void system in granular masses and its distribution density function are anisotropic. This anisotropy is represented by the orientation of the major axis of the distribution density function. It indicates the direction of the void system in an average sense. In addition to this, we also consider another measure called the anisotropy ratio, which is the ratio of the maximum value to the average value of the distribution density function. This anisotropy ratio characterizes the shape of the voids. The larger the anisotropy ratio the more elongated are the voids. The anisotropy ratio is always greater than or equal to 1. When the anisotropy ratio equals 1, the distribution density function is a circle.

V.4. RESULTS AND DISCUSSION

Several different kinds of three-cycle simple shear tests have been investigated. Parameters of the tests are listed in Table 2. There are two kinds of packing, dense and loose, with different void ratios; for example, the void ratio e_0=18.07% is dense and the void ratio e_0=23.24% is loose. Talcum powder lubricant is applied to the cylindrical rod-like photo-elastic granules to decrease their frictional resistance. The intergranular friction angle is 52 degrees for non-lubricated, and 26 degrees for lubricated granules.

For test GRL1110, Fig. 6 shows the three cycles of shearing. Plastic flow takes place from stages 3 to 11 in first cycle, and hardening occurs over the same strain range in the second and third cycles, as a result of the change of the arrangement of particles in the course of deformation, leading to an increased stability in particle positions. The shear strain vs. the stress ratio response in three other tests, GRL1110, GRD1108, and GRD1003, are similar to that of Fig. 6.

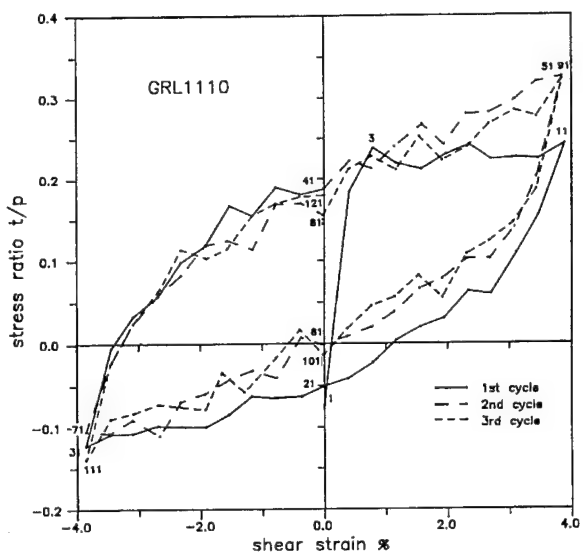

Fig. 6. Stress Ratio vs. Shear Strain for Test GRL1110

The volumetric strain and the shear strain in three cycles, for test GRL1110 (Fig. 7 a,b) shows that the volumetric strain decreases first during increased shear straining, but, then , it increases, as the

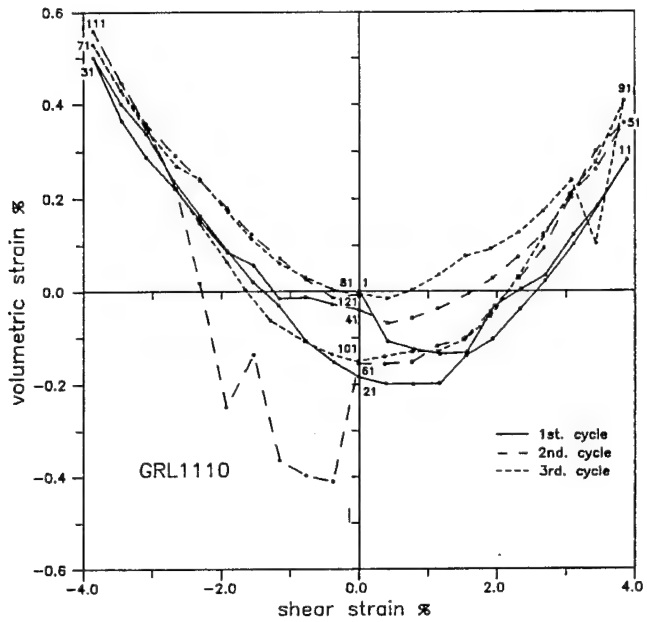

Fig. 7a. Volumetric Strain vs. Shear Strain for Test GRL1110

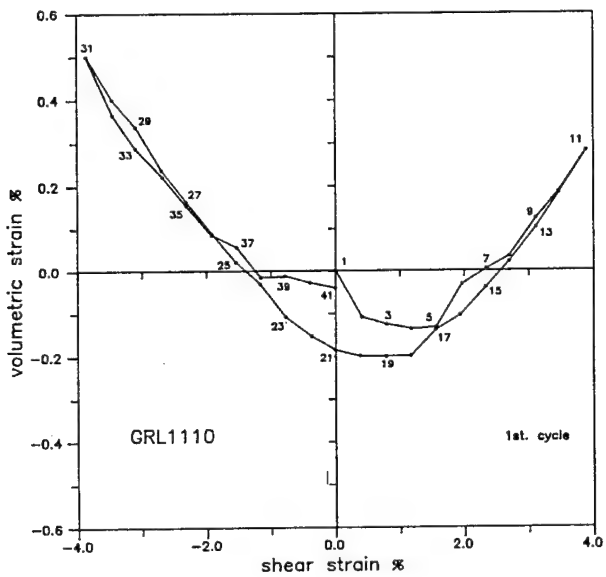

Fig. 7b. Volumetric Strain vs. Shear Strain for Test GRL1110

shear straining is continued. This dilatancy is a special behavior of frictional granular masses. At large shear strains, the volumetric strain is often dilatant. The variation of the volumetric strain is similar in all three cycles. Curves of the volumetric strain of test GRD1108 (Fig. 7c) are similar to curves of test GRL1110, although granules of test GRD1108 are packed densely. In both tests, the friction angle is 26 degrees and the granules are lubricated. Curves of the volumetric strain

and the shear strain for test GRD1003 (Fig. 7d) show that the variation of the volumetric strain is similar to test GRL1110. In test GRD1003 the volumetric strain is essentially negative, and in test GRL1110 and GRD1108 it is positive. This is due to the confining pressure and the fact that the friction in test GRD1003 is much greater than that in tests GRL1110 and GRD1108.

The actual, and the second- and fourth-order represrntation of the distributions density function of the orientation of the void- polygon vectors, weighted by their lengths, are shown at the test stages marked by numbers in Fig. 5. The orientation of the major axis of the distribution density function changes as the sample of the granules deforms. Its value at stage 1 for test GRL1110, in which the shear strain is zero, represents the original distribution and the original orientation which depend on the packing condition. The distribution density function of the stage 11 for test GRL1110, in which the shear stress and strain are maximum, has an orientation of about 135 degrees relative to the direction of the principal compressive stress. This distribution density function is long and narrow, showing that the voids are rotated and elongated in an average sense. These results show that the characteristics of the distribution density function of the void-polygon vectors are in good accord with the morphology of the void system in these experiments.

The variation of the orientation angle of the distribution density function of the void-polygon vectors with the test stage, for test GRL1110 (Fig. 8), under cyclic loading shows that this orientation

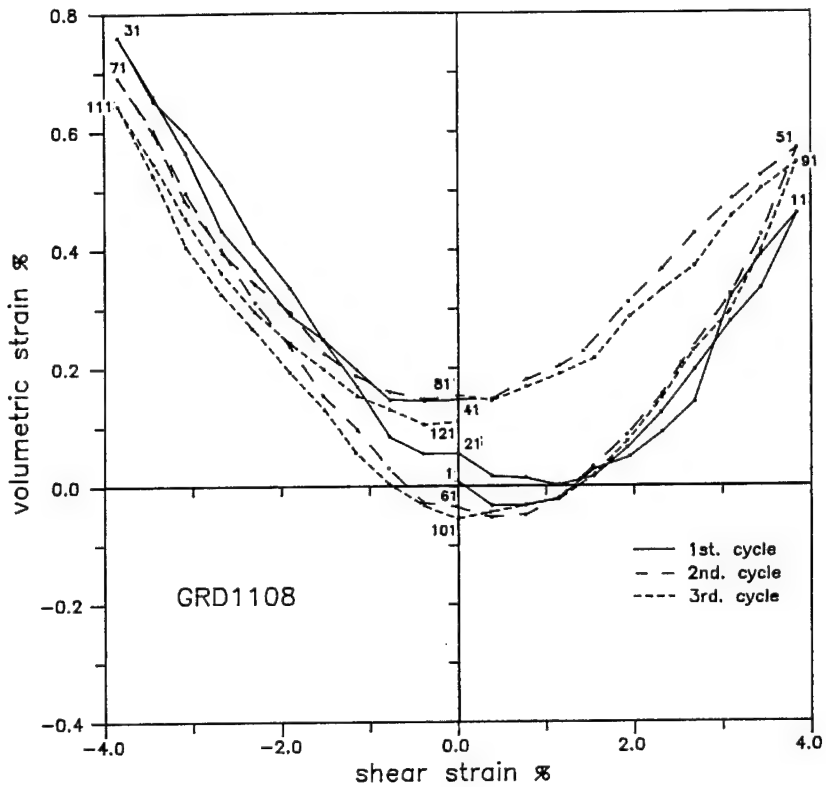

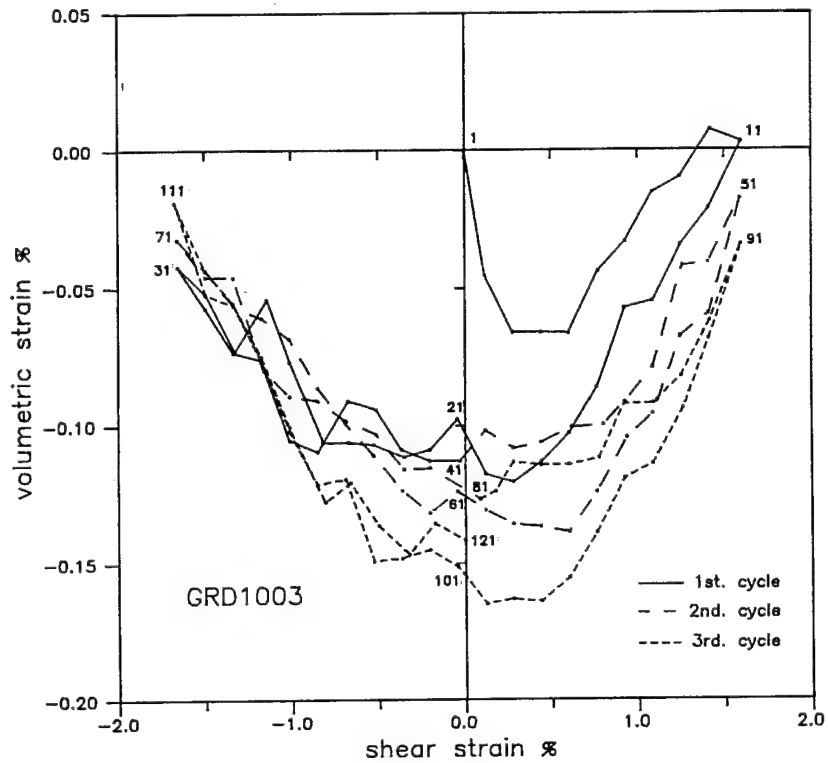

Fig. 7c,d. Volumetric Strain vs. Shear Strain for Tests GRD1008,1003

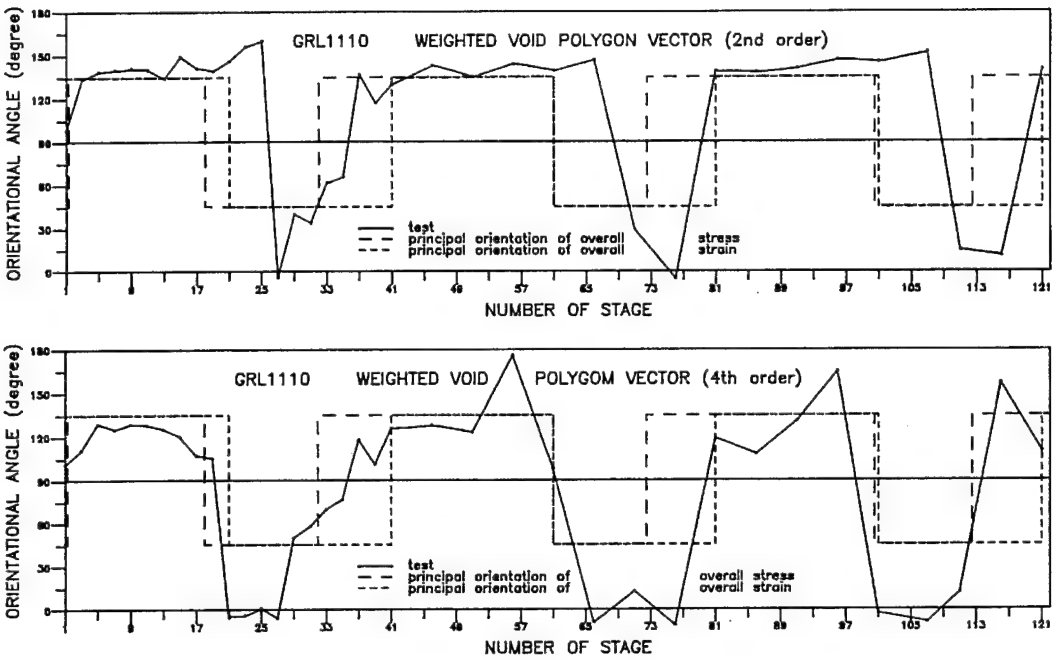

Fig.8. Variation of Orientation for Test GRL1110

follows the direction of the principal compressive stress; in Figs. 8 to 11, the horizontal axes, denoted by "NUMBER OF STAGES" refer to the test stages marked by the corresponding numbers on the associated stress-strain curves. The rotation of the orientation of the fourth-order representation of the distribution density function is nearly the same as the direction of the principal compressive stress. Results of test GRD1108 (Fig. 9) are similar to the results of test

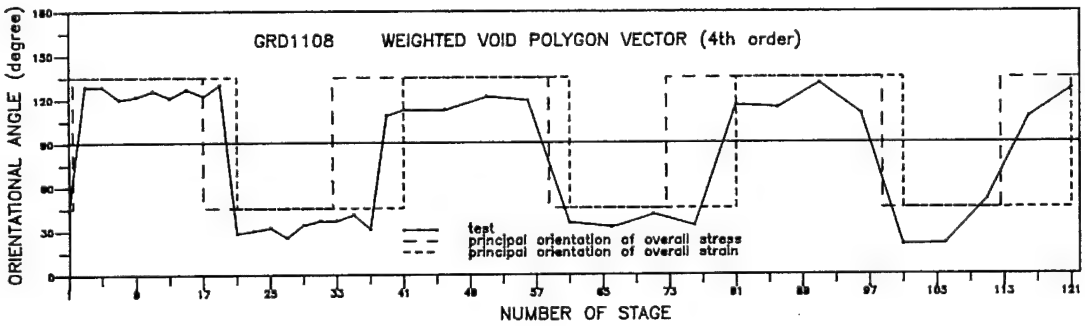

Fig.9. Variation of Orientations for Test GRD1108

GRL1110, although the packing of the granules is dense in test GRD1108. It is clear that the rotation of the orientation of the distribution density function of the void-polygon vectors is induced by, and approaches that of the direction of the principal compressive stress.

The variation of the orientation angle of the distribution density function of the void-polygon vectors with loading stages denoted by "NUMBER OF STAGES", for test GRD1003 (Fig. 10), under cyclic loading shows that the rotation of the distribution

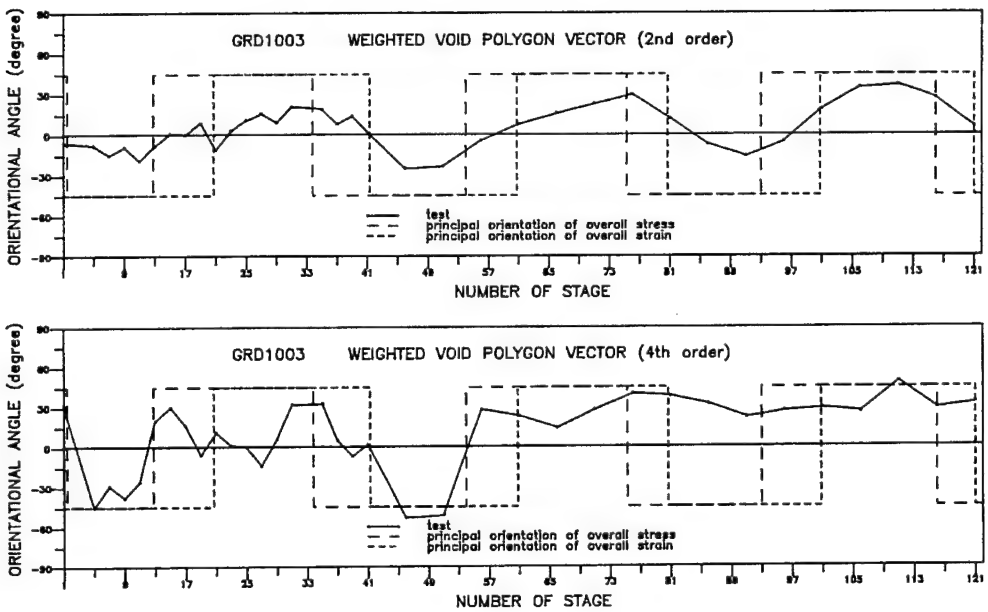

Fig.10. Variation of Orientations for Test GRD1003

density function waves around zero degrees and follows the direction of the principal compressive stress gradually, from the first cycle to the third cycle for second-order distribution, and that the rotation of the orientation of the distribution density function of the void-polygon vectors waves around zero degrees and as in the first cycle, it remains a constant at about 30 degrees in the second and third cycle for fourth-order distribution. This shows that the rotation of the direction of the voids for test GRD1003 is limited due to the presence of a large friction among the granules.

The variation of the anisotropy ratio of the distribution density function of the void-polygon vectors with the NUMBER OF STAGE, under cyclic loading (Fig. 11) show that the peak of the

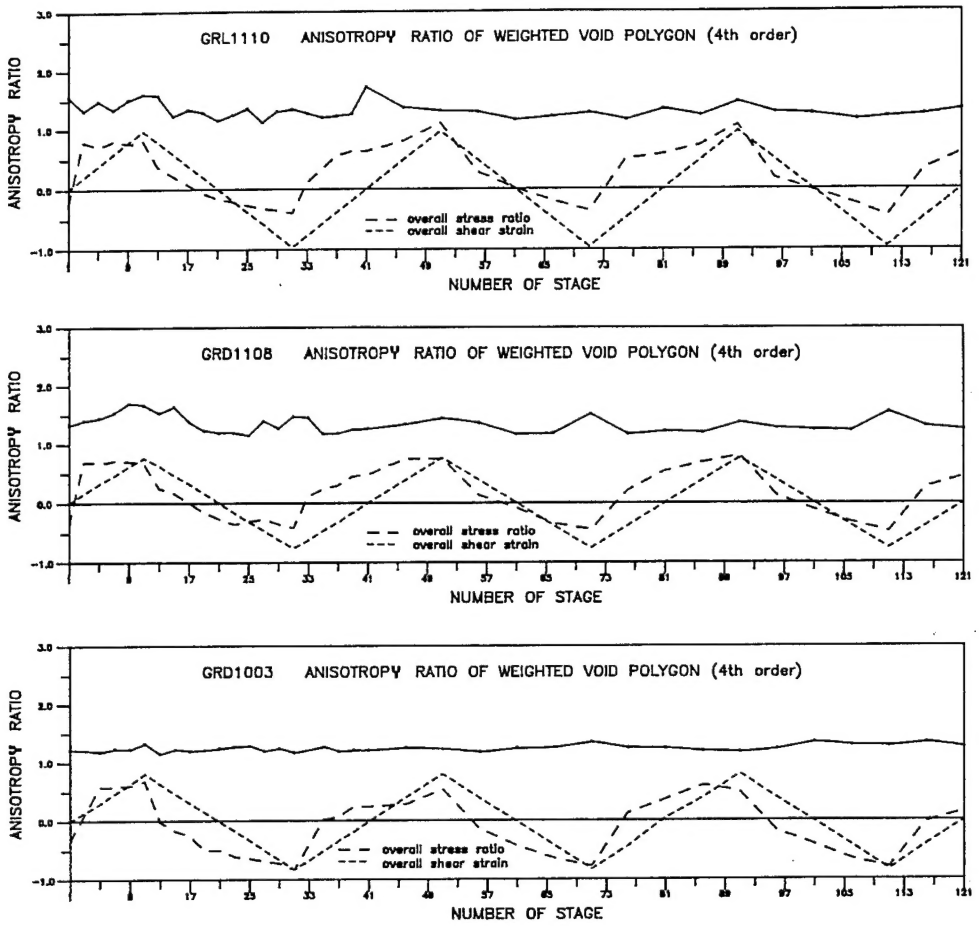

Fig.11. Variation of Anisotropy Ratios

anisotropy coincides with the peak of the stress ratio. The figures of the anisotropy ratio of the distribution density function of the void-polygon vectors of test GRL1110 and GRD1108 are similar. The anisotropy ratio for test GRD1003 changes only slightly. The anisotropy ratio of test GRD1003 is less than in tests GRL1110 and GRD1108, because the friction in test GRD1003 is larger than that in tests GRL1110 and GRD1108. It is clear that the voids in tests GRL1110 and GRD1108 are elongated more than those in test GRD1003.

V.5. CONCLUSIONS

(1) The distribution of the void-polygon vectors closely relate to the morphology of the voids in granular masses, and can be used for their statistical representation.

(2) The orientation of the distribution density function of the void-polygon vectors closely follows the direction of the principal compressive stress for small intergranular friction. The direction of the void is parallel to the direction of the principal compressive stress in a statistical average sense. The rotation of the orientation of the distribution density function of the void-polygon vectors is limited for large intergranular friction. The effect of friction is greater than the effect of packing of the granular mass during rotation of the direction of the voids.

(3) The peak of the anisotropy ratio of the distribution density function of the void polygon vector appears at the peak of the principal compressive stress, and the shape of the voids in granular masses is elongates in the direction of the maximum principal compressive stress in the course of deformation. The greater the principal compressive stress, the more elongated the voids.

(4) The variation of the orientation and the anisotropy ratio of the distribution density function of the void-polygon vectors are similar and stable in each cycle, under cyclic loading.

V.6. ACKNOWLEDGMENT

This work has been supported by Air Force Office of Scientific Research under Grant No. F49620-92-J-0117 to the University of California, San Diego. The authors wish to express their gratitude to Dr. M. Beizai and Mr. Jon B. Issacs for their kind advice.

V.7. REFERENCES

Christoffersen, J., M. M. Mehrabadi and S. Nemat-Nasser, "A Micromechanical Description of Granular Material Behavior," Journal of Applied Mechanics, 48 (1981) 339-344.

Kanatani, K., "Distribution of Directional Data and Fabric Tensors," Int'l. Journal of Engineering Science, 22 (1984) 149-164.

Konishi, J., M. Oda and S. Nemat-Nasser, "Induced Anisotropy in Assemblies of Oval Cross-Sectional Rods in Biaxial Compression," in: J.T.Jenkins and M. Satake, eds.,Mechanics of Granular Materials: New Models and Constitutive Relations, (1983) 31-39.

Konishi, J. and F. Naruse, "A Note on Fabric in Terms of Voids," Micromechanics of Granular Materials, edited by M. Satake and J.T. Jenkins, Elsevier Science Publishers B.V., Amsterdam, (1988) 39-46.

Mehrabadi, M. M. and S. Nemat-Nasser, "Stress, Dilatancy and Fabric in Granular Materials," Mechanics of Materials, 2 (1983) 155-161.

Mehrabadi, M. M., S. Nemat-Nasser, H. M. Shodja and G. Subhash, "Some Basic Theoretical and Experimental Results on Micromechanics of Granular Flow," Proc. U.S.- Japan Seminar on the Mechanics of Granular Materials, (1988) 253-262.

Nemat-Nasser, S. and M. M. Mehrabadi, "Stress and Fabric in Granular Masses," Proc. U.S.-Japan Seminar in the Mechanics of Granular Materials, (1983) 1-8.

Nemat-Nasser, S. and M. M. Mehrabadi, "Micromechanically Based Rate Constitutive Descriptions for Granular Materials," Proc. Int'l. Conf. on constitutive Laws for Engineering Materials: Theory and Application, Tucson, AZ, Wiley, New York (1983).

Nemat-Nasser, S., "Anisotropy in Response and Failure Modes of Granular Materials," in: J. P. Boehler, ed. Yielding, Damage and Failure of Anisotropy Elastic Solids, (EGF5), Mechanical Engineering Publications, London (1989).

Oda, M., S. Nemat-Nasser and M. M. Mehrabadi, "A Statical Study of Fabric in a Random Assembly of Spherical Granules," Int'l Journal for Numerical and Analytical Methods in Geomechanics, 6 (1982) 77-94.

Oda, M., S. Nemat-Nasser and J. Konishi, "Stress-Induced Anisotropy in Granular Masses," Soil and Foundations, 25 (1985) 85-97.

Satake, M., "A Discrete-Mechanical Approach to Granular Materials," Int. J. Engng Sci. 30 (1992) 1525-1533.

Satake, M., "New Formulation of Graph-Theoretical approach in the Mechanics of Granular Materials," Mechanics of Materials 16 (1993) 65-72.

Subhash, G., S. Nemat-Nasser, M. M. Mehrabadi and H. M.Shodja, "Experimental Investigation of Fabric-Stress Relations in Granular Materials," Mechanics of Materials, 11 (1991) 87-106.

Turner, C. H. and S. C. Cowin, "Dependence of Elastic Constants of an Anisotropic Porous Material upon Porosity and Fabric," Journal of Materials Science, 22 (1987) 3178-3184.

V. 8. TABLES

Table 1. **SIZE OF PARTICLES (Oval I)**

Size	D (mm)	d (mm)	D/d
Large	14.97	13.23	1.13
Medium	9.64	8.96	1.08
Small	6.34	6.07	1.04

Table 2. **SHEAR TEST**

	GRL1110	GRD1108	GRD1003
Confining pressure	1200 g.	1200 g.	1400 g.
Oval	I	I	I
Void ratio (initial)	23.24%	18.07%	19.18%
Porosity (initial)	18.86%	15.30%	16.09%
Friction angle	26° (lubricated)	26° (lubricated)	52° (non-lubricated)
Packing	Loose		Dense
Dense			
Max shear strain	5%	5%	2%